

Abstract

This study investigates how anisotropy in solid-liquid surface energy influences orientation selection during repeated nucleation in polycrystalline film growth and its impact on crystallographic texture formation. A novel methodology was developed to determine the nucleation probability as a function of substrate and nucleus orientation, derived from the equilibrium shape of the nucleus under given conditions. Two approaches were devised to determine this shape: a multi-phase field method and an analytical geometric solution. The former, extensively developed for this work, is applicable in cases lacking an analytical solution. Multiple model variants were examined, with a custom MATLAB solver implemented to assess their performance against benchmark problems. While the models showed consistent performance in reproducing the anisotropic curvature driving force, discrepancies were found in triple junction angle benchmarks, limiting the reliability of two models to isotropic or weakly anisotropic systems.

The analytic solution enabled the creation of shape factor-orientation maps, which were used in a Monte Carlo simulation algorithm to model polycrystal growth. This simulation demonstrated how anisotropic interface energy can influence texture evolution, leading to the identification of new texture evolution modes. These findings offer a qualitative explanation for the peculiar texture evolution observed in electrodeposited nickel, providing new insights into the effects of anisotropic nucleation on material properties.

Contents

Abstract	a
Contents	c
List of Figures	g
List of Tables	k
1 Introduction	1
1.1 General introduction	1
1.2 Goals of the thesis	3
1.3 Thesis overview	4
2 Nucleation and growth in systems with anisotropic interface properties	7
2.1 Specific surface and interface energy	7
2.2 Capillarity in solids	8
2.3 Capillary vector formalism	9
2.4 Interface stiffness	10
2.5 Wulff shape	12
2.6 Force balance and stability in triple junction	13
2.7 Equilibrium shapes of a particle with anisotropic interface energy on a planar substrate	17
2.8 Other types of Wulff-shape-related constructions	18
2.9 Nucleation fundamentals	19
2.9.1 Nucleation with isotropic interface energy	22
2.9.2 Nucleation with anisotropic interface energy	25
2.9.3 Nucleation in 2D	26
2.10 Anisotropy in interface energy vs. kinetic coefficient	27
2.11 Microstructure formation in coatings	29
3 Phase field method	35

3.1	General introduction	35
3.2	Allen-Cahn equation for two-phase system	36
3.3	Allen-Cahn equation for two-phase system including anisotropic interface energy	39
3.3.1	Fundamentals	39
3.3.2	Challenges and limitations	41
3.4	Allen-Cahn equations for multi-phase systems	42
3.4.1	Historical context and current state	42
3.4.2	Challenges and limitations	45
3.5	Benchmarking of phase field models	46
4	Phase field model benchmarking	47
4.1	Introduction	47
4.2	The phase-field model	49
4.2.1	Isotropic model	50
4.2.2	Anisotropic model and parameters assignment strategies	51
4.3	Numerical implementation	58
4.4	Methodology	61
4.4.1	Used anisotropy function and its Wulff shape	63
4.4.2	Quantifying the match in shape	65
4.4.3	Quantifying match in shrinkage rate	65
4.4.4	Wulff shape	66
4.4.5	Kinetically compensated anisotropic circle shrinkage	66
4.4.6	Triple junction angles	67
4.5	Results	68
4.5.1	Wulff shapes	68
4.5.2	Kinetically compensated anisotropic circle shrinkage	71
4.5.3	Equilibrium triple junction angles	73
4.6	Conclusions	74
5	Nucleation probability assessment - a phase field methodology	77
5.1	Introduction	77
5.2	Fundamentals	78
5.3	Methodology	80
5.4	Model	83
5.4.1	General Neumann boundary conditions to control interface inclination at domain boundary	83
5.4.2	Volume conserving multi phase field models	85
5.5	Numerical implementation	87
5.6	Validations	88
5.6.1	Tilted straight line	88
5.6.2	Particle on a plane (isotropic interface energy)	90

5.6.3	Control over interface inclination with inclination-dependent interface energy	93
5.7	Domain scaling of a particle on a grain boundary intersecting the surface (isotropic interface energy)	94
5.8	Discussion	101
5.9	Limitations of the presented methodology	102
5.10	Conclusion	103
6	Analytic nucleation probability assessment and Monte Carlo simulations	105
6.1	Introduction	105
6.2	Fundamentals	108
6.2.1	Isolated particle with anisotropic interface energy	108
6.2.2	Particle with anisotropic interface energy on a plane (Winterbottom construction)	112
6.2.3	Inverted solution in Winterbottom construction	114
6.2.4	Contact point stability	116
6.2.5	Terminology in heterogeneous nucleation	117
6.2.6	Heterogeneous spatial nucleation and shape factor	118
6.3	Nucleation probability assessment	120
6.3.1	Problem statement	120
6.3.2	Stability as function of the bottom grain orientation	122
6.3.3	Shape factor-orientation maps	123
6.4	Monte Carlo simulations	125
6.4.1	Algorithm description	127
6.4.2	Validation of anisotropic growth	130
6.4.3	Methodology	130
6.4.4	Results	132
6.4.5	Comparison to experiment and discussion	136
6.5	Conclusion	139
7	General conclusion	141
7.1	Conclusion	141
7.2	Outlook	144
A	Functional derivative	147
B	Model parameters determination - best practices	151
C	Implementation of finite difference method	157
D	Volume conservation using Lagrange multipliers	169
E	Selected Wulff shape properties	175

E.1 Selected geometric properties of Wulff shape	175
E.2 Shrinkage rate of a Wulff shape	176
List of publications	195

List of Figures

2.1	Various types of anisotropy functions in 2D	14
2.2	Illustration of regularization of cusped anisotropy function	15
2.3	Illustration of a triple junction in 2D	16
2.4	Illustration of the Winterbottom construction	17
2.5	Double Winterbottom construction	19
2.6	Generalized Winterbottom construction	20
2.7	Gibbs free energy change upon a particle insertion according to CNT	23
2.8	Sketch - heterogeneous nucleus with isotropic interface energy . .	24
2.9	Sketch - heterogeneous nucleus with anisotropic interface energy .	26
2.10	Illustration of geometric similarity between Equilibrium Crystal Shape and Kinetic Crystal Shape	29
2.11	Examples of Structure Zone Model and Winand diagram	31
3.1	Interface width in phase field method	36
4.1	PF model implementation - the near-interface regions $\Gamma_{out}, \Gamma_{inn}$.	61
4.2	PF model benchmarking, sketch - initial conditions in the different numeric experiments	62
4.3	Regularization of anisotropy function	64
4.4	Demonstration of the simulated Wulff shapes	69
4.5	Quantified match to the Wulff shape for the model modifications in the base run	70
4.6	Wulff shape shrinkage rate results	71
4.7	Results for kinetically compensated anisotropic shrinkage . . .	72
4.8	Results - models comparison in triple junction angles benchmark	74
5.1	Dependence of the total energy change on the radius of the inserted nucleus in 2D	79

5.2	Sketch - PF simulation domain geometry to obtain equilibrium stable shape of a particle on a plane	80
5.3	Nucleation barrier determination using domain scaling	81
5.4	Sketch - tilted line validation of the general NBC controlling interface inclination on the domain boundary	89
5.5	Results of tilted plane validation	89
5.6	Results - simulated shapes in isotropic particle on a plane	91
5.7	Results - shape factor for isotropic particle determined by domain scaling	92
5.8	Demonstration of control over interface inclination on the domain boundary with anisotropic particle.	93
5.9	Sketch - a particle on a grain boundary	94
5.10	Initial condition examples for the simulation of a particle on a grain boundary	95
5.11	Illustration of the three considered positions of grain boundary below the nucleus.	96
5.12	Time evolution of phase field contours in the simulation of a particle on a grain boundary	97
5.13	Results from the simulation of a particle on a grain boundary - velocity of shape motion and the shape factor	98
5.14	Fit of the final PF contours of a particle on top of a grain boundary using Bézier polynomials	100
6.1	Examples of full Wulff plots with 4-fold symmetry	109
6.2	Orders of Wulff shape corners, defined by the branches intersections, shown for 6-fold anisotropy and $\delta = 0.7$	110
6.3	Complete list of non-trivial equilibrium shapes of a particle with anisotropic interface energy on a plane	113
6.4	Illustration of the inverted Winterbottom construction	115
6.5	Winterbottom construction on a weak-anisotropy Wulff	120
6.6	Shape factor-orientation maps for four different strengths of anisotropy in 4-fold symmetry (180x180 points)	124
6.7	Process map of the Monte Carlo simulation with nucleation including anisotropic solid-liquid interface energy	126
6.8	Single iteration of orientation selection algorithm	127
6.9	MC algorithm validation - mean trajectory of a triple point on the bicrystal surface	131
6.10	MC simulation results - mean number of nucleation events for different initial conditions	132
6.11	MC simulation results - deposits and their texture evolution in different nucleation scenarios in the case IC_A, $\delta = 0.5$, $n = 4$ and $\beta = 30$ (rather fast deposition)	133

6.12 MC simulation results - deposits and their texture evolution in different nucleation scenarios in the case IC_H, $\delta = 0.5$ and $\beta = 10$ (fast deposition)	134
6.13 MC simulation results - deposits and their texture evolution in different nucleation scenarios in the case IC_H, $\delta = 0.5, n = 4$ and $\beta = 90$ (very slow deposition)	134
6.14 Experimental results of Ni electrodeposited on an amorphous substrat	138
C.1 Rearrangement of the matrix representing the system before application of the discrete deferential operators.	158
C.2 Effect of Neuman BC on the 5pt laplacian stencil on the boundary points	164
C.3 Layout of the mixed boundaries	166

List of Tables

4.1	PF model - characterization of the three parameter assignment strategies	52
4.2	PF model - inclination dependence of the variable model parameters in the respective models	55
4.3	Parameters from equation (4.34) describing anisotropic dependence of the Courant number C	60
4.4	PF model benchmarking - overview of the simulations carried out in every simulation experiment	61
4.5	PF simulation - numeric settings of different simulation runs	63
5.1	PF wetting simulation - the model parameters	88
5.2	PF wetting simulation of a particle with isotropic interface energy - simulation grid dimensions	90
5.3	PF wetting simulation of a particle with isotropic interface energy on a GB - contact angles and the simulation grid	97
5.4	PF wetting simulation of a particle with isotropic interface energy on a GB - comparison of measured contact angles	99
6.1	The approximate minimal strengths of anisotropy at which the corners of indicated order appear on the Wulff shapes in 4-fold and 6-fold anisotropy	111
6.2	MC simulation - parameters included in this parameter study . .	131
B.1	Coefficients of the new polynomials used in the parameters determination algorithm (IWc and IWvG models)	153

Chapter 1

Introduction

1.1 General introduction

Crystallographic texture has a marked influence on the properties of polycrystalline coatings. Seemingly unrelated properties such as corrosion resistance, hardness, magnetic properties, porosity, and contact resistance are all texture dependent [1]. Some properties such as macroscopic magnetic anisotropy do not even exist if the sample is not textured [2].

Every deposition method has its specific parameters used to control the process. These are used to optimize the resulting textures, but the relation to the fundamental texture-forming quantities (i.e. the local conditions on the deposited material surface) is usually missing. The problem is that they are inaccessible after the deposition and it is not clear how they could be measured during the deposition.

Irrespective of which type of deposition technique is used, texture formation is controlled by interfacial energy, surface diffusivity of adatoms, grain boundary mobility and grain boundary and lattice diffusion [3, 4]. These properties together then affect the fundamental processes: nucleation, crystal growth and grain boundary motion [5]. Understanding how the texture in films is formed and how it can be controlled during the deposition process, is beneficial for the development of methods of texture optimization [3].

The anisotropy in crystal growth in general must originate from the anisotropy on the interfaces of the growing crystal with its surroundings - the substrate and the parent phase. In electrodeposition, the surface conditions may dynamically

change due to local concentration evolution of the many present thermodynamic species in the solutions and their interactions with the deposit surface.

In such situations, mathematical models of the process are useful to suggest some interpretation to the observed behaviors to gain better insight. This thesis elaborates on the possible impact of anisotropy in interface energy on the orientation selection during repeated nucleation on the course of the film growth.

Of the deposition methods, the electrodeposition is particularly interesting, because

- the (anisotropic) surface conditions are highly adjustable by additives and deposition conditions,
- the current or voltage transients provide valuable integral feedback on the surface processes in-situ, so there is more information available than in other methods,
- it is industrially relevant.

For these reasons, this thesis focuses more on electrodeposition than on other deposition methods. However, the interface energy is relevant for all the others as well, hence the implications of its anisotropy are in principle applicable to any other deposition method.

Electrodeposition is a highly industrially relevant process used for many applications like metal deposition for the fabrication of integrated circuits, deposition for magnetic recording devices (heads, disks), and deposition of multilayer structures [6], to name a few. Similarly like in other methods, the electrodeposits are usually polycrystalline and exhibit pronounced crystallographic texture, which is affected by many factors.

The interface energy is particularly important for the nucleation, which is in turn the main process of how grains with new orientations are introduced during the film growth. To the best of author's knowledge, the relation between the interface energy anisotropy and the anisotropy in nucleation barrier as function of local crystallographic orientation has not been fundamentally investigated. This work intends to bring more insight into this relation using different simulation approaches.

1.2 Goals of the thesis

There are two primary goals of this thesis:

1. Develop a methodology based on the multi-phase-field model [7] capable of determining the nucleation barrier anisotropy
2. Bring insight into the role of anisotropy in interface energy for nucleation during polycrystalline film growth and the possible impact on texture evolution.

To achieve these goals, several key tasks must be undertaken. The initial step involves developing and benchmarking the multi-phase-field model with the inclusion of anisotropic interface energy. Since existing variants of the model have not consistently incorporated inclination-dependent interface energy, it is necessary to derive the governing equations for each of these variants. Quantitative benchmark problems will then be defined to validate the model's implementation and assess its ability to capture the anisotropic curvature driving force. A custom numerical solver will be developed to facilitate these comparisons, and conclusions will be drawn regarding the most suitable model variant for the application at hand.

Another important task is to establish a methodology that uses the multi-phase-field model to determine nucleation barrier anisotropy. This involves conceptualizing the entire methodology, specifying the model requirements and simulation geometry, and, if needed, extending the model further. Once developed, the model will be implemented and validated by applying it to a problem with a known solution. Its applicability will then be demonstrated on a more complex problem where no known solution exists, showing the methodology's practical value.

A subsequent critical step is investigating how the anisotropy of nucleation barrier relates to the anisotropy in interface energy and local crystallography. This requires a thorough analysis of the problem and the creation of a solver that can compute the nucleation barrier for each pair of substrate and particle orientations. The resulting solver will be used to explore how nucleation barriers depend on these orientations. In order to provide relevant resolution in the 2D space of orientations (of the nucleus and substrate), the solver must be reasonably efficient.

Furthermore, to illustrate how nucleation barrier anisotropy can influence texture evolution during film growth, a 2D Monte Carlo simulation will be developed. This simulation will incorporate an orientation-sampling algorithm based on anisotropic nucleation probability and will be validated to ensure

accuracy. A parameter study will be conducted to examine the effect of isotropic and anisotropic interface energy on texture evolution under different conditions.

In addition to these technical milestones, the gained theoretical insights will be applied to a real-world practical system, demonstrating the broader relevance of the findings. Finally, the research will conclude with a synthesis of the results, outlining directions for future studies that can build upon the work presented in this thesis.

Overall, this work will contribute both methodologically and theoretically to the understanding of nucleation barrier anisotropy and its implications for polycrystalline film growth.

1.3 Thesis overview

This thesis explores how anisotropy in surface energy affects the course of crystallographic texture evolution in polycrystalline coatings, with emphasis on orientation selection in repeated nucleation seen within the framework of classical nucleation theory.

The Chapters 2 and 3 provide the necessary fundamentals and relevant literature review. The subsequent chapters contain the original research carried out by the author.

The Chapter 2 provides fundamentals related to the surface energy, like the capillary vector formalism used to describe its anisotropy, interface stiffness, the Wulff shapes, the force balance in triple junctions and Winterbottom construction to obtain equilibrium stable shapes on a plane. Fundamentals of classical nucleation theory are provided as well.

The Chapter 3 introduces the phase-field method. In a step-wise manner, the fundamentals of the method are covered. First, the Allen-Cahn equation is described, which represents phase evolution under the effect of isotropic curvature driving force. Then, the standard ways of adding a) anisotropy in interface energy, b) multiple phase-fields in the simulation domain (and both) are reviewed. Challenges and limitations of the various phase-field models are discussed. Also, a section was included, commenting on the importance of benchmarking the performance of applied multi-physics phase-field models and the current practice of their usage and presentation within the scientific community.

In the Chapter 4, there is a comprehensive description of an existing multi-phase field model and how and why it was extended. Three different variants

of the same model were obtained. Two different benchmark problems to quantitatively test how the models reproduced the anisotropic curvature driving force were developed. A thorough parameter study was conducted to provide exhausting information on the model behavior in different settings. Only in a third benchmark problem involving triple junctions showed, that there was in fact a significant difference in the behavior of the model variants. Results in this chapter were published in [8].

The Chapter 5 presents the *domain scaling* methodology, which was developed to determine so-called shape factor of a heterogeneous nucleus. That quantity is closely tied with nucleation barrier and thus the nucleation probability. The multi-phase field model was used to obtain the equilibrium stable shape of nucleus needed for *domain scaling* to work. Because the model extensions carried out in Chapter 4 were still not sufficient to realize the developed methodology, additional extensions were introduced, building on top of the knowledge and implementation in Chapter 4. The methodology was validated and showcased on an example of a nucleus on top of a grain boundary within a substrate, which is a case where the shape does not have analytic solution.

Then follows the Chapter 6, which employs the so-called Winterbottom construction to obtain the equilibrium stable shape of the nucleus. Because this method is very computationally efficient, the nucleation barrier as function of the substrate and nucleus orientation could be determined with great resolution. The obtained *shape-factor-orientation maps* are a visualization of the nucleation barrier orientation dependence (orientation of both the substrate and nucleus with anisotropic interface energy). These were then used as an input to a custom orientation-sampling algorithm for the nuclei. Using this, the orientation of nuclei introduced during a Monte Carlo simulation of 2D polycrystalline film growth was determined. A parametric study was conducted to identify the impact of the anisotropy in interface energy on the texture evolution, when compared to the isotropic interface energy. The obtained insights were used to qualitatively explain an abrupt change in texture which observed in electrodeposited nickel [9]. Results in this chapter were published in [10].

The Chapter 7 summarizes the work and its main contributions and proposes directions for future research.

A number of appendices are included in the work to provide relevant information, which was not essential for understanding the results in the main text. They mostly contain mathematical derivations, details on implementation of numerical methods or other supplementary information improving transparency and reproducibility of this research. In order to achieve even higher reproducibility, all the source MATLAB code used to deliver the results in the published works was made available in online repositories [11] and [12], together with usage

instructions.

Chapter 2

Nucleation and growth in systems with anisotropic interface properties

2.1 Specific surface and interface energy

Be there an isothermal isolated thermodynamic system consisting of a block of solid material in a vacuum. When the block is reversibly cleaved, two equal areas A are created on each side of the cleavage, newly facing the vacuum. The total energy change upon cleavage is equal to the reversible work W done on the system. The reversible work thus transforms into *surface energy* (unit J) of the cleavage areas $W = 2A\sigma$, where the symbol σ stands for the *specific surface energy* (unit J/m²) [13].

Should the system consist of the solid block within a liquid, the specific surface energy would be lower due to interactions between the liquid and solid (e.g. specific interactions of the molecules within the liquid with the surface or double layer formation in case of electrified surface). The same in fact holds for blocks of two different materials joined together by an *interface*, meaning that the *interface energy* will be lower than the sum of the individual surface energies (by *adhesion energy*). The interface is then characterized by *specific interface energy*. Even though some sources strictly distinguish the *interface* to occur between two solid phases and use the word *surface* for the solid in both vacuum or liquid [13], it is valid to see the *interface* between two dissimilar phases (e.g.

solid and liquid) and reserve the term surface energy strictly for the solid in vacuum. This thesis rather sees what separates the liquid from solid as *interface*, but care was taken to be always explicit enough to make it clear what is the particular quantity in question.

The word *specific* in the *specific surface energy* indicates that the quantity is intensive, i.e. in this case per unit of area. However, especially in phase field literature it is rather common to denote the intensive quantity simply by *surface energy* or *interface energy*. These two are often used interchangeably in this thesis.

In liquid-gas or liquid-liquid interfaces, the terms surface tension or surface stress are sometimes used interchangeably. There, they are equivalent in meaning to the surface energy as defined above [14]. However, in solid-fluid or solid-solid interfaces the term surface stress is reserved for the reversible work carried out in elastic deformation of an existing surface with a given surface energy [14]. Because this thesis does not involve deformation of the interfaces in any way, it will not be discussed further.

2.2 Capillarity in solids

In the context of understanding how the shape of solids is affected by anisotropic interface energy, the concept of capillarity plays a crucial role. Anisotropic interface energy means that the energy associated with a surface varies depending on its orientation. This variation in surface energy impacts the equilibrium shape of a solid, particularly for crystals where the atomic arrangement varies across different facets. Capillarity is linked to this, as it refers to the phenomenon where surface tension (interface energy) influences the curvature and shape of the interface between two phases, such as a solid and a liquid or vapor.

The Gibbs-Thomson equation is fundamental to this discussion as it describes how the equilibrium chemical potential between a small crystal and its surrounding phase (often vapor) depends on the crystal's curvature. For a spherical droplet, the equation links the chemical potential of the vapor in equilibrium with the droplet to the radius of the droplet and the surface energy. However, when the surface energy is anisotropic, as it often is for crystalline materials, the classic Gibbs-Thomson equation needs to be generalized. In this generalized form, it accounts for the anisotropic surface energy and describes how the shape of a crystal, in equilibrium with its vapor, adjusts to minimize the total free energy [15, 16].

The Herring equation further refines this by providing a way to describe the

equilibrium chemical potential at different points on a crystal's surface, taking into account the surface's curvature and anisotropy. Herring's work shows that the equilibrium shape of a crystal is the one that minimizes the total surface free energy, a concept captured by Wulff's construction. Wulff's theorem geometrically determines the equilibrium shape of a crystal from the anisotropic surface energy by constructing a surface that has the lowest energy for a given volume [15].

The importance of these equations lies in their ability to predict and control material properties. In processes like Ostwald ripening, where small particles dissolve and larger ones grow, the shape and size of precipitates are influenced by these principles. Similarly, in metallurgical processes involving solidification, the anisotropy of interface energy can determine whether the resulting microstructure is dendritic or faceted, which in turn affects the material's mechanical properties. Understanding and manipulating these energies and equations allow scientists and engineers to tailor materials for specific applications [16].

2.3 Capillary vector formalism

Let the interface energy σ depend on the local orientation of the interface described by its unit normal \mathbf{n} , i.e. $\sigma = \sigma(\mathbf{n}) = \sigma_0 h(\mathbf{n})$. The function $h(\mathbf{n})$ is called anisotropy function and σ_0 is a scaling parameter with dimensions of interface energy. Formal requirements on the anisotropy function can be found e.g. in [17]. A very useful formalism for thermodynamic description of these anisotropic interfaces is the so-called capillary vector ξ (a.k.a. Cahn-Hoffmann vector or ξ -vector), defined as [18, 19]

$$\xi = \text{grad}(r\sigma(\mathbf{n})), \quad (2.1)$$

where r is radial distance from the origin, which can be also seen as the magnitude of the scaled normal vector $\mathbf{r} = r\mathbf{n}$. Level sets of the scalar function $r\sigma(\mathbf{n})$ are geometrically similar to the anisotropy function $h(\mathbf{n})$, which is continuously scaled by the radius r .

Capillary vector was introduced and investigated by Hoffman and Cahn in [18, 19], who showed that this formalism is consistent with major laws governing behavior of (anisotropic) interfaces like Gibbs-Thompson equation (relating chemical potential and isotropic surface curvature), Herring's equation (chemical potential on anisotropic curved surface), Wulff shape construction, force balance at multi-junctions and others.

A defining property of capillary vector is that its component normal to the surface ξ_{\perp} is in magnitude equal to the local value of the interface energy and the surface-tangent component points in the direction of steepest change in interface energy and is proportional to the change. More specifically

$$\xi_{\perp} = \boldsymbol{\xi} \cdot \mathbf{n} = \sigma(\mathbf{n}) \quad (2.2)$$

$$\xi_{\parallel} = \left(\frac{\partial \sigma}{\partial \theta} \right)_{max}, \quad (2.3)$$

where θ is the angle representing change in orientation of \mathbf{n} in the direction of maximal angular rate change. The vector can thus be written

$$\boldsymbol{\xi}(\mathbf{n}) = \sigma(\mathbf{n})\mathbf{n} + \left(\frac{\partial \sigma}{\partial \theta} \right)_{max} \mathbf{t}, \quad (2.4)$$

with \mathbf{t} being unit vector tangent to the surface pointing in the described direction. Useful is expression of capillary vector in spherical coordinates

$$\boldsymbol{\xi}(\theta, \phi) = \sigma(\theta, \phi)\hat{\mathbf{r}} + \left(\frac{\partial \sigma}{\partial \theta} \right) \hat{\mathbf{\theta}} + \frac{1}{\sin(\theta)} \left(\frac{\partial \sigma}{\partial \phi} \right) \hat{\mathbf{\phi}}, \quad (2.5)$$

which is only function of the polar and azimuthal angle θ, ϕ , respectively. In 2D in polar coordinates the normal and tangent vector can be written as functions of the interface normal angle θ as

$$\boldsymbol{\xi}(\theta) = \sigma(\theta) \begin{bmatrix} \cos(\theta) \\ \sin(\theta) \end{bmatrix} + \left(\frac{\partial \sigma}{\partial \theta} \right) \begin{bmatrix} -\sin(\theta) \\ \cos(\theta) \end{bmatrix}. \quad (2.6)$$

2.4 Interface stiffness

The interface stiffness is the coefficient of the interface curvature in the description of the capillarity contribution to the chemical potential. In curvature-driven interface migration, the interface velocity is proportional to the interface stiffness, mobility and curvature. [20] The so-called Herring's equation originally published in 1951 and reprinted in [21] states the chemical potential of atoms on a curved surface μ_{surf} due to the capillarity in a point P

$$\mu_{surf} = V_m \left(\sigma + \frac{\partial^2 \sigma}{\partial n_1^2} \right) \frac{1}{R_1} + V_m \left(\sigma + \frac{\partial^2 \sigma}{\partial n_2^2} \right) \kappa_2 \quad (2.7)$$

where n_1, n_2 are the orthogonal projections of the variable unit vector \mathbf{n} , on which the surface energy $\sigma(\mathbf{n})$ depends, onto a plane tangent to the surface

at the point in question, the direction axis 1 being chosen in the direction of the principal curvature $1/R_1$, the y axis in that of $1/R_2$ and V_m is the molar volume [21]. For isotropic interface energy σ

$$\mu_{surf} = V_m \sigma (\kappa_1 + \kappa_2) \quad (2.8)$$

which means the chemical potential is proportional to mean curvature in the point P.

In 2D, the Herring equation simplifies to

$$\mu_{surf} = V_m (\sigma + \sigma''(\theta)) \frac{1}{R}, \quad (2.9)$$

where a prime indicates differentiation and θ is angle of the normal to the surface.

The interface stiffness $\hat{\sigma}$ in 2D is the scalar quantity $\hat{\sigma} = \sigma + \sigma''(\theta)$, whereas in 3D it is a 2nd rank tensor (i.e. 2x2 matrix), the diagonal terms of which in principal coordinates are $(\sigma + \frac{\partial^2 \sigma}{\partial n_1^2}), (\sigma + \frac{\partial^2 \sigma}{\partial n_2^2})$ [20, 22–24].

The interface velocity due to capillary forces alone v_σ is proportional to the chemical potential and the interface mobility M [20–24]

$$v_\sigma = M \mu_{surf}, \quad (2.10)$$

which is valid in this form for both 2D and 3D. This is the way the capillary driving force moves the surface. As a result, the interface stiffness is the key material property that relates interface curvature to interface thermodynamics and kinetics. [20]

Interface stiffness tensor in 3D is very difficult to measure [20]. Efforts were made to determine it from models of the interfaces, like e.g. in [20], using molecular dynamics simulations [22, 23] or phase-field crystal method [25]. An attempt to measure part of the anisotropy in grain boundary energy in the Pb-Sn system experimentally was carried out in [26].

Once the values of the anisotropic interface energy are known in the different directions, the interface stiffness can be computed. In the work [27], Olmsted carried out a large number of atomistic calculations to provide the grain boundary energy in Al and Ni (face centered cubic metals). These results were later generalized to any fcc metal using a model with only two input material-specific parameters using MATLAB program GB5DOF [28] and recently were fitted to provide the interface stiffness for selected grain boundary types [24].

2.5 Wulff shape

Wulff shape is such a shape, which minimizes the interface energy given a constant volume. In 2D it can be obtained as the inner convex hull of all straight lines perpendicular to the radial direction drawn in every point of the anisotropy function $h(\theta)$ in polar coordinates. This can be used to define the Wulff shape W as a set of points \mathbf{x} [17, 29, 30] (here in 2D)

$$W = \{\mathbf{x} \in \mathbb{R}^2 | \mathbf{x} \cdot \mathbf{n} \leq \sigma(\mathbf{n}) \text{ for all } \mathbf{n} \text{ on unit circle}\}, \quad (2.11)$$

which is algebraic representation of what was said above - a point \mathbf{x} is part of the Wulff shape when its projection to a direction \mathbf{n} is lesser than value of the anisotropy function for that angle $f(\mathbf{n})$. Every point in the \mathbb{R}^2 plane is assessed for all possible directions \mathbf{n} . In 2D, this condition produces the above mentioned straight lines passing through heads of radial vectors ending on the anisotropy function. Their inner hull are the points which belong to Wulff shape. This construction is illustrated in Figure 2.1 in the last column of graphs for different anisotropy functions.

When the heads of capillary vectors for all interface normal angles θ are connected (having a common starting point in the origin), so-called ξ -plot is obtained. It turns out, that the ξ -plot coincides with the Wulff shape [17, 18] (see third column in Figure 2.1a). Hence, the parametric expression (2.6) can be used to plot the 2D Wulff shape in Cartesian coordinates. This is entirely true as long as there are no corners or facets on the Wulff shape, in which cases the use of capillary vector for Wulff shape plotting must be appropriately modified (see below for details).

In [19] the authors re-state the problem of finding equilibrium shapes of crystals with anisotropic interfaces under general conditions. The shape is found as a solution to equation

$$\Delta\Omega_v + \nabla_S \cdot \boldsymbol{\xi} = 0, \quad (2.12)$$

where $\Delta\Omega_v$ is the bulk driving force, specifically the difference in grand-canonical potential of the two phases, and $\nabla_S \cdot$ is surface divergence. The surface \mathbf{r} is sought, complying with the above equation. A simple trick is used to find the shape of an isolated particle. Surface divergence over the surface itself is simply $\nabla_S \cdot \mathbf{r} = 2$, hence we can write

$$1 = \nabla_S \cdot \mathbf{r}/2 = -\nabla_S \cdot \boldsymbol{\xi}/\Delta\Omega_v \quad (2.13)$$

$$\nabla_S \cdot (\mathbf{r} + 2\boldsymbol{\xi}/\Delta\Omega_v) = 0, \quad (2.14)$$

leading to the result

$$\mathbf{r} = -\frac{2}{\Delta\Omega_v} \boldsymbol{\xi}. \quad (2.15)$$

This is why the ξ -plot coincides with the Wulff shape.

Two different types of singularities may occur in Wulff shapes, which must be treated in a specific way: corners and facets [17, 31]. These are related to two specifics of the anisotropy function: (i) the corners are related to non-convexity of the Frank's plot $1/h(\theta)$ (non-convex means that there are two such points, which when connected by a straight line will have the connecting line passing outside of the shape) and (ii) the facets occur in anisotropy functions which are not twice differentiable, hence their interface stiffness cannot be computed.

Corners represent a discontinuity of normal angle along the Wulff shape perimeter. They occur when the anisotropy of the interface energy is such, that interface stiffness gets negative for some normal angles θ_f . These angles are called forbidden, because they are thermodynamically unstable. For this reason, they are not present on the Wulff shape. They always lay in an interval of angles, for which the Frank's plot $1/h(\theta)$ is non-convex. Examples of such anisotropy functions are in the first column of Figures 2.1b-d, their Frank's plots are in the second column.

There are normal angles θ , which have positive interface stiffness, but regardless do not appear on the Wulff shape because they belong to the non-convex part of the Frank's plot. These angles and the forbidden ones form the "ears" which can be seen in the Figure 2.1b, third column with ξ -plot of this anisotropy function. By replacing the non-convex part of this function by straight lines in Frank's plot a regularized inverse anisotropy function $1/\bar{h}(\theta)$ is obtained (see Figure 2.1c, second column). Wulff shape corresponding to the regularized anisotropy function $\bar{h}(\theta)$ does not contain the "ears" behind the corners (see Figure 2.1c, third column). The interface stiffness of both the allowed and forbidden angles which form the "ears" were effectively set to zero.

The facets occur under angles where there are cusps in the anisotropy function (see Figure 2.1d, first column). The angles for which there is a cusp in the anisotropy function do not have defined the derivative $d/d\theta$. In practical simulations, this can be solved by replacing the anisotropy function by such, which is continuous and twice differentiable, but closely approximates the cusped function, see e.g. [32, 33]. This principle is illustrated in Figure 2.2.

2.6 Force balance and stability in triple junction

A triple junction in 2D is simply a point and a force balance between the three meeting interfaces is achieved if the capillary vectors of the three interfaces sum

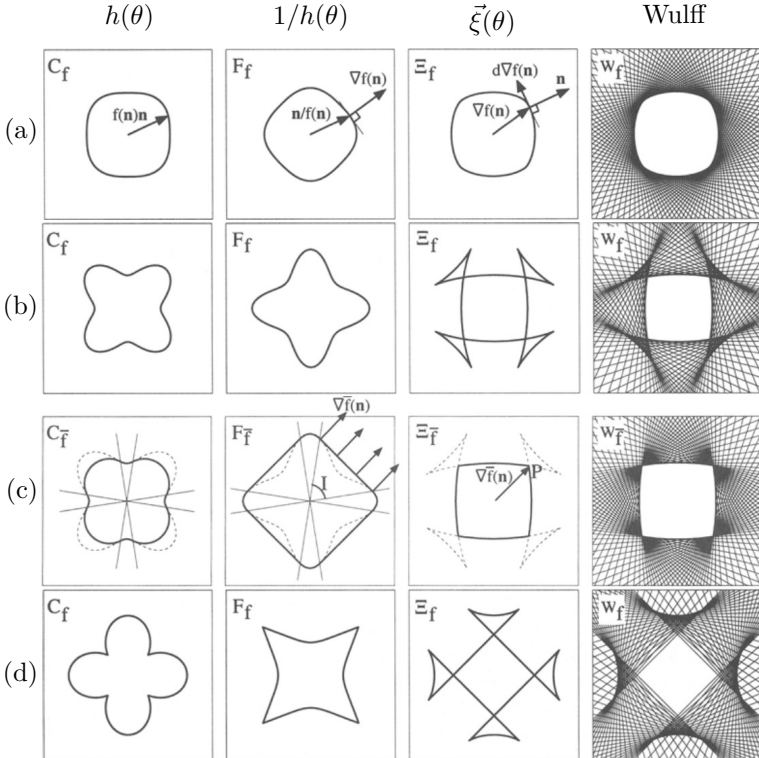


Figure 2.1: Illustration of various anisotropy functions and their singularities, taken from [17]. In every column there are, respectively: anisotropy function $h(\theta)$, its Frank's plot $1/h(\theta)$, its ξ -plot and the Wulff shape with indication of the straight lines used in its construction. The rows correspond to different anisotropy functions: in (a) $h(\theta) = 1 + \delta \cos(4\theta)$ with $\delta = 0.05$ (convex, twice differentiable in θ), in (b) $h(\theta) = 1 + \delta \cos(4\theta)$ with $\delta = 0.25$ (non-convex, twice differentiable in θ), in (c) thick lines indicate regularized anisotropy function from (b), which is dashed in the respective graphs (convexified, twice differentiable in θ). In (d) there is $h(\theta) = 1 + \alpha(|\cos(2\theta)| - 1/2)$ with $\alpha = 0.25$ (non-convex, not twice differentiable in θ).

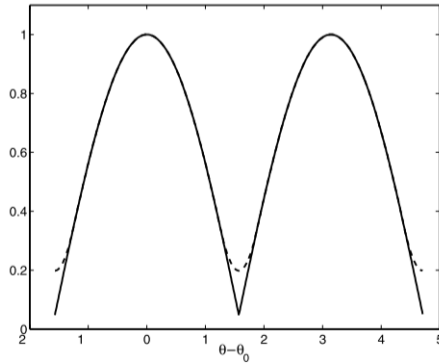


Figure 2.2: Illustration of regularization of cusped anisotropy function. Such an anisotropy function is used instead of the cusped one, which deviates only in the vicinity of the cusp. There, it is twice differentiable and thus the interface stiffness is defined for every θ . Curvature of the rounded cusp is scalable by setting a function parameter to appropriate value, i.e. it can be made much smaller to improve the approximation.

to zero, i.e. [18]

$$\xi_{12} + \xi_{23} + \xi_{13} = 0. \quad (2.16)$$

This is equivalent to so-called Herring relations which were published in 1951 [21] and were re-derived by Marks [34]

$$\sum_{i=1}^3 \left[\sigma_i(\vartheta_i) \hat{\mathbf{t}}_i + \frac{d\sigma_i}{d\vartheta_i} \hat{\mathbf{n}}_i \right] = 0, \quad (2.17)$$

where the subscripts now denote interfaces numbered from 1 to 3. $\vartheta_1, \vartheta_2, \vartheta_3$ are angles under which the tangent of each interface is oriented (all with respect to x axis, see the Figure 2.3), the anisotropic interface energies are $\sigma_i(\vartheta_i)$. The triple junction configuration is defined by the triplet of the angles ϑ_i . However, it was pointed out, that the above equivalent conditions are only *necessary* for the triple junction configuration to be stable, i.e. it does not guarantee the configuration stability. Validity of (2.17) assures a stationary point in Gibbs free energy, but in order to have a stable configuration, the energy must be in local minimum. To confirm that, second derivatives of Gibbs free energy with respect to angles $\vartheta_1, \vartheta_2, \vartheta_3$ must be assessed, giving rise to the following two

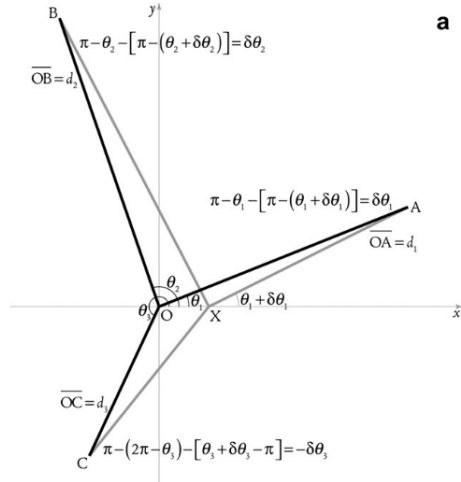


Figure 2.3: Illustration of a triple junction in 2D taken from [34]. Infinitesimal translation in x direction and the corresponding change in the triple junction configuration is illustrated. In the figure the tangent angles of the individual interfaces are denoted θ_i , whereas in the text they are written as ϑ_i .

conditions (both of which must hold in stable configuration)

$$0 < \sum_{i=1}^3 \left[\frac{d^2\sigma_i}{d\vartheta_i^2} + \sigma_i(\vartheta_i) \right] \frac{\sin^2(\vartheta_i)}{d_i} \quad (2.18)$$

$$\begin{aligned} 0 < & \left[\frac{d^2\sigma_1}{d\vartheta_1^2} + \sigma_1(\vartheta_1) \right] \left[\frac{d^2\sigma_2}{d\vartheta_2^2} + \sigma_2(\vartheta_2) \right] \frac{\sin^2(\vartheta_1 - \vartheta_2)}{d_1 d_2} + \\ & + \left[\frac{d^2\sigma_2}{d\vartheta_2^2} + \sigma_2(\vartheta_2) \right] \left[\frac{d^2\sigma_3}{d\vartheta_3^2} + \sigma_3(\vartheta_3) \right] \frac{\sin^2(\vartheta_2 - \vartheta_3)}{d_2 d_3} + \\ & + \left[\frac{d^2\sigma_1}{d\vartheta_1^2} + \sigma_1(\vartheta_1) \right] \left[\frac{d^2\sigma_3}{d\vartheta_3^2} + \sigma_3(\vartheta_3) \right] \frac{\sin^2(\vartheta_3 - \vartheta_1)}{d_3 d_1}, \end{aligned} \quad (2.19)$$

where d_i are lengths from the triple junctions to anchor points, which are not relevant for the current work. Each term in the brackets is interface stiffness of the respective interface.

If the second condition is equal to 0, these conditions are not conclusive, i.e. it is not possible to assess the nature of the stationary point (higher-order derivatives are needed then).

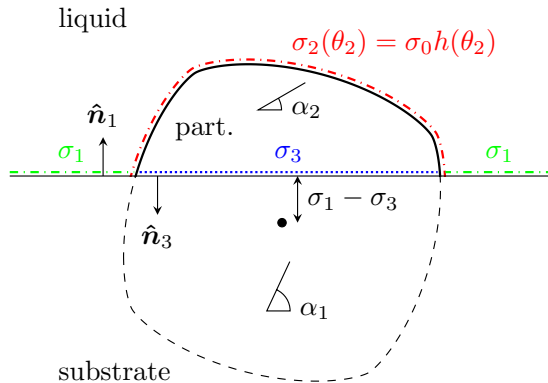


Figure 2.4: Illustration of the Winterbottom construction. The symbols $\sigma_1, \sigma_2(\theta), \sigma_3$ denote the interface energies of the respective interfaces, σ_0 is the scaling interface energy. α_1 is the orientation of the substrate, α_2 of the substrate.

The assessment of stability of triple junction configuration is an important part of discussion of an equilibrium shape of a particle with anisotropic interface energy on a substrate plane, as will be shown in Chapter 6.

2.7 Equilibrium shapes of a particle with anisotropic interface energy on a planar substrate

This problem has attracted considerable attention since it is of high practical importance, especially in applications like nucleation [35], preparation of functional deposits for electrochemical catalysis [36] or in solid-state dewetting [37–39]. The classical solution to the problem is by Kaischew for crystalline anisotropy with faceted shape [40] (cited by Milchev in [13] but the original paper was not found) and by Winterbottom [41] (interface energy as continuous function). Here it is demonstrated using the capillary vector formalism, but the described procedure in its result follows the so-called Winterbottom construction.

In the following, only 2D cross section is discussed. See the Figure 2.4 for illustration. It is assumed that the particle-substrate interface (denoted here with index 1) is linear with the substrate-parent phase (index 3), but with

anti-parallel normal vector. Let the substrate plane be parallel with x axis. The particle-parent phase interface is denoted by index 2. The normal vectors of the respective interfaces in the contact point are $\hat{\mathbf{n}}_1 = (0, 1)^T$, $\hat{\mathbf{n}}_3 = (0, -1)^T$ and $\hat{\mathbf{n}}_2$ is to be found from (2.16). Apparently, with the interfaces 1 and 3 fixed at orientations $\theta_1 = \pi/2$ and $\theta_3 = -\pi/2$, the force balance can be reduced to a single equation, when the particle-parent phase capillary vector ξ_2 is projected to the surface normal $\hat{\mathbf{n}}_S = \hat{\mathbf{n}}_3$. But that is merely the y-component of the capillary vector. The force balance can thus be written as

$$\sigma_3(\pi/2) - \sigma_1(-\pi/2) = \sigma_2(\theta_2) \sin(\theta_2) + \sigma'_2(\theta_2) \cos(\theta_2). \quad (2.20)$$

Geometric interpretation of this equation is that the force equilibrium in the triple junction is achieved when normal angle θ_2 of the particle-parent phase interface in the triple junction is that one, which has the y coordinate of the Wulff shape equal to the difference $\sigma_3(\pi/2) - \sigma_1(-\pi/2)$. The equilibrium shape of anisotropic particle on a substrate is thus that of an isolated particle but truncated at a position, which derives from the force balance in the triple junction. The truncated part of isolated particle counts, which is above the truncating line.

When all the three interfaces are isotropic, the well known Young's equation is obtained

$$\sigma_3 - \sigma_1 = \sigma_2 \sin(\theta_2) \quad (2.21)$$

$$= \sigma_2 \cos(\vartheta_2), \quad (2.22)$$

where in the second equation it was used that $\vartheta_2 = \theta_2 - \pi/2$.

2.8 Other types of Wulff-shape-related constructions

There is a whole range of Wulff-shape-related constructions [42]. This section will briefly discuss the following three, which apply to supported particles: double Winterbottom construction [43], Summertop construction [44] and generalized Winterbottom construction [39].

The double Winterbottom construction does not assume planar interface between the particle and the substrate. This applies to systems with soft substrates or where sufficient time and temperature were provided for such capillarity-induced shape modification. First, the the Winterbottom construction is applied to the supported particle (above the substrate) and then the second time

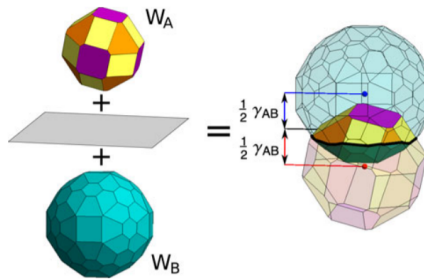


Figure 2.5: The principle of double Winterbottom construction, taken from [43].

for a hypothetical particle of a substrate material in the supported particle environment (below the substrate plane). The resulting shape is obtained as an intersection of the particles. See Figure 2.5 for illustration. It should be noted that double Winterbottom construction was not considered in the context of this thesis, because a) in repeated nucleation, the particle and substrate are of the same material, hence the substrate is not softer than the particle, and b) the deposition process is assumed to be too fast to allow for extensive shape accommodation due to capillarity. Even though the latter is no general rule, especially in electrodeposition this argument is supported by the fact that it is usually carried out near room temperature, or at least at temperatures far from the melting points.

The Summertop construction applies to equilibrium shapes in 2D space occurring in corners. This construction applies a principle of inversion, which possibly results in non-convex shapes. Using this principle in Chapter 6, new solutions for strongly anisotropic Wulff shapes were discovered.

The generalized Winterbottom construction applies to anisotropy function of the type $h(\theta) = 1 + \delta \cos(n\theta)$ with strong anisotropy (where the Wulff shape has corners and "ears" behind them). The Winterbottom construction is extended by including the allowed-angle parts of the "ears" in the construction, which may result in new solutions to the equilibrium stable shape, see Figure 2.6 for illustration.

2.9 Nucleation fundamentals

Great majority of phase transformations in metals occurs by nucleation and growth [45]. Nucleation is the physical process in which tiny crystals or clusters

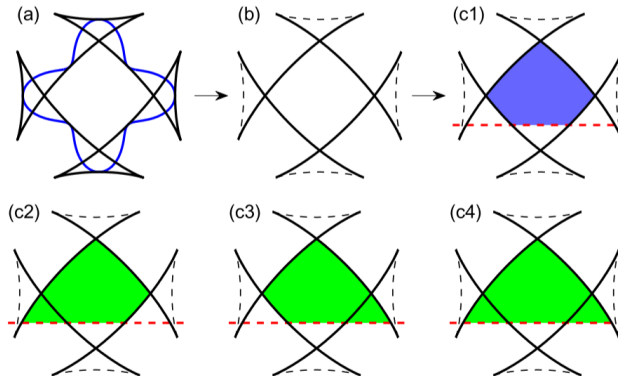


Figure 2.6: The principle of Generalized Winterbottom construction, taken from [39]. In (a) the anisotropy function and Wulff shape with "ears", in (b) the forbidden angles were disregarded from the Wulff shape, in (c) the solution given by regular Winterbottom construction and in (c1)-(c3) the new solutions enabled by inclusion of the allowed parts of the "ears".

of a new phase appear at certain sites within the matrix of a metastable parent phase. Once formed, these nuclei can grow on the expense of the parent phase. The nucleation rate and nuclei spatial distribution strongly affect the resulting microstructure. The above described process corresponds to homogeneous nucleation. Heterogeneous nucleation, on the other hand, involves a surface of which the nucleus appears.

Heterogeneous nucleation is closely related to film deposition. There are three different types of film growth (termed Volmer-Weber, Frank Van der Merve and Stranski-Krastanov), which are based on two growth mechanisms, termed simply 2D and 3D nucleation. In the 3D nucleation, nuclei appear on the surface of the support as localized 3D clusters and further grow in all directions. In 2D nucleation, monoatomic layers are successively deposited on top of the surface. Volmer-Weber type of growth occurs via the 3D nucleation mechanism, the Frank Van der Merve type via the 2D nucleation and Stranski-Krastanov starts with 2D nucleation but then switches to 3D nucleation. The factor deciding the nucleation mechanism are the wetting conditions, as will be described farther below.

Nucleation is a thermally activated process, hence the probability P of finding the nucleus at a certain spot follows the Arrhenius relation

$$P \approx \exp\left(-\frac{\Delta G_c^*}{RT}\right), \quad (2.23)$$

where R is the universal gas constant, T absolute temperature and ΔG_c^* is a *critical nucleation barrier*, which is to be overcome by the thermal fluctuations in order to form a stable nucleus. Nucleus with the critical volume V_c is metastable. The nucleation barrier ΔG_c^* is the *nucleation work* [13], the maximal positive change in Gibbs free energy associated with the nucleus insertion.

The Classical Nucleation Theory poses several fundamental assumptions. In the first place, it assumes that the nuclei are large enough to have defined volume and surface, i.e. that they consist of such number of atoms that is not inadequate to assume continuum-like properties. With nuclei consisting of only a few atoms, these and the derived quantities (e.g. specific surface energy) cannot be defined. Additionally, for the purpose of nucleation probability it assumes that the creation of a nucleus is an instantaneous process, where the necessary number of thermally vibrating atoms suddenly occur mutually close enough to overcame the critical nucleation barrier and became a stable growing nucleus.

"It is worth reminding that, for example, a silver sphere of a radius of only three atomic diameters already contains 106 silver atoms ($d_{\text{Ag}} = 0.252 \text{ nm}$). Cluster sizes of this order are sometimes considered as a lowest limit of the classical nucleation theory validity." [46] The above assumptions seem to be contradictory to some extent, because when imagining thermally fluctuating atoms, it is hard to imagine that *at least* hundreds of them would collide at the same time near a single point and instantaneously thus overcame the nucleation barrier. Some limitations of the classical nucleation theory in this regard are solved by atomistic nucleation theory, which drops the assumption on the continuum and allows to work with individual atoms in the cluster [46, 47].

Shape of the nucleus is strongly determined by the interface energy anisotropy. More specifically, shape of the critical nucleus is such, which minimizes the interface energy, because any other shape would give rise to larger surface energy contribution. The equilibrium shape with isotropic interface energy is a sphere, with an anisotropic one it is a Wulff shape.

Below, the different basic cases are introduced, starting with homogeneous nucleation with isotropic interface energy, then heterogeneous nucleation with isotropic interface energy and subsequently the anisotropic interface energy is introduced. The basis of the analysis rests always on the assessment of the total energy change in the system upon insertion of the nucleus. The total energy change depends on the exact values of the bulk and interface energy contributions in the respective cases.

2.9.1 Nucleation with isotropic interface energy

Homogeneous nucleation

In homogeneous nucleation isolated nuclei within a parent phase form. The equilibrium shape is a sphere with radius R , surface area $A = 4\pi R^2$ and volume $V_{hom} = (4/3)\pi R^3$. The total system energy change upon insertion of one spherical nucleus is due to replacement of the parent phase by the nucleated one in volume V_{hom} (resulting in reduction of total energy, because there is a driving force to form the nucleated phase) and due to the interface creation A (resulting in energy increase). Let the parent phase be denoted by 1 and the nucleated one 2. The difference in the individual energy densities is $\Delta G_v = G_v^1 - G_v^2$ and the interface energy 1-2 be σ . The change in Gibbs free energy ΔG_{hom} as function of the particle radius is

$$\Delta G_{hom} = -\Delta G_v V_{hom} + \sigma A \quad (2.24)$$

$$= \frac{4}{3}\pi(-\Delta G_v R^3 + 3\sigma R^2), \quad (2.25)$$

and was visualized in Figure 2.7a. From (2.25) the expression for the critical radius R_c is found as stationary point $d(\Delta G_{hom})/dR = 0$, giving the classical result

$$R_c = \frac{2\sigma}{\Delta G_v} \quad (2.26)$$

and the nucleation barrier is the energy difference value $\Delta G_{hom}(R_c)$ (as can be seen in Figure 2.7a)

$$\Delta G_{hom}(R_c) = \Delta G_c^* = \frac{4}{3}\pi \frac{4\sigma^3}{\Delta G_v^2} \quad (2.27)$$

$$= \hat{V}_{hom} \frac{4\sigma^3}{\Delta G_v^2}, \quad (2.28)$$

where in the second line there was introduced a non-dimensional volume of homogeneous nucleus $\hat{V}_{hom} = V/R^3$.

Heterogeneous nucleation

In Figure 2.8 there is illustrated a 2D section through a hemispherical cap on a plane. The three different phases or grains are 1, 2 and 3. Interfaces 1-3 and 2-3 form the substrate plane and are assumed to be immobile. The equilibrium angle α must establish a balance of the tractions due to surface energies of

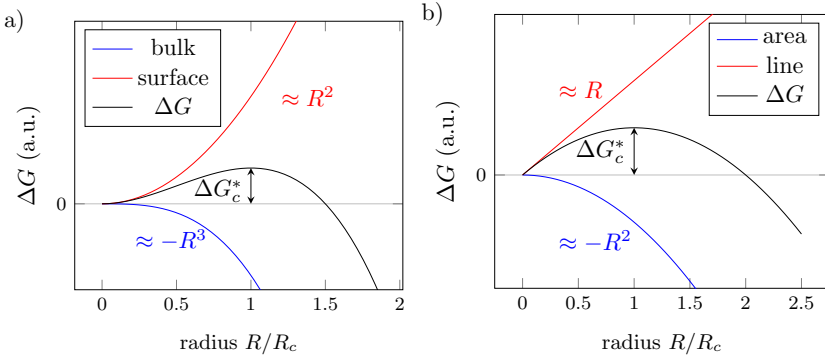


Figure 2.7: Bulk (blue) and interface (red) energy contributions to the Gibbs free energy change ΔG (black) upon nucleus insertion as function of nucleus radius R/R_c . Nucleation barrier ΔG_c^* indicated. In a) as applicable to 3D geometry, in b) as to 2D geometry (see text for details).

the three distinct interfaces. When the three tractions are projected to the substrate plane, the Young's equation is obtained

$$\sigma_{1,3} = \sigma_{2,3} + \sigma_{1,2} \cos(\alpha), \quad (2.29)$$

which allows to find the wetting angle α

$$\alpha = \arccos \left(\frac{\sigma_{2,3} - \sigma_{1,3}}{\sigma_{1,2}} \right). \quad (2.30)$$

The distance of the sphere center to the substrate plane is $R \cos(\alpha)$, which implies

$$\Gamma = \cos(\alpha) = \frac{\sigma_{2,3} - \sigma_{1,3}}{\sigma_{1,2}}. \quad (2.31)$$

Upon the nucleus 2 insertion, the change in Gibbs free energy is

$$\Delta G_{het} = -\Delta G_v V_{het} + (\sigma_{2,3} - \sigma_{1,3}) A_{2,3} + \sigma_{1,2} A_{1,2} \quad (2.32)$$

$$= \frac{4}{3} \pi (-\Delta G_v R^3 + 3\sigma R^2) S(\theta), \quad (2.33)$$

where $S(\theta) = (2 + \cos \theta)(1 - \cos \theta)^2/4$ is the so-called shape factor. The second equation was obtained by using the expressions for the spherical cap volume¹,

¹ $V_{het} = \pi R^3 (2 + \cos \theta)(1 - \cos \theta)^2/3$

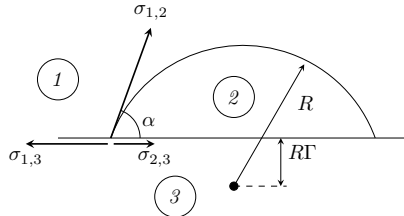


Figure 2.8: Heterogeneous nucleation with isotropic interface energy. Force balance in the contact point during surface of 3 wetting by a nucleus of 2 emerging from 1. Nucleus radius R and equilibrium shape center indicated.

area² and with $A_{2,3}$ being a disc³. Two features of (2.33) are to be noted. First, the heterogeneous ΔG_{het} is equal as in (2.25) except for the factor $S(\theta)$, and second, the $S(\theta) = V_{het}/(\frac{4}{3}\pi R^3) = V_{het}/V_{hom}$. The shape factor is thus the ratio of the equilibrium volumes of the heterogeneous and homogeneous nuclei of the same interface energy $\sigma_{1,2}$.

Because the R -dependence in $\Delta G_{het}(R)$ is equal as in $\Delta G_{hom}(R)$, the critical radius is as in (2.26), hence the critical nucleation barrier is

$$(\Delta G_c^*)_{het} = \hat{V}_{hom} S(\theta) \frac{4\sigma^2}{\Delta G_v} \quad (2.34)$$

$$= (\Delta G_c^*)_{hom} S(\theta) \quad (2.35)$$

Shape factor $S(\theta)$ is thus not only ratio of the equilibrium nuclei volumes, but also of the nucleation barriers. The shape factor with isotropic interface energy is always $0 \leq S(\theta) \leq 1$. The balance of forces along the contact point of the three phases determines wetting of the surface by the nucleus 2 which in turn decides about the shape factor and thus the nucleation barrier and also the nucleation mechanism.

Should the wetting parameter Γ be close to or larger than 1, then (nearly) nothing remains of the nucleus *above* the support plane, the shape factor is (nearly) $S = 0$ and the 2D nucleation occurs.

² $A_{1,2} = 2\pi R^2(1 - \cos \theta)$

³ $A_{2,3} = \pi(R \sin \theta)^2$

2.9.2 Nucleation with anisotropic interface energy

When the 1-2 interface energy is anisotropic, the mathematical formalism gets more complicated, but the underlying principles are identical with those in the isotropic case. The Gibbs free energy change is again due to competition between the volumetric and interface energy contributions, but now the interface energy is a function of the interface normal \mathbf{n} , i.e. $\sigma = \sigma(\mathbf{n}) = \sigma_0 f(\mathbf{n})$, with σ_0 being a scalar and $f(\mathbf{n})$ an anisotropy function. The nucleus volume is V_{hom}^{ani} and its interface with parent phase is a parameteric surface \mathcal{S} . Due to the anisotropy, the interface energy contribution is obtained as a surface integral of $\sigma(\mathbf{n})$ over \mathcal{S} , giving (in homogeneous nucleation) the Gibbs free energy difference

$$\Delta G_{hom}^{ani} = -\Delta G_v V_{hom}^{ani} + \int_{\mathcal{S}} \sigma(\mathbf{n}) dA. \quad (2.36)$$

In [48] it was shown, how this can be worked out using the Cahn-Hoffmann ξ -vector formalism to reach the familiar expression

$$\Delta G_{hom}^{ani} = (-\Delta G_v X_0^3 + 3\sigma_0 X_0^2) \hat{V}_{hom}^{ani}. \quad (2.37)$$

where X_0 is a scaling parameter for the nucleus size and \hat{V}_{hom}^{ani} the non-dimensional volume $\hat{V}_{hom}^{ani} = V_{hom}^{ani}/X_0^3$. As can be seen, the formulas for isotropic critical radius (2.26) and critical nucleation barrier (2.28) can be generalized for the anisotropic case as

$$X_c = \frac{2\sigma_0}{\Delta G_v} \quad (2.38)$$

and

$$(\Delta G_c^*)_{hom}^{ani} = \hat{V}_{hom}^{ani} \frac{4\sigma_0^2}{\Delta G_v}. \quad (2.39)$$

Also the anisotropic heterogeneous nucleation shows many similarities to the isotropic case. It was already shown by Cahn [19], that when the contact line of the substrate and particle is a closed planar curve, the equilibrium heterogeneous nucleus is obtained by truncation of the Wulff shape (in the isotropic case a sphere was truncated). The wetting conditions develop from the force balance along the contact line. That decides how the Wulff shape should be truncated. The force balance includes some extra terms compared to the isotropic case, which will be discussed in the next section.

The shape factor $S(\Gamma, \mathbf{n}_\beta) = V_{het}^{ani}/V_{hom}^{ani}$ represents the ratio of volume of the truncated portion of the Wulff shape relative to volume of the untruncated one. It depends on the wetting condition, described by parameter

$$\Gamma = (\sigma_{2,3} - \sigma_{1,3})/\sigma_0 \quad (2.40)$$

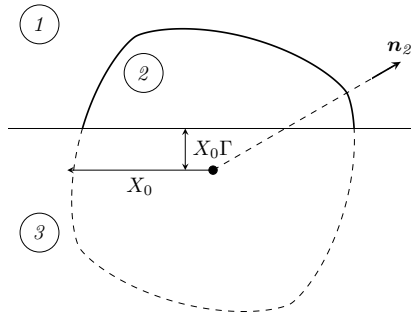


Figure 2.9: Anisotropic nucleus of phase 2 oriented under direction \mathbf{n}_2 wetting the supporting plane 3. Generalized radius X_0 and center shift are indicated.

and on the nucleus orientation relative to the supporting plane \mathbf{n}_2 . As in the isotropic case,

$$\Delta G_{het}^{ani} = \Delta G_{hom}^{ani} S(\Gamma, \mathbf{n}_\beta), \quad (2.41)$$

which together with (2.50) implies that also in the anisotropic case the shape factor relates the nucleation barriers as

$$(\Delta G_c^*)_{het}^{ani} = (\Delta G_c^*)_{hom}^{ani} S(\Gamma, \mathbf{n}_\beta). \quad (2.42)$$

2.9.3 Nucleation in 2D

Not to be confused with 2D nucleation. 2D nucleation is a process occurring in 3D space, while this section discusses the ideas from the above sections in two-dimensional space. The ideas are equally valid in 2D, but the removed dimension has its consequences on the formulas. Importantly, the volumes are replaced by areas and the surfaces by lines. The Gibbs free energy difference upon a nucleus insertion in the system is then due to competition between area and line energy contributions (see also Figure 2.7b). Be A_{hom} the nucleus area and its interface be described by a parametric curve \mathcal{C} . In the isotropic case \mathcal{C} is a circle and the interfacial contribution is simply σL , where $L = 2\pi R$ is the interface length. The Gibbs free energy difference of a free nucleus is then (with ΔG_A being supersaturation)

$$\Delta G_{hom} = -\Delta G_A A_{hom} + \sigma L \quad (2.43)$$

$$= (-\Delta G_A R^2 + 2R\sigma)\pi, \quad (2.44)$$

which implies the critical radius

$$R_c = \frac{\sigma}{\Delta G_A} \quad (2.45)$$

and critical nucleation barrier

$$(\Delta G_c^*)_{hom} = \hat{A}_{hom} \frac{2\sigma^2}{\Delta G_A}, \quad (2.46)$$

where the non-dimensional nucleus area is $\hat{A}_{hom} = A_{hom}/R^2 = \pi$.

In heterogeneous nucleation, the shape factor $S(\theta) = A_{het}/A_{hom}$ has equal role as in the 3D space, implying

$$\Delta G_{het} = S(\theta) \Delta G_{hom} \quad (2.47)$$

similarly as for the nucleation barrier

$$(\Delta G_c^*)_{het} = S(\theta) (\Delta G_c^*)_{hom}. \quad (2.48)$$

When the interface energy is inclination-dependent $\sigma(\theta) = \sigma_0 h(\theta)$, the interface energy contribution is a line integral $\int_C \sigma(\theta) dl$, which can be expressed in analogy with the 3D case [48] as (X_0 being the generalized radius of the Wulff shape with area A_{hom}^{ani})

$$\int_C \sigma(\theta) dl = \frac{2\sigma_0}{X_0} A_{hom}^{ani}, \quad (2.49)$$

which eventually allows to write the Gibbs free energy difference of a free nucleus

$$\Delta G_{hom}^{ani} = (-\Delta G_A X_0^2 + 2\sigma_0 X_0) \hat{A}_{hom}^{ani} \quad (2.50)$$

and further its nucleation barrier

$$(\Delta G_c^*)_{hom} = \hat{A}_{hom}^{ani} \frac{2\sigma^2}{\Delta G_A}. \quad (2.51)$$

In the heterogeneous anisotropic nucleation the difference in Gibbs free energy is like in equation (5.5), having ΔG_{hom}^{ani} as in (2.50) and the nucleation barrier like in (5.6), only with modified shape factor correspondingly to the Wulff shape.

2.10 Anisotropy in interface energy vs. kinetic coefficient

A fundamental work by Damjanovic [49] reports the morphology of copper depositions on different Cu monocrystalline substrates. It also states, that

the exchange current densities i_0 for Cu electrodeposition on the different crystallographic planes (i.e. kinetic coefficient in the deposition/dissolution reaction) are in the following sequence of magnitude:

$$i_0^{(111)} < i_0^{(001)} < i_0^{(011)}. \quad (2.52)$$

Interestingly, the same order comes for the *interface energies* of the respective planes in vacuum for both Cu and Ag based both on broken bond model by Wang [50] and DFT calculations by Tran [51].

In addition to that, it is known that the fundamental crystal forms obtained assuming a single anisotropy in both interface energy and kinetic coefficient (i.e. growth rate) are geometrically similar [17, 30]. More specifically, if the total interface energy of an isolated crystal is minimized with a constant volume, the resulting so-called Wulff shape depends on the interface energy anisotropy. This Wulff shape is geometrically similar to the shape obtained by growth of a spherical crystal under the effect of anisotropic growth rate with the same anisotropy as the interface energy had. This idea is illustrated in Figure 2.10.

It is not surprising to have the anisotropies in the interface energy and kinetic coefficients somehow related, because they both must derive from the state of the same interface. However, it is certainly interesting to realize that despite them being substantially different physical quantities, used for description of different processes, their anisotropy may manifest in similar ways.

This was supported also by simulations of 2D growth of polycrystalline zeolite film using multi-phase field method [52]. Reportedly, the same microstructures were obtained when assuming the same anisotropy in either interface energy or in the kinetic coefficient.

While in crystal growth, the anisotropy in interface energy and kinetic coefficient may be interchangeable to some extent in terms of effect on the resulting shape (not on the shape evolution, though), there are necessarily processes where there is no overlap due to different nature of the quantities. For example, in nucleation, the nucleation barrier depends on the interface energy but does not depend on the kinetics.

This interchangeability makes the experimental determination of these properties in-situ during deposition very complicated. However, in models of the deposition and in simulations, it is in fact necessary to distinguish the two quantities and then it is possible to distinguish also their impact of their anisotropy on the process. The mentioned phase-field method is one of the methods capable to implement these quantities independently.

In the light of previous paragraphs, it is clear that while in some simulations it may not be a big problem to neglect anisotropy in either kinetic coefficient or

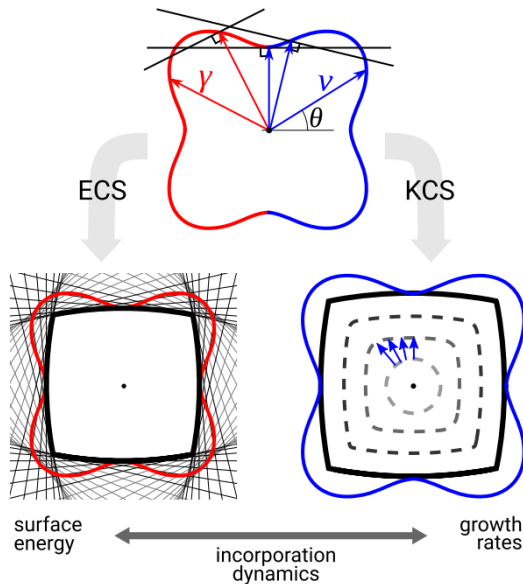


Figure 2.10: Illustration of geometric similarity between Equilibrium Crystal Shape (ECS) driven by anisotropy in interface energy and Kinetic Crystal Shape (KCS) obtained by growth with growth rate having the same anisotropy. The top polar plot is the anisotropy function $h(\theta)$. Source: [30].

interface energy as long as it is preserved in the other quantity. However, in the processes where these quantities are not interchangeable (e.g. anisotropic interface energy in nucleation barrier), neglecting the implications of anisotropy results in incomplete representation of the process.

2.11 Microstructure formation in coatings

This section contains review of literature related to formation of textures in polycrystalline coatings with emphasis on the underlying processes which are common to all the deposition methods, like electrodeposition, physical vapor deposition or sputtering.

Microstructure here denotes both the morphology on the surface, shape and size of grains and their crystallographic texture.

The experimental investigations of the texture-forming factors in deposits are usually specific for the particular deposition method, like physical vapour deposition (PVD), sputtering or electrodeposition. Despite some obvious differences between the methods, it is natural to expect the textures to be formed by the same mechanisms. These are necessarily altered by the method-specific deposition conditions, thus giving rise to some behaviors which are then considered as standard for that type of deposition.

For example, the Structure Zone Model (SZM) [5, 53] is often used to describe the dependence of microstructure on the relative deposition temperature in PVD and sputtering methods. The structure-zone model was extended several times to new parameter regions, for an example of a rather recent model see Figure 2.11b. On the other hand, in the electrodeposition rather the Winand diagram [54] is used instead, having the axes representing degree of chemical surface inhibition and current density, i.e. deposition rate (see Figure 2.11a). Both of these can be perceived as state diagrams, where the individual regions qualitatively indicate the one microstructure/morphology which is most likely to be stable for those deposition conditions. Interestingly, in electrodeposition the crystallographic texture of the coating does not necessarily imply a particular deposit morphology [54].

Barna [5] claims, that the different crystallographic textures observed in PVD or sputter deposition can be correlated to the respective *structure zone*. Specifically, he uses the terms *competitive growth texture* and *restructuration growth texture*, which correspond to the ones where the resulting texture depends on either the anisotropy in growth rate or on the concurrent minimization of surface and grain boundary energy, respectively.

In electrodeposition, the situation is more complicated than in PVD or sputtering by the presence of the double layer on the metal surface and the complex interplay of the electric field and chemical reactions between all the species. Nevertheless, experimental work largely shows that, as far as three-dimensional nucleation is concerned, the same observations are made in electrocrystallization and in physical crystallization [54]: increasing the deposition rate and/or increasing the inhibition usually results in increased nucleation rate and thus eventually in the reduction in the deposit grain size.

The inhibition refers to some specific interactions between the deposit and the parent phase. The inhibiting species attaches to low-energy sites where the growth might easily proceed and then the adatoms must find another spot to settle down, having their lifetime before being incorporated into the crystal potentially prolonged and thus increasing the nucleation probability [54]. The inhibitor may be a natural constituent of the electrolyte in electrodeposition or simply some impurity. In PVD deposition of Al with variable amounts of

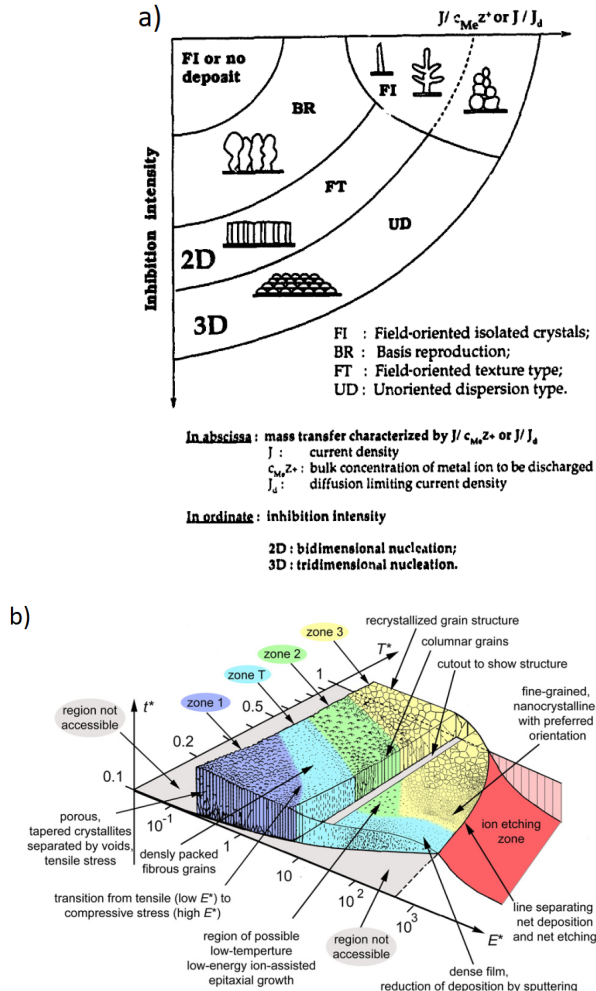


Figure 2.11: Simplified empirical diagrams, in a) Winand diagram for electrodeposition [54], in b) Structure-zone model for high-energy deposition from vapor [53].

oxygen, it was observed that increased oxygen amounts reduced the grain size up to nanocrystalline or even amorphous coating of alumina [5].

A separate field of research involves stress in the deposits [55–58]. Both tensile and compressive stress are observed in the deposits depending on the deposition conditions and deposited material. Generally speaking, two typical scenarios of stress evolution were observed: (i) a compressive stress develops with increasing thickness of the film, but after the deposition stops, the stress either completely or partly relaxes, and (ii) tensile stresses, which do not relax after the deposition termination. The first case, where at least partial relaxation of the compressive stress occurs, was observed rather at higher temperatures and lower deposition rates (conditions favoring surface diffusion). On the other hand, the tensile stress persisting after the deposition was usually observed with rather high growth rates and low deposition temperature (conditions suppressing surface diffusion).

Based on many experiments, Chason et al. [57, 59] hypothesized that self-diffusion coefficient of the deposited materials plays a very important role in interpretation of what is high or low deposition temperature/rate in this context. Materials with low melting points (e.g. like tin) tend to have higher self-diffusion coefficients and exhibit the behavior with compressive stress buildup and (partial) release. Reversely, in materials with higher melting points (like iron or nickel), the self-diffusion coefficients are lower and the overall behavior is rather the one with persisting tensile stress.

Another source of stress can be interactions with the substrate, which is closely related to epitaxy. The (in)compatibility of the crystal lattices of the deposited material and substrate strongly determine the crystallographic state of thin films.

Stress can suppress or promote grain growth [56]. It is then natural to consider stress relaxation as another texture-forming process. However, it is not clear how it is related to the fundamental texture forming factors mentioned in the Introduction: interfacial energy, surface diffusivity of adatoms, grain boundary mobility and grain boundary and lattice diffusion [3, 4]. These quantities are coupled to the immediate state of the material and only their synergistic effect on the texture evolution is observed.

Thompson [56] developed an abstracted model of columnar microstructure and expressed its total strain and total interface energy as function of thickness. Because the thickness dependence of these energies was different, the model suggested that the texture could be dominated by minimization of interface energy below certain (temperature-dependent) thickness and above it, the texture would be dominated by the strain energy minimization. Especially in

the light of the previous paragraph, it is clear that the stress state of a real deposit does not depend only on the deposit thickness. Nevertheless, the idea of having different mechanisms competing over the course of texture/morphology evolution as the film thickness increases is strongly based on experimental observation. Also, the terms *interface-energy minimization texture* or *strain-energy minimization texture* are used in practice [9].

Specifically in electrodeposition, the inhibition in relation to the morphology and texture was studied extensively [54]. Amblard [60] determined the particular species responsible for the texture variation in nickel electrodeposits from Watts electrolyte when varying the pH, current density and adding separately a brightening and leveling agents. These species selectively inhibited the metal surface and thus introduced different textures. A more recent study [61] reviewed other hypotheses about the possible texture-forming processes in nickel electrodeposition from Watts electrolyte and after transmission electron microscopy study of one deposit, they concluded that the inhibition was the most likely scenario.

The same group later proposed [62], that the texture of an electrodeposit could develop from a zone mainly affected by the substrate (epitaxy, chemical reactions), through a zone of mixed control to a zone affected solely by the deposition conditions (selective inhibition, deposition rate). However, in a more recent study [9] involving microtexture measurement through thickness of the nickel electrodeposits obtained at different pH and current density, the authors could not confirm the existence of the transition zone as a simple mixture of the substrate- and conditions-affected zones.

Chapter 3

Phase field method

3.1 General introduction

Phase field method is a diffuse-interface approach to solving moving-boundary problems. In materials science it is usually used as meso-scale method. It has numerous applications such as e.g. (multi-component) solidification, grain growth, Ostwald ripening, solid-solid phase transitions (martensitic, precipitation, spinodal...), two-phase flow, nucleation, wetting and much more.

The method is based on the principle of total system energy minimization. The free energy density of the system is a function of all the possibly mutually coupled physical fields, including the fields representing the phases. These are typically called phase fields, order parameters or continuum fields. The other (bulk) physical fields can be e.g. concentration, temperature, electric charge or others. The total energy of the system is then spatial integral of the free energy density over the simulation domain - the free energy functional.

The governing equation(s) for the phase fields are derived using principles of variational calculus, which ensure the fields evolution so that the free energy functional is minimized along the direction of steepest descent, i.e. the most likely way towards the equilibrium. Additionally, the curvature driving force and the possible coupling with the bulk fields are represented. That is the reason for high versatility of the method and its capability to simulate coupled multiphysics.

Due to the thermodynamic nature of the method, the interface energy is naturally included as an input parameter. Multigrain or multiphase systems

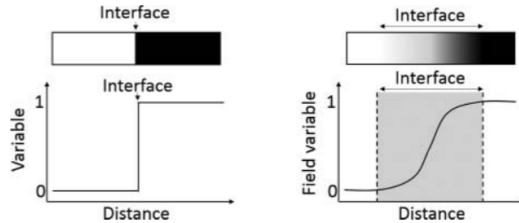


Figure 3.1: Illustration of the diffuse interface in phase field method (on the right) and the comparison to an actual, sharp interface (on the left). [64]

with interfaces of various properties can be simulated with multi phase field models. Some of these allow to include also inclination dependence of interface energy. In fact, it was phase field simulation which revealed the paramount importance of interface energy anisotropy in pattern formation during dendritic solidification [63].

A phase (or phases) in an inhomogeneous system is described by a continuous function (called phase field, order parameter or continuum field), having different constant values in the bulk of the phases (typically 1 and 0 or 1 and -1). At the interface between phases, the phase field varies smoothly between the values and the interface region is thus characterized by a certain width, as sketched in Figure 3.1. This interface width is an important input parameter in phase field models. In quantitative phase field models, the model behavior is in principle not affected by the particular value of interface width chosen, which allows to make quantitative simulations at mesoscale (whereas the real interface width is in the order of units of nm).

The governing equations for the phase fields are typically either conservative (Cahn-Hilliard type of equation, conserving volume) or non-conservative (Allen-Cahn type of equation). The latter is more relevant for this work. In the following, no coupling to other physical fields is assumed.

3.2 Allen-Cahn equation for two-phase system

It was shown that the Allen-Cahn equation is a diffuse-interface approximation of a curvature-driven system (even for anisotropic interface energy [65]). It represents evolution of a non-conserved field $\eta(\mathbf{r})$ in a domain $\Omega \in \mathbb{R}^3$ with

boundary $\partial\Omega$ and can be written as

$$\frac{\partial\eta}{\partial t} = -L \frac{\delta F}{\delta\eta} \quad \text{in } \Omega \quad (3.1)$$

$$\nabla\eta \cdot \mathbf{n} = 0 \quad \text{at } \partial\Omega, \quad (3.2)$$

where L is a positive constant and the function $\frac{\delta F}{\delta\eta}$ stands for functional derivative of the free energy functional F . The functional is an integral with free energy density $f(\eta, \nabla\eta) = f_{hom}(\eta) + f_{int}(\nabla\eta)$ comprising of the homogeneous and interfacial free energy densities

$$F = \int_V f_{hom}(\eta) + f_{int}(\nabla\eta) dV \quad (3.3)$$

$$= \int_V m\eta^2(1-\eta)^2 + \frac{\kappa}{2}|\nabla\eta|^2 dV \quad (3.4)$$

with positive constants m, κ being the double barrier height and gradient energy coefficient, respectively. The homogeneous free energy density f_{hom} in the form of the double-well function assures two stable states for the field variable in values 0 and 1. The gradient energy contribution is lessened by the diffuse interface widening, whereas conversely the homogeneous free contribution is lessened by its narrowing. When minimizing the full integral, a balance between the two effects is reached in equilibrium.

As described in more detail in the Appendix A, the functional derivative is computed as

$$\frac{\delta F}{\delta\eta} = \left[\frac{\partial f}{\partial\eta_p} - \nabla \cdot \frac{\partial f}{\partial(\nabla\eta_p)} \right] \quad (3.5)$$

where $\nabla \cdot \partial f / \partial(\nabla\eta_p)$ is divergence of vector field $\partial f / \partial(\nabla\eta_p)$ defined by relation

$$\frac{\partial f}{\partial(\nabla\eta_p)} = \frac{\partial f}{\partial(\partial_x\eta_p)} \mathbf{n}_x + \frac{\partial f}{\partial(\partial_y\eta_p)} \mathbf{n}_y + \frac{\partial f}{\partial(\partial_z\eta_p)} \mathbf{n}_z \quad (3.6)$$

with $\partial_x, \partial_y, \partial_z$ being operators for unidirectional derivatives in the corresponding directions and $\mathbf{n}_x, \mathbf{n}_y, \mathbf{n}_z$ coordinate base vectors.

When applied applied to the above functional, it will result in the Allen-Cahn equation

$$\frac{\partial\eta}{\partial t} = -L[f'_{hom}(\eta) - \kappa\nabla^2\eta] \quad (3.7)$$

$$= -L[2m\eta(1-\eta)(1-2\eta) - \kappa\nabla^2\eta]. \quad (3.8)$$

In equilibrium, the interface is static, $\partial\eta/\partial t = 0$, which means that the forces narrowing and widening the interface are in balance, i.e. $f'_{hom}(\eta) = \kappa\nabla^2\eta$, or equivalently (in 1D)

$$2\eta(1-\eta)(1-2\eta) = \frac{\kappa}{m} \frac{\partial^2\eta}{\partial x^2}. \quad (3.9)$$

Solution to this equation provides the equilibrium profile of the phase field (centered in $x = 0$), which in this case is the following sigmoid function

$$\eta(x) = \frac{1}{2}\tanh\left(\sqrt{\frac{m}{2\kappa}}x\right). \quad (3.10)$$

The equilibrium also implies, that the homogeneous and interfacial energies are equal except for a constant, i.e. $f_{hom} = f_{int} + C$, which can be shown to be zero $C = 0$ (see e.g. [7]).

Interface width l_{int} (unit m) can be defined using the reciprocal maximal slope in the interface (present in $\eta = 0.5$)

$$l_{int} = \frac{1}{d\eta/dx|_{max}} = \frac{1}{\sqrt{2f_{hom}/\kappa}} \Big|_{\eta=0.5} = 2\sqrt{2}\sqrt{\frac{\kappa}{m}}, \quad (3.11)$$

where the relation $d\eta/dx = \sqrt{2f_{hom}/\kappa}$ is derived from $f_{hom} = f_{int}$.

The excess free energy σ (the *interface energy*, unit J/m²) at a flat interface can be computed as an 1D integral of the free energy density along perpendicular line through the interface

$$\sigma = \int_{-\infty}^{+\infty} f_{hom} + \frac{\kappa}{2}|\nabla\eta|^2 dx. \quad (3.12)$$

From $f_{hom} = f_{int}$ it can be written $dx = \sqrt{\kappa/2f_{hom}}d\eta$, which allows to solve (3.12) by substitution as follows

$$\sigma = \int_{-\infty}^{+\infty} 2f_{hom} dx \quad (3.13)$$

$$= \int_0^1 \sqrt{2f_{hom}\kappa} d\eta \quad (3.14)$$

$$= \frac{\sqrt{2}}{6} \sqrt{m\kappa}. \quad (3.15)$$

In practice, the model is parameterized by the interface width l_{int} and interface energy σ , from which the model parameters m, κ must be computed. The

necessary formulas are obtained from (3.11) and (3.15) as

$$\kappa = \frac{3}{2} \sigma l_{int} \quad (3.16)$$

$$m = 12 \frac{\sigma}{l_{int}} \quad (3.17)$$

The l_{int} is chosen depending on the scale of the problem, disregarding the real physical interface width.

As shown in [7], the following equality between the model parameters and the interface mobility μ holds

$$\mu\sigma = L\kappa, \quad (3.18)$$

which allows to express the phase field kinetic coefficient as

$$L = \frac{2}{3} \frac{\mu}{l_{int}}, \quad (3.19)$$

where the equation (3.16) was used.

3.3 Allen-Cahn equation for two-phase system including anisotropic interface energy

3.3.1 Fundamentals

The most straightforward way to introduce anisotropy in the interface energy in the model is to make either or both of the model parameters κ, m a function of the inclination angle respecting both the anisotropy function and the defining parameter relations.

Tschukin [66] proposes the terminology of *classical* and *natural* models (corresponding to the notation VIW and VIE, respectively, as used by Fleck [31], standing for *Variable Interface Width* and *Variable Interface Energy*). The classical models [29, 63, 67–69], introduce anisotropy in the gradient energy coefficient κ , whereas the natural models [7, 31, 70, 71] in both the gradient energy coefficient κ and homogeneous energy density barrier m . The main difference between the classical and natural formulations is that in the first case the diffuse interface width varies proportionally to the local interface energy (see equation (3.11)), whereas in the latter the interface width can be decoupled from the interface energy and the interface width maintained constant (see (3.11) and (3.15)). Below, more details are provided on both model formulations.

Let's assume that the interface energy is inclination-dependent in the following form (in 2D)

$$\sigma(\theta) = \sigma_0 h(\theta), \quad (3.20)$$

with the inclination angle θ of the interface normal $\mathbf{n} = [n_x, n_y]^T$ being defined as $\theta = \text{atan2}(n_y/n_x)$ ¹ and σ_0 a constant with physical dimensions J/m². The interface normal can be calculated as

$$\mathbf{n} = \frac{\nabla\eta}{|\nabla\eta|}. \quad (3.21)$$

First, a classical model with anisotropy only in κ will be developed. The equations (3.15) and (3.20) are combined

$$\sigma(\theta) = \sigma_0 h(\theta) = \frac{\sqrt{2}}{6} \sqrt{m\kappa(\theta)} \quad (3.22)$$

and allow to express the anisotropic $\kappa(\theta)$

$$\kappa(\theta) = \kappa_0 [h(\theta)]^2 \quad \text{and} \quad \sigma_0 = (\sqrt{2}/6) \sqrt{m\kappa_0}, \quad (3.23)$$

which recovers the interface energy anisotropy (3.20).

Since θ depends on $\mathbf{n}(\nabla\eta)$, any θ -dependence in the model parameters introduces new terms in the governing equations. These arise from the divergence of the functional derivative, $\nabla \cdot \partial f / \partial(\nabla\eta_p)$, where the free energy density is differentiated with respect to the gradient components

This anisotropy implementation implies that the interface width l_{int} varies proportionally to the interface energy (see (3.11)), which must be taken into account in practice so that there are no excessively large or narrow interfaces in the domain. Additionally, the interface width variation introduces nonphysical anisotropy in the kinetic coefficient L (see (3.19)), which should be compensated in the formula for L .

In strongly anisotropic systems, the variable interface width poses a practical problem. However, it can be prevented by including the anisotropy also in the parameter m . When the anisotropy is assigned in the natural model formulation as

$$\kappa(\theta) = \kappa_0 h(\theta) \quad (3.24)$$

$$m(\theta) = m_0 h(\theta), \quad (3.25)$$

¹for details on the function `atan2(y, x)` please see e.g. <https://en.wikipedia.org/wiki/Atan2>

the interface width is constant $l_{int} = 2\sqrt{2}\sqrt{\frac{\kappa_0}{m_0}}$ (see (3.11)) and the following relation holds as well

$$\sigma_0 h(\theta) = \frac{\sqrt{2}}{6} \sqrt{m(\theta)\kappa(\theta)}. \quad (3.26)$$

Because both κ and m depend on θ , even more terms derive from the divergence in the functional derivative, as described earlier.

Another notable approach uses Finsler geometry to replace the Euclidean metric in the simulation domain by an anisotropic one [72, 73]. Formally, the anisotropic Allen-Cahn equation is then not much more complicated than the isotropic one, even though new terms arise as well. The interface width is constant, though.

3.3.2 Challenges and limitations

The main challenges come from the type of anisotropy function and from the strength of anisotropy. So far, it was implicitly assumed that the anisotropy function is continuous and twice-differentiable homogeneous of order 1. The problem arising from forbidden angles was worked in some detail in section 2.5, but here it will be put into a context specific for phase field method.

Generally, two types of singularities may occur on the Wulff shapes of the first order (for the terminology see section 6.2.1): corners and facets. These two depend on the following properties of the particular anisotropy function

1. (non-)convexity of the Frank's plot, i.e. $1/h(\theta)$ and
2. (non-)differentiability with respect to the polar angle (typically presence of a cusp).

The first produces corners (when non-convex) and the second facets (when non-differentiable).

The easiest solution to the non-differentiability is to replace the anisotropy function by one, in which the cusps are smooth tips. These functions are typically formulated in such a way, that the sharpness of the tip is scalable, but formally the function is always smooth. This allows to approximate the former anisotropy close enough while assuring validity of the formulas relying on the differentiability. This was employed for example in [32, 33, 74].

The non-convexity of the Frank's plot does not have so easy solution. It causes the governing equations to be ill-posed, which means that their solution is either not existing, unique or does not depend continuously on the initial/boundary conditions. In this case the uniqueness is the problem, because it is not clear,

whether a certain segment on the surface should align with the "ear" orientation or some on the Wulff plot of the first order. In practice, it causes corrugations of the phase field contour near the corners, see e.g. [66]. The ill-posedness (and thus the corrugations) can be removed by regularization, which can be done in several ways. The following approaches are known to the author

1. regularization of the anisotropy function [17, 29, 68],
2. inclusion of higher order terms in expansion of interface energy in the free energy functional [66, 69, 71],
3. models incorporating the Finsler geometry do not need regularization [72, 73],
4. one study reports numerical regularization which occurred after using spectral solver [75].

All of the above approaches were successful in delivering cornered or faceted Wulff shapes of the first order and anisotropic crystals grown in either temperature or concentration field. These were the main applications of these models so far. Very likely, each of these will have its own limitations in the future applications, but currently the author is unaware of any systematic comparison of these in the literature and himself only implemented the approach 1. from the list, i.e. the regularization of anisotropy function.

3.4 Allen-Cahn equations for multi-phase systems

3.4.1 Historical context and current state

Multi-phase field models emerged from the need to simulate systems with more than two phases. At first, these models were developed to simulate ideal grain growth in systems with isotropic grain boundary energy. That is a natural choice, because the grain coarsening is curvature driven and the Allen-Cahn equation approximates the mean curvature flow. However, additional complexity arises from the number of entities (grains) which need to be simulated, while making sure that their interactions are representative of the physical process. There can be even tens of thousands grains in large scale grain growth simulations [76].

Even though there were published many model formulations, all those known to the author can be attributed to one of three main branches of development: one initiated by the work of Long-Qing Chen in 1994 [77], other by the one of Steinbach in 1996 [78] and the last one by Kobayashi et al. in 1998 [79]. The

first and second approach represent every grain (and/or phase) by its own field variable and the last one involves the concept of orientation field and will be discussed separately from the former two. The most fundamental difference between the models of Chen and Steinbach is that in the Steinbach's branch, the field variables are interpreted as local phase fractions, whereas in the Chen's one there is no direct physical interpretation of the field variables. For this reason, it is not accurate to call the latter multi-phase-field models (MPF), but the difference is rather technical and not obvious to broader scientific community. When there is the need to differentiate the two groups of models, the multi-continuum-field (MCF) [80] or multi-order-parameter (MOP) [75, 81] model are some alternative terms denoting the models in Chen's legacy.

Both multi-phase-field and multi-continuum-field models were extensively developed beyond the ideal grain growth, and nowadays the two model families are comparable in terms of maturity and applicability. The models incorporated anisotropy in interface energy and kinetic coefficient (pair-distinct isotropic as well as the inclination dependence), coupling to multi-component systems using the Onsager's theory, possibly employing the thermodynamic databases to express the concentration dependence of the free energy density. Both are also available in complex simulation frameworks: MPF model in MICRESS (MICRostructure Evolution Simulation Software) [82] and MCF model in MOOSE (Multiphysics Object Oriented Simulation Environment) [83].

The models derived from the work of Kobyashi et al. [79] include one field to indicate phase and then a set of orientation fields, representing the angles defining the local orientation. One orientation field then contains e.g. the x-component of the orientation vector in grains throughout the system. The conceptual advantage in comparison to MPF and MCF models is that the number of equations does not scale with the number of simulated grains, i.e. with the system size. This results in great reduction in the number of equations, as there could be thousands or even tens of thousands simulated grains [84]. However, to the best of the author's knowledge, this model nor its descendants are not available in any publicly available software, which makes them less accessible. Overall, this approach is less developed, as can be noted also from the fact that only in 2019 this concept was extended to 3D [85].

Real interfaces (including the grain boundaries) exhibit anisotropic (inclination-dependent) interface energies [27, 28], hence a significant effort was made to introduce this feature in some multi-phase field [52, 75, 86, 87], continuum-field models [7, 88] and also in an orientation-field model [89].

Notable methodic work on MPF models was done by Toth et. al [75], who identified fundamental criteria a consistent MPF model must meet. These criteria allowed systematic comparison of a number of MPF models and

highlighted problems specific for the MPF approach. The criteria are listed below [75]:

1. The MPF descriptions view the phase field variables $u_i(r, t)$ as the local and temporal volume/mass/mole fraction of the component/grain, prescribing $\sum u_i(r, t) = 1$.
2. The physical results should be independent of the labeling of the variables ("principle of formal indistinguishability" of the fields).
3. The solution of the dynamic equations should tend towards the equilibrium solution obtained from the respective Euler-Lagrange equations (ELEs).
4. As time evolves, the free energy of the total system should decrease monotonically (second law of thermodynamics).
5. The formulations for different numbers of phases or grains in a fixed system should be consistent with each other.
6. The two-phase planar interfaces should represent a stable equilibrium and should be free of additional phases.
7. The model should allow the prescription of independent data for the interfacial properties and the kinetic coefficient of the individual phase pairs.

The criterion 1 emphasized the defining property of the MPF models and the criterion 3 is the implication of it, because the ELE equation is the technical way how the local sum of phase fields is mathematically assured to be 1. These are not applicable to MCF models. The criteria 2 and 5 are rather formal and the MCF models comply with them. The monotonical energy decrease required in the criterion 4 is assured, when the governing equations are derived following all rules of the variational calculus - this statement is valid for both MPF and MCF models. Every time the model deviates from the proper variational formulation, there is a risk that this criterion will not be met. The criterion 6 contains two conditions - stable equilibrium present on a planar interface between two phases and absence of ghost phases. The stable equilibrium on a planar interface is a fundamental assumption based on which the model of Moelans [7, 8] is formulated (hence it is met), but to avoid ghost phases in non-trivial and the following subsection discusses this topic in more detail. The last criterion 7 requires that every pair of phase fields can have interface properties independently assigned, which is also met by the model of Moelans [7].

3.4.2 Challenges and limitations

A pragmatic requirement on these models not listed in [75] is that they must correctly reproduce force balance in triple and higher-order junctions. Despite high maturity of the models and great relevance of triple junctions for the grain coarsening, only very recently there was a structured attempt to quantify the performance of different models in how they reproduced the triple junction behavior in well defined scenarios [81].

This study emphasized, that probably the largest challenge for both MCF and MPF models are the ghost phases. These manifest as a finite amount of a third phase within an interface between two other fields. Ghost phases are unphysical and their amount was correlated with the (poorer) quality of match of dihedral angles in the triple junctions benchmark problems [81].

The ghost phases mitigation strategies include in the first place reformulation of either homogeneous or gradient energy contributions to avoid problematic driving force terms emerging from the functional derivative, then additions of ternary terms, or even neglecting the problematic driving force terms. In continuum-field models, the ghost phases were eliminated by a specific way the model parameters were made anisotropic, but at the cost of having variable interface width.

The orientation field models are based on a completely different concept than MPF and MCF models. Even though the ghost phases do not affect them, the energy formulation is prone to long-range interaction between interfaces [90] in 2D and must be optimized in order to remove the resulting topological defects. The author is not aware of any systematic comparison between the orientation field models and the MPF or MCF ones, but certainly the developed benchmark problems are well suited for that.

The community has just acquired for itself the tools to quantify the models performance in triple junctions of interfaces with isotropic interface energies [81]. Certainly, a challenge ahead are the triple junctions of interfaces with inclination-dependent interface energy. First, a benchmark problem must be developed and then used to compare the models. However, before such study, no simulation of grain growth with inclination dependent interfaces including the triple junctions is reliable. In the multi-phase field models including the inclination dependent interface energy there are many more terms in the governing equations, which makes the ghost phases prevention by model reformulation significantly more complicated than in the pair-distinct isotropic case.

3.5 Benchmarking of phase field models

The community produces many applications of the phase field method, often involving complicated multi-physics, to deliver solutions to complex engineering and scientific problems. However, the know-how related to the individual modeling approaches seems to be rather fragmented into the individual groups and works comparing different models are rather exceptional. Different models for the same purpose may have different formulations, but the differences in their behavior are not obvious, especially because there is no unified, generally accepted validation procedure for quantitative assessment of performance in terms of represented physics.

Another source of confusion about the limits of phase field method in general is that some works claim to deliver "quantitative" or "thermodynamically consistent" phase field models of complicated multiphysics problem (e.g. electrodeposition of lithium [91]) after doing some lower-dimensional check on a not-coupled problem. This way of presentation makes the impression that everything is possible, when in fact the more equations are coupled, the easier it is to hit reasonable limits of applicability for the model.

Where exactly lay the limits of the current models is also partially obscured by the fact, that it is not a norm to publish the codes used to produce published results, which significantly affects their reproducibility.

Systematic and reproducible parametric studies in well-defined problems are needed for quantitative assessment of phase field models reliability. The lack of benchmarking is present in terms of physics and also of models comparison. It is critical especially in models coupling many physical driving forces. In order to confidently and honestly interpret results of quantitative phase field simulations, both physical models and numerical implementations must be validated and verified [92]. Recent initiative PFHub addresses the need for benchmarking of the multitude of software and numeric approaches for solving the phase field governing equations.

Usually, the validation of models with inclination-dependent interface energy was carried out by visual comparison of the phase field contours to corresponding Wulff shapes for single or several values of strength of anisotropy [29, 31, 66, 70, 86]. Such approach does not reveal the limits of reliability of these models, though.

The cited study comparing the MPF and MCF models in the triple junctions benchmarks [81] was initiated by the author of this thesis. Usage of the presented benchmarks for assessment of the new models or existing implementations adds more reliability whenever the tested multi-phase field models will be used.

Chapter 4

Phase field model benchmarking

This chapter is based on work of the author published as [8]: M. Minar and N. Moelans. “Benchmarking of different strategies to include anisotropy in a curvature-driven multi-phase-field model”. In: *Physical Review Materials* 6 (10 Oct. 2022), p. 103404. ISSN: 2475-9953. DOI: 10.1103/PhysRevMaterials.6.103404. URL: <https://link.aps.org/doi/10.1103/PhysRevMaterials.6.103404>

4.1 Introduction

In order to confidently and honestly interpret results of quantitative phase field simulations, both physical models and numerical implementations must be validated and verified [92]. Recent initiative PFHub addresses the need for benchmarking of the multitude of software and numeric approaches for solving the phase field governing equations. However, benchmarks validating anisotropic interface energy or multi phase field models have not been included yet.

Grain coarsening is assumed to be curvature-driven, hence it is an appealing application for only-interface-driven multi-phase field models. Real interfaces (including the grain boundaries) exhibit anisotropic (inclination-dependent) interface energies [27, 28], hence a significant effort was made to introduce this feature in some multi-phase field models too [52, 75, 86–88].

The models have different formulations, but the differences in their behavior are not obvious, especially because there is no unified validation procedure for quantitative comparison. Systematic and reproducible parametric studies in well-defined problems are needed for quantitative assessment of phase field models reliability.

There are several ways to introduce anisotropic interface energy in the Allen-Cahn equation (irrespective of whether the model is single- or multi-phase field). Tschukin [66] proposes the terminology of *classical* and *natural* models (corresponding to the notation VIW and VIE, respectively, as used by Fleck [31], standing for *Variable Interface Width* and *Variable Interface Energy*). The classical models [29, 63, 67–69], introduce anisotropy in the gradient energy coefficient, whereas the natural models [7, 31, 70, 71] in both the gradient energy coefficient and homogeneous energy density barrier. The main difference is that in the first case the diffuse interface width varies proportionally to the local interface energy, whereas in the latter they are decoupled and the interface width is constant. Another notable approach uses Finsler geometry to replace the Euclidean metric in the simulation domain by an anisotropic one [72, 73].

Usually, the validation of models with inclination-dependent interface energy was carried out by visual comparison of the phase field contours to corresponding Wulff shapes for single or several values of strength of anisotropy [29, 31, 66, 70, 86]. Such approach does not reveal the limits of reliability of these models, though.

This paper proposes two benchmarks for quantitative assessment of a) the anisotropic curvature driving force, and b) the anisotropic curvature driving force in combination with anisotropic kinetic coefficient. Both are 2-phase systems, hence could be simulated using a single phase field model. Nevertheless, because the multi-phase field models allow simulations of multiple phases, they have wider application potential than single phase models. For this reason, the validations are demonstrated on a multi-phase field model [7]. However, the nature of these benchmarks is independent on the model formulation.

In order to provide more complete comparison of the models, another supplementary benchmark was carried out, which determined equilibrium triple junction angles.

The multi-phase field model by Moelans [7] is an established [93] quantitative phase field model of grain growth with anisotropic grain boundary properties. Using asymptotic analysis, Moelans derived that in the original model [7], the local interface energy and width are related to three model parameters. Because these are two equations of three variables, the system is undetermined and one of the model parameters is free. This degree of freedom introduces the possibility

of many different parameters assignment strategies, all of which represent the same physical input. The effect of different but equivalent parameters choices can thus be investigated in this model. Moelans proposed such parameters assignment strategy [7], which assured constant interface width irrespective of the strength of anisotropy in interface energy (a kind of *natural* formulation). Two of the three model parameters (γ and κ) were made anisotropic in order to achieve such behavior. However, this approach (here denoted IWc - *Interface Width constant*) does not reproduce well the angles between interfaces in triple junctions for stronger anisotropies. This was already first noted by Moelans in [94]. An alternative parameters assignment strategy with only parameter γ anisotropic was used in [93, 95], but no systematic comparison was made. In this approach, the interface width is not constant in anisotropic systems, but it is not simply classifiable as *classical* anisotropy formulation, because the gradient energy coefficient is constant. It will be denoted IWvG (*Interface Width variable and Gamma anisotropic*). The third compared parameters assignment strategy is the *classical* formulation, varying only gradient energy coefficient κ to achieve the desired interface energy anisotropy (denoted IWvK - *Interface Width variable and Kappa anisotropic*). Additionally, the inclination dependence of interface energy in IWvG and IWvK have not yet been addressed in the framework of Moelans' model.

This paper is organized as follows: firstly, the base model and its three variants are introduced, including the inclination dependence in interface energy. Secondly, the methodology is explained in detail, which involves quantitative matching of the shrinking shape to the analytic one and also the determination of shrinkage rate (also known analytically). The approach taken in triple junction angles determination is explained as well. Then, the validations were carried out in the order: shrinking Wulff shape, kinetically compensated anisotropically shrinking circle and triple junction angles. For all simulations the effect of interface width and number of grid points through the interface are investigated by re-running the simulations using different numerical settings.

4.2 The phase-field model

The system consists of n non-conserved continuous-field variables (further denoted phase fields) $\eta_1(\mathbf{r}, t), \eta_2(\mathbf{r}, t), \dots, \eta_n(\mathbf{r}, t)$, which are functions of space and time. The total free energy of the system is expressed as functional of the phase fields and their gradients $\nabla\eta_1(\mathbf{r}, t), \nabla\eta_2(\mathbf{r}, t), \dots, \nabla\eta_n(\mathbf{r}, t)$

$$F = \int_V \left\{ m f_0(\vec{\eta}) + \frac{\kappa}{2} \sum_{i=1}^n (\nabla \eta_i)^2 \right\} dV, \quad (4.1)$$

where the homogeneous free energy density $f_0(\vec{\eta}) = f_0(\eta_1, \eta_2, \dots, \eta_n)$ is expressed as

$$f_0(\vec{\eta}) = \sum_{i=1}^n \left(\frac{\eta_i^4}{4} - \frac{\eta_i^2}{2} \right) + \gamma \sum_{i=1}^n \sum_{i>j} \eta_i^2 \eta_j^2 + \frac{1}{4}. \quad (4.2)$$

The parameters m, κ, γ are model parameters, which together define interface energy and interface width (see the following section for more details).

The governing equations for each phase field η_p are obtained based on the functional derivative of the free energy functional with respect to η_p , assuming that the phase-fields are non-conserved, i.e.

$$\frac{\partial \eta_p}{\partial t} = -L \frac{\delta F}{\delta \eta_p} = -L \left[\frac{\partial f}{\partial \eta_p} - \nabla \cdot \frac{\partial f}{\partial (\nabla \eta_p)} \right], \quad (4.3)$$

where L is the kinetic coefficient (also dependent on the model parameters), f is the full integrand in (4.1) and $\nabla \cdot \partial f / \partial (\nabla \eta_p)$ is divergence of vector field $\partial f / \partial (\nabla \eta_p)$ defined by relation

$$\frac{\partial f}{\partial (\nabla \eta_p)} = \frac{\partial f}{\partial (\partial_x \eta_p)} \mathbf{n}_x + \frac{\partial f}{\partial (\partial_y \eta_p)} \mathbf{n}_y + \frac{\partial f}{\partial (\partial_z \eta_p)} \mathbf{n}_z \quad (4.4)$$

with $\partial_x, \partial_y, \partial_z$ being operators for unidirectional derivatives in the corresponding directions and $\mathbf{n}_x, \mathbf{n}_y, \mathbf{n}_z$ coordinate base vectors.

4.2.1 Isotropic model

In a system with uniform grain boundary properties, the interface energy is equal for all interfaces and hence the phase-field model parameters m, κ, γ (and interface width l) are constant in the system.

Then, using the expression (4.3), the governing equation for each phase field η_p takes the following form

$$\frac{\partial \eta_p}{\partial t} = -L \left[m \left(\eta_p^3 - \eta_p + 2\gamma \eta_p \sum_{j \neq p} \eta_j^2 \right) - \kappa \nabla^2 \eta_p \right] \quad (4.5)$$

The interface energy σ of the system is related to the model parameters via

$$\sigma = g(\gamma) \sqrt{m\kappa}, \quad (4.6)$$

where $g(\gamma)$ is a non-analytic function of parameter γ . The interface width l is expressed as

$$l = \sqrt{\frac{\kappa}{mf_{0c}(\gamma)}}, \quad (4.7)$$

where $f_{0c}(\gamma)$ is the value of $f_0(\eta_i, \text{cross}, \eta_j, \text{cross})$ in the points where the two phase fields η_i, η_j cross. $f_{0c}(\gamma)$ is a non-analytic function too. Values of both $g(\gamma)$ and $f_{0c}(\gamma)$ were tabulated and are available in [95]. Both functions are positive and monotonously rising.

Usually, the interface energy σ is known as material property and l is chosen for computational convenience, together with γ . Then, the parameter values are assigned from the following formulae

$$\kappa = \sigma l \frac{\sqrt{f_{0c}(\gamma)}}{g(\gamma)} \approx \frac{3}{4} \sigma l \quad (4.8)$$

$$m = \frac{\sigma}{l} \frac{1}{g(\gamma) \sqrt{f_{0c}(\gamma)}} \approx 6 \frac{\sigma}{l} \quad (4.9)$$

$$L = \frac{\mu}{l} \frac{g(\gamma)}{\sqrt{f_{0c}(\gamma)}} \approx \frac{4}{3} \frac{\mu}{l} \quad (4.10)$$

The symbol μ stands for interface mobility. The approximate relations above hold exactly when $\gamma = 1.5$ and are well applicable when $0.9 \leq \gamma \leq 2.65$ [7].

4.2.2 Anisotropic model and parameters assignment strategies

Two cases of interface energy anisotropy may occur, together or separately. Firstly, in the system there may be multiple interfaces with different interface energies (termed *misorientation dependence* in [7], here *pair-distinct isotropy* for greater generality). Secondly, there may be an interface with inclination-dependent interface energy. Additionally, the kinetic coefficient L can be inclination dependent.

In both cases of anisotropy in interface energy, some of the model parameters m, κ, γ must become spatially dependent in order to assure correct local representation of the interface energy and width. In other words, the equations (4.6) and (4.7) must hold in every point of the anisotropic system. These two equations locally form an undetermined system of three variables, hence one of the model parameters is free and many different parameters assignment strategies are possible.

In this paper, the parameter m is always a constant, because when m was spatially varied [7], the model behavior in multijunctions was reported to be strongly affected by the interface width. Such model would be non-quantitative and thus will not be further regarded in this paper.

Three different parameters assignment strategies are considered, which differ in value of m and further in which of parameters κ, γ is constant and which varies in space to keep equation (4.6) valid. The three strategies are denoted: IWc (variable γ, κ so that interface width is constant [7]), IWvG (variable interface width and γ [95]) and IWvK (variable interface width and κ). Table 4.1 summarizes, which parameters are kept constant and which vary to capture the anisotropy in the different strategies. The detailed procedure of the parameters assignment and ways to control the width of the narrowest interface are described in Appendix B. Note that for the IWc model we propose a single-step parameters determination procedure, which is more predictable and simpler than the original iterative one [7]. The two are equivalent, though.

Below follow details about the incorporation of pair-distinct isotropy and inclination-dependence in the model.

Table 4.1: Characterization of the three parameter assignment strategies: the one with constant interface width (IWc), with variable interface width and all anisotropy in γ (IWvG) and with variable interface width and all anisotropy in κ (IWvK). In the latter, it is inconvenient to choose other value of γ than $\gamma = 1.5$. IW stands for interface width, other symbols have meaning as in the text.

	IWc	IWvG	IWvK
fixed parameters	IW, m	κ, m	γ, m
varying parameters	γ, κ	IW, γ	IW, κ

Systems with pair-distinct isotropic IE

In the system with n phase fields, there are $n(n - 1)/2$ possible interfaces, each of which may have different (mean) interface energy $\sigma_{i,j}$. The indices i, j denote interface between phase fields η_i, η_j . A set of parameters $m, \kappa_{i,j}, \gamma_{i,j}, L_{i,j}$ (all scalars) is obtained by appropriate procedure (depending on the strategy, see Appendix B) so that the relations (4.6) and (4.7) are valid for each interface independently (equations (4.8)-(4.10) hold for each interface ($i-j$)). Then, these are combined together to produce the model parameter fields $\kappa(\mathbf{r}), \gamma(\mathbf{r}), L(\mathbf{r})$:

$$\kappa(\mathbf{r}) = \frac{\sum_{i=1}^n \sum_{j>i} \kappa_{i,j} \eta_i^2 \eta_j^2}{\sum_{i=1}^n \sum_{j>i} \eta_i^2 \eta_j^2} \quad (4.11)$$

$$\gamma(\mathbf{r}) = \frac{\sum_{i=1}^n \sum_{j>i}^n \gamma_{i,j} \eta_i^2 \eta_j^2}{\sum_{i=1}^n \sum_{j>i}^n \eta_i^2 \eta_j^2}, \quad (4.12)$$

$$L(\mathbf{r}) = \frac{\sum_{i=1}^n \sum_{j>i}^n L_{i,j} \eta_i^2 \eta_j^2}{\sum_{i=1}^n \sum_{j>i}^n \eta_i^2 \eta_j^2} \quad (4.13)$$

which stand in place of κ, γ in the functional in equation (4.1) and in place of L in the governing equation (4.3).

Notice that from Table 4.1 stems that in IWvG is $\kappa(\mathbf{r}) = \text{const}$ by definition (i.e. all the $\kappa_{i,j}$ s are equal) and similarly in IWvK $\gamma(\mathbf{r}) = \text{const} = 1.5$ (i.e. all $\gamma_{i,j}$ s are equal).

The free energy functional for IWc is then (those for IWvG and IWvK are equal, only with either $\kappa(\mathbf{r})$ or $\gamma(\mathbf{r})$ being constants, respectively):

$$F = \int_V \left\{ m f_0(\vec{\eta}) + \frac{\kappa(\mathbf{r})}{2} \sum_{i=1}^n (\nabla \eta_i)^2 \right\} dV, \quad (4.14)$$

$$f_0(\vec{\eta}) = \sum_{i=1}^n \left(\frac{\eta_i^4}{4} - \frac{\eta_i^2}{2} \right) + \sum_{i=1}^n \sum_{i>j} \gamma_{i,j} \eta_i^2 \eta_j^2 + \frac{1}{4}. \quad (4.15)$$

Both parameter fields $\kappa(\mathbf{r}), \gamma(\mathbf{r})$ are functions of phase fields $\vec{\eta}$. This dependence should produce new terms in the governing equations (from $\partial f / \partial \eta_p$ in equation (4.3)). However, because the denominator of $\gamma(\mathbf{r})$ cancels out in the functional, the new terms only arise from $\partial \kappa / \partial \eta_p$.

The governing equations then are

$$\begin{aligned} \frac{\partial \eta_p}{\partial t} = & -L(\mathbf{r}) \left[m \left(\eta_p^3 - \eta_p + 2\eta_p \sum_{j \neq p} \gamma_{p,j} \eta_j^2 \right) \right. \\ & \left. + \frac{1}{2} \frac{\partial \kappa}{\partial \eta_p} \sum_{i=1}^n (\nabla \eta_i)^2 - \kappa(\mathbf{r}) \nabla^2 \eta_p \right] \end{aligned} \quad (4.16)$$

The above procedure is fully variational, nevertheless inclusion of the term proportional to $\partial \kappa / \partial \eta_p$ enables the model to reduce the total energy of the system by introduction of so called third phase contributions (also ghost or spurious phases) at diffuse interfaces. [7] That is a common problem in multi-phase field models [75], where a third phase field attains non-zero value within an interface of two other phase fields. This mathematical artefact affects triple junction angles and in general is not physically justified. Several ways

of elimination or suppression of ghost phases were described in [75] and the references therein.

In this work, the ghost phases were eliminated by neglecting the term proportional to $\partial\kappa/\partial\eta_p$. However, because such model is not fully variational, the thermodynamic consistency can no longer be guaranteed in IWc and IWvK. This does not affect IWvG, because there is $\partial\kappa/\partial\eta_p = 0$ anyway. That accounts for a clear advantage of the IWvG model, as no ghost phases appear even when fully variational.

Systems with inclination-dependent interface energy

The orientation of an interface in a 2D system is given by the interface normal, inclined under the angle θ . The local value of interface energy may be a function of local interface inclination, i.e. $\sigma = \sigma(\theta)$. In Moelans' model [7], the normal at interface between η_i, η_j , denoted $\hat{\mathbf{n}}_{i,j}$, is defined as

$$\hat{\mathbf{n}}_{i,j} = \frac{\nabla\eta_i - \nabla\eta_j}{|\nabla\eta_i - \nabla\eta_j|} = \begin{bmatrix} (\hat{n}_{i,j})_x \\ (\hat{n}_{i,j})_y \end{bmatrix} \quad (4.17)$$

and the definite inclination of that normal

$$\theta_{i,j} = \text{atan2}[(\hat{n}_{i,j})_y, (\hat{n}_{i,j})_x], \quad (4.18)$$

which is the standard 2-argument arctangent function.

In 2D, the inclination-dependence of interface energy can be expressed as

$$\sigma_{i,j}(\theta_{i,j}) = \sigma_{i,j}^0 h_{i,j}(\theta_{i,j}) \quad (4.19)$$

where $\sigma_{i,j}^0$ is a scalar and $h_{i,j}(\theta_{i,j})$ is anisotropy function. The used anisotropy function was

$$h_{i,j}(\theta_{i,j}) = 1 + \delta \cos(n\theta_{i,j}), \quad (4.20)$$

with δ being strength of anisotropy and n the order of symmetry. Some properties of this anisotropy function and the resulting Wulff shapes are given in E.1.

The inclination dependence of $\sigma_{i,j}$ implies that some of the model parameters $\gamma_{i,j}, \kappa_{i,j}$ must be taken inclination-dependent too. Depending on the model used (IWc, IWvG or IWvK), the local validity of equation (4.6) is achieved using different inclination dependence of the variable parameters (see Table 4.2 for details).

Because the inclination-dependent $\kappa_{i,j}, \gamma_{i,j}$ are functions of components of gradients $\nabla\eta_i, \nabla\eta_j$, the divergence term in the functional derivative

Table 4.2: Inclination dependence of the variable parameters in the respective models. The interface energy is $\sigma_{i,j}(\theta_{i,j}) = \sigma_{i,j}^0 h_{i,j}(\theta_{i,j})$. Symbols $\kappa_{i,j}^0, \gamma_{i,j}^0$ stand for scalar values of the parameters determined from $\sigma_{i,j}^0$ (see B in [96]). Expressions for $\gamma_{i,j}(\theta_{i,j})$ follow the so called *weak anisotropy approximation* [7], i.e. they assume that the values of $\gamma_{i,j}(\theta_{i,j})$ do not diverge far from 1.5, so that the approximation $g^2[\gamma_{i,j}(\theta_{i,j})] \approx 16[2\gamma_{i,j}(\theta_{i,j}) - 1]/9[2\gamma_{i,j}(\theta_{i,j}) + 1]$ is applicable (see [7] for details). Second row contains expressions used in equations 4.23 and 4.24.

model	IWC	IWvG	IWvK
variable parameter(s)	$\kappa_{i,j}(\theta_{i,j}) = \kappa_{i,j}^0 h_{i,j}(\theta_{i,j})$	$\gamma_{i,j}(\theta_{i,j}) = -\frac{9}{4} \frac{[g(\gamma_{i,j}^0)h_{i,j}(\theta_{i,j})]^2 + 1}{[g(\gamma_{i,j}^0)h_{i,j}(\theta_{i,j})]^2 - 2}$	$\kappa_{i,j}(\theta_{i,j}) = \kappa_{i,j}^0 [h_{i,j}(\theta_{i,j})]^2$
	$\gamma_{i,j}(\theta_{i,j}) = -\frac{9}{2} \frac{g^2(\gamma_{i,j}^0)h_{i,j}(\theta_{i,j}) + 1}{g^2(\gamma_{i,j}^0)h_{i,j}(\theta_{i,j}) - 2}$		
$\partial \kappa_{i,j}/\partial h_{i,j}$ and $\partial \gamma_{i,j}/\partial h_{i,j}$	$\frac{\partial \kappa_{i,j}}{\partial h_{i,j}} = \kappa_{i,j}^0$	$\frac{\partial \gamma_{i,j}}{\partial h_{i,j}} = \frac{9g^2(\gamma_{i,j}^0)}{\left[\frac{9}{2}g^2(\gamma_{i,j}^0)h_{i,j}(\theta_{i,j}) - 2\right]^2}$	$\frac{\partial \gamma_{i,j}}{\partial h_{i,j}} = 2\kappa_{i,j}^0 h_{i,j}(\theta_{i,j})$
		$\frac{\partial \gamma_{i,j}}{\partial h_{i,j}} = \frac{18g^2(\gamma_{i,j}^0)h_{i,j}(\theta_{i,j})}{\left\{\frac{9}{2}g^2(\gamma_{i,j}^0)h_{i,j}(\theta_{i,j}) - 2\right\}^2}$	

(equation (4.3)) produces additional driving force terms. In the general case with multiple inclination-dependent interfaces, the divergence term equals

$$\begin{aligned}
\nabla \cdot \frac{\partial f}{\partial(\nabla \eta_p)} &= 2m\eta_p \nabla \eta_p \cdot \left[\sum_{j \neq p} \eta_j^2 \frac{\partial \gamma_{p,j}}{\partial(\nabla \eta_p)} \right] \\
&\quad + 2m\eta_p^2 \sum_{j \neq p} \left[\eta_j \nabla \eta_j \cdot \frac{\partial \gamma_{p,j}}{\partial(\nabla \eta_p)} \right] \\
&\quad + m\eta_p^2 \sum_{j \neq p} \eta_j^2 \left[\nabla \cdot \frac{\partial \gamma_{p,j}}{\partial(\nabla \eta_p)} \right] \\
&\quad + \frac{1}{2} \left[\nabla \cdot \frac{\partial \kappa}{\partial(\nabla \eta_p)} \right] \sum_{i=1}^n (\nabla \eta_i)^2 \\
&\quad + \frac{1}{2} \frac{\partial \kappa}{\partial(\nabla \eta_p)} \cdot \left[\nabla \sum_{i=1}^n (\nabla \eta_i)^2 \right] \\
&\quad + \nabla \kappa(\mathbf{r}) \cdot \nabla \eta_p + \kappa(\mathbf{r}) \nabla^2 \eta_p.
\end{aligned} \tag{4.21}$$

The vector field $\partial \kappa / \partial(\nabla \eta_p)$ is

$$\frac{\partial \kappa}{\partial(\nabla \eta_p)} = \frac{\sum_{j \neq p}^n \left(\frac{\partial \kappa_{p,j}}{\partial(\nabla \eta_p)} \right) \eta_p^2 \eta_j^2}{\sum_{k=1}^n \sum_{l>k} \eta_k^2 \eta_l^2} \tag{4.22}$$

where the sum in the numerator goes through all distinct interfaces of $\eta_p(\mathbf{r})$. The vector fields $\partial \kappa_{p,j} / \partial(\nabla \eta_p)$ are expressed

$$\frac{\partial \kappa_{p,j}}{\partial(\nabla \eta_p)} = \frac{1}{|\nabla \eta_i - \nabla \eta_j|} \frac{\partial \kappa_{p,j}}{\partial h_{p,j}} \frac{\partial h_{p,j}}{\partial \theta_{p,j}} \begin{bmatrix} -(\hat{n}_{i,j})_y \\ (\hat{n}_{i,j})_x \end{bmatrix}. \tag{4.23}$$

Note, that the above vector field is nonzero only in IWc and IWvK models at the interfaces ($p-j$) with inclination-dependent IE. Likewise, the below vector field is nonzero only in IWc and IWvG

$$\frac{\partial \gamma_{p,j}}{\partial(\nabla \eta_p)} = \frac{1}{|\nabla \eta_i - \nabla \eta_j|} \frac{\partial \gamma_{p,j}}{\partial h_{p,j}} \frac{\partial h_{p,j}}{\partial \theta_{p,j}} \begin{bmatrix} -(\hat{n}_{i,j})_y \\ (\hat{n}_{i,j})_x \end{bmatrix}. \tag{4.24}$$

The multipliers $\partial \kappa_{p,j} / \partial h_{p,j}$ and $\partial \gamma_{p,j} / \partial h_{p,j}$ differ in individual models and are also provided in Table 4.2. The term $\partial h_{p,j} / \partial \theta_{p,j}$ is defined by the inclination-dependence at the interface ($p-j$).

The governing equation then is

$$\frac{\partial \eta_p}{\partial t} = -L(\mathbf{r}) \left[m \left(\eta_p^3 - \eta_p + 2\eta_p \sum_{j \neq p} \gamma_{p,j}(\theta_{p,j}) \eta_j^2 \right) - \nabla \cdot \frac{\partial f}{\partial (\nabla \eta_p)} \right]. \quad (4.25)$$

Note, that the term proportional to $\partial \kappa / \partial \eta_p$ was neglected here.

In models with variable interface width (IWvG, IWvK), at the interfaces with inclination-dependent interface energy, the interface width is a function of the inclination, i.e. $l_{i,j} = l_{i,j}(\theta_{i,j})$. Because the kinetic coefficient $L_{i,j}$ is inversely proportional to the interface width $l_{i,j}$ (see equation (4.10)), the kinetic coefficient is inclination-dependent as well (even for *constant* grain boundary mobility $\mu_{i,j}$). The inclination dependence of $L_{i,j}(\theta_{i,j})$ due to interface width variation is in the IWvG model

$$L_{i,j}(\theta_{i,j}) = L_{i,j} h_{i,j}(\theta_{i,j}) \quad (4.26)$$

and in the IWvK model

$$L_{i,j}(\theta_{i,j}) = L_{i,j} / h_{i,j}(\theta_{i,j}), \quad (4.27)$$

where $h_{i,j}(\theta_{i,j})$ is the anisotropy function in interface energy (4.19).

The equations (4.26),(4.27) were derived from an alternative expression for the kinetic coefficient $L_{i,j}$

$$L_{i,j} = \frac{\mu_{i,j} \sigma_{i,j}(\theta_{i,j})}{\kappa_{i,j}(\theta_{i,j})}, \quad (4.28)$$

where the inclination dependencies of the right-hand side were expressed correspondingly to the model (see Table 4.2 for $\kappa_{i,j}(\theta_{i,j})$).

Due to varying number of driving force terms in the three parameter assignment strategies, the governing equations are different in each and hence it is justified to call them different models.

Systems with inclination-dependent mobility

Let the interface $(i-j)$ have isotropic interface energy and inclination-dependent grain boundary mobility with anisotropy function $h_{i,j}^\mu(\theta_{i,j})$, i.e. $\mu_{i,j} = \mu_{i,j}(\theta_{i,j}) = \mu_{i,j}^0 h_{i,j}^\mu(\theta_{i,j})$. From equation (4.10) we can see that the kinetic

coefficient must have the same anisotropy, i.e. $L_{i,j}(\theta_{i,j}) = L_{i,j}^0 h_{i,j}^\mu(\theta_{i,j})$, where $L_{i,j}^0 = \mu_{i,j}^0 g(\gamma_{i,j})/l_{i,j} f_{0c}(\gamma_{i,j})$.

If the interface energy is inclination-dependent as well and a model with variable interface width is used (either IWvG or IWvK), the inclination dependence in $L_{i,j}(\theta_{i,j})$ due to the interface width variation must be included similarly like in (4.26) and (4.27). The physical inclination-dependence is independent from the one due to interface width variation, implying the following expression for IWvG model

$$L_{i,j}(\theta_{i,j}) = L_{i,j}^0 h_{i,j}(\theta_{i,j}) h_{i,j}^\mu(\theta_{i,j}) \quad (4.29)$$

and for the IWvK model analogically

$$L_{i,j}(\theta_{i,j}) = L_{i,j}^0 \frac{h_{i,j}^\mu(\theta_{i,j})}{h_{i,j}(\theta_{i,j})}, \quad (4.30)$$

where $h_{i,j}(\theta_{i,j})$ is the interface energy anisotropy function.

Interface profiles in different models

The main difference in the model modifications is how the interface width varies as function of local interface energy. Obviously, in IWc the width is constant. In IWvK (with $\gamma = 1.5$) the width of interface $i-j$ can be computed as

$$l_{i,j} = 6 \frac{\sigma_{i,j}}{m}. \quad (4.31)$$

Apparently, in IWvK model the interface width is proportional to the interface energy, i.e. the larger the interface energy, the larger the interface width.

In IWvG the width can be expressed from (4.7) and (4.6) assuming $\frac{4}{3}\sqrt{f_{0,c}}(\gamma_{i,j}) = g(\gamma_{i,j})$ (which holds for small values of $\gamma_{i,j}$). Then, it goes approximately

$$l_{i,j} \approx \frac{\kappa}{\sigma_{i,j}}, \quad (4.32)$$

and apparently the larger interface energies are associated with lower interface widths in IWvG.

4.3 Numerical implementation

All models were implemented in a single MATLAB function, where the governing equations were solved by centered finite differences of second order, explicit

Euler time stepping and boundary conditions implemented using ghost nodes. For more details on the used finite difference schemes, refer to the Appendix C. The minimal code to run the simulations is available in the dataset [11]. During the parameters assignment in models with variable interface width (IWvG, IWvK), there was assured control over the minimal interface width, i.e. that there would be no interface narrower than the user-specified one. That is to prevent unphysical behavior of the interface due to too small grid resolution. Different strategies had to be adopted in IWvK and IWvG, respectively. They are described in Appendix B together with other best practices in parameters determination for the respective models. The MATLAB functions which were used for parameters determination were also included in the dataset [11].

In the simulations with inclination-dependent interface energy, the vector field $\partial\kappa/\partial(\nabla\eta_p)$ was computed as in equations (4.22) and (4.23), the fields $\partial\gamma_{p,j}/\partial(\nabla\eta_p)$ as in equation (4.24) and their divergences (see equation (4.21)) were computed numerically (by centered differences), as well as the gradient $\nabla\kappa(\mathbf{r})$. All the above terms were computed in the IWc model, whereas in the models with variable interface width some of them could be omitted (as explained in section 4.2.2).

When the anisotropy in inclination-dependent interface energy was strong (i.e. $\delta > 1/(n^2 - 1)$ or $\Omega > 1$), the anisotropy function had to be regularized as described in [29] in order to avoid ill-posedness of the governing equations for interfaces with missing inclination.

In finite difference method, the ratio of the time step Δt to the grid spacing Δx determines the numeric stability of the simulation. Specifically, the so-called Courant number C must be $0 < C < 0.5$, where in this model

$$C = \min[\kappa(\mathbf{r})L]\Delta t/(\Delta x)^2. \quad (4.33)$$

In practice, the time step was computed using equation (4.33) assuming the value of $C \leq 0.3$. For stronger anisotropies C had to be reduced farther. When $0.129 \leq \sigma_{min}/\sigma_{max} \leq 0.2$, the value $C = 0.12$ was used, when $0.2 < \sigma_{min}/\sigma_{max} \leq 0.3$, $C = 0.17$ and for $\sigma_{min}/\sigma_{max} > 0.3$ the used Courant number was $C = 0.3$. The latter value of Courant number was also applied in simulations with inclination-dependent interface energy and smooth Wulff shapes ($\Omega \leq 1$). For cornered Wulff shapes ($\Omega > 1$), the following dependence was obtained from visual inspection of the interface normal inclination field $\theta(\mathbf{r})$ defined in equation (18) ($\theta(\mathbf{r})$ was sensitive to the numeric instabilities) during the simulation

$$C(\Omega) = \frac{1}{a\Omega + b}. \quad (4.34)$$

The Table 4.3 contains the values of a, b in the respective model modifications.

Table 4.3: Parameters from equation (4.34) describing anisotropic dependence of the Courant number C in simulations with inclination-dependent interface energy and strong anisotropy $\Omega > 1$.

	IWc	IWvG	IWvK
a	1.38	1.43	0.98
b	1.95	1.91	2.35

The following 9-point stencil was used for computation of the laplacian in grid point (k, l)

$$\begin{aligned}
 (\nabla^2 \eta)_{k,l} = & \frac{1}{6h^2} [4(\eta_{k-1,l} + \eta_{k+1,l}\eta_{k,l-1} + \eta_{k,l+1}) \\
 & + \eta_{k+1,l+1} + \eta_{k-1,l-1} + \eta_{k-1,l+1} + \eta_{k+1,l-1} \\
 & - 20\eta_{k,l}].
 \end{aligned} \tag{4.35}$$

When the interface energy is inclination-dependent, it can be seen in equations (4.23), (4.24) that some driving force terms are proportional to $1/|\nabla\eta_i - \nabla\eta_j|$. In fact, some are even proportional to $1/|\nabla\eta_i - \nabla\eta_j|^3$ when worked out analytically. Far enough from the interface, the magnitude $|\nabla\eta_i - \nabla\eta_j|$ inevitably gets smaller than the numeric resolution, which causes severe numeric instabilities due to locally very large driving forces. For this reason, all the driving force terms from equation (4.21) were only computed in a region close enough to the interface. Two such regions $\Gamma_{out}, \Gamma_{inn}$ (outer and inner) were selected based on the local value of $|\nabla\eta_i - \nabla\eta_j|$ (see Figure 4.1). The region Γ_{inn} was a subset of Γ_{out} . The interface inclination field $\theta_{i,j}$ was computed in Γ_{out} , where $|\nabla\eta_i - \nabla\eta_j|^3(\Delta x)^3 > C_{out}^3$ and the driving force terms $\nabla \cdot \partial f / \partial(\nabla\eta_p)$ were computed in region Γ_{inn} where $|\nabla\eta_i - \nabla\eta_j|^3(\Delta x)^3 > C_{inn}^3$. The constants $C_{out} = 10^{-6}$ and $C_{inn} = 0.005$ have the meaning of minimal local change in value of phase field which is acceptable to the respective near-interface region (this is exactly true for $\gamma = 1.5$ and approximate otherwise). Note, that the driving force from homogeneous free energy density (i.e. $\partial f / \partial\eta_p$) and the laplacian term $\kappa(r)\nabla^2\eta_p$ were computed and applied in the whole simulation domain.

In the Wulff shape simulations, the accuracy of match to the analytical shape with IWvG phase field contour turned out to be sensitive to alignment of the shape within the numerical grid. For strong anisotropies $\Omega > 1$, when the corner laid exactly on some grid line, the IWvG contours were slightly deformed, making the model perform seemingly worse than IWc and IWvK (which were not affected by this). This problem was solved by shifting the center of the initial shape by half a pixel in both x and y direction. No corner than laid on

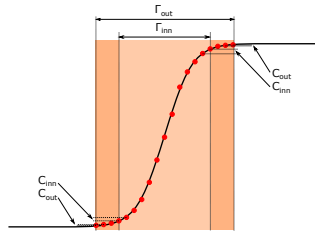


Figure 4.1: Illustration of the near-interface regions $\Gamma_{out}, \Gamma_{inn}$, defined by absolute values of difference in phase fields between neighbouring points.

Table 4.4: Overview of the simulations carried out in every simulation experiment. Note that these were carried out for every model modification (i.e. IWc, IWvG and IWvK) and simulation run (see Table 4.5). Number of simulations in every experiment is provided in the column Count. See text for more details.

Experiment	Varied par.	Values	Count
Wulff shape	Ω (-)	0.2, 0.4, 0.6, 0.8, 1.0, 2.3, 3.6, 4.9, 6.2, 7.5	10
Kin.comp.aniso. circle	Ω (-)	0.1, 0.3, 0.5, 0.7 , 0.9	5
Triple junction	σ_1/σ_2 (-)	0.13, 0.2, 0.3, 0.4, 0.5, 0.6, 0.7, 0.8, 0.9, 1.0, 1.1, 1.2, 1.3, 1.4, 1.5, 1.6, 1.7, 1.8, 1.9, 2.0	20

any grid line and that solved the problem. Rotating the Wulff shape relative to the grid had similar effect. All the results in the main text were simulated with the shifted initial shape. This is not likely to play any significant role in grain growth simulations as the corner motion along a grid line is very unlikely with arbitrary grain structure and local grain orientation.

4.4 Methodology

Three different simulation experiments were performed: a shrinking Wulff shape, kinetically compensated anisotropic curvature-driven circle shrinkage and triple junction angles. The initial-state geometries and grid dimensions are in Figure 4.2. Except for the shrinking circles simulation, a parametric study was carried out in every experiment in order to validate the model behavior. Table 4.4 summarizes the variable parameters in every experiment.

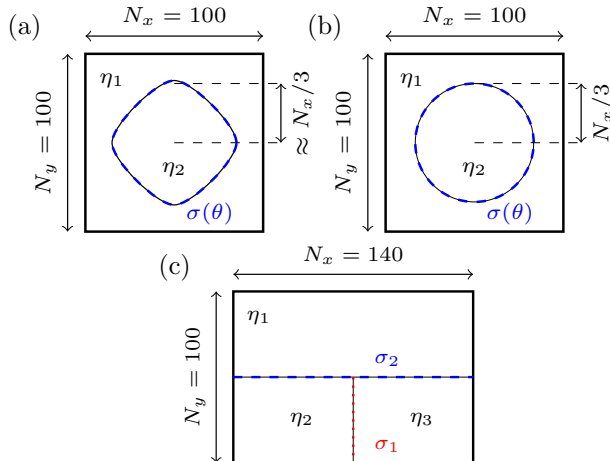


Figure 4.2: Initial conditions in the different numeric experiments with indicated interface energies. In a) Wulff shape shrinkage, b) kinetically compensated anisotropic curvature-driven circle shrinkage and c) measurement of triple junction angle. Grid dimensions correspond to the base run and 1000IW run (see text for details). All interfaces have equal mobilities.

Each of the experiments was simulated using all the three model modifications (IWc, IWvG and IWvK) successively and the results were quantitatively compared.

In order to distinguish the behavior of the model from the artefacts of numeric discretization, the above described series of simulations was re-run for several numeric settings. Throughout the paper, these large series are called 'runs'.

Results of four runs are presented in this paper, the basic settings of which are summarized in Table 4.5. The difference between the runs were: a) the minimal set interface width l_{min} and b) the number of points in the interface. The runs are denoted base run, IW/2, 14IWpts and 1000IW. The base run had rather coarse grid and 7 points in the interface, which should in general be reliable yet not very computationally heavy settings. The minimal interface width was $l_{min} = 1 \text{ nm}$. In the run IW/2 the interface width was halved ($l_{min} = 0.5 \text{ nm}$) and the number of points in the interface was 7 again. In the 14IWpts run, the interface width was as in the base run but the points in the interface were doubled (to be 14). Physical dimensions of the simulated domain were equal in the described runs but the grid spacing was halved in IW/2 and 14IWpts runs. In the last 1000IW run, the grid was equal as in the base run, but the physical dimensions were scaled by a factor of 1000, meaning the minimal interface

Table 4.5: Numeric settings of different simulation runs (for each simulation experiment and model). l_{min} is the minimal interface width. N_x and N_y are grid dimensions in the base run as shown in Figure 4.2

	base run	IW/2	14IWpts	1000IW
grid dimensions	$N_x \times N_y$	$2N_x \times 2N_y$	$2N_x \times 2N_y$	$N_x \times N_y$
l_{min} (nm)	1	0.5	1	1000
points in l_{min}	7	7	14	7

width $l_{min} = 1 \mu\text{m}$. This is the practical settings for the actual grain growth simulations. The latter run validated that the meso-scale behavior of the model is equal to that one at the nanometer scale.

In the simulation experiments, the position of the interface in the respective geometry was compared to the expected shape. Depending on the parameters assignment strategy, the phase field profiles may not be symmetric about the point 0.5 in Moelans' model. For this reason, it was considered that the position of the interface $i-j$ was in points $\mathbf{r} = (x, y)$ of the domain, where $\eta_i(\mathbf{r}) = \eta_j(\mathbf{r})$, i.e. where the two profiles crossed. This way the contours were always well defined and could be quantitatively compared to appropriate analytical models even for Wulff shape simulations, where the profile shape varies along the interface.

The below subsections describe in detail the analytic solutions of the problems and results processing in the individual simulation experiments.

4.4.1 Used anisotropy function and its Wulff shape

The anisotropy function $h(\theta) = 1 + \delta \cos(n\theta)$ was used, together with the normalized strength of anisotropy $\Omega = \delta(n^2 - 1)$. Ω easily distinguishes weak from strong anisotropy, because for $0 < \Omega < 1$ the Wulff shape is smooth, whereas for $1 \leq \Omega < n^2 - 1$ it has corners. Section E.1 provides more details about this anisotropy function. Fourfold symmetry was assumed (i.e. $n = 4$).

Ill-posedness of the governing equations for forbidden orientations on Wulff shapes for strong anisotropies ($\Omega > 1$) was treated by regularization of the anisotropy function as in [29]. This procedure identifies intervals of angles θ_{nc} , where the function $1/h(\theta)$ (so-called Frank plot) is non-convex. Not every of these angles θ_{nc} is forbidden (i.e. exhibiting negative interface stiffness), but every forbidden angle belongs to θ_{nc} . Regularization of $h(\theta)$ is equivalent to convexification of $1/h(\theta)$, where the latter means to replace the non-convex parts by straight lines. This is illustrated in Figure 4.3b. The procedure is

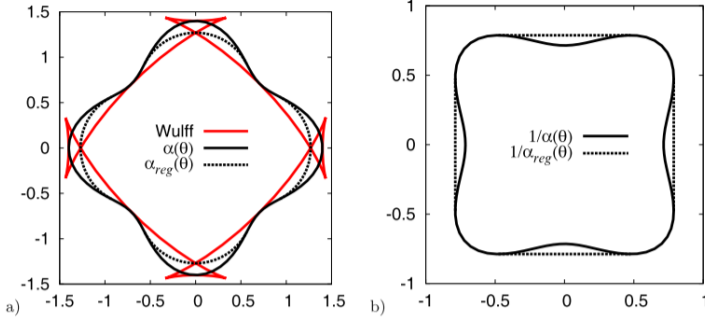


Figure 4.3: Regularization of the anisotropy function $h(\theta) = 1 + \delta \cos(n\theta)$ (in the figure denoted as $\alpha(\theta)$). In (a) the anisotropy function, regularized anisotropy function and Wulff plot, in (b) the Frank's plot of the anisotropy function and regularized anisotropy function. Taken from [31].

farther described below for one of the n symmetric intervals, $(-\pi/n, \pi/n)$ (note that in this case $n = 4$). Let $h_{reg}(\theta)$ be the regularized anisotropy function and $0 < \theta_{nc}^{edge} < \pi/n$ be the largest angle of the non-convex interval (i.e. on its edge). In the current case, the interval of angles with non-convexity in the Frank's plot is $(-\theta_{nc}^{edge}, \theta_{nc}^{edge})$.

$$h_{reg}(\theta) = \frac{h(\theta_{nc}^{edge})}{\cos(\theta_{nc}^{edge})} \cos(\theta) \quad \text{for } |\theta| \leq \theta_{nc}^{edge} \quad (4.36)$$

$$h_{reg}(\theta) = h(\theta) \quad \text{for } \theta_{nc}^{edge} < |\theta| < 2\pi/n.$$

In Figure 4.3a can be seen, that the straight line in $1/h(\theta)$ polar plot shows in the $h_{reg}(\theta)$ as a circular arc spanning between the points $h(-\theta_{nc}^{edge})$ and $h(-\theta_{nc}^{edge})$. The n -fold rotation provides the θ_{nc}^{edge} angles in the other $n - 1$, symmetrically equivalent intervals.

For validation of the kinetics of shrinkage, an analytic expression for Wulff shape shrinkage rate was derived in E.2. Measurement of area/volume occupied by a grain/phase is trivial in phase field method, hence the rate of its change (i.e. the shrinkage rate) can be easily used for validation or benchmark. The derivation in [96] delivers the expression

$$\frac{dA_W}{dt} = -2\pi\mu\sigma_0 \frac{C_W(\Omega, n)}{1 - \delta} \quad (4.37)$$

where $C_W(\Omega, n) = A_W/A_{circle}$ is an anisotropic factor relating the area of a Wulff shape and a circle of equal radius. For fourfold symmetry it was

numerically computed and fitted by polynomial $C_W(\Omega, 4) = \sum_{i=0}^4 a_i \Omega^{N-i}$ with $a_0 = -0.00032$, $a_1 = 0.00639$, $a_2 = -0.04219$, $a_3 = 0.00034$, $a_4 = 1.00000$ (rounded to the relevant decimal digits). As can be seen, the analytical shrinkage rate is a constant, which is consistent with [68].

With isotropic interface energy ($\delta = \Omega = 0$) the steady state shape is a circle and the anisotropic factor is $C_W/(1 - \delta) = 1$, hence the isotropic curvature-driven shrinkage rate of a circle is (as also e.g. in [80])

$$\frac{dA}{dt} = -2\pi\mu\sigma_0. \quad (4.38)$$

4.4.2 Quantifying the match in shape

The *Hausdorff distance* was used for quantification of the match in shape. Let the 2D curves $\mathbf{w}, \mathbf{w}_{PF}$ be the analytical shape and the phase-field contour, respectively. The Hausdorff distance $d_H(\mathbf{w}, \mathbf{w}_{PF}) = \lambda$ between them implies, that λ is the smallest number such that \mathbf{w} is completely contained in λ -neighborhood of \mathbf{w}_{PF} and vice-versa [97]). Formally, it is defined between sets P and Q as

$$d_H(Q, P) = \max(\tilde{d}_H(P, Q), \tilde{d}_H(Q, P)), \quad (4.39)$$

where

$$\tilde{d}_H(P, Q) = \max_{x \in P} \min_{y \in Q} \|x - y\| \quad (4.40)$$

is *directed Hausdorff distance*. It is always $d_H(\cdot, \cdot) \geq 0$, and the closer to zero, the more alike the compared sets are. It has been extensively used for image matching and pattern recognition [98].

For comparability in the two validation experiments with inclination-dependent interface energy, it is essential that the two curves $\mathbf{w}, \mathbf{w}_{PF}$ are co-centric and scaled to unit radius.

Note that the data set [11] includes also MATLAB functions for the contour shape matching.

4.4.3 Quantifying match in shrinkage rate

The shrinkage rate was obtained as mean value of shrinkage rates in a simulation time interval where the area of the shape was in between 0.95-0.6 fraction of the initial area. This choice should prevent the diffuse interface from being too large compared to the shape itself, in which case it would affect the kinetics.

Additionally, this approach turned out to be rather insensitive to the particular numeric settings, which is convenient for validations.

The results are presented as relative error δx , defined in the following convention

$$\delta x = 100 \frac{x_0 - x}{x} \%, \quad (4.41)$$

where x_0 is the measured value and x is the expected one. In this convention, the shrinkage was *slower* than expected when $\delta x < 0$, and *faster* when $\delta x > 0$.

4.4.4 Wulff shape

Shrinking Wulff shapes with different strengths of anisotropy were simulated. The match to the analytic shape was measured in Hausdorff distance. The shrinkage rate was expressed analytically and used for validation as well.

The Neumann boundary conditions were applied to all boundaries in a system with initial condition like in Figure 4.2a. The initial condition in every simulation was the analytic Wulff shape of the corresponding strength of anisotropy Ω as discretized by the grid. The radius was taken such that the initial shape occupied the area fraction in the domain of at least 0.25. Because the initial Wulff shape already minimized the interface energy, the shrinkage with constant rate as in (4.37) was expected and any change in the shape was a departure from the analytic solution.

4.4.5 Kinetically compensated anisotropic circle shrinkage

This simulation experiment validates the inclination-dependence of the kinetic coefficient in combination with inclination-dependent interface energy. Specifically, the anisotropy of kinetic coefficient was chosen such that it compensated the anisotropic driving force so that the resulting interface motion was isotropic.

Again, the match to the steady-state shape (a circle) was quantified by Hausdorff distance and the mean shrinkage rate was measured when the shape area was a fraction 0.95-0.6 relative to the initial condition. Parametric study in Ω were carried out to validate the model.

The initial condition for the simulation experiment was as in Figure 4.2b, i.e. a two-phase-field system of a circular grain in a matrix.

Normal velocity v_n of a curvature-driven interface with inclination-dependent interface energy is [23]

$$v_n(\theta) = \frac{\mu}{\varrho} \sigma_0 [h(\theta) + h''(\theta)], \quad (4.42)$$

where μ is interface mobility, ϱ is local radius of curvature and $\sigma_0[h(\theta) + h''(\theta)]$ is the interface stiffness. With $h(\theta) = 1 + \delta \cos(n\theta)$ the inclination-dependent factor in (4.42) is $[h(\theta) + h''(\theta)] = 1 - \delta(n^2 - 1) \cos(n\theta) = 1 - \Omega \cos(n\theta)$.

When the interface mobility is set anisotropic as

$$\mu(\theta) = \frac{\mu_0}{1 - \Omega \cos(n\theta)}, \quad (4.43)$$

the resulting interface normal velocity v_n does not depend on interface inclination θ anymore, i.e. it is isotropic. The shrinkage rate is then (4.38).

The below presented simulations were all carried out with $\Omega < 1$, because the kinetic coefficient as in equation (4.43) is then positive for all interface inclinations.

The ratio of maximal to minimal interface velocity due to the anisotropic interface energy is $(1 + \Omega)/(1 - \Omega)$, which indicates rather strong kinetic anisotropy when Ω is close to 1. E.g. with $\Omega = 0.9$ the ratio of maximal to minimal interface velocity is 19 (assuming constant ϱ for all inclinations, which holds for a circle). Note that the corresponding ratio of maximal to minimal interface energy is only 1.0664 (with four-fold symmetry).

4.4.6 Triple junction angles

In this experiment, triple junction angles are measured in systems with different combinations of pair-distinct isotropic interface energies. This approach validates how well the triple junction force balance is reproduced by the model.

The initial geometry was as shown in Figure 4.2b, with periodic left and right boundaries, and Neumann boundary conditions on the top and bottom boundaries. The individual interfaces are isotropic but have different interface energies. The initially straight interface segments (1-2) and (1-3) with grain boundary energy σ_2 evolve into circular arcs, which then move towards the center of curvature, i.e., downwards. The two grains, η_2 and η_3 , shrink, and in the steady state, the angle α between the arcs (see Figure 4.8a) at the triple junction is described by Young's law [45] (Section 3.3.3):

$$\alpha = 2\arccos(\sigma_1/2\sigma_2). \quad (4.44)$$

The ratio σ_1/σ_2 was varied in the parametric study to validate the model (see Table 4.4). It was always $\sigma_1 = 0.3 \text{ J/m}^2$ and σ_2 was computed from the ratio.

The phase field contours of interfaces (1-2) and (1-3) were analyzed using two methods to determine the triple junction angle α . First, the points on both arcs nearest to the triple junction were fitted with a straight line (indicated by red segments in Figure 4.8a). Second, the remaining arc points were fitted with a circular arc (shown by green segments in Figure 4.8a). A simple geometric construction allows the determination of the angle α from the fitted parameters in the latter case [80] as

$$\alpha = 2\arccos(x/R), \quad (4.45)$$

where R is the fitted circle arc radius and x is the horizontal distance from the triple junction (see the scheme in Figure 4.8a). The width of the interval in which the arcs were fitted with straight lines (the width of the pink rectangles in Figure 4.8a) was set to the width of interface (2-3) (i.e., half of the width on each side).

The accuracy of the line fitting is especially affected by the width of the above interval, and the accuracy of the circle arc fitting is mostly influenced by the shape of the simulated arc.

4.5 Results

4.5.1 Wulff shapes

The Figures 4.4a-4.4f visually compare the Wulff shapes obtained from simulation by the different models (in base run) to the analytic ones. As can be seen, the overall match is very good in all the three models, although a rather round contour near the corners in strong-anisotropy Wulff shapes are observed (this is more apparent in Figure 4.5b, which shows detail of the contours near a corner for $\Omega = 7.5$). That was expected, as no special finite difference scheme was used near corners (in [29] a one-sided finite difference scheme was proposed to avoid corners rounding).

Figure 4.5a, shows the match to Wulff shape as function of normalized strength of anisotropy Ω in the base run. As can be seen, the IWvG model slightly outperformed the other two in strong anisotropies because it was able to resolve the corners the best (see Figure 4.5b). However, when the interface width was halved in the IW/2 run, all the models performed nearly equally well because with smaller interface width the rounding near the corners was reduced. Interestingly, the IWvG model performed comparably in the IW/2 and base runs, which is in contrast to IWc and IWvK, which improved markedly with

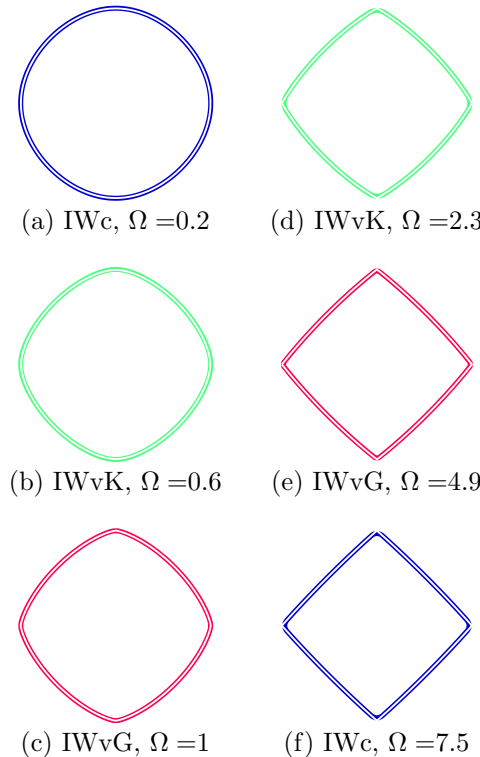


Figure 4.4: Demonstration of the simulated Wulff shapes for strengths of anisotropy Ω with the different models (base run). The white line is the analytic Wulff shape and the colored ones are the extracted phase field contours.

narrower interface width.

The best results in match to Wulff shape were obtained in the 14IWpts run with IWvG model. IWc and IWvK models performed comparably in the 14IWpts and IW/2 runs.

The mean shrinkage rates of the Wulff shapes as function of strength of anisotropy are in Figure 4.6a for the base run. At first sight, all the models perform comparably well, following the analytical prediction within an absolute error of 3 %. The Figures 4.6b and 4.6c show the time evolution of shrinkage rate with $\Omega = 7.5$ in the base and IW/2 runs, respectively. It can be seen that despite the mean shrinkage rates being near the prediction, in the base run, the shrinkage rate of IWvG model did not converge to the analytic prediction (see the inset of Figure 4.6b, where the IWvG curve clearly declines). In the

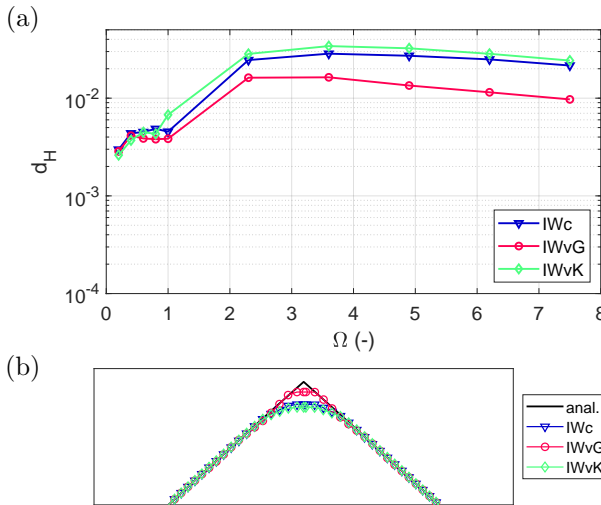


Figure 4.5: In (a) the match to Wulff shape for the model modifications in the base run as function of normalized strength of anisotropy Ω . In (b) a detail of the phase field contours near the Wulff shape corner for simulation with $\Omega = 7.5$.

IW/2 run the IWvG model did converge close to the analytic shrinkage rate (see also the inset of Figure 4.6c) and all the mean values are a little closer than in the base run. Note that in the IWvG model the lowest-energy interface has the widest interface width and that the cornered Wulff shape contains only interface orientations with lower energy. For this reason it required narrower interface width to reach constant shrinkage rate.

The relative error in mean shrinkage rate obtained with this methodology was nearly the same in the base and IW/2 runs though (both within $\pm 3\%$). Apparently, the difference is that with narrower interface the attained shrinkage rate is more steady. Additional run with even finer grid was carried out and no improvement in the mean values of shrinkage rates was observed. It can thus be concluded that the methodology is robust enough to assess the shrinkage rate even in the domain 100x100 (i.e. base run).

In addition to the four simulation runs discussed so far, the Wulff shapes simulations were re-run also with 4 and 5 points in the interface. The match to Wulff shape was worse than with 7 or 14 points, but the shapes were resolved qualitatively well regardless. The shrinkage rates were smaller than expected though, due to grid pinning. Seven points in the interface were thus confirmed

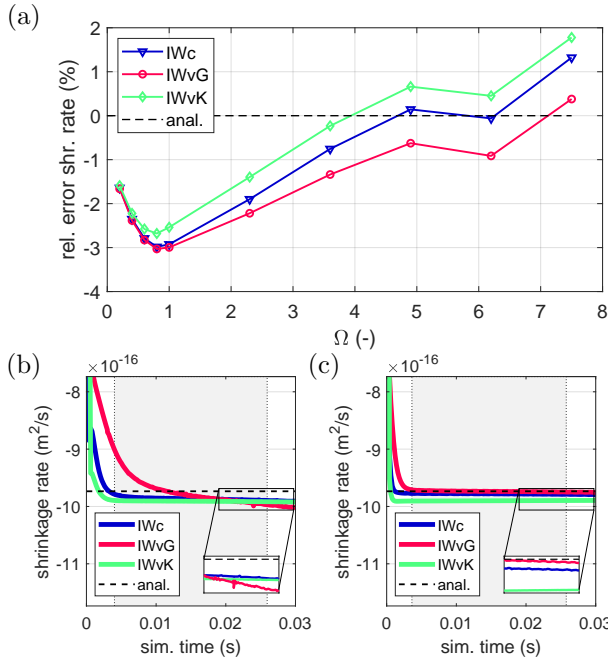


Figure 4.6: Wulff shape shrinkage rate results. In (a) the mean shrinkage rate in the base run as function of normalized strength of anisotropy Ω , in (b) and (c) there is time evolution of shrinkage rate for $\Omega = 7.5$ in the base and IW/2 runs, respectively. The shaded areas in b) and c) indicate the time interval from which the mean shrinkage rate was computed.

as a reasonable value for the validations and practical simulations.

No significant effect of interface width scaling in the run 1000IW was found.

4.5.2 Kinetically compensated anisotropic circle shrinkage

The quantified match to the circle and the mean shrinkage rate as functions of strength of anisotropy Ω are in Figures 4.7a and 4.7b, respectively (results of the base run showed). All models and runs retained the initial circle well or up to excellent geometrical match. Nevertheless, the IWvG model gave the best results, except for the strongest anisotropy, where the IWvK model was better. Only minor improvement in the match was achieved in the IW/2 run when compared to the base run. As with Wulff shapes simulations, the best match was obtained in the 14IWpts run, which also exhibited the best mean

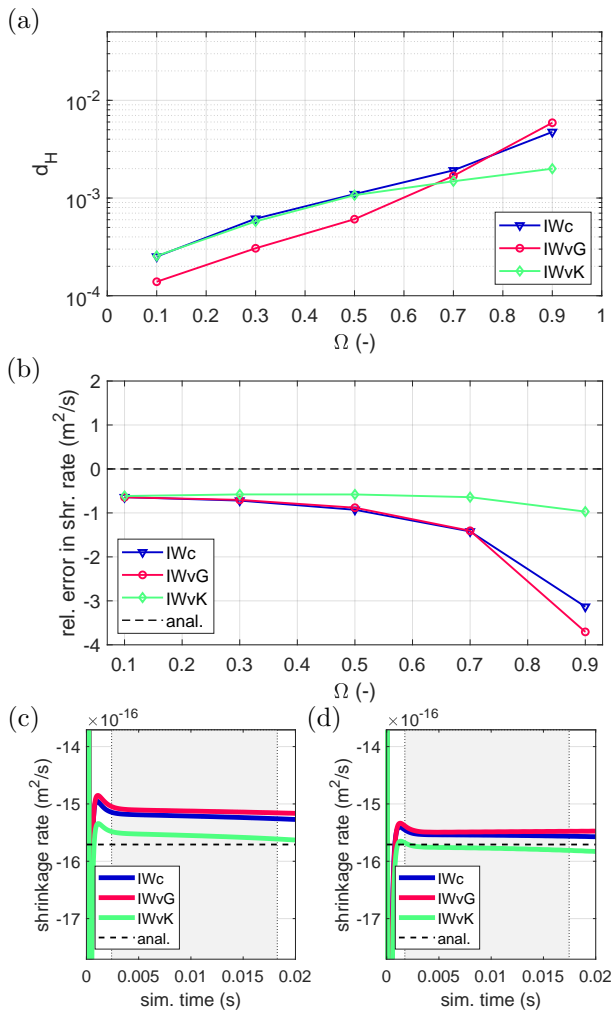


Figure 4.7: Results for kinetically compensated anisotropic shrinkage. In (a) the match to circle for the base run, in (b) the mean shrinkage rate for 14IWpts run, in (c) and (d) the shrinkage rate time evolution in simulation with $\Omega = 0.9$ in the base run and 14IWpts runs, respectively.

shrinkage rates (for all the three models).

The relative error in shrinkage rates in Figure 4.7b shows slightly decreasing trend with Ω for IWc and IWvG models (i.e. slowing down). The values of IWvK model were not affected and were constant. Apparently, the symmetric profiles of IWvK model provide an advantage for preserving the expected kinetics in simulations with strong kinetic anisotropy.

Time evolution of shrinkage rate for the strongest considered anisotropy (i.e. $\Omega = 0.9$) in Figures 4.7c and 4.7d (base and 14IWpts runs, respectively), shows that in both runs the lines slightly diverge (this being applicable to all Ω s). The convergence was better in IW/2 run, but the mean shrinkage rates were worse than in the 14IWpts run.

Apparently, optimal results would be obtained here with more points than 7 in the interface and with smaller interface-width-to-circle ratio than in the base run and 14IWpts runs. However, as noted earlier, the kinetic anisotropy is very strong in the case of $\Omega = 0.9$. For weaker anisotropy the discussed effects are less pronounced and there is little difference in the shrinkage rates among the models.

There was no significant difference between the results of base and 1000IW runs.

4.5.3 Equilibrium triple junction angles

Figures 4.8b-4.8d show the simulation results from the triple junction simulations as function of σ_1/σ_2 . Neither of IWc or IWvK models show good agreement to Young's law when deviating farther from an isotropic system (which has ratio $\sigma_1/\sigma_2 = 1$). The model IWvG, on the other hand, always shows very good agreement in at least one of the fitting methods along the whole range of probed ratios of interface energies. With σ_1/σ_2 closer to 2 in IWvG modification, the grains shape was slightly elongated in the vertical direction, resulting in too small radius of the fitted arcs to cross in the triple junction. The angles could not be determined this way then and the linear fit is more reliable.

For the ratios approximately $\sigma_1/\sigma_2 \leq 0.45$ the IWc model behaves non-physically. The triple junction was observed to move in the opposite than expected direction (i.e. upwards, as if the triple junction angle was larger than 180°). The overall shape of contours was not as in Figure 4.8a because the green arcs curved in the other way. In IWvK this behavior was not observed, but the Young's law is not followed. Qualitative explanation is that the IWc and IWvK models are not fully variational.

No significant change was observed in the results of the triple junction angles in runs IW/2, 14IWpts or 1000IW when compared to the base run. Quality of the results is thus not improved when more points in the interface than 7 are

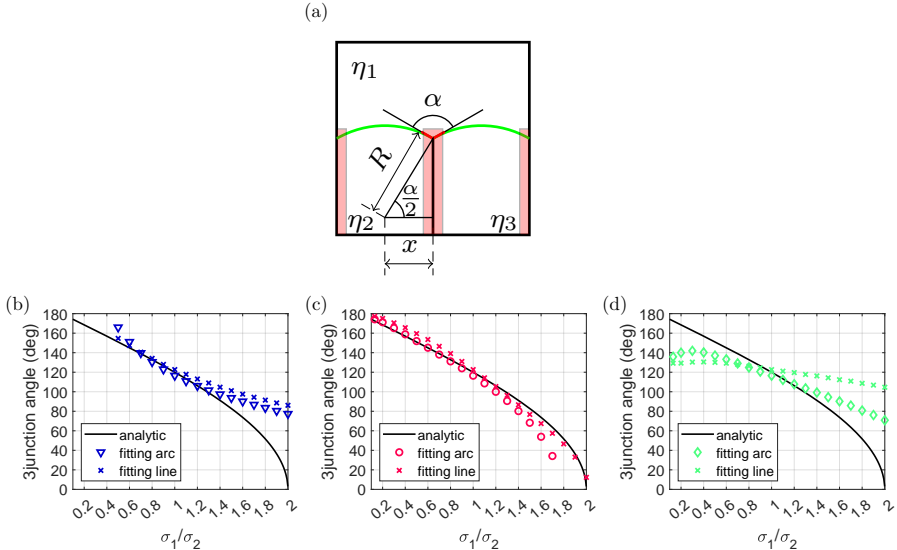


Figure 4.8: Triple junction angles. In a) the two methods for angles determination are illustrated (points fitted by straight lines in red and those fitted by circular arc in green). Subfigures b)-d) show the simulation results for different models, these being: in b) IWc, in c) IWvG and in d) IWvK. The hollow symbols correspond to the the angles determined by arc fitting and crosses to the lines fitting.

used. Also it implies, that the model behavior (for all parameters assignment strategies) is not affected by reducing the interface-width-to-feature ratio or the interface width scaling. The latter confirms that the model is quantitative.

4.6 Conclusions

This chapter presented a quantitative methodology for assessment of the anisotropic curvature driving force in phase field method. It was demonstrated in comparison of three different modifications of a multi-phase field model. The match to the expected shape and the shrinkage rate were quantified in two different benchmark problems. The methodology was sensitive enough to capture differences between the model modifications and is suitable for validation and benchmarking of different models and numerical solvers.

The overall performance of the three model modifications in the benchmarks

was comparable. Both match to the steady-state shapes and the shrinkage rates followed the expected results as in the anisotropic mean curvature flow. However, a significant difference was noted in a supplementary benchmark simulation where triple junction angles were measured. It was observed that only the IWvG model modification (with only the parameter γ anisotropic) reproduced the triple junction angles in the full interval 0.13-2 of σ_1/σ_2 , whereas IWc and IWvK modifications failed for ratios farther from 1. It is noted that these two modifications were not fully variational in order to avoid ghost phases, whereas IWvG is fully variational and yet the ghost phases do not appear.

Even though the triple junction benchmark did not involve interfaces with inclination-dependent interface energies, one conclusion can be made about that case regardless. As the IWc and IWvK were shown unreliable in the simpler pair-distinct isotropic case, there is no reason why they should be reliable in the more complicated one. Further development and validations should thus focus on the IWvG model modification.

No results were significantly affected by the interface width scaling. Also, it was confirmed that 7 points in the interface were sufficient for retaining the expected kinetics in most cases, unless the inclination dependence of the kinetic coefficient was very strong.

The results in this chapter are reproducible with codes provided in the data set [11].

Chapter 5

Nucleation probability assessment - a phase field methodology

5.1 Introduction

This chapter develops a methodology to obtain insight about the nucleation barrier from the equilibrium stable shapes of particles on a planar support in 2D. The developed multi-phase phase field model is used to obtain the interface-energy-minimizing shapes and the below described *domain scaling* is then used to find the shape factor. As recalled in the next section, the shape factor S is closely related to the nucleation barrier of the heterogeneous nucleus (having the equilibrium shape), thus to the nucleation probability.

Even though this method was primarily developed to bring insight into the anisotropy in the nucleation barrier as a function of the orientations of both the substrate and nucleus (which is in principle possible), later it was decided to rather use the Winterbottom construction for this purpose (in Chapter 6), because it was much more efficient. Regardless, the method presented in this chapter retains its usefulness because it can be used without any assumption on the shape itself (except for the contact angles it has with the substrate). This was exploited in solving a problem of heterogeneous nucleation on top of a grain boundary intersecting surface of a polycrystalline substrate.

Grain boundaries in nanocrystalline catalytic materials can be seen as a source

of surface chemical functionality [99]. They are defects in the crystalline structure, hence they are associated with certain excess energy, which makes them active sites for many chemical or electrochemical processes [99–101], including nucleation.

In order to find the equilibrium stable shape for arbitrary orientation and wetting conditions using the Moelans' multi-phase field model [7] described also in chapter 4, it was necessary to implement two model extensions: volume conservation and such boundary conditions, which allow control of the interface inclination at the domain boundary. That way, the shape could be simulated in a two-phase 2D system as long as the contact angles were known.

The combination of methods used to obtain the shape factors (phase field and domain scaling) utilizes that the interface in phase field method is implicitly tracked, i.e. it evolves without any assumption on its position. Additionally, it makes use of the fact, that in the simulated geometry, the total energy of the system is in fact the total particle-liquid interface energy. Advantage of the method is that it does not a-priori assume any shape, it is thus in principle usable for non-analytic cases, where the solution is not known, e.g. a particle on a grain boundary.

The below sections first recall some fundamentals relevant for the subsequently described *domain scaling* methodology. Then follows technical description of how the phase field model was extended to conserve volume and to have control over the inclination of interfaces at the domain boundary. Then, some details about the numerical implementation are included, followed by validations of the implementation in terms of how well the contact angles are reproduced for straight interface and the domain scaling methodology is then validated for circular segments with different contact angles, which is the case of heterogeneous nucleation with isotropic interface energy in 2D. The domain scaling method is then applied to the case with a particle with isotropic interface energy on top of a grain boundary intersecting a substrate surface. Limitations and prospects of this approach are assessed based on the results.

5.2 Fundamentals

In 2D, the Gibbs free energy difference upon a nucleus insertion in the system is due to competition between area and line energy contributions (see also Figure 5.1). Be A_{hom} the nucleus area and its interface be described by a parametric curve \mathcal{C} . In the isotropic case, \mathcal{C} is a circle and the interfacial contribution is simply σL , where $L = 2\pi R$ is the interface length and σ the isotropic specific interface energy. The Gibbs free energy difference of a free nucleus is then (with

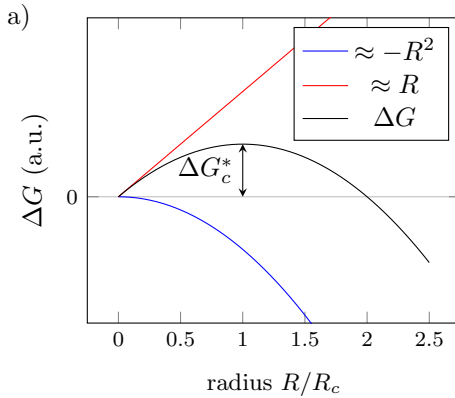


Figure 5.1: Schematic dependence of the total energy change on the radius of the inserted nucleus in 2D.

ΔG_A being the 2D equivalent of bulk driving force, i.e. with units J/m^2)

$$\Delta G_{hom} = -\Delta G_A A_{hom} + \sigma L \quad (5.1)$$

$$= (-\Delta G_A R^2 + 2R\sigma)\pi, \quad (5.2)$$

which implies the critical radius

$$R_c = \frac{\sigma}{\Delta G_A} \quad (5.3)$$

and critical nucleation barrier

$$(\Delta G_c^*)_{hom} = \hat{A}_{hom} \frac{\sigma^2}{\Delta G_A}, \quad (5.4)$$

where the non-dimensional nucleus area is $\hat{A}_{hom} = A_{hom}/R^2 = \pi$.

In the heterogeneous nucleation, the shape factor $S(\theta) = A_{het}/A_{hom}$ scales the homogeneous total energy change upon nucleus insertion ΔG_{hom} as

$$\Delta G_{het} = S(\theta)\Delta G_{hom}, \quad (5.5)$$

which for the heterogeneous nucleation barrier implies

$$(\Delta G_c^*)_{het} = S(\theta)(\Delta G_c^*)_{hom}. \quad (5.6)$$

The nucleus radius is equal in both homogeneous and heterogeneous nucleation.

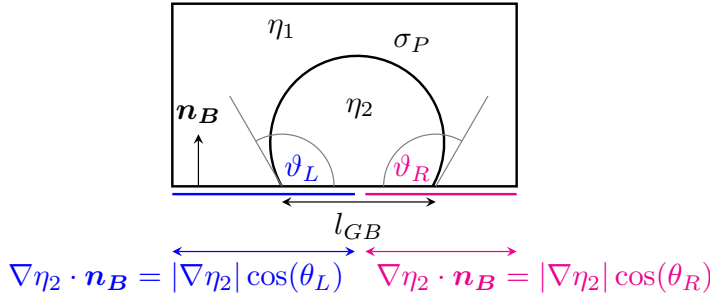


Figure 5.2: Sketch of the geometry in the phase-field simulations used in the domain scaling methodology for shape factor assessment. The symbols ϑ_L, ϑ_R denote tangent angles in the contact points and θ_L, θ_R the normal ones. The two intervals on the bottom domain boundary with the different interface inclination imposed are indicated by blue color on the left half of the domain and by magenta on the right one (note that η_1 has analogous boundary conditions which must be consistent). l_{GB} is the length of the grain boundary interval between the contact points. σ_P is the particle-liquid interface energy.

5.3 Methodology

The simulated system geometry is sketched in Figure 5.2. A two-phase system of a particle in a liquid was described by two phase field variables in Moelans' model, one representing the liquid parent phase (η_1) and the second (η_2) representing the particle (possibly with anisotropic interface energy). The bottom domain boundary then represents the substrate and the interface inclination ϑ_L, ϑ_R in the two contact points is controlled by the boundary condition as indicated in the figure.

Volume conservation was assured using the fictitious concentration field described in the section 5.4.2.

The particle-liquid interface energy σ_P was assumed, together with the contact angles ϑ_L, ϑ_R between the solid-liquid interface and the bottom domain boundary. How these angles were imposed is described in section 5.4.1.

The domain scaling methodology is in fact a post-processing of the result of phase field simulation. By the result, it is meant the phase fields corresponding to the liquid and to the particle within the simulation grid. Then, the grid spacing Δx is scaled and the model parameters are re-computed accordingly. The particle area fraction $\xi = A_P/A_D$ in the scaled system remains the same, but its area A_P and perimeter are scaled accordingly. Using the (unchanged) phase

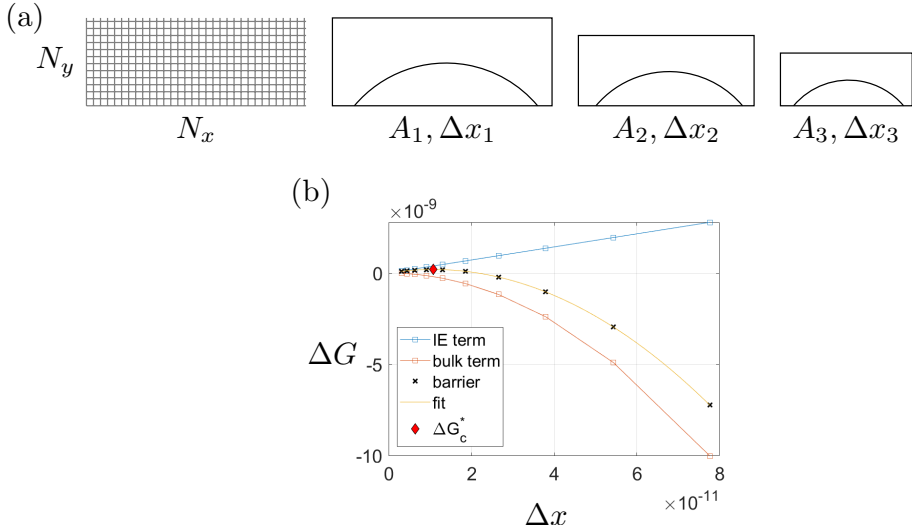


Figure 5.3: Nucleation barrier determination using domain scaling. In (a) sketch of domain scaling. The area fraction of the particle is preserved, as well as the number of grid points N_x, N_y . A_i are scaled areas of the domain and Δx_i is the i -th scaled grid spacing in meters. In (b) the energy contributions were plotted for each Δx_i , the barrier being denoted by black crosses and the critical nucleation barrier determined by fitting of parabolic function is indicated by red diamond.

fields and re-computed parameters, the total interface energy is re-evaluated by the free energy functional $F(\eta, \nabla\eta)$ for the new scale. The domain scaling is sketched in Figure 5.3a.

Note that the free energy functional $F(\eta, \nabla\eta)$ only accounts for the solid-liquid interface energy, but in the total energy change upon nucleus insertion, there must be included also the term representing the replacement of the former planar substrate-liquid interface with specific energy σ_S by the grain boundary: $l_{GB}(\sigma_{GB} - \sigma_S)$. Because the Young's equation for triple junctions of isotropic interfaces reads

$$\sigma_S = \sigma_{GB} + \sigma_P \cos(\vartheta), \quad (5.7)$$

the grain-boundary-energy term can thus be written as $l_{GB}(\sigma_{GB} - \sigma_S) = -l_{GB}\sigma_P \cos(\vartheta)$, which allows us to disregard the values of the substrate and grain boundary energy. In the phase field simulation, the distance between the contact points is interpreted as l_{GB} (see Figure 5.2) and the above term is added to the total interface energy change upon the nucleus insertion ΔG_σ ,

hence when denoting the free energy functional as $F(\eta, \nabla\eta)$ it can be written

$$\Delta G_\sigma = F(\eta, \nabla\eta) - l_{GB}\sigma_P \cos(\vartheta). \quad (5.8)$$

Note that l_{GB} is necessarily scaled as well during the domain scaling procedure.

The above procedure provided the total interface energy change upon the particle insertion as function of the length scale (Δx_i in Figure 5.3a). Even though it is not the particle radius as in (5.2), the grid spacing has the same physical dimension (length), which assures that the order of the polynomial $\Delta G(\Delta x) = a(\Delta x) - b(\Delta x)^2$ is the same as in (5.2).

When the driving force ΔG_A is explicitly assumed, the bulk energy contribution ΔG_B to the energy change can be computed using each of the absolute values of the scaled particle area $A_P(\Delta x_i)$ as $\Delta G_B(\Delta x_i) = \Delta G_A A_P(\Delta x_i)$. Because the interface energy contribution $\Delta G_\sigma(\Delta x_i)$ was already computed for each scaled system, it is possible to subtract the two to obtain the total energy change in insertion of those particles, as is shown in Figure 5.3b and below

$$\Delta G(\Delta x_i) = \Delta G_B(\Delta x_i) - \Delta G_\sigma(\Delta x_i) \quad (5.9)$$

In Figure 5.3b, there were multiple scaling steps taken for illustration, but with the simple parabolic dependence of $\Delta G(\Delta x_i)$ in 2D, only 3 points would suffice to unambiguously determine its parameters. Finding the critical nucleation barrier ΔG_c^* , i.e. value of the parabola maximum is then trivial.

The critical nucleation barrier of the investigated heterogeneous equilibrium shape was thus found. However, a more practical quantity is the corresponding shape factor S , which can then be obtained from equations (5.4) and (5.6) as

$$S = (\Delta G_c^*) \frac{\Delta G_A}{\hat{A}_{hom}\sigma_0^2}. \quad (5.10)$$

Note, that one needs to know the non-dimensional area of the isolated equilibrium shape $\hat{A}_{hom} = A_{hom}/R^2$. Essentially, that is an area of the isolated Wulff shape of unit radius (in this study it was obtained numerically from Wulff shapes plotted with fine resolution).

Recall, that the contact angles of the particle with the substrate were the input to the phase field simulation, hence the obtained shape factor S is a function of the particular assumed conditions.

The domain scaling procedure does not depend on whether the interface energy was isotropic or anisotropic, because the used formulas leading to (5.10) are equal in the two cases [48]. Only in the case with inclination-dependent interface energy more steps are required in evaluation of the free energy functional $F(\eta, \nabla\eta)$ because the formulas for model parameters are more complicated than in the isotropic case.

5.4 Model

Because the Moelans' model with anisotropic interfaces was already extensively introduced in section 4.2.1, this section covers only the necessary extensions to simulate the system as sketched in Figure 5.2,

5.4.1 General Neumann boundary conditions to control interface inclination at domain boundary

This model extension was inspired by [102]. It allows to control the interface inclination angle ϕ at the boundary, which thus becomes an input parameter. The principle is explained using a single phase field $\eta(\mathbf{r})$. First, we remark that the standard Neumann boundary conditions $\nabla\eta \cdot \mathbf{n}_D = 0$ must be a special case of the general Neumann boundary conditions (\mathbf{n}_D is the domain boundary normal). The regular Neumann boundary condition implies perpendicularity of the phase field gradient to the domain boundary normal. In other words, the interface is perpendicular to the domain boundary. Generally, we can write $\mathbf{n}_D \cdot \nabla\eta = |\nabla\eta| \cos(\phi)$. In the model by Granasy [102], the local magnitude of phase field gradient may be expressed using the local phase field value, giving rise to the following expression for the boundary condition

$$\mathbf{n}_D \cdot \nabla\eta = \frac{\cos(\phi)}{\delta\sqrt{2}} \eta(1 - \eta), \quad (5.11)$$

where δ is the interface width. At the domain boundary, the gradient $\nabla\eta$ is expressed as a polynomial, which allows straightforward implementation of the condition, especially in rectangular simulation domains.

In Moelan's model, the interface normal between the phase fields η_i , η_j denoted $\mathbf{n}_{i,j}$ is defined as local difference in neighboring phase field gradients (see equation 4.17). In the spirit of the introductory example we can write

$$\mathbf{n}_D \cdot \mathbf{n}_{i,j} = \cos(\phi) \implies \mathbf{n} \cdot (\nabla\eta_i - \nabla\eta_j) = |\nabla\eta_i - \nabla\eta_j| \cos(\phi). \quad (5.12)$$

Now we have single boundary condition with the correct physical interpretation (fixed inclination angle at the boundary) but because the governing equations are solved for the phase fields, a set of equivalent boundary conditions (one for each phase field) must be derivable from the above. In these independent boundary conditions, it must be possible to express the gradient magnitude (the introductory example finds a polynomial of local phase field values equal to the gradient magnitude).

The first problem (i.e. coupling in the boundary conditions) would be solved if

one gradient could be written as a function of the other and vice versa. However, this dependence is non-analytical for all $\gamma_{i,j} \neq 1.5$. For $\gamma_{i,j} = 1.5$ it is simply $\eta_i = 1 - \eta_j$ and therefore also $\nabla\eta_i = -\nabla\eta_j$. [7]

The second problem (i.e. the expression for gradient magnitude) is also enabled by the choice $\gamma = 1.5$, as in such a case there have been in 1D derived the analytic expressions for the gradients in $\nabla\eta_i, \nabla\eta_j$ as functions of the phase field values [7], similar to those in [102]. To generalize them into higher dimensions, several steps need to be made: the equation 7 from [7] for 2D/3D writes

$$mf_0(\eta_i, \eta_j) + \frac{\kappa_{i,j}}{2} [|\nabla\eta_i|^2 + |\nabla\eta_j|^2] = 0. \quad (5.13)$$

From this, the 2D/3D equivalents of equations 8a and 8b can be written, where $\frac{d\eta}{dx}$ is replaced by $|\nabla\eta|$

$$\begin{aligned} |\nabla\eta_i| &= \sqrt{\frac{2mf_0}{\kappa_{i,j} \left[1 + \left(\frac{d\eta_j}{d\eta_i} \right)^2 \right]}} \\ |\nabla\eta_j| &= \sqrt{\frac{2mf_0}{\kappa_{i,j} \left[1 + \left(\frac{d\eta_i}{d\eta_j} \right)^2 \right]}}. \end{aligned} \quad (5.14)$$

Assuming $\gamma_{i,j} = 1.5$ implies $\eta_i = 1 - \eta_j$, hence $\left(\frac{d\eta_j}{d\eta_i} \right)^2 = 1$. In addition to that, the homogeneous free energy density $f_0(\eta_i, \eta_j)$ can be expressed as a function of only one of the two fields (see the equation 19 from [7])

$$f_0(\eta_i, 1 - \eta_i) = 2\eta_i^2(1 - \eta_i)^2. \quad (5.15)$$

After substitution in 5.14, the gradients are expressed in 2D/3D as functions of the respective field values

$$\begin{aligned} |\nabla\eta_i| &= \sqrt{\frac{2m}{\kappa_{i,j}}} \eta_i(1 - \eta_i) \\ |\nabla\eta_j| &= \sqrt{\frac{2m}{\kappa_{i,j}}} \eta_j(1 - \eta_j). \end{aligned} \quad (5.16)$$

In systems with more than two phase fields, the general expression for the gradient magnitude is more complex. However, the same relations are satisfied far enough from the triple junction.

With the above, we can thus write

$$\begin{aligned}\mathbf{n} \cdot (\nabla \eta_i - \nabla \eta_j) &= 2\mathbf{n} \cdot \nabla \eta_i = 2|\nabla \eta_i| \cos(\phi) \\ &= -2\mathbf{n} \cdot \nabla \eta_j = -2|\nabla \eta_j| \cos(\phi),\end{aligned}\tag{5.17}$$

which provides very similar BC like in the introductory example for each of the two phase fields.

The only way how to use these relations is to have $\gamma_{i,j} = 1.5$. In the case of inclination-dependent interface energy $\sigma_{i,j}(\theta_{i,j}) = \sigma_{i,j}^0 h_{i,j}^\sigma(\theta_{i,j})$, it is necessary to express the anisotropy fully by the parameter $\kappa_{i,j}(\theta_{i,j})$, i.e. to use the IWvK model.

5.4.2 Volume conserving multi phase field models

There are several approaches which accomplish the volume conservation of some species or phases. Each has its drawbacks though. It was not clear which of the possible approaches was the most convenient for coupling with inclination-dependent interface energy in curvature-driven systems.

Three conceptually different solutions can be used in a multi-phase field model, which are known to the author: Cahn-Hilliard equation, Lagrange multipliers and fictitious concentrations field.

In order to bring insight into the impact of interface energy anisotropy in textures formation, a parameter study would be needed involving many simulations. Moreover, the intended application with anisotropic interface energy involves complicated driving force terms, hence a less computationally demanding option than the Cahn-Hilliard equation was sought, because that one is a partial differential equation of 4-th order in space.

The approach using Lagrange multipliers to conserve volume was thoroughly considered, but eventually it was found out that for Moelan's model it is not a suitable solution. The reason is that the volume of a single phase/grain is defined using all other phase fields, which introduces excessive computational complexity in application of the principles leading to volume conservation. All related details and explanations can be found in Appendix D.

The approach using a fictitious concentration field was eventually assessed as the most convenient one. It is not new in combination with Moelans' multi-phase field model (see e.g. [84, 103]). It is briefly reviewed in the following subsection.

Fictitious concentration field

The idea in the fictitious concentration field approach to conserve volume of a phase field is to couple the Allen-Cahn equation to a conserved concentration field in such a way, that the change in phase fraction is only possible with exchange of species between phases. If the concentration of the independent species is set to equilibrium value and the energy valley is steep enough, no phase transformation occurs and the volume of the phase fraction should be conserved through the system.

In the description below, it is assumed that there are two phases, one solid and the other liquid.

The free energy functional is then

$$F_{cons} = \int_V [f_{hom}(\vec{\eta}, \nabla \vec{\eta}, c) + f_{grad}(\vec{\eta}, \nabla \vec{\eta})] dV, \quad (5.18)$$

with

$$f_{hom}(\vec{\eta}, \nabla \vec{\eta}, c) = f_0(\vec{\eta}, \nabla \vec{\eta}) + f_{chem}(\vec{\eta}, c) \quad (5.19)$$

$$f_{chem}(\vec{\eta}, c) = h_S(\vec{\eta})f_S(c) + h_L(\vec{\eta})f_L(c) \quad (5.20)$$

$h_S(\vec{\eta}), h_L(\vec{\eta})$ are solid and liquid interpolation functions. Assuming that the solid phase is composed of s phase fields $\eta_{S1}, \eta_{S2}, \dots, \eta_{Ss}$ and the liquid phase of l phase fields $\eta_{L1}, \eta_{L2}, \dots, \eta_{Ll}$ we can write

$$h_S(\vec{\eta}) = \frac{\sum_i^s \eta_{Si}^2}{\sum_i^s \eta_{Si}^2 + \sum_j^l \eta_{Lj}^2} \quad (5.21)$$

$$h_L(\vec{\eta}) = \frac{\sum_j^l \eta_{Lj}^2}{\sum_i^s \eta_{Si}^2 + \sum_j^l \eta_{Lj}^2}. \quad (5.22)$$

Parabolic energy approximation will be used for the concentration dependence of the homogeneous phase free energy densities $f_S(c), f_L(c)$ as

$$f_S(c_S) = A(c_S - c_{S,eq})^2 \quad (5.23)$$

$$f_L(c_L) = B(c_L - c_{L,eq})^2. \quad (5.24)$$

An ideal solution approximation was adopted.

The governing equations for two phase fields are then

$$\frac{\partial \eta_1}{\partial t} = -L \left[\frac{\partial f_0}{\partial \eta_1} - \nabla \cdot \frac{\partial F}{\partial (\nabla \eta_1)} + \frac{\partial h_S}{\partial \eta_1} [f_S(c_S) - f_L(c_L) - (c_S - c_L)\mu] \right] \quad (5.25)$$

$$\frac{\partial \eta_2}{\partial t} = -L \left[\frac{\partial f_0}{\partial \eta_2} - \nabla \cdot \frac{\partial F}{\partial (\nabla \eta_2)} + \frac{\partial h_S}{\partial \eta_2} [f_S(c_S) - f_L(c_L) - (c_S - c_L)\mu] \right] \quad (5.26)$$

$$\mu = 2A(c_L - c_{L,eq}) \quad (5.27)$$

$$\frac{\partial c}{\partial t} = \frac{D}{A} \Delta \mu = 2D\Delta(c_L - c_{L,eq}) \quad (5.28)$$

where the diffusion coefficient D is a constant.

The interpolation functions have the following property

$$\frac{\partial h_S}{\partial \eta_p} = -\frac{\partial h_L}{\partial \eta_p} \quad (5.29)$$

5.5 Numerical implementation

The numerical approach to solving the governing equations 5.25-5.28 was the same as in the Chapter 4, i.e. finite difference method of the second and of first order for the spatial and temporal derivatives, respectively. Own solver was written in MATLAB.

The Appendix C contains the necessary modifications to the finite-difference algorithm when implementing the general Neumann boundary conditions. Eventually, the changes affected all the finite difference operators (standing in place of unidirectional or mixed derivatives and laplacian), but only in the parts of the matrices, which involve the nodes at the domain boundary.

The parameters of the phase field simulations needed to reproduce the results are in Table 5.1. Regarding the volume conservation, it was validated that with the listed parameters, the area of the conserved field would change no more than about 1 % from its initial value in practical simulations, which is sufficient for the equilibrium shape simulations and subsequent barrier determination.

The re-computation of the model parameters during the domain scaling was carried out using the same MATLAB functions [11] as used in chapter 4 and [8].

Table 5.1: Parameters in the phase field simulation (unless stated otherwise). The parameters in the top part correspond to the Moelans' model, in the bottom one to the diffusion equation used in the fictitious concentration field approach to conserve volume of the simulated particle. The not mentioned parameters m, κ, L in Moelans' model can be determined using the dedicated published MATLAB functions [11].

symbol	parameter	units	values
l_{IW}	interface width	m	1×10^{-9}
σ_P	particle-liquid isotropic interface energy	J/m ²	1
Δx	grid spacing	m	$l_{IW}/7$
C	Courant number	-	0.18
μ_P	particle-liquid interface mobility	m ⁴ /Js	7.5×10^{-16}
Δt	time step	s	using (4.33)
A	steepness of parabolas	J/m ³	3.1623×10^{-11}
D	diffusion coefficient	m ² /s	$0.3\Delta x^2/\Delta t$
$c_{L,eq}$	equilibrium molar fraction in liquid	-	0.02
$c_{S,eq}$	equilibrium molar fraction in solid	-	0.98
M	diffusion coefficient in C-H equation	m ⁵ /Js	$M = D/A$

5.6 Validations

5.6.1 Tilted straight line

The implementation of general Neumann boundary conditions controlling the inclination angle at the domain boundary was validated in simulations sketched in Figure 5.4. Note that the volume was not conserved in these simulations. A slightly different approach had to be taken in the case with isotropic and anisotropic interface energy, as described below.

In the case with isotropic interface energy, the initial condition for the simulation was a tilted line, which was inclined under different angle ϑ_{init} than the imposed inclination angle ϑ . The simulation ran until the total energy converged (i.e. until the change in energy per time step was smaller than a threshold). The final state was expected to be a line aligned under the target angle ϑ . From linear fit of the final phase field contour, the resulting inclination angle was read out. A range of angles between 15°-165° was probed, and the results were plotted in Figure 5.5a. As can be seen, a perfect match was achieved.

When validating the same with inclination-dependent interface energy, the methodology had to be modified slightly: the straight line was placed in its imposed position already in the initial condition, i.e. $\vartheta_{init} = \vartheta$. That was

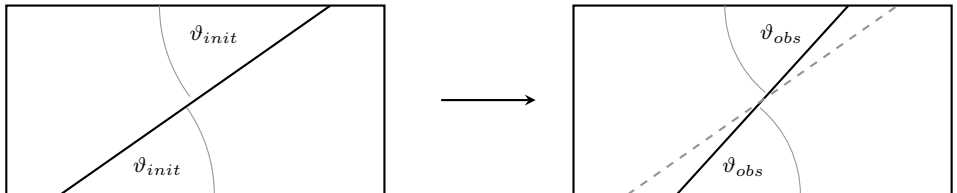


Figure 5.4: Validation of the general NBC for control of the inclination angle at the boundary - tilted line simulations (isotropic interface energy). The initial angle ϑ_{init} evolves towards ϑ_{obs} , while ϑ is imposed by the boundary condition. In the simulations with inclination-dependent interface energy there was $\vartheta_{init} = \vartheta$, see the text for more details.

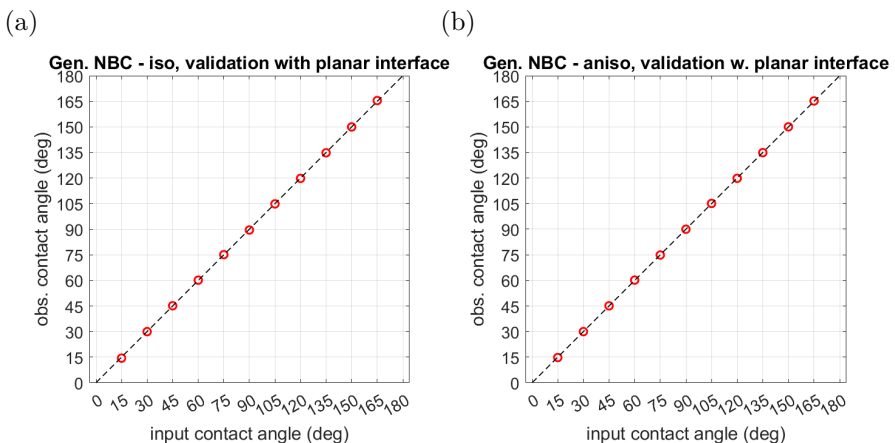


Figure 5.5: Results of tilted plane validation, as sketched in Figure 5.4. In a) the result with isotropic interface, in b) with anisotropic one.

because once any curvature appeared in the straight line (which happened when the interface was forced to move by the boundary conditions), it began deforming and there remained no straight line. To assure that the tilted line be the equilibrium state of the system, the anisotropy function was always rotated so that the target inclination angle ϑ corresponded to the minimal interface energy. Only then the straight line could be immobile and the general Neumann BC could be validated in the same way as with the isotropic interface energy, i.e. simulation until energy convergence and linear fit of the contour. The target angle was observed very accurately in this case as well, as can be seen in Figure 5.5b.

Table 5.2: Simulation grid dimensions in individual simulations of a particle with isotropic interface energy on a plane in 2D. The grid aspect ratio was determined based on the expected shape aspect ratio.

ϑ	$N_x \times N_y$
15	546×42
30	382×51
45	308×64
60	261×75
75	226×87
90	198×99
105	176×111
120	162×121
135	152×129
150	145×135
165	141×139

5.6.2 Particle on a plane (isotropic interface energy)

This section shows the validation simulation of a circular segment on a plane using the above model including control of the interface inclination on the domain boundary and subsequent application of the domain scaling method for determination of the shape factor S for this shape. Hence, it is a combined validation of the contact angles reproduction in a more practical simulation than the one with the tilted line, the domain scaling method and also the volume conservation.

In heterogeneous nucleation with isotropic interface energy in 2D, the equilibrium shape is a circular segment and the shape factor as function of the tangent contact angle (wetting angle) ϑ (see Figure 5.2) is

$$S(\vartheta) = \frac{2\vartheta - \sin(2\vartheta)}{2\pi}. \quad (5.30)$$

A series of phase field simulations was run in the geometry as in Figure 5.2 with $\vartheta_L = \vartheta_R$ to assess the above dependence of shape factor on the wetting angle. See Table 5.2 for details on the simulation grid in the respective simulations. The simulation was terminated when the total interface energy converged. Total interface energy was not evaluated at every time step, but only at evenly distributed logging points. The condition for termination due to convergence in energy was that the relative difference of the current energy value from the mean of the last 10 logging points was less than $5 \cdot 10^{-4}$. Two examples of the resulting shapes are provided in Figure 5.6.

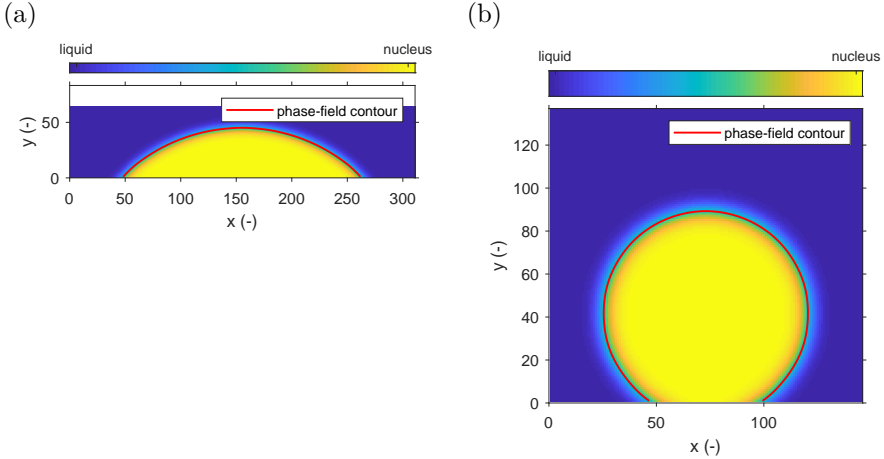


Figure 5.6: Examples of resulting shapes obtained by phase field simulation of a particle with isotropic interface energy resting on a plane. In (a) with the contact angle $\vartheta = 45^\circ$, in (b) with $\vartheta = 150^\circ$. In both, the phase field contour was denoted by solid red line. It was defined as the zero-value contour of $\eta_{\text{liquid}} - \eta_{\text{particle}}$.

The contact angles were the same as in the tilted plane validation, i.e. from $\vartheta = 15^\circ$ to $\vartheta = 165^\circ$ with a 15° step. The initial condition corresponded to the target circle segments to reduce the computation time. Using the equation (5.10) and taking into account that the non-dimensional area for a circle is $\hat{A}_{\text{circle}} = \pi$, the results in Figure 5.7 were obtained.

The contours obtained by phase field simulation were fitted by a circle, which provided the radius R_{circ} and the circle center position $(x_{\text{circ}}, y_{\text{circ}})$. A simple derivation delivers the following formula for determination of the contact angle

$$\vartheta = \arccos \left(-\frac{y_{\text{circ}}}{R_{\text{circ}}} \right), \quad (5.31)$$

which provided the observed values of contact angle ϑ . In Figure 5.7a, there are relative differences of the observed contact angles from the imposed ones and it can be seen that the overall shapes are reproduced very well. The contact angle was also determined from the contour endpoints, but this yielded significantly greater discrepancy, as can be seen in Figure 5.7b showing the difference between the observed and imposed angles.

Different settings of the phase field input parameters were compared to eliminate effect of the method itself on the results. In the base run, the interface width

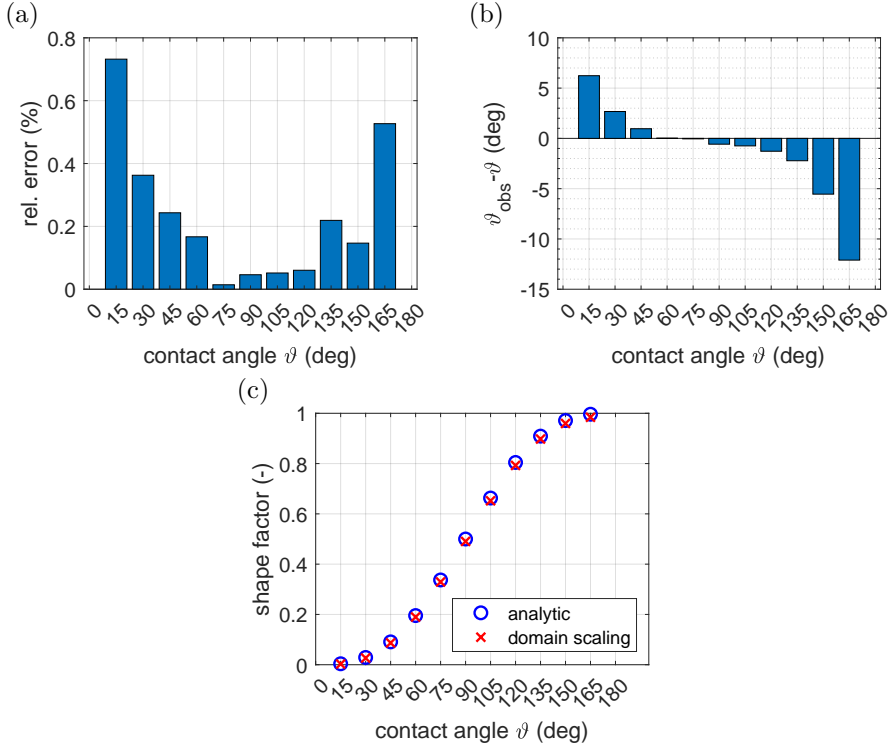


Figure 5.7: Results of the phase field simulation for determination of shape factor in heterogeneous nucleation with isotropic interface energy. In (a) the relative error of the contact angle obtained by fitting the shape by a circle, in (b) the error in observed contact angles evaluated from two contour end points and in (c) the shape factor as obtained by domain scaling method.

was $l_{IW} = 1 \times 10^{-9}$ m, with 7 points through the interface. The compared simulations probed the effect of a) increasing the domain area, while keeping the l_{IW} equal (effectively narrowing the physical interface width relative to the simulation initial condition) and of adding points to the interface (both actions refined the grid below the simulated initial condition) and both might improve phase field simulation accuracy in different regards. That did not happen in terms of the contact angles determined by the two contour endpoints, though.

However, the resulting shapes were always reproduced close to the expectation, which is why the shape factor determination was not affected heavily. This is confirmed also by the obtained values of shape factor plotted in Figure 5.7c, which follow closely the analytic prediction. Apparently, only few points

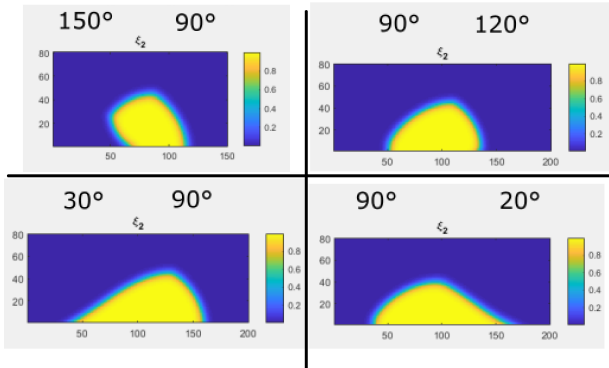


Figure 5.8: Demonstration of control over interface inclination on the domain boundary with anisotropic particle. All four particles have the anisotropy function $h(\theta) = 1 + 1.625 \cos(4(\theta + 15))$ and a kind of arbitrary angles were imposed on both sides of the particle, as indicated above each graph.

near the domain boundary deviated from the expected circular shape. The different interface parametrization mentioned in the previous paragraphs yielded slight improvement in the shape factor values, but not relevant for the current application.

5.6.3 Control over interface inclination with inclination-dependent interface energy

The tilted plane validation with interface having inclination-dependent interface energy proved that the implementation is working also in this more complicated case. Nevertheless, for demonstration, in Figure 5.8 there are shown four particles as they were simulated using the model. All of them have the same anisotropic function, but had different (arbitrary) contact points imposed on both contact points. It can be seen that the interface inclination is indeed controlled.

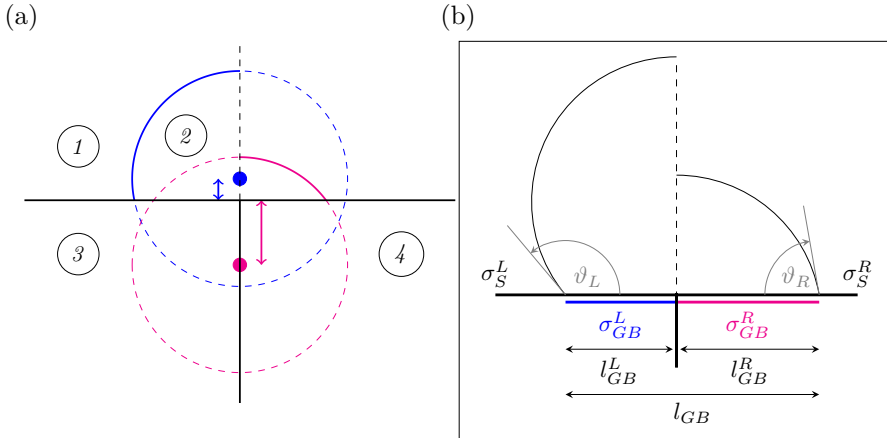


Figure 5.9: A particle on a grain boundary. In (a) the impact of different wetting on the two sides of the grain boundary is indicated and in (b) the annotations relevant for explanations in text were added: the specific interface energies $\sigma_S^{L/R}$ belong to the substrate-solution interfaces, the grain boundary energies $\sigma_{GB}^{L/R}$ and lengths $l_{GB}^{L/R}$ to the respective grain boundaries and l_{GB} is the total grain boundary length.

5.7 Domain scaling of a particle on a grain boundary intersecting the surface (isotropic interface energy)

The present section investigates the theoretical case when the nucleus extends over the grain boundary and thus its wetting condition is unequal on the two sides. Such a situation was sketched in Figure 5.9a. The radius of the particle is given by the particle-liquid interface energy and the bulk driving force (see (5.3)), hence the particle tries to emerge/submerge differently on each side of the grain boundary.

The geometry of the resulting problem is sketched in Figure 5.9b. When the two sides are wetted differently, it implies different contact angles. The curvature K (reciprocal radius) is in principle equal on both sides of the grain boundary, however due to the obvious shape discontinuity it cannot be constant along the whole shape. The chemical potential μ_{surf} (the capillary driving force, see (6.1)) is

$$\mu_{surf} = \sigma K \quad (5.32)$$

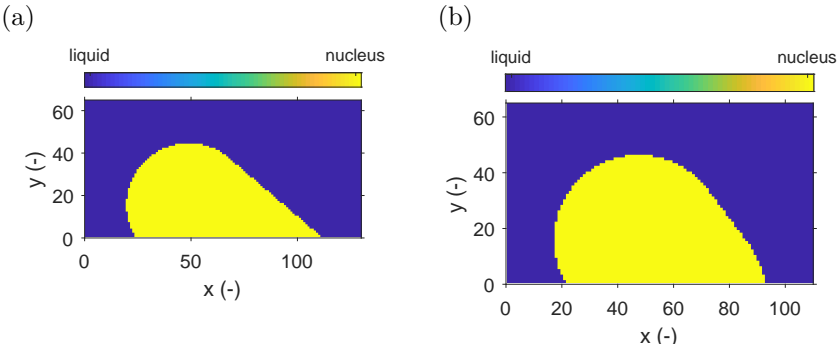


Figure 5.10: Initial condition examples for the simulation of a particle on a grain boundary. In (a) with the contact angles $\vartheta_L = 120^\circ$, $\vartheta_R = 45^\circ$, in (b) with $\vartheta_L = 120^\circ$, $\vartheta_R = 75^\circ$

and must be constant in order to have the stable shape in equilibrium. But for a constant σ that cannot be achieved under these conditions. However, the nuclei in classical nucleation theory do not necessarily have the interface-energy minimizing shape, even though that one is the most likely (because it has the smallest nucleation barrier of all shapes). Hence, even if the shape is not in equilibrium, we assume that it could nucleate. Implications of the shape instability are discussed farther, below the results section.

It was expected that the resulting shape will be some combination of the equilibrium shapes from both sides (see Figure 5.9). To reduce the simulation time, the initial condition was a kind of artificial compound shape: halves of both equilibrium shapes next to each other, connected by a straight line to avoid dents in the shape. The imposed contact angles on both sides were always approximately present already in the initial condition. Two examples of the initial shapes were plotted in Figure 5.10.

In the computation of the total grain boundary energy (meaning the energy of the substrate-particle interface), there will be two segments now, one on the left and one on the right side from the grain boundary (see Figure 5.9b). These have lengths l_{GB}^L, l_{GB}^R and specific grain boundary energies $\sigma_{GB}^L = \sigma_S^L - \sigma_P \cos(\vartheta_L)$ and $\sigma_{GB}^R = \sigma_S^R - \sigma_P \cos(\vartheta_R)$. The symbols σ_S^L, σ_S^R stand for the substrate surface energy on either side of the grain boundary and σ_P is the particle-liquid interface energy. It turns out, that to express the total interface energy change (upon the insertion of the particle on top of the grain boundary) ΔG_σ , it is

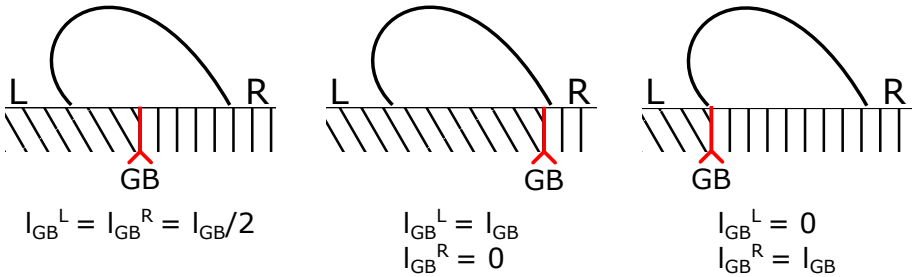


Figure 5.11: Illustration of the three considered positions of grain boundary below the nucleus.

sufficient to assume only $\sigma_P, \vartheta_L, \vartheta_R$, as can be seen below

$$\Delta G_\sigma = F(\eta, \nabla\eta) + l_{GB}^L(\sigma_{GB}^L - \sigma_S^L) + l_{GB}^R(\sigma_{GB}^R - \sigma_S^R) \quad (5.33)$$

$$= F(\eta, \nabla\eta) - \sigma_P[l_{GB}^L \cos(\vartheta_L) + l_{GB}^R \cos(\vartheta_R)]. \quad (5.34)$$

The symbol $F(\eta, \nabla\eta)$ again stands for the total particle-parent phase interface energy. In the general case, the individual segments l_{GB}^L, l_{GB}^R will have different length, depending on where the grain boundary is positioned below the particle.

Because the position of the grain boundary below the particle is chosen here, three scenarios were assumed and illustrated in Figure 5.11. In each of the scenarios, the grain boundary below the particle is placed in a different spot, hence there will be different total interface energy changes upon the particle insertion ΔG_σ , which leads to determination of different shape factors eventually. The three scenarios are below in detail

1. $l_L = l_R = l_{GB}/2$, then $\Delta G_\sigma = F(\eta, \nabla\eta) - 0.5\sigma_P l_{GB}[\cos(\vartheta_L) + \cos(\vartheta_R)]$
2. $l_L = l_{GB}, l_R = 0$, then $\Delta G_\sigma = F(\eta, \nabla\eta) - \sigma_P l_{GB} \cos(\vartheta_L)$,
3. $l_L = 0, l_R = l_{GB}$, then $\Delta G_\sigma = F(\eta, \nabla\eta) - \sigma_P l_{GB} \cos(\vartheta_R)$ and

In the first case, the substrate grain boundary is just in the middle between the contact points. The second and third ones are limiting cases, when the contact point is infinitesimally just behind the substrate grains grain boundary, hence the full substrate-particle grain boundary lays on the either higher- or lower-energy grain.

See Table 5.3 for details on the simulation. The contact angles ϑ_L, ϑ_R were input to the simulation. In the presented results, it was assumed that $\vartheta_L = 120^\circ$ and ϑ_R was varied between 30° - 90° .

Table 5.3: Summary of the contact angles and the simulation grid dimensions in grid points for the simulation of a particle on a grain boundary. Other parameters for the simulation are equal as in Table 5.1.

ϑ_L (°)	ϑ_R (°)	$N_x \times N_y$
120	-30	140 × 65
120	-45	130 × 65
120	-60	110 × 65
120	-75	110 × 65
120	-90	110 × 65

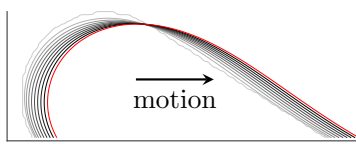
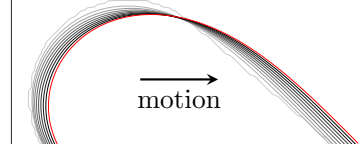
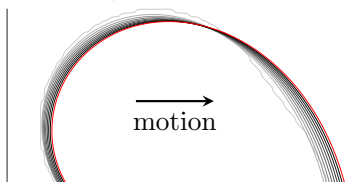
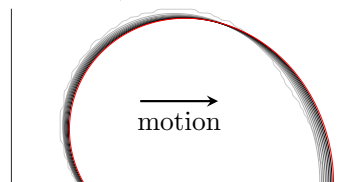
(a) $\vartheta_L = 120^\circ$, $\vartheta_R = -30^\circ$ (b) $\vartheta_L = 120^\circ$, $\vartheta_R = -45^\circ$ (c) $\vartheta_L = 120^\circ$, $\vartheta_R = -75^\circ$ (d) $\vartheta_L = 120^\circ$, $\vartheta_R = -90^\circ$ 

Figure 5.12: Time evolution of phase field contours in the simulation of a particle on a grain boundary. The time evolves from gray to black contours, the last contour in the simulation is red.

The first observation from the simulations is that the shape evolves, but even when it stops evolving, it moves as a block towards the side which has lower grain boundary energy. For the time evolution of the phase field contours in different cases see Figure 5.12. The intuitively correct direction of motion (i.e. such which lowers the total grain boundary energy) is reproduced by the model, even though the system energy minimized in the phase field simulation does not account for the particle-substrate interface explicitly. The reason is that the curvature driving force acts towards the center of curvature and as can be seen in Figure 5.12, the side with greater contact angle (and thus higher grain boundary energy) is more curved. The flatter is the opposite side, the less is the curvature driving force balanced.

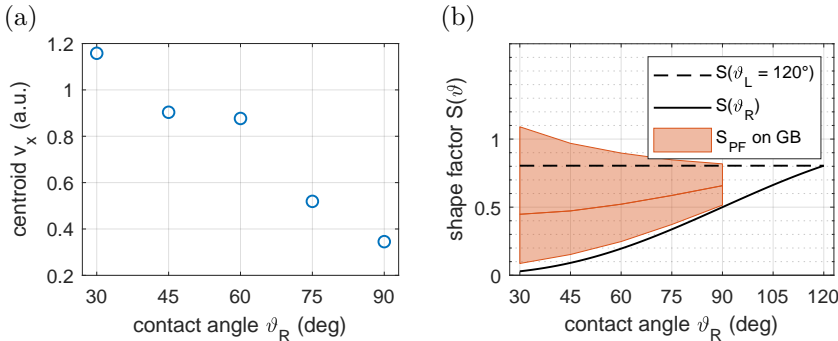


Figure 5.13: Results from the simulation of a particle on a grain boundary. In (a) the x-direction velocity of the shape centroid as function of the right contact angle ϑ_R and in (b) the shape factor corresponding to the shape at the end of the simulation (i.e. red contours from Figure 5.12) compared to the shape factors for the equilibrium shapes on either the low-energy (solid black line) or high-energy (dashed black line) side of the grain boundary within the substrate. As explained in the text, position of the substrate grain boundary strongly affects the shape factor, hence it is shown as the red area for the phase field simulation results S_{PF} . The red line in the center corresponds to the case when the grain boundary was in the middle of the particle.

The velocity of the shape centroid in the x direction was obtained from linear fit through the x centroid coordinate in time, see Figure 5.13a. The result quantifies the above reasoning, as it can be seen that lower ϑ_R (i.e. flatter right side) were associated with faster translation to the right.

The computed shape factors of the compound shapes were plotted in Figure 5.13b as red area indicating the possible span of values depending on the grain boundary position below the particle. In the same figure, the shape factors corresponding to the shapes nucleating on either side of the substrate grain boundary were indicated by a black dashed line for the high-energy side and a solid black line for the lower-energy side. The grain boundary energy contribution in the total energy of the particle (now understand the grain boundary between the particle and substrate) seems to be a crucial factor for the nucleation probability. When the particle is sufficiently shifted to the lower-energy side, the deviation in shape may not cause dramatic increase in the nucleation barrier. In the opposite case (the particle is rather on the high-energy side), the nucleation can even be less likely than that of an isolated particle (homogeneous nucleation, $S = 1$). In the extreme high-energy case for nearly all simulated ϑ_R , the nucleation on top of the boundary was less likely than

Table 5.4: Comparison of the contact angles in the two simulations which are shown fitted by Bézier polynomials in Figure 5.14. All values are shown in degrees °. In column BC the angles are as imposed by the boundary condition, in OBS how they were observed based on the slope between the last two points on the contour on either end, and then based on the control points of the Bézier polynomial of degree n .

angle	BC	OBS	$n = 3$	$n = 4$	$n = 5$
ϑ_L	120	118.0	91.6	116.5	129.3
ϑ_R	-30	-30.4	-51.7	-13.8	-34
ϑ_L	120	118.0	110.7	128.1	125.7
ϑ_R	-90	-89.4	-102.0	-96.8	-85.0

simply nucleating only on the high-energy part of the substrate.

An effort was made to characterize the obtained shapes using Bézier polynomials, which are often used in computer graphics and for description of both smooth curves and those with corners. The used method minimized the sum of squared differences between the contour and points on Bézier curve by optimization of the Bézier polynomial control points (the blue circles connected by dashed blue line in Figure 5.14). The used method was linear, hence the handles could be obtained in a single computational step and represent the best match of the chosen order of polynomial to the data.

The shapes seem rather simple so it was expected that the cubic Bézier polynomial ($n = 3$) might suffice for their description, but the match was in fact not very good (see examples in Figure 5.14a and 5.14b). Especially the contact points were notably off. The contours were then fitted by Bézier polynomials of orders 4 and 5 to confirm, whether an improvement was possible this way. The polynomials of order 5 provided qualitatively good match to the contours, even though some minor inaccuracy still remained (see Figure 5.14e and 5.14f).

The inaccuracy in Bézier polynomial fit to the contours can be noted on the contact angles the fitted curve had, see Table 5.4. For all the used orders it can be seen that there is some discrepancy.

Because the Bézier polynomials do not have any physical interpretation in this context, the particular relation of the polynomial control points to the simulation input parameters was not investigated further. However, it can certainly be concluded that the shapes minimizing the isotropic solid-liquid interface energy resting on top of a grain boundary intersecting a planar surface can at least be approximated by Bézier curves of fifth order.

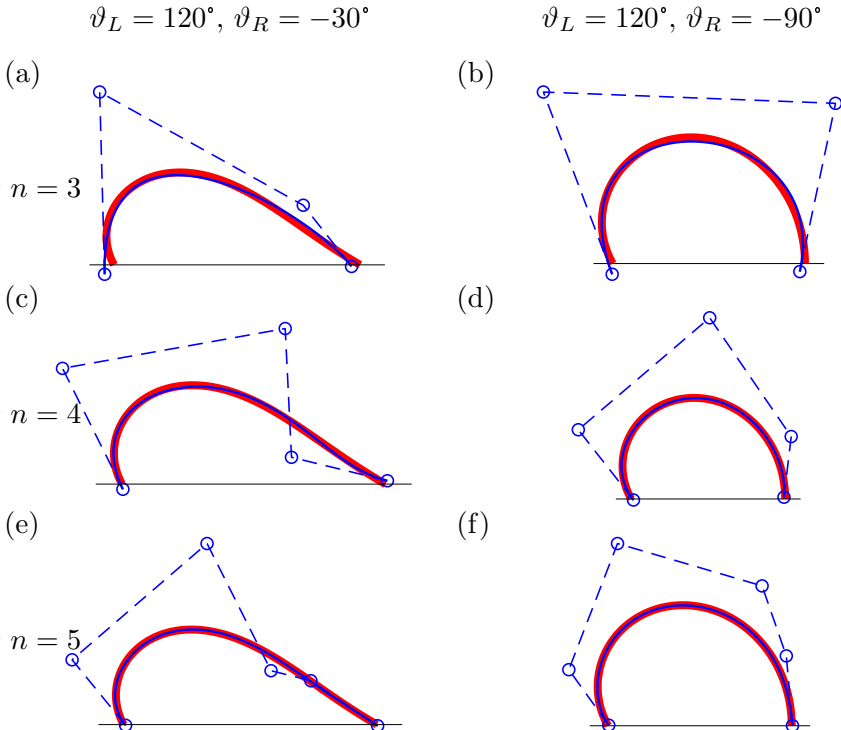


Figure 5.14: Using Bézier polynomials of various orders to fit the contour of a particle on top of a grain boundary. In (a), (c), (e) the contours from simulation with contact angles $\vartheta_L = 120^\circ$ and $\vartheta_L = -30^\circ$ fitted using the Bezier polynomial of order $n = 3, 4, 5$, respectively. In (b), (d), (f) the same orders of Bezier polynomials were applied to contours with contact angles $\vartheta_L = 120^\circ$ and $\vartheta_L = -90^\circ$.

5.8 Discussion

The domain scaling methodology was used to provide the shape factor for the hypothetical case of a particle on top of a grain boundary within otherwise planar surface. As mentioned before, such shape is not the equilibrium one, because for the isotropic particle-solution interface energy σ_P it cannot achieve constant curvature, hence in this context a constant chemical potential along the particle surface.

Given sufficiently large local energy fluctuation, such shapes which do not minimize the interface energy may occur in nucleation. Within the context of classical nucleation theory, the particle is assumed to appear at once. Once it occurs on the grain boundary as presented here, it is unstable and thus should either dissolve, separate into two smaller pieces on either side of the grain boundary (and then probably dissolve due to being of too small to overcome the nucleation barrier) or slide to the lower-energy side of the boundary and attain the energy minimizing shape there. Motion of very small clusters on a surface during electrodeposition was observed experimentally [104]. The sliding scenario is in principle imaginable with liquids but is questionable with continuum-like solids, considered here.

The splitting scenario is in fact very unlikely in liquids as well, because it would require spontaneous creation of new interface on the particle-liquid interface and simultaneous neglection of the jump in interface energy between the particle and substrate. The jump in interface energy will drive the system to expand the low-energy area on the expense of the high-energy area. In fact, the above simulations results showed that the interface energy acting on the compound equilibrium (unstable) shapes was moving them, not splitting. All the particle interfaces are thus subject to forces acting in the direction to the lower energy substrate side. This means that the particle is either expected to dissolve or to slide towards the low-energy side of the grain boundary on the substrate surface.

The taken approach is in fact not convenient for description of a solid phase nucleation on top of a grain boundary. Even though the exact mechanisms of the nucleation in grain boundaries during deposition are not known, it is more meaningful to imagine such growth rather on the atomic level than assuming the continuum-like nuclei. What is more, the grain boundary width in reality may be of comparable size like the nucleus. That implies that i) the assumption of infinitesimally narrow jump in surface properties is too simplistic and ii) that the grain boundary itself must interact with the particle in some way. Possibly by enabling nucleation in place of some local defect in the grain boundary. Additionally, given the assumed continuum aspect of the particle and its solid

state, the only viable resolution of the shape instability in 2D is to dissolve straight away.

In 3D, the grain boundary intersecting the substrate surface can be seen as a triple junction, a line defect which has its energy as well [13]. Upon insertion of the nucleus, part of this line energy would be replaced by the line energy of the triple junction between the two grains and the nucleated particle. If the triple junction with the environment had higher energy than the triple junction with the particle, a reduction in the triple junction line energy would occur in the system. However, it is out of the scope of this work to hypothesize to what extent this might become a factor in (meta)stabilization of the particle.

However, should the nucleating phase be liquid (e.g. electrodeposited eutectic gallium-indium alloy [105], the present study has shown that nucleation of the shape which mostly rests on the low-energy side of the substrate surface (while still being in contact with the high-energy side) is comparably probable like nucleation on the low-energy side alone. This can be seen on proximity of the lower edge of the red area in Figure 5.13b to the solid black line indicating the shape factor the shape nucleating straight on the low-energy side of the substrate.

5.9 Limitations of the presented methodology

One of the methodology limitations is that sharp angles of the interface inclination require finer grids, because the interface width is finite in the phase field simulation and its projection to the domain boundary can be long with the sharp angles. In fact, the sharpest simulated contact angle in this study was 15° . That may suffice in many applications with isotropic interface energy, but should a Wulff shape be simulated in arbitrary configuration, even sharper angle might be needed depending on the particle orientation. Using a finer grid should solve the related problems, but the validations have not been carried out and the method already is rather computationally intensive, especially when compared to the Winterbottom construction.

One of the reasons to use the multi-phase field model is that in principle multiple grains or particles could be simulated. However, the interface-inclination-controlling boundary condition assumes that no triple junction is near the interface-boundary contact point. Therefore, until this is somehow resolved, the advantage of using multi-phase field model for this purpose is limited.

A remark is due towards the original intended application of the methodology, i.e. to bring insight into the nucleation barrier anisotropy. As presented in

the next chapter, the basis for that is an analytic model relating the local interface energetics to the local crystallographic orientations of the particle and the substrate. Then it is possible to say how the shape wets the surface and what are the contact angles, hence the equilibrium shape could be obtained using this methodology. However, the insight may only be obtained by probing the substrate and particle orientation space, which implies large number of simulations at similar, yet unequal conditions. The domain scaling methodology would in principle be usable for the purpose, but at some points it would probably hit its limits, because it may not be so accurate in delivering minute details and it is not clear how well it would handle the cases with the contact points close to each other and other scenarios. Additionally, for a single pair of substrate-particle orientations there may be multiple stable solutions, each of which would have to be simulated in order to select the most likely one.

5.10 Conclusion

In this chapter, the author developed and implemented a novel method for determination of a shape factor of a heterogeneous nucleus seen within the framework of classical nucleation theory. This domain scaling method takes as input the contour of the shape on a plane. In combination with the phase-field model which implicitly tracks the interface it is possible to determine shapes of particles on a plane, where the equilibrium stable shape is not a-priori known e.g. from the Winterbottom construction. The case of a particle with isotropic interface energy on a grain boundary where the analytical solution was not known was analyzed.

In order to deliver the contours to the domain scaling method, the existing multi-phase field model [7, 8] was extended in several regards to allow such simulation. Importantly, volume conservation and general Neumann boundary conditions for control of interface inclination on the domain boundary were added. The model was systematically validated in several benchmarks.

The main results of the investigation of the particle with isotropic interface energy on top of the grain boundary within the substrate are the following:

- Shape factors were obtained for five different cases of particles on top of grain boundary,
- Position of the substrate grain boundary below the particle strongly determined the shape factor, hence the nucleation probability,
- When most of the particle rests on the low-energy side, the shape factor was comparable to the heterogeneous nucleation on the lower-energy side,

- The shapes which minimized the particle-liquid interface energy could be well approximated by Bézier polynomials of 5th order, but no physical interpretation was provided. The match could be probably improved by further increasing the order of the polynomial, but no added value was seen in that,
- The simulated contours moved towards the lower-energy side of the simulated domain, but it was explained that it was only due to the shape of the contour together with the curvature driving force, not because the simulation would explicitly include the particle-substrate energetics (only the contact angles are the input to the simulation).

Chapter 6

Analytic nucleation probability assessment and Monte Carlo simulations

This chapter is based on work of the author published as [10]: M. Minar and N. Moelans. “Influence of surface energy anisotropy on nucleation and crystallographic texture of polycrystalline deposits”. In: *Computational Materials Science* 231 (Jan. 2024), p. 112575. ISSN: 0927-0256. DOI: 10.1016/J.COMMATSCI.2023.112575. URL: <https://www.sciencedirect.com/science/article/abs/pii/S0927025623005694>.

6.1 Introduction

Irrespective of the deposition method, it is known that the process parameters often have pronounced effect on crystallographic texture and microstructure of polycrystalline deposits. Evaporation, sputtering, chemical vapour deposition or electrodeposition are just examples of these methods. Each is tied with a unique combination of physical and chemical interactions at the interface between the deposit and parent phase. The as-deposited texture is the result of synergy of many factors. However, the anisotropy on the deposit/parent phase interface during the film growth certainly plays an important role.

Typically, nucleation in film deposition is studied as a phenomenon occurring

on substrates, rather than on the deposit itself. However, there seems to be no obvious reason to neglect such an option, given the complicated anisotropy of grain boundary energy and local deposition conditions, varying possibly in both space and time.

A widely accepted theory by Thompson [56] suggests that the texture in deposits is controlled by two main factors: minimization of interface energy and minimization of strain energy. The first favors growth of grains with low-energy interfaces facing the parent phase and the second aligns the grains in the deposit to accommodate the stress. The energy densities are explicitly expressed for an abstracted columnar microstructure and compared as functions of the film thickness. He concluded that thin enough deposits have the texture controlled by minimization of interface energy. Above certain thickness, the strain energy overtakes. Later, additional factors contributing to the strain energy were included in the theory [106], allowing sensible interpretation of textures observed in sputter-deposited CdTe and electrodeposited Cu, but the results of some others are in agreement with the theory as well [107, 108].

A more phenomenological work by Rasmussen et al. [62] studied Cu electrodeposits on crystalline and amorphous substrates and proposed that in electrodeposition, the two competing texture-forming factors are the influence of the substrate and that of deposition conditions. Through the film thickness, three zones are defined: A (substrate-controlled texture), B (mixed) and C (deposition-conditions-controlled texture). The effect of the substrate in zone A can be e.g. epitaxy or chemical reactions, in zone C the anisotropy modifications are believed to be due to specific adsorption of different species [60, 61]. A more recent study of Ni electrodeposition [9] investigated the texture evolution through thickness with microscopic detail and showed, that the transition zone B does not seem to always occur as a simple mixture of A and C.

Despite the fact, that the anisotropy in interface energy is widely accepted to be one of the fundamental texture-forming factors, its effect on the orientation selection in nucleation remains fundamentally unclear. Two different theories by Pangarov [109, 110] and Kozlov [47] suggested that the textures of the electrodeposits are originated in the anisotropy of the nucleation barrier (*work of formation*), but each used a different reasoning. Pangarov treated 2D nuclei only and made the work of formation depending exclusively on overpotential (i.e. the driving force for the phase change) and lattice parameters. This theory was inconsistent with experimental observation of nuclei character as function of overpotential [28]. Kozlov studied the formation of initial texture on amorphous substrates in fcc metals by means of atomistic nucleation theory. Specifically, he computed the nucleation barriers and sizes of nuclei with three significant orientations. His prediction of initial $\langle 111 \rangle$ texture is in agreement with Thompson. It can thus be deduced, that in the initial stages of growth in

fcc metals on amorphous substrates, both the nucleation and growth may lead to the same fiber texture by means of interface energy minimization.

In practice, the interface energy anisotropy or deposition rate anisotropy cannot be measured directly during the deposition, which complicates the interpretation of the observed textures and microstructures. Additionally, the effect of the two above physical quantities on the polycrystalline deposit growth was shown to be equivalent in phase-field simulations to some extent [52]. It seems analogical to equilibrium Wulff shapes and kinetic Wulff shapes, which are geometrically similar [17]. However, this makes the fundamental discussion about how the growth is affected by interface anisotropy in general even more challenging, because the growth rate and interface energy are very different quantities, taking part in different processes.

The method developed in this paper obtains anisotropy in nucleation barrier (and, eventually, the nucleation probability) as function of the interface energy anisotropy, bottom grain orientation and the nucleus orientation. The method is based on principles of classical nucleation theory. Then, in order to demonstrate the effect of the anisotropic barrier on the film texture, a Monte Carlo algorithm was developed and used to simulate growth and nucleation in a polycrystalline film. The aim of this paper is to qualitatively explore the implications of the anisotropic interface energy for the orientation selection during repeated nucleation in the polycrystalline growth.

The paper is organized in five main parts. Firstly, the necessary fundamentals are described in Section 6.2 and some theoretical novelties regarding the Winterbottom construction are introduced. In Section 6.3, the problem specification defines all parameters in the orientation-dependent Winterbottom construction to be solved and successively the shape factor-orientation maps are presented and explained. These are used as input in the Monte Carlo simulations described in Section 6.4, together with their results. The Section 6.4.5 applies the obtained insights to a peculiar case of texture evolution in experiment [9] (electrodeposited nickel). There, a sudden change in texture occurred after thickness of $2\text{ }\mu\text{m}$, supposedly due to nucleation. The nucleation brought in new orientations, which succeeded in the growth competition. Interestingly, the said film was deposited very slowly, hence the high nucleation rate is rather unexpected when viewed in the perspective of classical nucleation theory with isotropic interface energy. However, with the anisotropic interface energy included as worked out here, a qualitative explanation was found.

6.2 Fundamentals

6.2.1 Isolated particle with anisotropic interface energy

It was already discovered in 1901, how to determine the stable equilibrium shape of a particle with crystalline anisotropy [111]. The chemical potential $\mu(\theta)$ must be constant along the surface of equilibrium shape [39]. Assuming that the surface is only under the influence of anisotropic capillary force, the chemical potential on the curved surface in 3D space depends on the local principal curvatures and interface energy anisotropy as follows from the Herring equation [15, 112]. In 2D the surfaces become curves and the expression for the chemical potential is simplified to

$$\mu(\theta) = \tilde{\sigma}(\theta)K, \quad (6.1)$$

with local interface normal angle θ and local curvature K . The interface stiffness $\tilde{\sigma}(\theta)$ is the thermodynamic driving force for the capillary motion and the local curvature κ is the thermodynamic coordinate. The interface stiffness is

$$\tilde{\sigma}(\theta) = \sigma_0[h(\theta) + h''(\theta)], \quad (6.2)$$

where $h(\theta)$ and $h(\theta)''$ stand for the anisotropy function and its second derivative, respectively. The anisotropy function defines the interface energy $\sigma(\theta)$

$$\sigma(\theta) = \sigma_0 h(\theta), \quad (6.3)$$

where σ_0 is a constant with physical dimensions of interface energy (i.e. J/m²). In this chapter it is assumed, that the anisotropy function takes the following form

$$f(\theta - \alpha) = 1 + \delta \cos(n(\theta - \alpha)), \quad (6.4)$$

where $0 \leq \delta < 1$ is the strength of anisotropy, n the order of symmetry and α the angle rotating the anisotropy function, representing the 2D crystal orientation. A normalized strength of anisotropy $0 \leq \Omega < (n^2 - 1)$ can be defined as $\Omega = \delta(n^2 - 1)$. In this paper, weak anisotropy will specifically refer to $\Omega < 1$ and strong anisotropy to $\Omega \geq 1$.

The interface stiffness then reads

$$\tilde{\sigma}(\theta) = \sigma_0 \{1 - \Omega \cos[n(\theta - \alpha)]\}. \quad (6.5)$$

The isolated particle with anisotropic interface energy takes on the well-known Wulff shape, which in 2D can be described as a parametric curve $\mathbf{w}(\theta) =$

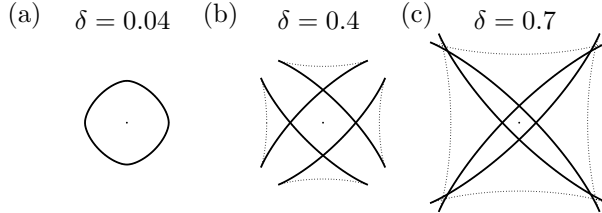


Figure 6.1: Examples of full Wulff plots (i.e. $-\pi \leq \theta \leq \pi$) of 4-fold symmetry with indicated strengths of anisotropy. The dotted segments are the forbidden orientations, solid lines are the allowed ones. The "ears" in b) do not contribute to the isolated particle shape. However, at even stronger anisotropy in c) another intersection occurs among the branches, which introduces new solutions to the equilibrium shape.

$$[w_x(\theta), w_y(\theta)]^T [17, 29, 113]$$

$$w_x(\theta) = R_W[h(\theta) \cos(\theta) - h'(\theta) \sin(\theta)] \quad (6.6)$$

$$w_y(\theta) = R_W[h(\theta) \sin(\theta) + h'(\theta) \cos(\theta)]. \quad (6.7)$$

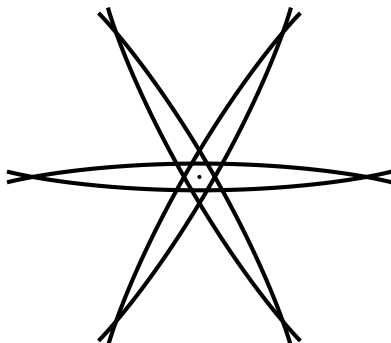
See Figure 6.1 for examples of 4-fold symmetry at various strengths of anisotropy δ .

From equation (6.5), it is easily seen that for $\Omega > 1$, there are such θ s, for which the interface stiffness is negative. These normal angles are unstable [17, 29, 39], hence they do not occur on the stable equilibrium Wulff shape (see the dotted segments in Figure 6.1) and are called missing or forbidden. Closer inspection of the anisotropy function (6.4) and its derivatives reveals that the forbidden angles correspond to interface energies near maxima of the anisotropy function. In fact, the latter is a general observation, independent on the particular anisotropy function (6.4).

For $\Omega > 1$, the equations (6.6)-(6.7) must be understood in a piece-wise fashion for the intervals of allowed θ s. Each of these allowed-angles interval produces a single branch in the Wulff curve. The discontinuity in allowed angles causes that the Wulff shape is no longer a smooth and continuous closed curve (like in Figure 6.1a). Instead, it is a piece-wise continuous and self-intersecting curve (Figure 6.1b-c), where the individual branches enclose a polygon-like closed curve with corners. In the case of Figure 6.1b, the outer parts of the shape (so-called ears) cannot contribute to the (isolated) crystal shape, but for strong enough anisotropy (like in Figure 6.1c) the ears cross again, giving rise to a multitude of other stable equilibrium solutions. That is because every single of the four spikes can be part of the solution but does not need to be. This

repeated crossing of the ears and its implications for the equilibrium shapes have not been reported in any work known to the author, hence it will be elaborated on in detail.

(a)



(b)

cross order 1



(c)

cross order 2



(d)

cross order 3

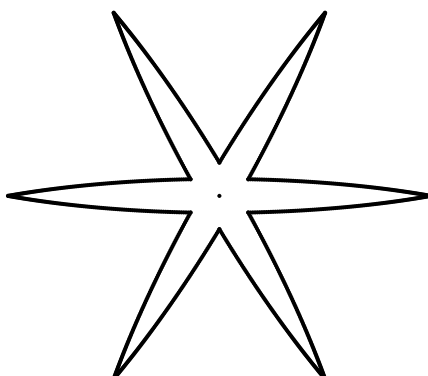


Figure 6.2: Orders of corners, defined by the branches intersections, shown for 6-fold anisotropy and $\delta = 0.7$. In a) there are all the allowed angles, in b)-d) are the stable equilibrium shapes defined by the b) first order, c) second order and d) third order of the corners. Any closed curve is a stable equilibrium shape, which connects these corners along the allowed-angles branches and has the interface normals pointing outwards in every point.

To emphasize the general features of this "crossed-ears" type of solutions, the Figure 6.2a provides another example of very strong, but 6-fold anisotropy, where

the ears cross even twice behind the polygon-like isolated Wulff shape. Then, Figures 6.2b-d show the different possible shapes, where the outer corners always correspond to branch intersection of the same type. The type of intersection can be characterized by the radial distance from the center, based on which they can be ordered. Practically, the corner of the first order is a corner on the polygon-like shape, where two branches forming adjacent sides of the polygon-like shape cross (Figure 6.2b). A corner of the second order is farther from the center and is the intersection of two branches forming two polygon sides separated by a single side (Figure 6.2c). A corner of the third order (Figure 6.2d) is the intersection of two branches separated by two sides etc.

For convenience, the shapes in Figures 6.2b-d will be called isolated Wulff shapes of first, second and third order, respectively.

Below, a summary of some key points is given:

- for $n \geq 2$ and $\delta \geq 1/(n^2 - 1)$ the Wulff shape comprises of n mutually crossing branches and the isolated shape (of first order) exhibits corners,
- for $n \geq 4$ multiple branches intersections occur for sufficiently large δ ,
- the branches intersections (corners) can be characterized by their radial distance from the center,
- the upper limit on the number of intersections of a single branch with others depends on the total number of branches, i.e. on the order of symmetry n ,
- as long as the orientation of the curve is respected (i.e. interface normal of all segments on the shape points outwards), any closed curve connecting the above mentioned corners along the branches is a stable equilibrium shape,

Table 6.1: The approximate minimal strengths of anisotropy at which the corners of indicated order appear on the Wulff shapes in 4-fold and 6-fold anisotropy. The first number is the strength of anisotropy δ and in parenthesis is the corresponding normalized strength of anisotropy $\Omega = \delta(n^2 - 1)$.

n	order of corner		
	1	2	3
4	0.06667 (1.00000)	0.60000 (9.00000)	x
6	0.02857 (1.00000)	0.16422 (5.74773)	0.62136 (21.74773)

- the shape of higher order contains all the lower-order shapes and has larger area than any of them. The first-order shape thus has the smallest area and, consequently the least total interface energy.

In Table 6.1, there are provided the minimal strengths of anisotropy at which the corners of indicated order appear on the Wulff shape in 4-fold and 6-fold anisotropy. Of these, only the first-order corners have an analytic expression, the higher-order corners were obtained numerically and thus are only approximate.

6.2.2 Particle with anisotropic interface energy on a plane (Winterbottom construction)

The problem of equilibrium shape of a particle with anisotropic interface energy on a planar substrate was treated in various works. It can either be derived from variational principles by total interface energy minimization [41, 48] or by the Cahn-Hoffman vector formalism [19].

The shape is strongly determined by the force balance of the three meeting interfaces: substrate-parent phase (σ_1), particle-parent phase (σ_2) and particle-substrate (σ_3). There are two such contact points in 2D (in 3D it is a triple line) and both must be in force balance in order to sustain a stable equilibrium shape.

Winterbottom construction identifies which segments on the full Wulff shape are (or can be) part of the equilibrium shape of a particle with anisotropic interface energy on a plane.

For tractability of the general solution (of the particle shape), it is essential to assume co-planarity of the particle-substrate and substrate-parent phase interfaces [19, 39, 41].

In 2D, the stability of the shape derives from the stability of the two contact points. In this geometry, all interface energies are known and the orientations of two of the interfaces are known (the former substrate plane). The orientation of the last interface (the particle) in the left and right contact points are expressed by normal angles θ_c^L, θ_c^R , respectively. These are found using the Young's equation with inclination dependence, solved in every contact point

$$\sigma_1 - \sigma_3 = \sigma_2(\theta_2) \sin(\theta_2) + \sigma'_2(\theta_2) \cos(\theta_2), \quad (6.8)$$

which can be written in a non-dimensional form

$$\Gamma = h(\theta_2) \sin(\theta_2) + h'(\theta_2) \cos(\theta_2), \quad (6.9)$$

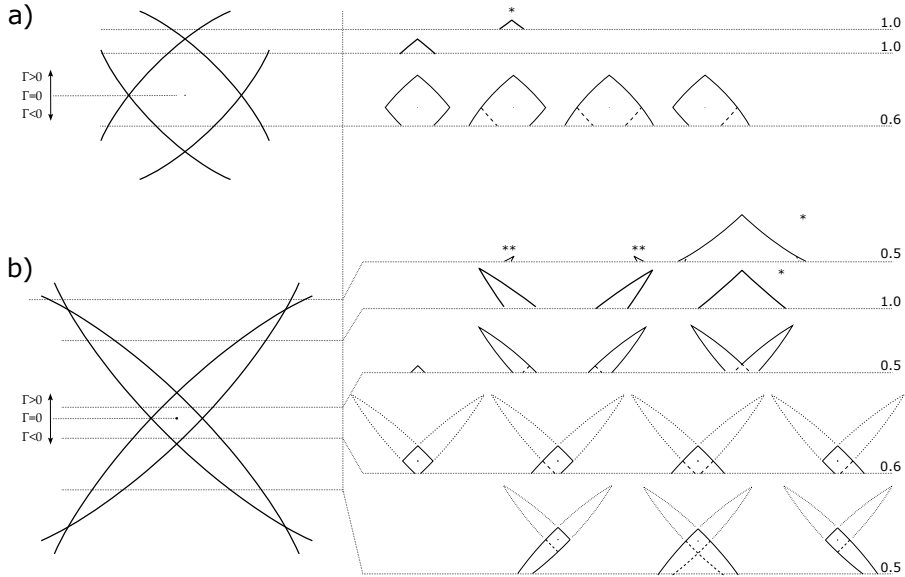


Figure 6.3: Complete list of non-trivial equilibrium shapes of a particle with anisotropic interface energy on a plane (right part of the sketches) as derived from full Wulff shapes (left part of the sketches) using generalized Winterbottom construction. In a) for strength of anisotropy $\delta = 0.3$, in b) with $\delta = 0.7$. The horizontal dotted lines indicate different truncating lines for the Wulff shape and at the same time the substrate for the equilibrium shapes. The scale of the equilibrium shapes relative to the full Wulff shapes on the left is provided on the right on every respective line. Inverted shape solutions of first order are indicated by asterisk *, of the second order by **. The dashed lines within some of the the equilibrium shapes show the segments on the Wulff shape which were enclosed by the equilibrium shape. The dotted lines above the equilibrium shapes in b) indicate the crossed-ears solutions, which either may be present both, separately or both be absent. The new solutions can be seen in b).

where $\Gamma = [\sigma_1 - \sigma_3]/\sigma_2^0$ will be denoted *wetting parameter* in this paper. It can be both positive or negative.

The solutions are from the ranges $3\pi/2 > \theta_c^L > \pi/2$ and $\pi/2 > \theta_c^R \geq -\pi/2$ and must be allowed angles. When (6.9) is compared to (6.7), it is obvious that the solutions θ_c^L, θ_c^R are found as normal angles in points with y coordinate equal to Γ on an unit-radius Wulff shape. Thus, the resulting particle shape is a segment of the isolated shape, where the position of the sectioning plane Γ is determined by the force balance. That is the Winterbottom construction.

Originally, it served to find the shape of the least interface energy, but Bao [39] generalized it for any stable equilibrium shape. For illustration of the generalized Winterbottom construction depending on the position of the truncating line see Figure 6.3.

When the anisotropy is strong, multiple stable equilibrium shapes may exist even when the isolated shape has only a single equilibrium stable shape. All these solutions are illustrated in Figure 6.3a for 4-fold anisotropy, moderately strong [39]. In Figure 6.3b all possible solutions are presented for very strong 4-fold anisotropy, which involves the new solutions derived from the second-order corners.

If multiple solutions existed in the isolated particle in the above-truncating-line part, this multiplicity is present in the possible solutions on the plane too (Figure 6.3b). Compared to the isolated case, additional solutions are present, when the truncating line passes below the center of the isolated shape, with the shape being defined also by the "ears" extending behind the corners (in both Figure 6.3a and 6.3b).

An exceptional class of the solutions is the *inverted shape solution* (indicated by asterisk in Figure 6.3), which is found *below* the sectioning plane, as described by Bao [39] on a shape like in Figure 6.3a. However, due to the inverted shape symmetry, it is not clear, what operation(s) of symmetry the "inversion" refers to according to Bao and how to construct the solution in a general case. More detailed characterization of this solution type was given in the following section 6.2.3. It should be noted that in systems with corners of higher order, multiple orders of the inversion shape are possible (also indicated in Figure 6.3 by asterisk * and described in more detail in 6.2.3).

6.2.3 Inverted solution in Winterbottom construction

The inverted shape in a Winterbottom construction with single plane was described by [39] in a highly symmetric case. The same idea was used much sooner in the Winterbottom construction in a corner (meaning Wulff shape resting on two lines at once, intersecting in a corner) by Zia et al. [44] ("Summertop construction"). Below, the inverted shape construction is described, taking into account the higher-order intersection solutions and arbitrary rotations.

Let the Wulff shape exhibit strong anisotropy, i.e. be there at least corners of first order. Further, let the wetting parameter Γ be such, that the truncating line passes at least above the isolated shape of the first order, i.e. the first-order shape is submerged below the substrate plane.

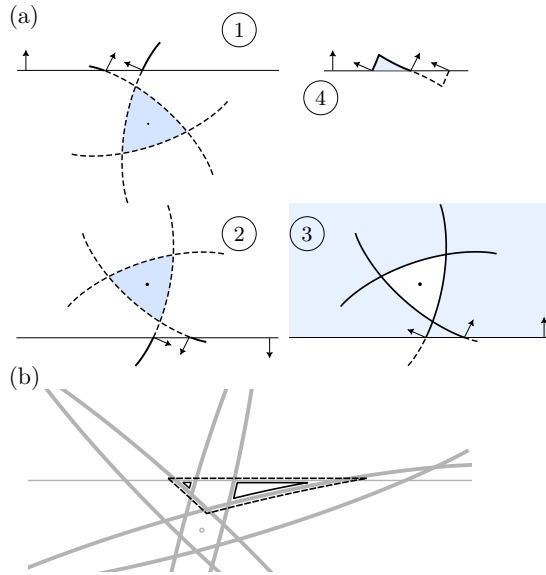


Figure 6.4: Illustration of the inverted Winterbottom construction. In (a) explained in 4 steps and in (b) illustration of inverted solutions of higher orders. In (a) the plane normal points from the substrate to the parent phase, the solid lines of the Wulff plot are thus above the substrate plane and the dashed ones are below. Interface normals in the contact points are indicated as well. In 1 is the initial state, in 2 after center inversion, in 3 after the curve orientation flip and in 4 is the resulting shape next to the original part of the Wulff plot. In (b) the dashed black line indicates inverted shape of the first order, the solid line that of second order.

Then it may happen, that the truncating line intersects two branches, which crossed below it (see Figure 6.4a1). Such situation allows a solution, where the equilibrium shape is the part *below* the substrate plane, but *above* the corner where the two branches intersect. Two steps must be followed to obtain the inverted equilibrium shape:

1. point inversion of the whole system (Wulff plot + truncating line) about the center of the Wulff shape (see Figure 6.4a2)
2. flip orientation of both the inverted Wulff plot and inverted truncating line, i.e. flip the inverted inward and outwards directions (see Figure 6.4a3)

The first operation places the truncating line below the said corner, where the

two branches intersect. At the same time, the whole shape is inverted. The second operation turns the outside of the Wulff plot to be inside - i.e. instead of having a crystal in the shape of inverted Wulff plot in some medium, we have a medium in the shape of Wulff plot surrounded by the crystal.

Then, the resulting inverted shape as in Figure 6.4a4 is obtained as an enclosed intersection of the anisotropic Wulff plot and a half-space above the line. All the interface normal orientations on the surface of the inverted shape are the same as on the non-inverted part of the Wulff plot. Importantly, this includes the normal angles in the contact points, as can be seen in Figure 6.4a4.

The order of the intersection in which the two Wulff branches intersect, determines the order of the inverted shape. Figure 6.4b shows an example of strong 6-fold anisotropy with such truncation, that it allows two orders of inverted shapes at once.

6.2.4 Contact point stability

The contact points mentioned above are essentially triple junctions. The Young's equation with inclination dependence (6.8) represents equilibrium of the tractions due to the interfaces on the junction in the x direction. It concerns a special case, where the position of two of the three interfaces are fixed to lay on the x axis and the third has inclination-dependent interface energy. However, the *stability* of the triple junction configuration is not guaranteed by Young's equation alone [34]. In the present case, the configuration means a solution θ_2 to (6.8). Technically, the solutions to (6.8) are stationary points of the triple junction energy as function of virtual translations, but not necessarily its minimum (i.e. the stable configuration). Stability of the found solutions should be thus tested using additional conditions derived from second-order derivatives of the triple junction energy with respect to the virtual translations [34]:

$$0 < \tilde{\sigma}_1 s_1 + \tilde{\sigma}_2 s_2 + \tilde{\sigma}_3 s_3 \quad (6.10)$$

$$0 < \tilde{\sigma}_1 \tilde{\sigma}_2 S_{12} + \tilde{\sigma}_2 \tilde{\sigma}_3 S_{23} + \tilde{\sigma}_1 \tilde{\sigma}_3 S_{13}, \quad (6.11)$$

where $\tilde{\sigma}_i$ are the respective interface stiffnesses, $s_i = \cos^2(\theta_i)/d_i$, $S_{ij} = \sin^2(\theta_i - \theta_j)/d_i d_j$. In the present geometry, interfaces 1 and 3 are fixed with $\theta_1 = \pm\pi/2$ and $\theta_3 = \mp\pi/2$, hence it follows that $s_1 = s_3 = 0$ and also that $S_{13} = 0$. Note also that $s_2 > 0$ and $S_{12} = S_{23} = S > 0$. By the geometry alone, the conditions are thus simplified to

$$0 < \tilde{\sigma}_2 \quad (6.12)$$

$$0 < \tilde{\sigma}_1 \tilde{\sigma}_2 + \tilde{\sigma}_2 \tilde{\sigma}_3, \quad (6.13)$$

where only the interface stiffnesses matter. Using the first equation, the second one may further be simplified

$$0 < \tilde{\sigma}_1 + \tilde{\sigma}_3 . \quad (6.14)$$

The condition (6.12) implies, that the particle-parent phase interface must be oriented under allowed angle in the contact point. That is fulfilled automatically by the truncated Wulff shape solution, because it contains only the allowed angles.

Note that the interfaces 1 and 3 have fixed orientations and are assumed to be planar. The condition (6.14) is surely fulfilled when both interfaces 1 and 3 have positive interface stiffness in their orientations. That holds automatically in weak or no anisotropies. When either or both of the two interfaces exhibit strong anisotropy, it means that there are normal angles where the interface stiffness is negative, hence the condition (6.14) may be violated and must be verified in the given configuration.

6.2.5 Terminology in heterogeneous nucleation

3D nucleation and 2D nucleation are terms used in classical nucleation theory to describe two different nucleation mechanisms on a plane in 3D space.

In 3D nucleation, the nuclei form as 3D clusters on the flat substrate and their interface energy is derived mostly from their curved surface. The possible edge and vortex energies are usually neglected. The clusters grow and coalesce.

In 2D nucleation, the nucleus is a mono-atomic step (usually assumed in a shape of a disc) on the (theoretically) atomically smooth surface. In the total nucleus interface energy, the edge energy cannot be neglected. The nuclei grow along the surface layer by layer.

These concepts can be reduced to 2D space, where the 3D nucleation is equivalent to 2D nucleation and the 2D nucleation to 1D nucleation. In order to simplify the terminology when describing the results from 2D space, the terms spatial and interfacial nucleation are introduced, which indicate the difference in the mechanism irrespective of the used dimension.

This paper only deals with the anisotropy in nucleation barriers of nuclei created in *spatial* nucleation. That is because it is not expected that the grain orientation could change during the *interfacial* nucleation, which is essentially a localized epitaxial growth. In the following, the *spatial nucleus* denotes a nucleus created in spatial nucleation.

6.2.6 Heterogeneous spatial nucleation and shape factor

Note that the formulas and their description in this section are given for 2D space, but they could easily be generalized to 3D.

Because nucleation is a thermally activated process, the probability P of finding the critical nucleus at a certain spot follows the Arrhenius relation

$$P \approx \exp\left(-\frac{\Delta G_c^*}{kT}\right), \quad (6.15)$$

where k is the Boltzmann constant, T absolute temperature and ΔG_c^* is the *critical nucleation barrier* (in J), which is to be overcome by the thermal fluctuations in order to form a critical nucleus. A nucleus with the critical area A_c is metastable. The nucleation barrier ΔG_c^* is the *nucleation work* [13] to be done in order to insert a critical nucleus. Subcritical nuclei dissolve, the supercritical ones grow.

In heterogeneous nucleation (i.e. nucleation on a wall), a shape factor $S \geq 0$ is the ratio of the heterogeneous nucleus area A_{het} to the area of the isolated particle A_{hom} (homogenous nucleus) generated at equivalent conditions. It can thus be written as a proportionality factor

$$A_{het} = S A_{hom}. \quad (6.16)$$

The force balance of the meeting interfaces determines the wetting, which decides the value of S . When $S = 0$, no spatial nucleus (here 2D nucleus) is inserted, because complete wetting occurs and only interfacial (1D) nucleation is possible.

Because it was shown in [48], that the nucleation barrier is proportional to the actual area of the nucleus, the shape factor relates the nucleation barriers too, hence

$$\Delta G_{het}^* = S \Delta G_{hom}^*. \quad (6.17)$$

The above implies, that knowing the homogeneous nucleation barrier and the shape factor for a particular heterogeneous nucleus allows to determine the heterogeneous nucleation barrier and also the relative difference in nucleation probability. This reduces the problem of heterogeneous nucleation probability to the determination of a shape factor, obtained as ratio of areas of heterogeneous and homogeneous nucleus.

It should be emphasized, that in the case of multiple possible shape solutions (like e.g. in Figure 6.2a), the Wulff shape of the first order (Figure 6.2b) was always assumed as the homogeneous nucleus in the shape factor determination.

That choice was made because the nucleation barrier is proportional to the inserted nucleus area (see (6.18)), which implies that smaller nuclei have larger nucleation probability. The Wulff shape of the first order is the smallest one, hence the most likely to occur.

In 2D, the critical homogeneous nucleation barrier $(\Delta G_c^*)_{hom}$ depends on the scalar interface energy σ_0 from $\sigma(\theta) = \sigma_0 h(\theta)$ (i.e. as in (6.3)) and the bulk driving force for the phase transformation ΔG_V as

$$(\Delta G_c^*)_{hom} = \hat{A}_{hom} \frac{\sigma_0^2}{\Delta G_V}. \quad (6.18)$$

where $\hat{A}_{hom} = A_{hom}/R^2$ is a non-dimensional area of the nucleus, R being a radius of the nucleus. If the nucleus is a particle with anisotropic interface energy, then R is a generalized radius, a scalar factor scaling the area of the particle. In classical nucleation theory in 2D (with both isotropic and anisotropic interface energy [48]) it is simply

$$R = \frac{\sigma_0}{\Delta G_V} \quad (6.19)$$

In order to get a reasonable nucleation rate of $1 \text{ cm}^{-3}\text{s}^{-1}$ and larger, the homogeneous nucleation barrier ought to be $(\Delta G_c^*)_{hom} \leq 78 kT$, but at the same time it should be $(\Delta G_c^*)_{hom} \geq 10 kT$, because the nucleus radius then gets so small, that the applicability of the continuous approach of classical nucleation theory becomes questionable [45, pp.195].

Let the symbol

$$\beta = \hat{A}_{hom} \frac{\sigma_0^2}{\Delta G_V} \frac{1}{kT} \quad (6.20)$$

stand for the non-dimensional nucleation barrier, i.e. the nucleation barrier expressed in multiples of kT . Apparently, $10 \leq \beta \leq 78$, in order to observe a reasonable amount of nucleation describable by classical nucleation theory. Then, the homogeneous nucleation probability can be written as

$$P_{hom} = \omega \exp(-\beta) \quad (6.21)$$

and the heterogeneous one

$$P_{het} = \omega \exp(-\beta S). \quad (6.22)$$

The vibration frequency ω represents the number of nucleation attempts per unit of time (assumed to be a constant in this paper).

Note that β aggregates information about temperature, the driving force and the interface energy. In this paper, the temperature T and σ_0 are assumed to

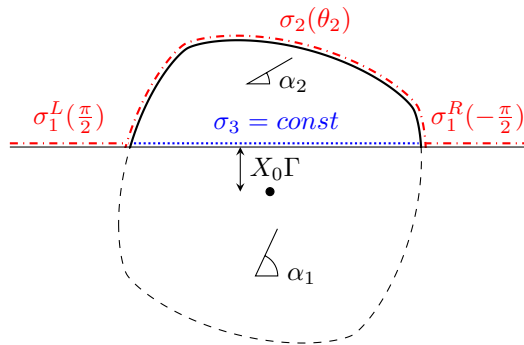


Figure 6.5: Winterbottom construction on a weak-anisotropy Wulff shape with indication of the distinct types of interfaces: red and dash-dotted line is the anisotropic solid-liquid interface and the blue and dotted line is the Read-Shockley grain boundary (independent on interface inclination).

be constant. Consequently, when β varies, the bulk driving force ΔG_V is varied inversely, as can be seen from the equation (6.20). This way, the variations in β are also related to the deposition rate, because the higher the driving force, the higher the deposition rate.

6.3 Nucleation probability assessment

6.3.1 Problem statement

A polycrystalline film grows from a liquid parent phase. Nucleation during the film growth is expected, which then occurs on the same material, as is being deposited. In this system there are two distinct types of interfaces: the solid-liquid interface with inclination-dependent interface energy; and the grain boundary following the Read-Shockley dependence on misorientation (inclination-independent, though). Every grain has a particular crystallographic orientation (in 2D characterized by a single angle α). The grain orientation α coincides with the rotation of the solid-liquid interface energy anisotropy function (6.4).

A single nucleation event is always assumed to take place on a straight solid-liquid interface. The nucleus is assumed to take on an energy-minimizing equilibrium shape. Hence, in the case of multiple possible solutions, the one with the smallest area is selected.

A sketch of a single nucleation event is in Figure 6.5. The substrate is a plane, hence the orientation of its normal and the interface energy are equal on both sides of the particle. However, due to the problem geometry it is seen differently in the polar coordinate systems associated with the left and right contact angle - the normal is $+\pi/2$ on the left and $-\pi/2$ on the right, hence $\sigma_1^L(\frac{\pi}{2}) = \sigma_1^R(-\frac{\pi}{2})$.

Specifically, the solid-liquid interface energy is

$$\sigma_{SL}(\theta) = \sigma_{SL}^0 h(\theta), \quad (6.23)$$

where $h(\theta)$ is the anisotropy function (6.4). The Read-Shockley grain boundary energy dependence is a function of disorientation $\Delta\alpha(\alpha_1, \alpha_2)$

$$\sigma_{GB}(\alpha_1, \alpha_2) = \begin{cases} \sigma_{GB}^0 \frac{\Delta\alpha(\alpha_1, \alpha_2)}{\Delta_{lim}} \ln \left(\frac{\Delta\alpha(\alpha_1, \alpha_2)}{\Delta_{lim}} \right) & \Delta\alpha \leq \Delta_{lim} \\ \sigma_{GB}^0 & \Delta\alpha > \Delta_{lim} \end{cases}, \quad (6.24)$$

with $\Delta_{lim} = 15^\circ$ used here. Note that due to the problem symmetry of order n , the Read-Shockley dependence must be periodic too, hence the common disorientation definition $\Delta\alpha = |\alpha_1 - \alpha_2|$ cannot be used. The periodicity can be achieved using *modulo with rounded division convention* [114]

$$\Delta\alpha(\alpha_1, \alpha_2) = \text{mod}(\alpha_1 - \alpha_2, 2\pi/n), \quad (6.25)$$

where $\text{mod}(x, y) = x - y \text{round}(x/y)$. This way, the disorientation is always within $-\pi/n \leq \Delta\alpha \leq \pi/n$ and the minimum of Read-Shockley appears at $k\pi/n$, where $k = -1, 0, 1$.

The bottom grain orientation is α_1 and the nucleus orientation is α_2 . The respective interface energies are expressed as

$$\sigma_1^L(\frac{\pi}{2}) = \sigma_1^R(-\frac{\pi}{2}) = \sigma_{SL}^0 h(\frac{\pi}{2} - \alpha_1) \quad (6.26)$$

$$\sigma_2(\theta_2) = \sigma_{SL}^0 h(\theta_2 - \alpha_2) \quad (6.27)$$

$$\sigma_3 = \sigma_{GB}(\alpha_1, \alpha_2). \quad (6.28)$$

Then, the wetting parameter Γ can be expressed as a function of the bottom grain and nucleus orientations

$$\Gamma(\alpha_1, \alpha_2) = \frac{\sigma_1^L(\frac{\pi}{2}) - \sigma_3(\alpha_1, \alpha_2)}{\sigma_{SL}^0} \quad (6.29)$$

$$= h\left(\frac{\pi}{2} - \alpha_1\right) - \frac{\sigma_{GB}(\alpha_1, \alpha_2)}{\sigma_{SL}^0}. \quad (6.30)$$

It was assumed that $\sigma_{GB}^0 = \sigma_{SL}^0 = 0.3 \text{ J/m}^2$.

With all above, the geometric problem is fully specified by the pair of orientations (α_1, α_2) , both of which are from the interval $0 \leq \alpha < 2\pi/n$. The top grain orientation α_2 specifies the rotation of the equilibrium shape and the wetting parameter (6.30) specifies where the truncating line passes.

6.3.2 Stability as function of the bottom grain orientation

If the stability conditions (6.12) and (6.14) do not hold for either of the two contact angles, the shape is not stable. The condition (6.12) is fulfilled by default in the (generalized) Winterbottom construction. The condition (6.14) is simplified by the assumption of the grain boundary being inclination independent, because then $\tilde{\sigma}_3 = \sigma_3$. Using the interface stiffness definition (6.2) and the interface energies (6.26), (6.28), the condition (6.14) can be written

$$h\left(\frac{\pi}{2} - \alpha_1\right) + h''\left(\frac{\pi}{2} - \alpha_1\right) > -\frac{\sigma_{GB}(\alpha_1, \alpha_2)}{\sigma_{SL}^0}, \quad (6.31)$$

which holds for any twice-differentiable anisotropy function $h(\theta)$. Apparently, the right-hand side is always negative and it is the term $h''(\frac{\pi}{2} - \alpha_1)$, which decides the stability. As stated before, the interface stiffness is only negative for forbidden angles, around maxima of the anisotropy function. Hence, the above condition may be violated only when the substrate normal is aligned with a forbidden angle. This conclusion stems from the problem geometry and energetics, it is independent of the form of anisotropy function $h(\theta)$.

After substitution of (6.5) into (6.14) and rearrangement, the second condition becomes

$$\cos\left[n\left(\frac{\pi}{2} - \alpha_1\right)\right] < \frac{1}{\Omega} \left(\frac{\sigma_{GB}(\alpha_1, \alpha_2)}{\sigma_{SL}^0} + 1 \right). \quad (6.32)$$

The right-hand side is always positive. Apparently, when the right-hand side is greater than 1, the triple junction configuration is stable for any bottom grain

orientation α_1 . That certainly holds for weak anisotropies, i.e. when $\Omega \leq 1$. For stronger anisotropies $\Omega > 1$, the right-hand side may get smaller than 1 and some orientations α_1 then do not meet the stability condition. The stronger the anisotropy, the closer is the right-hand side to zero and the interval of unstable α_1 orientations is wider.

Effectively, the (3D) nucleation is blocked on high-energy crystal facets due to the strong anisotropy.

6.3.3 Shape factor-orientation maps

Here, the shape factor-orientation map is the 2D plot of the shape factor as function of the top and bottom grain orientation, i.e. $S(\alpha_1, \alpha_2)$. For isotropic nucleation, the solid-liquid interface had constant interface energy σ_{SL}^0 and the grain boundary followed the Read-Shockley dependence (6.24). In anisotropic nucleation, the shape factor $S(\alpha_1, \alpha_2)$ was obtained from the generalized Winterbottom construction, with the wetting parameter $\Gamma(\alpha_1, \alpha_2)$ from (6.30). A solver was programmed in MATLAB, which found the possible solutions in the generalized Winterbottom construction and selected the one with the minimal area. It included all types of solutions discussed in this paper and it is available in Mendeley Data repository [12]. This solver was used to find $S(\alpha_1, \alpha_2)$ for all intended pairs of bottom and top grain orientations (α_1, α_2) .

Examples of the shape factor-orientation maps $S(\alpha_1, \alpha_2)$ for four different strengths of anisotropy in 4-fold symmetry are shown in Figure 6.6.

In Figure 6.6a, there is the map for the case of a particle with isotropic solid-liquid interface energy. There, the shape factor can be analytically determined, because the isolated equilibrium shape is a circle. Hence, the heterogeneous nucleus shape is a circular segment and from the basic geometric relations one can write

$$S = \frac{\phi - \sin(\phi)}{2\pi}, \quad (6.33)$$

where ϕ is the central angle of the circular segment, which relates to the wetting parameter Γ (6.30) simply as

$$\phi = 2\text{acos}(\Gamma). \quad (6.34)$$

Except for the regions of close orientations $\Delta\alpha \leq \Delta_{lim}$ (i.e. the diagonal and the corners of the map), there is constant $\Gamma = 0$, hence $\phi = \pi$ and $S = 0.5$ (i.e. the shape is a semicircle). For close orientations $\Delta\alpha \leq \Delta_{lim}$, the Read-Shockley grain boundary energy dependence implies smaller grain boundary energies (approaching 0 when the orientations are the same), which propagates

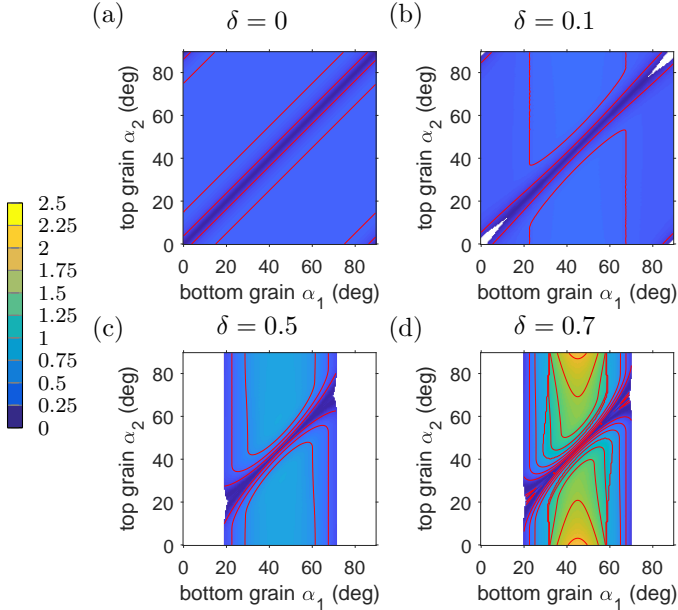


Figure 6.6: Shape factor-orientation maps for four different strengths of anisotropy in 4-fold symmetry (180x180 points). In (a) is the isotropic case, in (b)-(c) the anisotropic ones, the strength of anisotropy δ is indicated above. The white regions indicate the unstable orientations as by the condition (6.32). The levels are drawn with the increment of 0.25, like the colorbar spacing.

through the equations for Γ, ϕ and eventually causes the drop of S to zero. That corresponds to wetting behavior (and larger nucleation probability).

The diagonal valley due to the misorientation dependence of the grain boundary energy is a feature common to all the maps.

Another common feature of the anisotropic maps in Figure 6.5b-d is that the low-energy bottom grain orientations (in the 4-fold case around $\alpha_1 \approx 45^\circ$, see Figure 6.5b) are associated with larger values of the shape factor, i.e. with a rather de-wetting behavior, where the equilibrium shapes are rather emerged than submerged. As a result, the nucleation probability is lower on the low-energy planes. That is understandable, because such planes are in an energetically convenient configuration and the nucleation event would disturb that. Nevertheless, together with the nuclei instability on high-energy planes, it implies that there is no simple rule to foresee, where the nucleation is most likely.

Apparently, the landscape in the shape factor-orientation map is more hilly with stronger anisotropy. For $\delta = 0.7$ in Figure 6.6d there even are regions $S(\alpha_1, \alpha_2) > 1$.

In Figure 6.6b and c, all points in the map correspond to the basic solution of truncated isolated Wulff shape, but in Figure 6.6d there are also inverted shape and emerged Wulff solutions. This variability in solutions determines the more complex landscape.

These shape factor-orientations maps were used as input to the Monte Carlo simulation of growing polycrystalline film, described in the following section.

6.4 Monte Carlo simulations

The purpose of this section is to qualitatively demonstrate the possible impact of anisotropy in nucleation barrier due to anisotropic solid-liquid interface energy on the texture evolution during film growth and compare it to the case with isotropic solid-liquid interface energy. The shape factor-orientation maps were used together with a Monte Carlo simulation of growing 2D polycrystalline film.

One of the common microstructures observed in films deposited by various deposition techniques features V-shaped grains in columns (seen in the cross-section). That one occurs when the grain boundary has significantly lesser mobility than the advancing surface, and at the same time some grains have a growth advantage in the competition. It can be explained by either anisotropy in interface energy or in the growth rate [52].

There were two main requirements specifying the developed model. Firstly, it was to have the capability to simulate a columnar growth of polycrystalline film in 2D, where the total surface energy is minimized in time by favouring low-energy grains in the competition (i.e. interface-energy minimizing texture). Secondly, it should support inclusion of the nucleation with anisotropic interface energy as introduced in the preceding sections.

The used programme was written in MATLAB and is available in Mendeley Data repository [12].

In the following subsections are subsequently described: the Monte Carlo method itself, the methodology and the results.

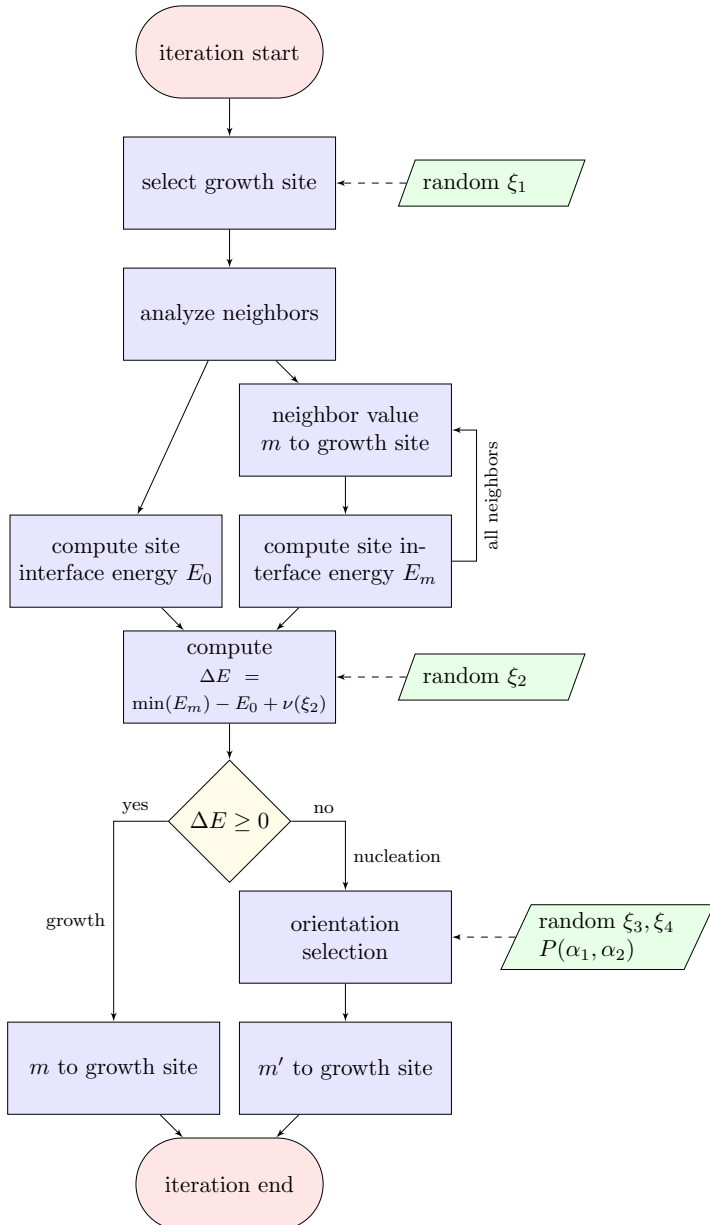


Figure 6.7: Process map of the Monte Carlo simulation with nucleation including anisotropic solid-liquid interface energy. In the model variant with no nucleation, the nucleation branch is omitted. In the model variant with isotropic nucleation, only ξ_3 is sampled and should the nucleation take place, the orientation is selected randomly.

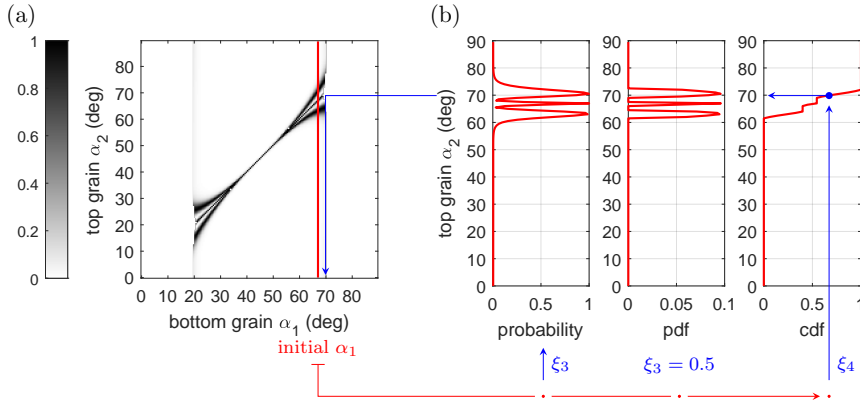


Figure 6.8: Single iteration of orientation selection algorithm. In (a) is the nucleation probability map $P(\alpha_1, \alpha_2) = \exp[-10S(\alpha_1, \alpha_2)]$ for $n = 4$, $\delta = 0.7$. A slice at bottom grain orientation $\alpha_1 = 67^\circ$ was indicated as the initial α_1 . In (b) there is the respective slice of the probability map, from which the probability distribution function (pdf) and then the cumulative distribution function (cdf) of the top grain orientation are computed. The uniformly sampled ξ_3 is used in specification of the pdf (see text), here $\xi_3 = 0.5$ was used. Then, ξ_4 is used for sampling of the cdf to obtain the top grain orientation. The top grain orientation reached in this sampling is $\alpha_2 = 70^\circ$.

6.4.1 Algorithm description

The Monte Carlo model was inspired by [115, 116], but significantly modified.

The simulation was carried out on a fixed square grid, where every node (or pixel, abbreviated px) had a value between 0-50. The value 0 represented the parent solution and 1-50 represented the crystalline solid of different crystallographic orientations from the interval $\langle 0, 2\pi/n \rangle$. Each pixel could interact with its nearest and second nearest neighbors. The growth took place in the bottom-up direction, starting with a solid seed row, where random orientations were assigned to each pixel. In every column, there was one *growth site*, which was a liquid site having a solid neighbor on its bottom side, i.e. the first liquid site just above the deposit.

The simulation proceeded in iterations, one of which is described in a process chart in Figure 6.7. Essentially, a growth site was first selected, its neighborhood analyzed and then it was decided whether either some neighbor value would be inserted to the growth site (the *growth* branch in the scheme) or whether a nucleation attempt would take place (the *nucleation* branch). The latter could

be omitted to produce only anisotropic growth without nucleation.

In the neighborhood analysis, the site interface energy E_0 was first computed for the initial case (when the growth site was occupied by the liquid) as

$$E_0 = \sigma_S(\alpha_1) = \sigma_{SL}^0 h \left(\frac{\pi}{2} - \alpha_1 \right). \quad (6.35)$$

As can be seen, the assumed surface orientation in every growth site was $\theta = \frac{\pi}{2}$ (the growth direction). In this sense, the deposit is assumed to be flat. Secondly, the site interface energies $E_{m''}$ were computed for all the neighbor orientations m'' . In case of multiple different orientations m'' in the neighborhood, there would be multiple $E_{m''}$ site energies computed at this step as

$$E_{m''} = \sum_{i,nn} \sigma_i + w_{snn} \sum_{i,snn} \sigma_i + \sigma_S(\alpha_1). \quad (6.36)$$

The symbol σ_i stands for the interface energy between the individual nearest neighbors (nn) or second nearest neighbors (snn). All the interfacial energies were taken positive. The second nearest neighbors were included with the weight $0 < w_{snn} < 1$ depending on the order of symmetry n . For 4-fold symmetry it was $w_{snn} = 1/4.4 = 0.2273$ (see 6.4.2 for details).

Upon replacement of liquid by solid there occurs an energy change ΔE , which was computed using the lowest site energy of all the available orientations m'' , i.e.

$$\Delta E = \min(E_{m''}) - E_0 + \nu(\xi_2), \quad (6.37)$$

where the noise term $\nu(\xi_2)$ represents local energy fluctuations and is commented in more detail below. As indicated in the scheme, when it was $\Delta E \geq 0$, the growth proceeded with the orientation m'' with the minimal site energy. On the other hand, when it was $\Delta E < 0$, the nucleation trial took place and the orientation was determined using the orientation selection algorithm described below.

In growing bicrystal simulations (without the nucleation) it was validated that such growth algorithm mimics the columnar growth with interface-energy-minimizing textures sufficiently for the purpose of this study. Details about the validation simulations are provided in the 6.4.2.

The noise term $\nu(\xi_2)$ was relevant for the nucleation. Every time the growth site was not near a grain boundary (i.e. there was only single neighbor orientation m''), the only possible interfacial energy change was strictly zero, i.e. $\Delta E = 0$. That was because the interface energy between like orientations was zero, hence in this case $E_{m''} = E_0$. This energy change corresponded to growth (see the scheme in Figure 6.7), hence no nucleation could occur in these sites. Generally speaking, the nucleation is certainly not limited only to the grain boundaries

intersecting the surface. In order to enable nucleation everywhere on the surface, the fluctuations $\nu(\xi_2)$ were added.

In absolute value, they were so small, that they did not affect the result of local energies comparison near the grain boundaries (i.e. in growth sites with multiple orientations m'' in the neighborhood). At the same time, the fluctuations had a finite value attaining the minus sign with a controlled probability (when $\Delta E < 0$, the nucleation trial occurred instead of growth). Specifically, the fluctuations were taken as

$$\nu(\xi_2) = a(\xi_2 - b), \quad (6.38)$$

where $a = 0.001\sigma_0$, $b = 0.25$ and $0 < \xi_2 < 1$ was sampled from the uniform distribution. Effectively, the parameter b controlled the density of nucleation attempts. With this particular parametrization, statistically every fourth growth site not adjacent to the grain boundary attempted to nucleate.

One nucleation attempt within the orientation selection algorithm is illustrated in Figure 6.8a-b. The orientation selection algorithm determined two things: i) whether anything nucleated and ii) with which orientation. Depending on the bottom grain orientation, there is a certain probability distribution for the top grain (nucleus) orientations, which derives from the nucleation probability map (see Figure 6.8a)

$$P(\alpha_1, \alpha_2) = \exp[-\beta S(\alpha_1, \alpha_2)]. \quad (6.39)$$

Should a random number drawn from uniform distribution be lower than the nucleation probability $P(\alpha_1, \alpha_2)$, the event takes place. This is the random number ξ_3 in the scheme in Figures 6.7 and 6.8. But after such sampling there possibly are multiple top grain orientations which could occur, i.e. such orientations α'_2 that $P(\alpha'_2) > \xi_3$ for given α_1 . Hence such probability density function (pdf) is used, which assigns zero nucleation probability to all α_2 orientations except for those α'_2 s. After computation of the corresponding cumulative distribution function (cdf), the top grain orientation can be sampled from the pdf created in the previous step (using random ξ_4 sampled from uniform distribution), as illustrated in Figure 6.8b.

Result of this iteration was either a new grain orientation or unsuccessful nucleation - that happened when the sampled $\xi_3 > P(\alpha_2)$ for all α_2 in the respective slice of the probability map. The growth site then remained liquid. Note though, that this was very unlikely for the demonstrative iteration in Figure 6.8, because it corresponds to high anisotropy and low nucleation barrier, which are strongly nucleation-favoring conditions. In general, however, the nucleation does not occur automatically, as can be seen in Figure 6.10, where the mean number of nucleation events clearly depends on the nucleation barrier β and the strength of anisotropy δ .

6.4.2 Validation of anisotropic growth

Let a planar surface in 3D be intersected by a grain boundary between two crystals with different surface energies. The in-plane capillary force acting on the triple junction line is equal to the difference in the respective surface energies and is independent of the anisotropic torque term [18].

The simulated bicrystal consisted of the maximum- and minimum-energy orientation for a given strength of anisotropy δ . With the anisotropy function (6.4) the maximal surface energy was thus $\sigma_{max} = \sigma_0(1 + \delta)$ and the minimal one $\sigma_{min} = \sigma_0(1 - \delta)$. The magnitude of in-plane force F_x on the junction is then

$$|F_x| = 2\sigma_0\delta. \quad (6.40)$$

The sign of F_x is such to expand the low-energy half-plane on the expense of the high-energy one.

The simulations were carried out for a range of strengths of anisotropy δ . The second-nearest neighbor weight w_{snn} from (6.36) was optimized to observe a linear trend in the slope of the triple point trajectory during the simulation. There were always made 30 runs in a system 100x200 and the mean path was fitted by a straight line. The weight $w_{snn} = 1/4.4$ produced the trajectories as in the Figure 6.9. In the inset of this figure, the slopes were plotted as function of δ and the trend is certainly sufficiently linear for a qualitative study in this paper.

6.4.3 Methodology

In this study, three deposition scenarios were compared:

1. No nucleation (NN) - only anisotropic growth.
2. Isotropic nucleation (IN) - $S(\alpha_1, \alpha_2)$ as in Figure 6.6a.
3. Anisotropic nucleation (AN) - $S(\alpha_1, \alpha_2)$ as obtained by the generalized Winterbottom construction, e.g. like in Figure 6.6b-d. 4-fold symmetry was assumed.

Because in the the anisotropic nucleation, the nucleation probability is a function of the bottom grain orientation, its manifestation depends on the initial texture, i.e. on the seed layer orientation distribution. For this reason, tree different initial conditions were investigated, where the orientations were always drawn from uniform distribution, but from different domains:

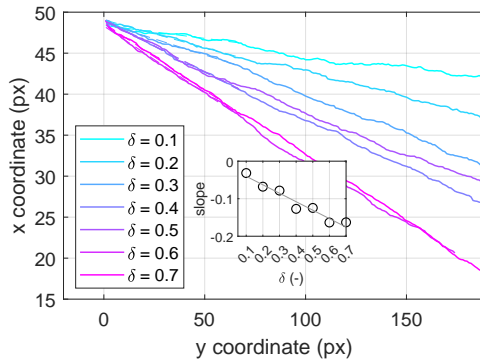


Figure 6.9: Mean trajectory of a triple point on the bicrystal surface during simulated growth for different strengths of anisotropy δ . The mean was taken from 30 runs in a system 100x200 px. The inset shows the slope of the trajectories and demonstrates that the greater was the anisotropy, the greater was he drag.

Table 6.2: Simulation conditions included in this study. Simulations at all combinations of the above parameters were run (except for those in parenthesis, which were combined only with some). In total, there were 116 simulation runs differing in these parameter combinations.

Parameter	Values	Total
nucleation scenario	NN, IN, AN	3
initial condition	IC_A, IC_L, IC_H	3
strength of anisotropy δ	0.1, 0.3, 0.5, 0.7	4
non-dim. nucl. barrier β	10, (30), 50, 90	3 (4)

1. IC_A: sampled from $\langle 0, 1 \rangle \frac{2\pi}{n}$, i.e. all orientations (theoretically, a deposition on amorphous substrate),
2. IC_L: sampled from $\langle 0.2, 0.8 \rangle \frac{2\pi}{n}$, i.e. in 4-fold symmetry centered around low-energy orientations ,
3. IC_H: sampled from $\langle 0, 0.3 \rangle \cup \langle 0.7, 1 \rangle \frac{2\pi}{n}$, i.e. in 4-fold symmetry centered around high-energy orientations.

The individual pixels in the seed layer were sampled independently, i.e. the intended grain size is 1 px. The conditions IC_H and IC_L both sample from the interval of orientations of width $0.6 \frac{2\pi}{n}$, which is wide enough to include at least part of both stable and unstable regions in both the conditions.

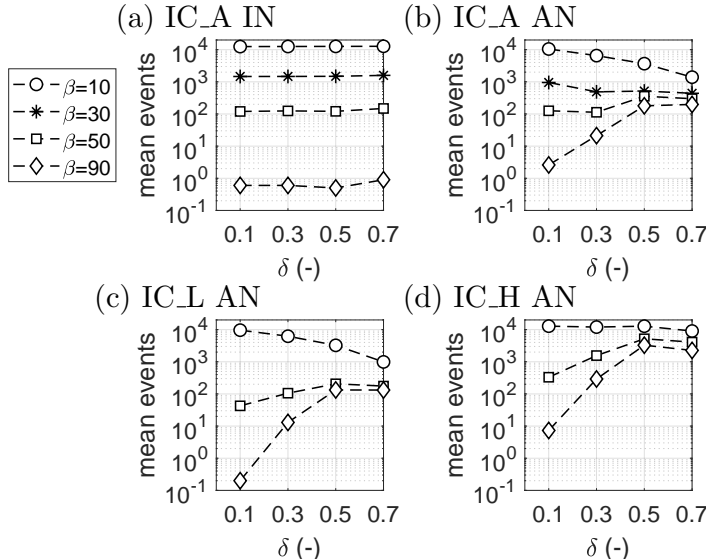


Figure 6.10: Mean number of nucleation events per single simulation run in the system 1500x200 for different initial conditions. The legend is common to all graphs, which all correspond to $n = 4, \delta = 0.5$. IC_A, IC_L and IC_H are the initial conditions (all orientations, low-energy orientations only and high-energy orientations only, respectively). IN and AN stand for the nucleation with isotropic and anisotropic solid-liquid interface energy, respectively.

Additionally, the strength of anisotropy δ and the non-dimensional nucleation barrier β were varied. Specifically, all the different parameter values are summarized in Table 6.2.

A single simulation run took place in a rectangular system on a grid 1500x200. In order to gain better statistics on the through-thickness orientation evolution and the nucleation behavior, 10 repetitions were carried out and the results were either averaged or interpreted from one pseudo system 15000x200.

6.4.4 Results

The presented results are based on analysis of 116 simulation runs, differing in the parameter combinations from Table 6.2.

In Figure 6.10, there is the mean of nucleation events (averaged over ten 1500x200 simulations) as a function of strength of anisotropy δ in series of

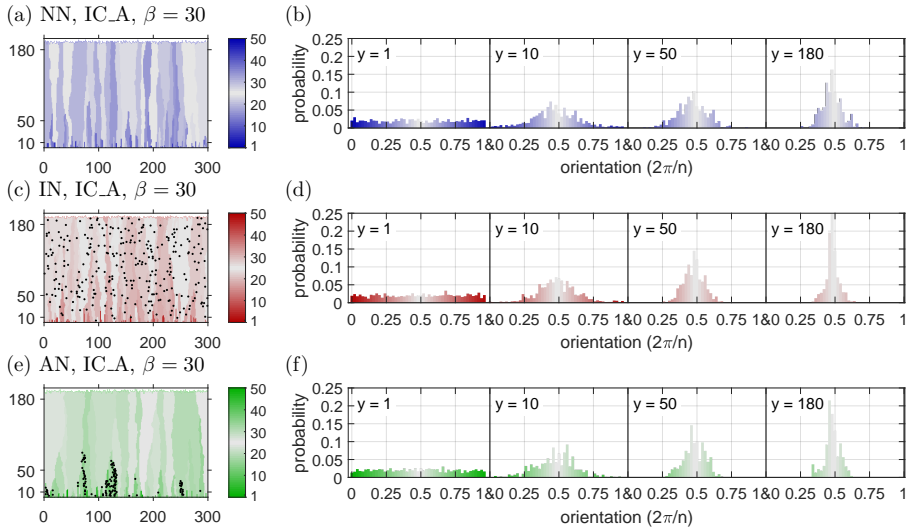


Figure 6.11: Deposits and their texture evolution in different nucleation scenarios and the initial condition IC_A, $\delta = 0.5$, $n = 4$ and $\beta = 30$. In (a), (b) is the no-nucleation scenario, in (c), (d) is isotropic nucleation and in (e), (f) is the anisotropic nucleation. In (a), (c) and (e) are the deposits, with the nucleation events indicated by black dots, and in (b), (d), (f) are the histograms of orientations in the indicated rows of the deposits. Light gray always corresponds to the low-energy orientations in both the deposits and histograms and the high-energy orientations are correspondingly color-coded in both plots of the same scenario.

nucleation barrier β and at different initial conditions. Figure 6.10a shows the result at initial condition IC_A, isotropic nucleation. In isotropic nucleation, the number of nucleation events was only dependent on the nucleation barrier β , not on the strength of anisotropy nor on the initial condition. Figure 6.10b shows the same initial condition (IC_A), but anisotropic nucleation. There, the number of nucleation events depends on both the strength of anisotropy δ and the nucleation barrier β . At small anisotropy, the dependence of mean events on β is similar to the isotropic nucleation. With increasing the strength of anisotropy, there is weaker dependence on β . It was observed, that even at otherwise prohibitively small nucleation barrier $\beta = 90$, hundreds of nucleation events occurred in the 1500×200 system for $\delta \geq 0.5$ and remained rather constant after increase to $\delta = 0.7$. On the other hand, at very low nucleation barrier $\beta = 10$, the mean events were decreasing when δ rose, approaching the same order of magnitude like in large nucleation barriers β . In Figure 6.10c, again the anisotropic nucleation is shown, now in the initial condition IC_L. With the

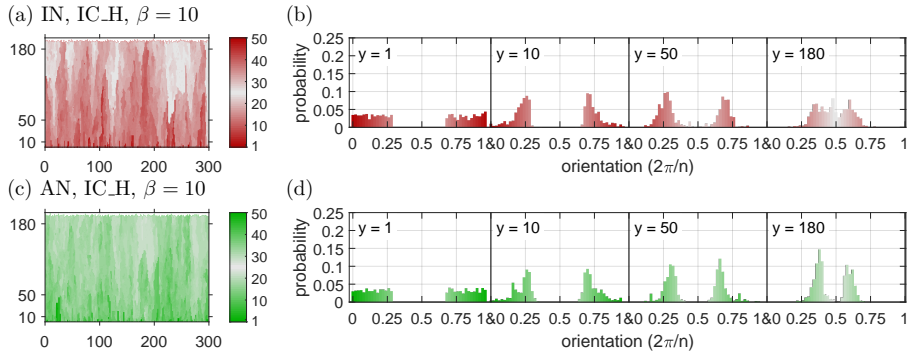


Figure 6.12: Deposits and their texture evolution in different nucleation scenarios and initial condition IC_H, $\delta = 0.5$ and $\beta = 10$. In (a), (b) is the isotropic nucleation scenario, in (c), (d) is anisotropic nucleation. The nucleation events are not shown, because they were too many. See caption of Figure 6.11 and the text for more details.

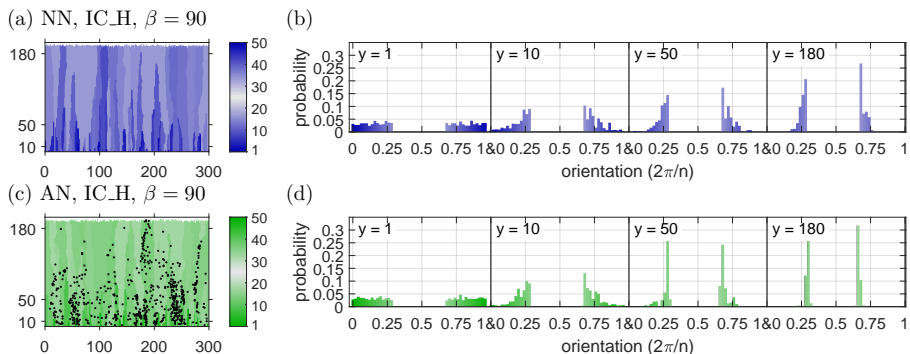


Figure 6.13: Deposits and their texture evolution in different nucleation scenarios and initial condition IC_H, $\delta = 0.5, n = 4$ and $\beta = 90$. In (a), (b) is the no-nucleation scenario, in (c), (d) is anisotropic nucleation. See caption of Figure 6.11 and the text for more details.

seed layer bias towards low-energy orientations, the results are very similar to those in Figure 6.10b, only the numbers are slightly smaller. Larger difference was observed in Figure 6.10d, initial condition IC_H, anisotropic nucleation. With the seed layer centered around high-energy orientations, $10^3 - 10^4$ of events were observed even at very high nucleation barrier $\beta = 90$ for $\delta \geq 0.5$.

Figure 6.11 presents the resulting deposits and their texture evolution in the three deposition scenarios in IC_A at $\delta = 0.5$ and $\beta = 30$. The no-nucleation scenario in Figure 6.11a-b shows the bias towards the low-energy orientations in the middle of the interval $(0, 1)^{\frac{2\pi}{4}}$ with increasing film thickness. this is the desired and a characteristic feature of the model. All three deposition scenarios exhibit the columnar microstructure.

At this nucleation barrier β and initial condition, the mean number of nucleation events was comparable in the isotropic and anisotropic nucleation (see Figures 6.10a-b at $\delta = 0.5$). At first sight, the biggest difference between the isotropic and anisotropic nucleation scenarios is the spatial distribution of the nucleation events. While in the isotropic case (Figure 6.11c) the nucleation was uniform, in the anisotropic one (Figure 6.11e) it is clearly located only at specific grains, which were apparently favourably oriented for nucleation. There, nucleation occurred densely. This is mainly attributed to two factors: i) the stability condition prohibits nucleation on too high-energy-interface grains and ii) nucleation on the lowest-energy planes is the least probable of the allowed ones (and with strong enough anisotropy practically prohibited as well). Eventually, the nucleation took place on the bottom grain orientations near the edges of the stable orientations region, where the shape factor is closer to zero (see the map in Figure 6.6c, where it is also $\delta = 0.5$). The (nucleated) top grain orientation will mostly be close to the bottom grain orientation. The effect of nucleation on texture is such that the low-energy orientation texture is stronger near the film surface. This is probably because nucleation introduces single-pixel orientation inhomogeneities, which are easy for neighboring lower-energy grains to overgrow. The different spatial distribution of events in the isotropic and anisotropic nucleation scenarios affects the texture in the same way - i.e. in this case a mild increase in strength of the low-interface-energy texture.

On the other hand, the textures of scenarios with nucleation were not recognizable from the no-nucleation scenario when the mean number of events per simulation was in the order of magnitude 10^2 and smaller. In the initial condition IC_A, some effect is noticeable with 10^3 events per simulation (as in Figure 6.11) and above. Apparently, the effect of nucleation on texture will be stronger with more events taking place.

An example of deposits and texture evolution at high nucleation rate at $\beta = 10$ in isotropic and anisotropic nucleation scenario is in Figure 6.12 (as before,

$\delta = 0.5, n = 4$). Note that the initial condition is IC_H, where the low-energy orientations are absent. Again, the mean number of nucleation events are comparable in the two scenarios. In the isotropic nucleation scenario (Figure 6.12a-b), some low-energy grains are eventually inserted (with equal probability as any other) and these would overtake given enough film thickness. Below the film surface (row 180, Figure 6.12b), the texture is already centered around the low-energy orientations with rather uniform distribution. On the other hand, in the anisotropic nucleation scenario (Figure 6.12c-d), the nucleation of low-energy grain is apparently much less likely than of other orientations. This delays the introduction of the interface energy minimizing texture, as can be seen in Figure 6.12d, row 180, where the central minimum-energy orientations are still missing.

The anisotropic nature of nucleation thus imposed a different than interface energy minimizing texture, which is a very interesting observation. Note that the probability of minimum-energy grain insertion is non-zero, so in principle the interface-energy-minimizing texture under the surface is the expected terminal state. However, depending on the anisotropy and other conditions it may as well be unlikely within the practical deposition thicknesses.

Figure 6.13 presents the case of very high nucleation barrier $\beta = 90$, again in the initial condition IC_H (and $\delta = 0.5, n = 4$). There occurs nearly no nucleation in the isotropic nucleation scenario (on average less than 1 event per simulation), so it is identical to the no-nucleation scenario (shown in Figure 6.13a-b). As can be seen, the lowest-available-energy grains overtake as before, but there is no mechanism to introduce orientations absent in the seed layer. In the anisotropic nucleation scenario (Figure 6.13c-d), still about 10^3 of nucleation events took place despite the very high nucleation barrier β . That was possible because of she shape factor anisotropy - the local nucleation barrier $S(\alpha_1, \alpha_2)\beta$ was small enough for some orientations. However, the introduction of low-energy orientations did not take place, so the nucleation only supported the grains with initially-present lowest interface energy in the growth competition,

6.4.5 Comparison to experiment and discussion

The presented theory can be used to qualitatively explain some recent experimental results by Alimadadi et al. [9]. They studied the through-thickness texture evolution in Ni electrodeposited on amorphous substrate in four samples, each of which exhibited different dominant fiber texture. The only variables in the deposition were pH and deposition rate, the resulting thickness was different in every sample, but around 20 μm .

The sample deposited at the smallest rate of 0.533 nm/s (i.e. an order of magnitude smaller than the others, the current density being 0.2 A/dm²) exhibited sudden change of texture in the low thickness of 0-4 µm, as can be seen in Figure 6.14. The ⟨100⟩ texture in the nanocrystalline zone A below the 2 µm of thickness is gone in the pole figure of 2-4 µm, where the ⟨110⟩ component starts developing and later strengthens with increasing thickness. Very few grains reaching the surface could be traced back to the nanocrystalline zone A, which means that nucleation had to take place [9]. The nucleation was apparently anisotropic (with a bias towards ⟨110⟩). The combination of nuclei density and their advantage in growth was able to set a completely new course to the texture evolution within a rather thin layer of the deposit.

In the other samples of Alimadadi, the initial texture contained the resulting dominant component, which gradually reinforced with thickness (similarly to how the sample in Figure 6.14 evolved from 2 µm on).

Interestingly, the nucleation in the discussed sample happened at very low growth rate, which in general implies high nucleation barriers. The nucleation barrier for the emerging nuclei had to be very small, though, because the nucleation took place regardless of the small driving force. The possibility of low nucleation barrier even with low driving force (given a convenient bottom grain orientation) was shown to be one of possible manifestations of anisotropic nucleation barrier (see Figure 6.13).

Detailed analysis of the possible competition between the interface-energy-minimization and strain-energy-minimization mechanisms of texture formation in this case is out of the scope of this paper. The sole fact that significant amount of anisotropic, growth-successful nuclei appeared at very low driving force is a peculiarity, which can be qualitatively explained by the presented results, though.

Possibly one mechanism sustained the texture by setting the rules for growth competition up to certain thickness. With the overtake of the other mechanism then, possibly the nuclei would suddenly have more chances in the growth competition. At the same time, the initial favourable-for-nucleation texture would still be in place, before overgrown by the nuclei.

An attempt to estimate the non-dimensional nucleation barrier β in the discussed experiment was made. However, with so small driving force, the effect of the (unknown) scaling interface energy σ_0 on the nucleation barrier is very large. The non-dimensional nucleation barrier β in multiples of kT then varied between 3 and 2950 for σ_0 equal to 0.1 and 1 J/m², respectively. The actual value of σ_0 cannot be reached, but if the nucleation barrier was so small due to the low σ_0 , a very high nucleation rate would be expected during the whole experiment. It

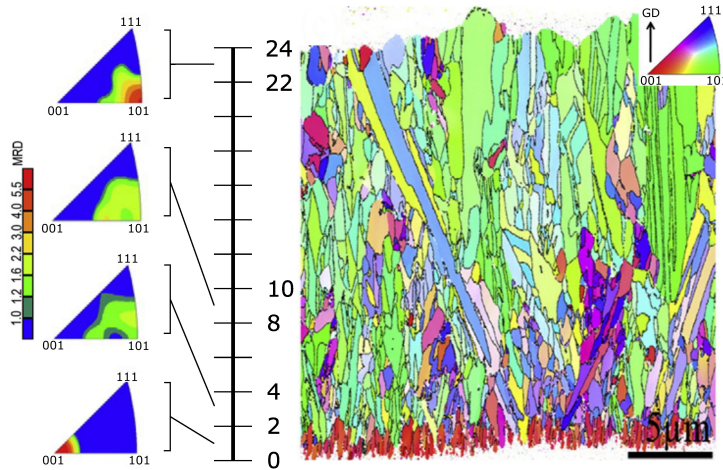


Figure 6.14: Experimental results of Ni electrodeposited on an amorphous substrate, adapted from [9]. On the right, an EBSD map of the deposit cross-section is shown, the inverse pole figure is in the top-right inset. The axis indicates the deposit thickness in μm . The pole figures on the left correspond to the indicated regions, their colorbar of MRD (Multiples of Random Distribution) is provided.

would not explain the observed sudden change in the texture (supposedly due to nucleation) and the long columnar grains seen in this sample (see Figure 6.14) should not occur at all.

Alimadadi et. al [9] did not investigate in depth what mechanisms were responsible for the texture change in this sample. The hereby presented interpretation is extending their discussion and there are no points of disagreement.

Should the anisotropy function produce Wulff shape with facets, there would be no self-intersection of the Wulff plot, because that one is formed essentially by single orientation per facet. However, in such shapes, nearly all orientations are forbidden, i.e. with negative interface stiffness. We remind that not all the forbidden orientations are to fail the stability condition (6.31), but they are the candidates for doing so. The stability condition thus has possibly large implications for anisotropic nucleation in 2D space in general.

6.5 Conclusion

This chapter investigated implications of the anisotropy in interface energy for orientation selection in repeated nucleation during polycrystal deposition.

First, the wetting parameter Γ was expressed as a function of the top and bottom grain orientations in order to enable the generalized Winterbottom construction for each orientation combination. Novel solutions to the stable equilibrium shape were employed in very strong anisotropies. The shape factor-orientation maps were produced and used as input to the columnar growth simulation using the developed Monte Carlo method.

The obtained results essentially indicate that with stronger anisotropy, there is less effect of the non-dimensional homogeneous nucleation barrier on the nucleation rate. In a system with constant scalar interface energy σ_0 and temperature, that means lesser effect of the bulk driving force on nucleation behavior (see (6.20)).

On the other hand, the initial texture becomes significant or even leading factor. Depending on the initial texture, it was shown to be possible to either have no nucleation irrespective of the driving force (should the initial texture contain only forbidden orientations) or to have large nucleation rate even with very small driving forces. The latter option was speculated to be one of mechanisms leading the abrupt change in texture in one of samples in [9], the one shown in Figure 6.14 in this paper.

Three improvements of the generalized Winterbottom construction were worked out: (i) the new solutions of stable equilibrium shapes, originating from multiple self-intersecting Wulff plot occurring at very strong anisotropies, (ii) detailed description of the inverted shape solution in arbitrary orientation and (iii) the contact point stability condition for the nucleus as a function of both the top and bottom grain orientations. The latter is a strong influence on the model behavior. It masked the full orientation-shape factor map only to its part, where the nucleation is less probable, except for some areas near the edge of the stable angles interval. There, on the other hand, the nucleation barrier could be so small, that nucleation would proceed as well at very low driving forces.

The used MATLAB codes are available in a Mendeley Data repository [12].

Chapter 7

General conclusion

7.1 Conclusion

The crystallographic texture of polycrystalline deposits, whether thin or thick, is a critical characteristic, as it significantly influences many other material properties. The deposition process must be optimized for specific applications to ensure that the final product meets the necessary requirements, often by achieving a particular crystallographic texture. It is widely accepted that surface energy and its anisotropy are among the fundamental factors driving texture formation. Additionally, the generation of new grains during repeated nucleation in film deposition can markedly affect the crystallographic texture. Interface energy plays a crucial role in nucleation, and its anisotropy is expected to influence the orientation dependence of the nucleation barrier.

However, the role of interface energy anisotropy in nucleation has not been extensively studied, especially in relation to its impact on the overall evolution of the deposit. This dissertation employed various simulation methodologies to explore this issue and provide new insights.

An approach was identified to bring insight into the role of interface or surface energy anisotropy on the nucleation during polycrystalline film growth: i) develop an analytical model that relates local crystallographic orientations to the corresponding local interface energetics, which ultimately determine the stable equilibrium shape for a given orientation configuration; and ii) create a computational framework that computes the stable equilibrium shape from the input local orientations and determines the shape factor for the corresponding configuration. This computational framework would systematically explore the

orientation space of the substrate and nucleus, determining the shape factor for each configuration. Ultimately, this process yields shape factor-orientation maps, which provide key insights into the anisotropy of the nucleation barrier, as conceptualized in this work.

This dissertation explored two different computational frameworks for determination of the equilibrium shapes: one based on the novel phase-field methodology (Chapter 5) and the other based on the Winterbottom construction (Chapter 6). Although the phase-field methodology was found to be computationally intensive compared to the latter, it provided a solid foundation for substantial methodical development (Chapters 4 and 5).

The main findings from the respective chapters of this thesis are summarized below:

Chapters 2 and 3 provided a comprehensive literature review and discussion of relevant fundamentals.

Chapter 4 described a multi-phase field model that incorporates the inclination dependence of interface energy. The chapter proposed two broadly applicable benchmark problems, which were used in a detailed parameter study to quantify the differences between three different model variants. Although the behavior of the model variants was largely similar, the quantitative benchmark allowed us to identify subtle differences in both the reproduction of the expected shape and the kinetics. The most significant difference between the models was observed in triple junction simulations across a wide range of configurations, revealing that only one model variant accurately reproduced the triple junction angles.

The development of good practices for determining model parameters (see Appendix B), along with the publication of MATLAB tools [11], was a crucial step that allowed the delivery of reproducible results and made the model [7] more accessible to the scientific community. The benchmark problems developed to quantitatively assess the performance of the anisotropic curvature driving force in moving interface simulations can be used for validating any method that involves such physics: phase-field methods, level set methods, or sharp-interface methods. The MATLAB tools used for matching contours to expected shapes were also made available [11]. The governing equations for the multi-phase field model [7] incorporating inclination-dependent interface energy were derived for all three compared model variants: IWc, IWvG, and IWvK (with IWvK and IWvG equations not previously published). The systematic approach in the triple junction benchmark identified that only the IWvG model should be used in practical simulations involving triple junctions, as IWc and IWvK did not correctly reproduce the triple junction angles, especially in strongly anisotropic systems.

Chapter 5 explained the novel phase-field methodology for obtaining the equilibrium stable shape, given the expected contact angles and interface energy anisotropy. The *domain scaling* method was then used to determine the shape factor. This methodology was applied to a case without an analytical solution (nucleus on top of a grain boundary within a substrate).

The phase-field model was enhanced by incorporating volume conservation and a boundary condition that imposed the contact angles of the particle interface on the domain boundary, which functioned as the particle-substrate interface. The method was successfully validated on a problem involving a particle with isotropic interface energy on a plane, where the shape factor was known. It was demonstrated that the nucleus atop a grain boundary within a planar substrate adopts an interface-energy-minimizing shape, which can be well approximated by a fifth-order Bézier polynomial. The probability of nucleating such a shape was shown to strongly depend on the position of the grain boundary beneath the particle. When most of the particle lay on the lower-energy side of the grain boundary, the likelihood of nucleation was not significantly reduced compared to nucleation on the lower-energy side. Due to the observed shape instability, it is suggested that atomistic simulations of nuclei on the substrate grain boundary may be more appropriate.

Chapter 6 implemented the Winterbottom construction to determine shape factors based on local crystallographic orientations and interface energy anisotropy. Shape factor-orientation maps, which describe the anisotropy of the nucleation barrier depending on local crystallographic orientations, were generated and used as input to a custom 2D Monte Carlo algorithm for growing polycrystalline films.

Novel solutions to the generalized Winterbottom construction were developed for cases involving strongly anisotropic interface energy and arbitrary orientations. A method was created to sample nucleus orientation when surface energy anisotropy and bottom grain orientations were known. Monte Carlo simulations indicated that with greater anisotropy strength, nucleation rates are less dependent on the driving force but more dependent on the initial texture. Depending on the seed texture, anisotropic surface energy could either accelerate or delay the evolution towards the interface-energy minimizing texture during nucleation. A qualitative explanation was proposed for an unusual crystallographic texture evolution observed in very slowly electrodeposited nickel, where the course of texture evolution was suddenly altered by nucleation despite the low growth rate.

The main objectives of this thesis were: to develop a phase-field based methodology capable of determining nucleation barrier anisotropy, and to gain insight into the potential role of interface energy anisotropy on repeated

nucleation in growing polycrystals and its impact on crystallographic texture. The key results summarized above from Chapter 5 and Chapter 6 clearly demonstrate that these primary objectives were successfully achieved.

7.2 Outlook

The following potential future research directions are proposed based on the findings of this thesis.

Improvements to the Multi-Phase Field Model: The multi-phase field model used in this work [7, 8] (specifically, the multi-continuum field model) is capable of reproducing the triple junction angles between distinct isotropic interfaces. However, for systems with strong anisotropy, the model suffers from variations in interface width. Developing a method to maintain a constant interface width while preserving thermodynamic consistency would enhance the utility and competitiveness of the model, particularly in comparison with other multi-phase field models [117, 118] that do not encounter this issue in systems with distinct isotropic interfaces.

Benchmark Problem for Triple Junctions with Inclination-Dependent Interface Energies: Another challenge related to multi-phase field models is simulating triple junctions of interfaces with inclination-dependent interface energy. While the most straightforward application of these models is grain growth—which in reality involves strong inclination dependence of grain boundary energy—no reliable phase field simulation of truly anisotropic grain growth has yet been conducted. Problems with ghost phases distorting the triple junction angles, as well as varying interface widths, persist even in simpler pair-distinct isotropic systems. Some models have been more successful than others in mitigating these issues, but the inclination dependence of interface energy at triple junctions adds an additional layer of complexity that requires optimization. The first step in this direction should be the development of a dedicated benchmark problem to quantify the accuracy of current models and identify potential weaknesses in their formulations.

Phase-Field Simulations of Wetting on Curved Surfaces with Control Over Inclination Angle: In this work, the numerical solution to the phase-field governing equations was obtained using the finite difference method, typically applied on rectangular domains. In simulations related to *domain scaling*, the bottom domain boundary represented the particle-substrate interface. By controlling its shape, further insights could be gained into equilibrium shapes on curved surfaces, where the Winterbottom construction cannot be used.

Implementing the finite element method with adaptive meshing could open new avenues for research in this area.

Developing More Sophisticated Models of Particle-Substrate Interactions: In the wetting simulations with controlled interface inclination angle at the domain boundary, an assumption is made regarding how the particle-liquid interface interacts with the substrate, and this determines the inclination angles that should be imposed on the interface in contact with the substrate. In this work, the contact angle was modeled as a step function with two constants along the bottom domain boundary, and the stable equilibrium shape was sought. However, more complex scenarios involving different spatial and/or temporal dependencies of the controlled inclination angle along the domain boundary are possible. These variations of the imposed contact angle may represent local variations of the substrate surface properties (e.g. on a substrate with some periodic pattern or very fine grain structure).

Simulation of Particle Dynamics: The phase-field simulations in this work were limited to static configurations, focusing on equilibrium shapes. Incorporating dynamic phenomena such as fluid flow or additional thermodynamic fields like concentration or temperature could provide further insights into how particles grow and/or interact with their environment over time. This would open up new possibilities for studying time-dependent processes, such as solid-state wetting, reactive liquid wetting or growth in various scenarios like deposition or solidification. It is possible to emulate change of the substrate-particle interactions on the course of simulation by temporal variation of the imposed contact angle of the solid-liquid particle interface at the domain boundary.

Application of Nucleus Orientation Sampling in Other Polycrystalline Growth Simulations: The nucleus orientation sampling algorithm developed here could be applied to more comprehensive models of polycrystalline growth. The algorithm is independent on the simulation method - it samples nucleus orientation based on the substrate orientation and the interface energies and their anisotropy. These simulations have the potential to bring further insights more applied to the specific context (e.g. solidification, chemical vapor deposition, electrodeposition).

Extension of Shape Factor-Orientation Maps: The shape factor-orientation maps developed in this thesis could be expanded to incorporate more complex anisotropy functions, such as three-dimensional anisotropy or variations in other bulk fields (e.g. adsorbent concentration or temperature). These extensions would add more independent variables to the shape factor-orientation maps, hence another dimension. Including such factors would make the processing more challenging but also would allow the maps to offer a more

complete picture of nucleation barrier anisotropy and extend their applicability to a wider range of materials and systems. Another possible extension is to assume that the particle-substrate interface is inclination-dependent and determine the equilibrium shapes using the double Winterbottom construction, which takes anisotropy of this interface into account as well.

Appendix A

Functional derivative

The Allen-Cahn equation describing evolution of a non-conserved field $\xi(\mathbf{r})$ in a domain $\Omega \in \mathbb{R}^3$ with boundary $\partial\Omega$ can be written as

$$\frac{\partial \xi}{\partial t} = -L \frac{\delta F}{\delta \xi} \quad \text{in } \Omega \quad (\text{A.1})$$

$$\nabla \xi \cdot \mathbf{n} = 0 \quad \text{at } \partial\Omega, \quad (\text{A.2})$$

where L is a positive constant and the function $\frac{\delta F}{\delta \xi}$ stands for functional derivative of the free energy functional F . The latter expresses how much the energy changes when the function $\xi(\mathbf{r})$ is infinitesimally varied by addition of some test function multiplied by small number, i.e. multiplied by $\varepsilon g(\mathbf{r})$, where $0 < \varepsilon \ll 1$.

The functional is a map from some function space to real numbers and in our case $F[\xi(\mathbf{r})] = \int f(\mathbf{r}, \xi(\mathbf{r}), \nabla \xi(\mathbf{r})) dV$ with the integrand being energy density. The change in functional value depending on ε is called *functional variation* and is defined $\delta F = F[\xi(\mathbf{r}) + \varepsilon g(\mathbf{r})] - F[\xi(\mathbf{r})]$. The term $F[\xi(\mathbf{r}) + \varepsilon g(\mathbf{r})]$ can be seen as a function of ε and the functional derivative is a *functional* defined as

$$\frac{\delta F}{\delta \xi}[\xi, g] := \left[\frac{d}{d\varepsilon} F[\xi + \varepsilon g] \right]_{\varepsilon=0} = \lim_{\varepsilon \rightarrow 0} \frac{F[\xi(\mathbf{r}) + \varepsilon g(\mathbf{r})] - F[\xi(\mathbf{r})]}{\varepsilon} \quad (\text{A.3})$$

The functional F is *differentiable* when the derivative A.3 exists and can be written in the form of an integral

$$\left[\frac{d}{d\varepsilon} F[\xi + \varepsilon g] \right]_{\varepsilon=0} = \int_{\Omega} \frac{\delta F}{\delta \xi}(\mathbf{r}) g(\mathbf{r}) dV \quad (\text{A.4})$$

the kernel of which $\frac{\delta F}{\delta \xi}(\mathbf{r})$ is the *function* appearing in the Allen-Cahn equation. The expression for $\frac{\delta F}{\delta \xi}(\mathbf{r})$ can be obtained using Taylor expansion of $F[\xi(\mathbf{r}) + \varepsilon g(\mathbf{r})]$ in $\varepsilon = 0$, which will be shown first in the case of an 1D system to illustrate the procedure.

The functional is $F[\xi(x)] = \int_a^b f(x, \xi, \xi') dx$, where the integration limits a, b are constant and $\xi = \xi(x), \xi' = \frac{d\xi}{dx}(x)$. The functional derivative is then

$$\begin{aligned}\frac{\delta F}{\delta \xi}[\xi, g] &= \lim_{\varepsilon \rightarrow 0} \frac{1}{\varepsilon} \int_a^b [f(x, \xi + \varepsilon g, \xi' + \varepsilon g') - f(x, \xi, \xi')] dx = \\ &= \lim_{\varepsilon \rightarrow 0} \frac{1}{\varepsilon} \int_a^b \left[\frac{\partial f}{\partial \xi} \varepsilon g + \frac{\partial f}{\partial \xi'} \varepsilon g' + \mathcal{O}(\varepsilon^2) \right] dx = \\ &= \int_a^b \left(\frac{\partial f}{\partial \xi} g + \frac{\partial f}{\partial \xi'} g' \right) dx = \\ &= \int_a^b \left(\frac{\partial f}{\partial \xi} - \frac{\partial}{\partial x} \frac{\partial f}{\partial \xi'} \right) g dx + \left[\frac{\partial f}{\partial \xi'} g \right]_a^b\end{aligned}\tag{A.5}$$

In the last equation sign per partes technique was used.

So far there was no assumption on test function $g(x)$, but in the simplest case the end points of ξ are fixed, i.e. $g(a) = g(b) = 0$, which removes the second term and allows to write

$$\frac{\delta F}{\delta \xi}(x) = \frac{\partial f}{\partial \xi} - \frac{\partial}{\partial x} \frac{\partial f}{\partial \xi'}.\tag{A.6}$$

If the left-hand side is replaced by zero, we obtain *Euler-Lagrange* equation, solution to which minimizes the functional F .

Now, in the case of functional in 3D space $F[\xi(\mathbf{r})] = \int_{\Omega} f(\mathbf{r}, \xi(\mathbf{r}), \nabla \xi(\mathbf{r})) d^3 r$ we must realize that dependence of the integrand on a vector variable means dependence on its components, i.e. $f(\mathbf{r}, \xi(\mathbf{r}), \nabla \xi(\mathbf{r})) = f(x_1, x_2, x_3, \xi, \partial_1 \xi, \partial_2 \xi, \partial_3 \xi)$, where $\partial_i = \frac{\partial}{\partial x_i}$. The functional derivative is then derived in a way analogous to the previous case, but now there is one term in the Taylor expansion per each gradient component. Before the derivation we define the following vector field

$$\begin{aligned}\frac{\partial f}{\partial(\nabla \xi)} &= \frac{\partial f}{\partial(\partial_1 \xi)} \mathbf{i} + \frac{\partial f}{\partial(\partial_2 \xi)} \mathbf{j} + \frac{\partial f}{\partial(\partial_3 \xi)} \mathbf{k} = \\ &= \frac{\partial f}{\partial(\frac{\partial \xi_p}{\partial x})} \mathbf{i} + \frac{\partial f}{\partial(\frac{\partial \xi_p}{\partial y})} \mathbf{j} + \frac{\partial f}{\partial(\frac{\partial \xi_p}{\partial z})} \mathbf{k}\end{aligned}\tag{A.7}$$

And we proceed to the functional derivative

$$\begin{aligned}
 \frac{\delta F}{\delta \xi}[\xi, g] &= \lim_{\varepsilon \rightarrow 0} \frac{1}{\varepsilon} \int_{\Omega} [f(x_i, \xi + \varepsilon g, \partial_i(\xi + \varepsilon g)) - f(x_i, \xi, \partial_i \xi)] d^3 r = \\
 &= \lim_{\varepsilon \rightarrow 0} \frac{1}{\varepsilon} \int_{\Omega} \left[\frac{\partial f}{\partial \xi} \varepsilon g + \sum_{i=1}^3 \frac{\partial f}{\partial (\partial_i \xi)} \varepsilon \partial_i g + \mathcal{O}(\varepsilon^2) \right] d^3 r = \\
 &= \int_{\Omega} \left[\frac{\partial f}{\partial \xi} g + \frac{\partial f}{\partial (\nabla \xi)} \cdot \nabla g \right] d^3 r \\
 &= \int_{\Omega} \left[\frac{\partial f}{\partial \xi} - \nabla \cdot \frac{\partial f}{\partial (\nabla \xi)} \right] g d^3 r + \int_{\partial \Omega} g \frac{\partial f}{\partial (\nabla \xi)} \cdot \mathbf{n} d\mathbf{n}
 \end{aligned} \tag{A.8}$$

In the last equation there was used Stokes' theorem¹ in combination with the rule for divergence of product of vector and scalar field². Hence, in order to null the surface integral in equation A.8, either the boundary values must be fixed (Dirichlet BCs) or the following boundary condition (so called *natural BC*) must be satisfied

$$\frac{\partial f}{\partial (\nabla \xi_p)} \cdot \mathbf{n} = 0. \tag{A.9}$$

Different choice of the boundary conditions will interfere with minimization of the functional. The safest option is when the interface does not come near the boundary.

¹with scalar field $f(\mathbf{r})$ and vector field $\mathbf{F}(\mathbf{r})$ the Stokes theorem gives: $\int_{\Omega} \nabla \cdot (\mathbf{F}f) = \int_{\partial \Omega} f \mathbf{F} \cdot d\mathbf{n}$, where \mathbf{n} is a vector normal to the domain boundary
² $\nabla \cdot (\mathbf{F}f) = (\nabla \cdot \mathbf{F})f + \mathbf{F} \cdot (\nabla f)$

Appendix B

Model parameters determination - best practices

The multi-phase field model by Moelans [7] is sensitive to how exactly the values of the parameters m, κ, γ are assigned in systems with anisotropic interface energy. In the model variants with variable interface width (IWvG and IWvK), it is important to assure that no interface becomes too narrow, so that grid pinning is prevented. Otherwise, the kinetics is no longer accurately reproduced by the implementation. The best practices in parameters determination described in this section were implemented in MATLAB functions, which were published in dataset [11], distributed under GPLv3 license.

Polynomial expressions for determination of γ

Interface energy and width are non-analytic functions of the parameter γ (equations (4.6) and (4.7) in the main text). In models IWc and IWvG with non-uniform interface energy, γ varies in space and depends on physical input (local interface energy σ) and chosen interface width. Assuming that κ, m and σ are known, $g(\gamma)$ is computed using equation (4.6) and must be inverted in order to obtain γ . For numeric convenience, functions $g^2 \rightarrow 1/\gamma$ and $1/\gamma \rightarrow f_{0,c}$ were fitted by polynomials using the tabulated values from [95]. The same approach was taken in [7]. Note that in one of the following subsections an alternative algorithm for determination of parameters in IWc is proposed.

The values of $f_{0,c}(\gamma), g(\gamma)$ were tabulated and published in [95] in the range

$0.52 \leq \gamma \leq 40$. However, the polynomials used in both [7, 95] did not describe the functions along the whole tabulated range. For inconvenient input, that resulted in a loss of control over the interface properties (even negative values of γ were obtained).

To improve the parameters determination, the functions $g^2 \rightarrow 1/\gamma$ and $1/\gamma \rightarrow f_{0,c}$ were fitted again so that all γ values from the interval $0.52 \leq \gamma \leq 40$ were reliably available. The new polynomials show good agreement along the given interval and their coefficients are listed in Table B.1.

IWvG model

This parameters determination algorithm [95] requires input of initializing interface energy σ_{init} , and width l_{init} which are assigned to interface with value $\gamma = 1.5$. There, the analytic relations between the model parameters are valid and the (constant) parameters κ, m can be computed:

$$\kappa = \frac{3}{4} \sigma_{init} l_{init} , \quad m = 6 \frac{\sigma_{init}}{l_{init}} . \quad (\text{B.1})$$

These are then used in equation (4.6) with individual interface energies $\sigma_{i,j}$ to determine $g^2(\gamma_{i,j})$ and further $\gamma_{i,j}$ (using the first polynomial from Table B.1). However, because the said polynomial was only fitted in the interval $0.52 \leq \gamma \leq 40$ (values tabulated in [95]), it is important to choose the value of σ_{init} such, that none of the interface energies $\sigma_{i,j}$ should be described by $\gamma_{i,j}$ out of the interval. From equation (4.6) with substituted $\sqrt{\kappa m}$ from B.1 we show that the values do not leave the above interval when σ_{init} complies with the following two inequalities

$$\frac{\sigma_{max}}{g(40)} \sqrt{\frac{2}{9}} \leq \sigma_{init} \leq \frac{\sigma_{min}}{g(0.52)} \sqrt{\frac{2}{9}} , \quad (\text{B.2})$$

where $\sigma_{min}, \sigma_{max}$ are minimal and maximal interface energy present in the system. Additionally, in order to fulfill these conditions, it must be satisfied that

$$\frac{\sigma_{min}}{\sigma_{max}} \geq \frac{g(0.52)}{g(40)} = \frac{0.1}{0.76} = 0.129 , \quad (\text{B.3})$$

which sets the maximal anisotropy in interface energy for which all $\gamma_{i,j}$ s may be determined in IWvG based on the values tabulated in [95].

Control over the width of the narrowest interface (with user-defined width l_{min}) is obtained when the parameters are determined in two steps as follows:

1. values of κ, m are calculated from equations (B.1) using appropriate σ_{init} together with l_{min}

Table B.1: Coefficients of the new polynomials used in the parameters determination algorithm (IW_c and IW_{vG} models). Based on fitting of the numeric values given in [95]. The polynomial of order N $p_N(x)$ is defined here together with its coefficients as $p_N(x) = \sum_{i=0}^N a_i x^{N-i}$. See text for details of use in the respective models.

order	a_0	a_1	a_2	a_3	a_4	a_5	a_6
$g^2 \rightarrow \frac{1}{\gamma}$	6	-5.73008	18.8615	-23.0557	7.47952	8.33568	-8.01224
$\frac{1}{\gamma} \rightarrow \sqrt{f_{0,c}}$	5	-0.072966	0.35784	-0.68325	0.63578	-0.48566	0.53703
$g\sqrt{f_{0,c}} \rightarrow \frac{1}{\gamma}$	6	103.397	-165.393	105.3469	-44.55661	24.7348	-11.25718

2. values of κ, m are recalculated from equations (B.1) with the same σ_{init} and interface width $l_{calib} = l_{min} \sqrt{8f_{0,c}(\gamma_{min})}$, where γ_{min} corresponds to the lowest value of all the $\gamma_{i,j}$ obtained in the previous step, i.e. to the interface with the largest interface energy σ_{max} .

After the second step, the interface with maximal interface energy will have the width l_{min} and all the other interfaces will have it equal or larger.

The other interface widths can be expressed

$$l_{i,j} = \frac{\sigma_{i,j}}{m} \frac{1}{g(\gamma_{i,j}) \sqrt{f_{0,c}(\gamma_{i,j})}} \quad (\text{B.4})$$

IWc model

The iterative parameters determining procedure assuring the constant interface width is described in [7]. The procedure requires initializing value of interface energy σ_{init} , which has decisive role for the parameters values. For inconvenient choice of σ_{init} , some of the parameters $\gamma_{i,j}$ may get out of range of applicability of the polynomials in Table B.1. Systematic investigation revealed that the value $\sigma_{init} = (\sigma_{max} + \sigma_{min})/2$ prevents occurrence of such effects for anisotropies $\sigma_{min}/\sigma_{max} \geq 0.03$.

Here we propose a simplified, yet equivalent single-step procedure. We assume constant interface width l and an initializing interface energy σ_{init} , for which $\gamma = 1.5$ and thus the analytic relations between the model parameters hold. As in the original iterative algorithm, the barrier height is computed

$$m = 6 \frac{\sigma_{init}}{l}. \quad (\text{B.5})$$

Then, the gradient energy coefficient $\kappa_{i,j}$ can be expressed from both equations (4.7) and (4.8), hence we can write

$$\kappa_{i,j} = f_{0,c}(\gamma_{i,j}) ml^2 = \sigma_{i,j} l \frac{\sqrt{f_{0,c}(\gamma_{i,j})}}{g(\gamma_{i,j})}, \quad (\text{B.6})$$

from where we obtain

$$g(\gamma_{i,j}) \sqrt{f_{0,c}(\gamma_{i,j})} = \frac{\sigma_{i,j}}{ml} = \frac{\sigma_{i,j}}{6\sigma_{init}}. \quad (\text{B.7})$$

In the last equation, m was substituted from (B.5). We denote $G(\gamma_{i,j}) = g(\gamma_{i,j}) \sqrt{f_{0,c}(\gamma_{i,j})}$. This function $\gamma \rightarrow G$ can be evaluated from the data tabulated in [95] and its inverse function $G \rightarrow \frac{1}{\gamma}$ was fitted by 6-th order

polynomial producing the coefficients in the last row of Table B.1. Apparently, evaluation of this polynomial in points $\sigma_{i,j}/6\sigma_{init}$ produces the searched $1/\gamma_{i,j}$. The gradient energy coefficients are then best computed as in B.6, where m was substituted from B.5:

$$\kappa_{i,j} = 6f_{0,c}(\gamma_{i,j})\sigma_{init}l. \quad (\text{B.8})$$

Here, the fitted polynomial $\frac{1}{\gamma} \rightarrow \sqrt{f_{0,c}}$ is used to obtain the values of $f_{0,c}(\gamma_{i,j})$.

Similarly like in IWcG model, there are conditions limiting suitable values of σ_{init}

$$\frac{\sigma_{max}}{6G(40)} \leq \sigma_{init} \leq \frac{\sigma_{min}}{6G(0.52)}, \quad (\text{B.9})$$

where $G(0.52) \approx 0.0069$, $G(40) \approx 0.4065$. Also must be satisfied

$$\frac{\sigma_{min}}{\sigma_{max}} \geq \frac{G(0.52)}{G(40)} = 0.017. \quad (\text{B.10})$$

The main advantage of the proposed algorithm is that no iterations are needed for parameters determination. In the original algorithm the number of iteration steps is uncertain (tens of repetitions are not exceptional though) and sometimes the results may not converge due to reasons tedious to debug. Obtaining each parameter in a single step thus provides better control over the process and simplifies the implementation. Moreover, the permissible values of σ_{init} and the maximal anisotropy $\sigma_{min}/\sigma_{max}$ are clearly defined.

Also, it should be noted that when σ_{init} is chosen close to the upper limit in the inequality B.9, the determined $\gamma_{i,j}$ s are rather closer to value 0.52 (corresponding to long-tailed interfaces). When σ_{init} is near the bottom limit, the values of γ_{max} are close to the value 40 and γ_{min} are much larger than in the previous case. Near the limiting anisotropy $\sigma_{min}/\sigma_{max} \approx 0.017$, the values always are $\gamma_{max} \approx 40$ and $\gamma_{min} \approx 0.52$. It is especially near the limits of admissible σ_{init} , where the original iterative parameters assignment strategy is not always reliable when compared to the proposed one.

IWvK model

When $\gamma = const = 1.5$, the analytic relations between the model parameters hold (i.e. equations (4.8)-(4.10)). Then, the minimal interface width l_{min} is controlled when

$$m = 6 \frac{\sigma_{min}}{l_{min}} \quad (\text{B.11})$$

and

$$\kappa_{i,j} = \frac{9}{2} \frac{\sigma_{i,j}^2}{m}. \quad (\text{B.12})$$

Interface width of an interface $i-j$ can then be computed as

$$l_{i,j} = 6 \frac{\sigma_{i,j}}{m}. \quad (\text{B.13})$$

Appendix C

Implementation of finite difference method

General information

The 2D system was discretized into a rectangular equidistant grid and rearranged into a single column vector as indicated in figure C.1. The differential operators were represented by finite-difference matrices left-multiplying the column vectors standing for field variables present on the grid. The finite-difference matrices are block matrices, where each block is a square matrix acting on a single column in the rearranged system.

Let the system be a matrix with n rows and m columns. All blocks are matrices with dimensions $n \times n$ and they are ordered in $m \times m$ grid giving rise to an $mn \times mn$ sparse finite-difference matrix .

The finite-difference matrix can perform linear combination of arbitrary points in the system in each grid point. It takes various form depending on the boundary conditions. However, it is always a toeplitz block matrix.

Second-order accurate centered finite-difference scheme in space and first-order in time (i.e. the Euler method) were used.

In the following sections, the symbol \mathbb{O} stands for $n \times n$ block matrix of zeros and \mathbb{I} for $n \times n$ identity matrix (i.e. matrix with ones in the diagonal and zeros otherwise). The finite difference method is abbreviated as FD in the following. In the finite-difference matrices below, some elements may be highlighted in red. These are the elements, which are involved in the boundary conditions.

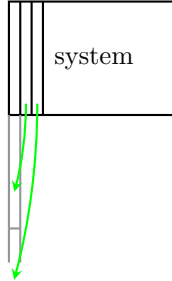


Figure C.1: Rearrangement of the matrix representing the system before application of the discrete differential operators.

Ghost nodes in Neumann boundary condition

Zero Neumann BCs

Neumann boundary conditions were implemented using ghost nodes. Ghost nodes are hypothetical nodes adjacent to the boundary nodes, in which the values can be specified using the given boundary condition. In order to have the derivatives in the boundary nodes second-order-accurate, centered difference can be used using the known values at ghost nodes. In the case $\nabla\eta \cdot \mathbf{n} = 0$ we can write at the left boundary edge (i.e. $x = 0$), where $(i, j) = (0, j)$

$$\begin{aligned}\frac{\partial\eta}{\partial x} = 0 \quad \text{at } x = 0 \quad \Rightarrow \quad \forall j \in m + 1 \quad (\Delta_x\eta)_{0j} = \frac{\eta_{1j} - \eta_{-1j}}{h} = 0 \quad \Rightarrow \quad \eta_{1j} = \eta_{-1j} \\ \frac{\partial\eta}{\partial y} = 0 \quad \text{at } x = 0 \quad \Rightarrow \quad \forall i \in n + 1 \quad (\Delta_y\eta)_{0j} = \frac{\eta_{ij+1} - \eta_{ij-1}}{h}\end{aligned}\tag{C.1}$$

The first equation provides the value at the ghost node. In order to have the centered difference in the respective direction zero at the boundary, apparently the value must be equal to the value in the neighbour on the opposite side.

General Neumann BCs

The boundary condition defining the inclination angle θ at the boundary is $\nabla\eta \cdot \mathbf{n} = |\nabla\eta| \cos(\theta)$. This expression implies at the left boundary $(i, j) = (0, j)$ that $\frac{\partial\eta}{\partial x} = |\nabla\eta| \cos(\theta)$ and $\frac{\partial\eta}{\partial y} = |\nabla\eta| \sin(\theta)$. By replacing the partial derivatives $\frac{\partial}{\partial x}, \frac{\partial}{\partial y}$ with finite differences Δ_x, Δ_y the values in ghost node $(-1, j)$ can be

expressed as

$$\forall j \in m+1 \quad (\Delta_x \eta)_{0j} = \frac{\eta_{1j} - \eta_{-1j}}{2h} = |\nabla \eta|_{0,j} \cos(\theta) \quad (C.2)$$

$$\implies \eta_{-1j} = \eta_{1j} - 2h|\nabla \eta|_{0,j} \cos(\theta). \quad (C.3)$$

At the right boundary $(i, j) = (n, j)$ the ghost nodes $(n+1, j)$ are

$$\forall j \in m+1 \quad (\Delta_x \eta)_{nj} = \frac{\eta_{n+1j} - \eta_{n-1j}}{2h} = |\nabla \eta|_{nj} \cos(\theta) \quad (C.4)$$

$$\implies \eta_{n+1j} = \eta_{n-1j} + 2h|\nabla \eta|_{nj} \cos(\theta). \quad (C.5)$$

And at the bottom and top, respectively, using the same principles we obtain

$$\forall i \in n+1 \quad \eta_{i,-1} = \eta_{i,1} - 2h|\nabla \eta|_{i,0} \cos(\theta) \quad (C.6)$$

$$\forall i \in n+1 \quad \eta_{i,m+1} = \eta_{i,m-1} + 2h|\nabla \eta|_{i,m} \cos(\theta). \quad (C.7)$$

Important observation is that the general Neumann BC indeed reduces to the zero condition for $\theta = 90^\circ$ and that the values at the ghost nodes are always derived from the neighbour on the opposite side.

First-order derivatives in FD

The centered finite difference was used with stencil $\boxed{-1 \ 0 \ 1}$ for x-direction

derivative and $\boxed{\begin{array}{c} 1 \\ 0 \\ -1 \end{array}}$ for y-direction derivative.

Periodic boundary conditions

For the y-direction derivative the FD matrix is

$$\frac{\partial}{\partial y} \approx \Delta_y = \frac{1}{2h} \begin{pmatrix} Y & O & O & \dots & O & O \\ O & Y & O & \dots & O & O \\ O & O & Y & \dots & O & O \\ \vdots & \vdots & \vdots & \ddots & \vdots & \vdots \\ O & O & O & \dots & Y & O \\ O & O & O & \dots & O & Y \end{pmatrix} \quad (C.8)$$

with

$$\mathbb{Y} = \begin{pmatrix} 0 & 1 & 0 & 0 & \dots & 0 & 0 & -1 \\ -1 & 0 & 1 & 0 & \dots & 0 & 0 & 0 \\ 0 & -1 & 0 & 1 & \dots & 0 & 0 & 0 \\ \vdots & \vdots & \vdots & \ddots & \vdots & \vdots & \vdots & \vdots \\ 0 & 0 & 0 & 0 & \dots & -1 & 0 & 1 \\ 1 & 0 & 0 & 0 & \dots & 0 & -1 & 0 \end{pmatrix} \quad (\text{C.9})$$

In the x-direction, the finite difference matrix is

$$\frac{\partial}{\partial x} \approx \Delta_x = \frac{1}{2h} \begin{pmatrix} \mathbb{O} & \mathbb{I} & \mathbb{O} & \mathbb{O} & \dots & \mathbb{O} & \mathbb{O} & -\mathbb{I} \\ -\mathbb{I} & \mathbb{O} & \mathbb{I} & \mathbb{O} & \dots & \mathbb{O} & \mathbb{O} & \mathbb{O} \\ \mathbb{O} & -\mathbb{I} & \mathbb{O} & \mathbb{I} & \dots & \mathbb{O} & \mathbb{O} & \mathbb{O} \\ \vdots & \vdots & \vdots & \ddots & \vdots & \vdots & \vdots & \vdots \\ \mathbb{O} & \mathbb{O} & \mathbb{O} & \mathbb{O} & \dots & -\mathbb{I} & \mathbb{O} & \mathbb{I} \\ \mathbb{I} & \mathbb{O} & \mathbb{O} & \mathbb{O} & \dots & \mathbb{O} & -\mathbb{I} & \mathbb{O} \end{pmatrix}. \quad (\text{C.10})$$

Neumann boundary conditions

The FD matrices are equal in both cases of the zero and general NBC, but in the case of the gernerl NBC the following vector must be added at the left and right boundary $|\nabla \eta| \begin{bmatrix} \cos(\theta) \\ \sin(\theta) \end{bmatrix}$ and the following one at the bottom and top boundary $|\nabla \eta| \begin{bmatrix} -\sin(\theta) \\ \cos(\theta) \end{bmatrix}$.

For the y-direction the FD matrix is the same as for the periodic boundary conditions in the block structure (equation C.32), and the block matrix \mathbb{Y} is only modified in its first and last row as

$$\mathbb{Y} = \begin{pmatrix} 0 & 0 & 0 & 0 & \dots & 0 & 0 & 0 \\ -1 & 0 & 1 & 0 & \dots & 0 & 0 & 0 \\ 0 & -1 & 0 & 1 & \dots & 0 & 0 & 0 \\ \vdots & \vdots & \vdots & \ddots & \vdots & \vdots & \vdots & \vdots \\ 0 & 0 & 0 & 0 & \dots & -1 & 0 & 1 \\ 0 & 0 & 0 & 0 & \dots & 0 & 0 & 0 \end{pmatrix} \quad (\text{C.11})$$

For the x-direction with Neumann boundary conditions

$$\frac{\partial}{\partial x} \approx \Delta_x = \frac{1}{2h} \begin{pmatrix} 0 & 0 & 0 & 0 & \dots & 0 & 0 & 0 \\ -I & 0 & I & 0 & \dots & 0 & 0 & 0 \\ 0 & -I & 0 & I & \dots & 0 & 0 & 0 \\ \vdots & \vdots & \vdots & \ddots & \vdots & \vdots & \vdots & \vdots \\ 0 & 0 & 0 & 0 & \dots & -I & 0 & I \\ 0 & 0 & 0 & 0 & \dots & 0 & 0 & 0 \end{pmatrix} \quad (C.12)$$

Mixed boundary conditions

In 2D system there are only two options when combining periodic and Neumann BCs: the periodic boundary is either parallel to x or y axis. The periodic boundary must always lay opposite to another periodic boundary. In a system with mixed boundaries the finite difference matrices in the x and y direction are combined from the above options so that the BCs are met at the corresponding boundary.

Laplacian in 2D

5-point stencil $\begin{array}{c|cc|c} 0 & 1 & 0 \\ \hline 1 & -4 & 1 \\ 0 & 1 & 0 \end{array}$ approximates 2D laplacian $\nabla^2 u = u_{xx} + u_{yy}$ on an bi-equidistant grid with spacing h in a grid point (i, j) as

$$(\nabla^2 u)_{ij}^{5p} = u_{ij,xx} + u_{ij,yy} = \frac{1}{h^2}(-4u_{ij} + u_{i-1j} + u_{i+1j} + u_{ij-1} + u_{ij+1}) + \mathcal{O}(h^4) \quad (C.13)$$

9-point stencil (denoted 9p8) $\begin{array}{c|cc|c} 1 & 1 & 1 \\ \hline 1 & -8 & 1 \\ 1 & 1 & 1 \end{array}$ is expressed in a grid point (i, j) as

$$\begin{aligned} (\nabla^2 u)_{ij}^{9p8} = \frac{1}{3h^2} & (-8u_{ij} + u_{i-1j} + u_{i+1j} + u_{ij-1} + u_{ij+1} + \\ & + u_{i+1j+1} + u_{i-1j-1} + u_{i-1j+1} + u_{i+1j-1}) + \mathcal{O}(h^4) \end{aligned} \quad (C.14)$$

9-point stencil (denoted 9p20) $\begin{array}{c|cc|c} 1 & 4 & 1 \\ \hline 4 & -20 & 4 \\ 1 & 4 & 1 \end{array}$ is expressed in a grid point (i, j) as

$$\begin{aligned} (\nabla^2 u)_{ij}^{9p20} = \frac{1}{6h^2} & [-20u_{ij} + 4(u_{i-1j} + u_{i+1j} + u_{ij-1} + u_{ij+1}) + \\ & + u_{i+1j+1} + u_{i-1j-1} + u_{i-1j+1} + u_{i+1j-1}] + \mathcal{O}(h^4) \end{aligned} \quad (\text{C.15})$$

The above formulas are derived from Taylor expansions of the values of function u at the points adjacent to (i, j) assuming the small displacement h in both x and y direction.

The above formulas are represented by matrix, which carries the weighted summation of the function values for each point similarly to the first-order derivatives. Below, the matrices are shown in detail depending on the BCs.

Periodic boundary conditions

For 5p stencil the blocks are unit matrix \mathbb{I} , zero matrix \mathbb{O} and the following matrix \mathbb{D}_P^{5p} (the red elements are the top-bottom periodic condition)

$$\mathbb{D}_P^{5p} = \begin{pmatrix} -4 & 1 & 0 & 0 & \dots & 0 & 0 & \textcolor{red}{1} \\ 1 & -4 & 1 & 0 & \dots & 0 & 0 & 0 \\ 0 & 1 & -4 & 1 & \dots & 0 & 0 & 0 \\ \vdots & \vdots & \vdots & \vdots & \ddots & \vdots & \vdots & \vdots \\ 0 & 0 & 0 & 0 & \dots & 1 & -4 & 1 \\ \textcolor{red}{1} & 0 & 0 & 0 & \dots & 0 & 1 & -4 \end{pmatrix}. \quad (\text{C.16})$$

and the finite-difference matrix \mathbb{L}_P^{5p} is ordered as follows (red elements are the left-right periodic boundary condition)

$$\mathbb{L}_P^{5p} = \frac{1}{h^2} \begin{pmatrix} \mathbb{D}_P^{5p} & \mathbb{I} & \mathbb{O} & \mathbb{O} & \dots & \mathbb{O} & \mathbb{O} & \textcolor{red}{\mathbb{I}} \\ \mathbb{I} & \mathbb{D}_P^{5p} & \mathbb{I} & \mathbb{O} & \dots & \mathbb{O} & \mathbb{O} & \mathbb{O} \\ \mathbb{O} & \mathbb{I} & \mathbb{D}_P^{5p} & \mathbb{I} & \dots & \mathbb{O} & \mathbb{O} & \mathbb{O} \\ \vdots & \vdots & \vdots & \vdots & \ddots & \vdots & \vdots & \vdots \\ \mathbb{O} & \mathbb{O} & \mathbb{O} & \mathbb{O} & \dots & \mathbb{I} & \mathbb{D}_P^{5p} & \mathbb{I} \\ \textcolor{red}{\mathbb{I}} & \mathbb{O} & \mathbb{O} & \mathbb{O} & \dots & \mathbb{O} & \mathbb{I} & \mathbb{D}_P^{5p} \end{pmatrix} \quad (\text{C.17})$$

For 9p20 stencil the blocks are a Toeplitz matrix \mathbb{D}_P^{9p20} , a Toeplitz matrix \mathbb{A} and a zero matrix \mathbb{O} . These are defined

$$\mathbb{D}_P^{9p20} = \begin{pmatrix} -20 & 4 & 0 & 0 & \dots & 0 & 0 & \textcolor{red}{4} \\ 4 & -20 & 4 & 0 & \dots & 0 & 0 & 0 \\ 0 & 4 & -20 & 4 & \dots & 0 & 0 & 0 \\ \vdots & \vdots & \vdots & \vdots & \ddots & \vdots & \vdots & \vdots \\ 0 & 0 & 0 & 0 & \dots & 4 & -20 & 4 \\ \textcolor{red}{4} & 0 & 0 & 0 & \dots & 0 & 4 & -20 \end{pmatrix} \quad (\text{C.18})$$

$$\mathbb{A} = \begin{pmatrix} 4 & 1 & 0 & 0 & \dots & 0 & 0 & \textcolor{red}{1} \\ 1 & 4 & 1 & 0 & \dots & 0 & 0 & 0 \\ 0 & 1 & 4 & 1 & \dots & 0 & 0 & 0 \\ \vdots & \vdots & \vdots & \vdots & \ddots & \vdots & \vdots & \vdots \\ 0 & 0 & 0 & 0 & \dots & 1 & 4 & 1 \\ \textcolor{red}{1} & 0 & 0 & 0 & \dots & 0 & 1 & 4 \end{pmatrix} \quad (\text{C.19})$$

and arranged

$$\mathbb{L}_P^{9p20} = \frac{1}{6h^2} \begin{pmatrix} \mathbb{D}_P^{9p20} & \mathbb{A} & \mathbb{O} & \mathbb{O} & \dots & \mathbb{O} & \mathbb{O} & \textcolor{red}{\mathbb{A}} \\ \mathbb{A} & \mathbb{D}_P^{9p20} & \mathbb{A} & \mathbb{O} & \dots & \mathbb{O} & \mathbb{O} & \mathbb{O} \\ \mathbb{O} & \mathbb{A} & \mathbb{D}_P^{9p20} & \mathbb{A} & \dots & \mathbb{O} & \mathbb{O} & \mathbb{O} \\ \vdots & \vdots & \vdots & \vdots & \ddots & \vdots & \vdots & \vdots \\ \mathbb{O} & \mathbb{O} & \mathbb{O} & \mathbb{O} & \dots & \mathbb{A} & \mathbb{D}_P^{9p20} & \mathbb{A} \\ \textcolor{red}{\mathbb{A}} & \mathbb{O} & \mathbb{O} & \mathbb{O} & \dots & \mathbb{O} & \mathbb{A} & \mathbb{D}_P^{9p20} \end{pmatrix} \quad (\text{C.20})$$

Neuman boundary conditions

For both zero and general NBCs the FD matrices are equal. Because the value at ghost nodes is either equal or derived from value of neighbour on the opposite side, the laplacian stencil behaves at the Neumann boundary as in Figure C.2.

The 5p stencil finite-difference matrix \mathbb{L}_N^{5p} with Neuman BC is composed of 4 different blocks: tridiagonal \mathbb{D}_N^{5p} , unit matrix \mathbb{I} , $2\mathbb{I}$ and zero matrix \mathbb{O} . These

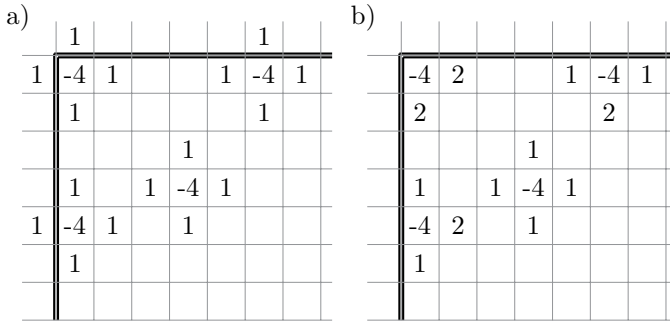


Figure C.2: Effect of Neuman BC on the 5pt laplacian stencil on the boundary points. Ghost points are outside the simulation domain but they can be accounted for thanks to knowing their value from equation C.1.

are:

$$\mathbb{D}_N^{5p} = \begin{pmatrix} -4 & 2 & 0 & 0 & \dots & 0 & 0 & 0 \\ 1 & -4 & 1 & 0 & \dots & 0 & 0 & 0 \\ 0 & 1 & -4 & 1 & \dots & 0 & 0 & 0 \\ \vdots & \vdots & \vdots & \vdots & \ddots & \vdots & \vdots & \vdots \\ 0 & 0 & 0 & 0 & \dots & 1 & -4 & 1 \\ 0 & 0 & 0 & 0 & \dots & 0 & 2 & 4 \end{pmatrix} \quad (C.21)$$

(C.22)

and are ordered as follows

$$\mathbb{L}_N^{5p} = \frac{1}{h^2} \begin{pmatrix} \mathbb{D}_N^{5p} & 2\mathbb{I} & \mathbb{O} & \mathbb{O} & \dots & \mathbb{O} & \mathbb{O} & \mathbb{O} \\ \mathbb{I} & \mathbb{D}_N^{5p} & \mathbb{I} & \mathbb{O} & \dots & \mathbb{O} & \mathbb{O} & \mathbb{O} \\ \mathbb{O} & \mathbb{I} & \mathbb{D}_N^{5p} & \mathbb{I} & \dots & \mathbb{O} & \mathbb{O} & \mathbb{O} \\ \vdots & \vdots & \vdots & \vdots & \ddots & \vdots & \vdots & \vdots \\ \mathbb{O} & \mathbb{O} & \mathbb{O} & \mathbb{O} & \dots & \mathbb{I} & \mathbb{D}_N^{5p} & \mathbb{I} \\ \mathbb{O} & \mathbb{O} & \mathbb{O} & \mathbb{O} & \dots & \mathbb{O} & 2\mathbb{I} & \mathbb{D}_N^{5p} \end{pmatrix} \quad (C.23)$$

In case of general NBC in 5-point stencil there must always be added or subtracted the term $2h|\nabla\eta|_{ij} \cos(\theta)$, where (i, j) are the boundary points. At the left and bottom boundary it is subtracted, at the right and top it is added.

The 9p20 stencil finite-difference matrix \mathbb{L}_N^{9p20} with Neuman BC is composed of 4 different blocks: tridiagonal \mathbb{D}_N^{9p20} , tridiagonal \mathbb{B} , $2\mathbb{B}$ and zero matrix \mathbb{O} . These

are

$$\mathbb{D}_N^{9p20} = \begin{pmatrix} -20 & 8 & 0 & 0 & \dots & 0 & 0 & 0 \\ 4 & -20 & 4 & 0 & \dots & 0 & 0 & 0 \\ 0 & 4 & -20 & 4 & \dots & 0 & 0 & 0 \\ \vdots & \vdots & \vdots & \vdots & \ddots & \vdots & \vdots & \vdots \\ 0 & 0 & 0 & 0 & \dots & 4 & -20 & 4 \\ 0 & 0 & 0 & 0 & \dots & 0 & 8 & -20 \end{pmatrix} \quad (C.24)$$

$$\mathbb{B} = \begin{pmatrix} 4 & 2 & 0 & 0 & \dots & 0 & 0 & 0 \\ 1 & 4 & 1 & 0 & \dots & 0 & 0 & 0 \\ 0 & 1 & 4 & 1 & \dots & 0 & 0 & 0 \\ \vdots & \vdots & \vdots & \vdots & \ddots & \vdots & \vdots & \vdots \\ 0 & 0 & 0 & 0 & \dots & 1 & 4 & 1 \\ 0 & 0 & 0 & 0 & \dots & 0 & 2 & 4 \end{pmatrix} \quad (C.25)$$

and are ordered as follows

$$\mathbb{L}_N^{9p20} = \frac{1}{6h^2} \begin{pmatrix} \mathbb{D}_N^{9p20} & 2\mathbb{B} & \mathbb{O} & \mathbb{O} & \dots & \mathbb{O} & \mathbb{O} & \mathbb{O} \\ \mathbb{B} & \mathbb{D}_N^{9p20} & \mathbb{B} & \mathbb{O} & \dots & \mathbb{O} & \mathbb{O} & \mathbb{O} \\ \mathbb{O} & \mathbb{B} & \mathbb{D}_N^{9p20} & \mathbb{B} & \dots & \mathbb{O} & \mathbb{O} & \mathbb{O} \\ \vdots & \vdots & \vdots & \vdots & \ddots & \vdots & \vdots & \vdots \\ \mathbb{O} & \mathbb{O} & \mathbb{O} & \mathbb{O} & \dots & \mathbb{B} & \mathbb{D}_N^{9p20} & \mathbb{B} \\ \mathbb{O} & \mathbb{O} & \mathbb{O} & \mathbb{O} & \dots & \mathbb{O} & 2\mathbb{B} & \mathbb{D}_N^{9p20} \end{pmatrix} \quad (C.26)$$

In case of general NBC in 9-point stencil the term $2h|\nabla\eta|_{ij} \cos(\theta)$ must be added or subtracted (depending on the boundary) correspondingly to the stencil, e.g. at the left boundary

$$\frac{1}{6h^2} \frac{1}{4} \begin{array}{c|c|c} 1 & 4 & 1 \\ \hline 4 & -20 & 4 \\ \hline 1 & 4 & 1 \end{array} \rightarrow \frac{1}{6h^2} \left[\begin{array}{c|c|c} 0 & 4 & 2 \\ \hline 0 & -20 & 8 \\ \hline 0 & 4 & 2 \end{array} - 2h \cos(\theta) (|\nabla\eta|_{0,j+1} + |\nabla\eta|_{0,j-1} + 4|\nabla\eta|_{0,j}) \right] \quad (C.27)$$

or e.g. at the top boundary

$$\frac{1}{6h^2} \frac{1}{4} \begin{array}{c|c|c} 1 & 4 & 1 \\ \hline -20 & 4 & 4 \\ \hline 1 & 4 & 1 \end{array} \rightarrow \frac{1}{6h^2} \left[\begin{array}{c|c|c} 0 & 0 & 0 \\ \hline 4 & -20 & 4 \\ \hline 2 & 8 & 2 \end{array} + 2h \cos(\theta) (|\nabla\eta|_{i+1,M} + |\nabla\eta|_{i-1,M} + 4|\nabla\eta|_{i,M}) \right] \quad (C.28)$$

Mixed boundary conditions

Imagine the system with BCs as indicated in figure C.3. The action of the finite

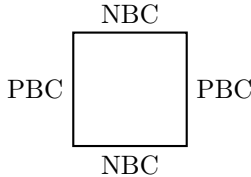


Figure C.3: Layout of the mixed boundaries. NBC and PBC stand for Neumann and periodic boundary conditions, respectively.

difference matrix in the y-direction is given by the structure of the individual block matrices and the x-direction by the arrangement of the blocks in the large matrix.

Specifically, with the periodic BCs present in the x-direction, the structure of the large matrix is as with periodic BCs only the diagonal block matrix. Showing on the example of the 5pt laplacian approximation with mixed BCs as in the figure C.3

$$\mathbb{L}_{PN}^{5p} = \frac{1}{h^2} \begin{pmatrix} \mathbb{D}_N^{5p} & \mathbb{I} & \mathbb{O} & \mathbb{O} & \dots & \mathbb{O} & \mathbb{O} & \textcolor{red}{\mathbb{I}} \\ \mathbb{I} & \mathbb{D}_N^{5p} & \mathbb{I} & \mathbb{O} & \dots & \mathbb{O} & \mathbb{O} & \mathbb{O} \\ \mathbb{O} & \mathbb{I} & \mathbb{D}_N^{5p} & \mathbb{I} & \dots & \mathbb{O} & \mathbb{O} & \mathbb{O} \\ \vdots & \vdots & \vdots & \vdots & \ddots & \vdots & \vdots & \vdots \\ \mathbb{O} & \mathbb{O} & \mathbb{O} & \mathbb{O} & \dots & \mathbb{I} & \mathbb{D}_N^{5p} & \mathbb{I} \\ \textcolor{red}{\mathbb{I}} & \mathbb{O} & \mathbb{O} & \mathbb{O} & \dots & \mathbb{O} & \mathbb{I} & \mathbb{D}_N^{5p} \end{pmatrix} \quad (\text{C.29})$$

In the 9p20 scheme the finite difference matrix is

$$\mathbb{L}_{PN}^{9p20} = \frac{1}{6h^2} \begin{pmatrix} \mathbb{D}_N^{9p20} & \mathbb{A} & \mathbb{O} & \mathbb{O} & \dots & \mathbb{O} & \mathbb{O} & \textcolor{red}{\mathbb{A}} \\ \mathbb{A} & \mathbb{D}_N^{9p20} & \mathbb{A} & \mathbb{O} & \dots & \mathbb{O} & \mathbb{O} & \mathbb{O} \\ \mathbb{O} & \mathbb{A} & \mathbb{D}_N^{9p20} & \mathbb{A} & \dots & \mathbb{O} & \mathbb{O} & \mathbb{O} \\ \vdots & \vdots & \vdots & \vdots & \ddots & \vdots & \vdots & \vdots \\ \mathbb{O} & \mathbb{O} & \mathbb{O} & \mathbb{O} & \dots & \mathbb{A} & \mathbb{D}_N^{9p20} & \mathbb{A} \\ \textcolor{red}{\mathbb{A}} & \mathbb{O} & \mathbb{O} & \mathbb{O} & \dots & \mathbb{O} & \mathbb{A} & \mathbb{D}_N^{9p20} \end{pmatrix} \quad (\text{C.30})$$

Anisotropic driving force terms

In phase field method, usually it is better to keep the interface away from the domain boundary as the boundary conditions often impose specific, non-physical behavior of the interface. In the case of general NBC and the intended use for

the energy assessment, the proximity of interface to the domain boundary is deliberate.

In the implementation of the inclination-dependent model, the anisotropic driving force terms are calculated from numeric derivatives of various fields. Care must be taken to each of the numerical derivative in order to assure the control over the interface inclination at the domain boundary.

When the interface inclination is fixed, the anisotropic driving force terms have fixed value (Dirichlet BC). Some of these fields are numerically differentiated again. However, their values at the ghost nodes are unknown (to be used in centered finite difference), hence one-sided FD scheme must be used at the boundaries. In order to keep second-order accuracy at the boundaries, the

following backward $\begin{bmatrix} 1/2 \\ -2 \\ 3/2 \end{bmatrix}$ and forward $\begin{bmatrix} -3/2 \\ 2 \\ -1/2 \end{bmatrix}$ FD schemes were used at the bottom and top boundary, respectively.

For the x-direction derivative the FD matrix is

$$\frac{\partial}{\partial x} \approx \Delta_x = \frac{1}{2h} \begin{pmatrix} -3\mathbb{I} & 4\mathbb{I} & -\mathbb{I} & 0 & \dots & 0 & 0 & 0 \\ -\mathbb{I} & 0 & \mathbb{I} & 0 & \dots & 0 & 0 & 0 \\ 0 & -\mathbb{I} & 0 & \mathbb{I} & \dots & 0 & 0 & 0 \\ \vdots & \vdots & \vdots & \ddots & \vdots & \vdots & \vdots & \vdots \\ 0 & 0 & 0 & 0 & \dots & -\mathbb{I} & 0 & \mathbb{I} \\ 0 & 0 & 0 & \dots & 0 & \mathbb{I} & -4\mathbb{I} & 3\mathbb{I} \end{pmatrix}. \quad (\text{C.31})$$

For the y-direction derivative the FD matrix is

$$\frac{\partial}{\partial y} \approx \Delta_y = \frac{1}{h} \begin{pmatrix} Y & 0 & 0 & \dots & 0 & 0 \\ 0 & Y & 0 & \dots & 0 & 0 \\ 0 & 0 & Y & \dots & 0 & 0 \\ \vdots & \vdots & \vdots & \ddots & \vdots & \vdots \\ 0 & 0 & 0 & \dots & Y & 0 \\ 0 & 0 & 0 & \dots & 0 & Y \end{pmatrix} \quad (\text{C.32})$$

with

$$Y = \begin{pmatrix} -3/2 & 2 & -1/2 & 0 & \dots & 0 & 0 & 0 \\ -1 & 0 & 1 & 0 & \dots & 0 & 0 & 0 \\ 0 & -1 & 0 & 1 & \dots & 0 & 0 & 0 \\ \vdots & \vdots & \vdots & \ddots & \vdots & \vdots & \vdots & \vdots \\ 0 & 0 & 0 & 0 & \dots & -1 & 0 & 1 \\ 0 & 0 & 0 & 0 & \dots & 1/2 & -2 & 3/2 \end{pmatrix} \quad (\text{C.33})$$

Appendix D

Volume conservation using Lagrange multipliers

Phase field equations under equality constraint - Lagrange multipliers

In multivariate calculus, the method of Lagrange multipliers is used to find extrema of a multivariate function under equality constraint, i.e. on a subset of its domain. For example, the extrema of the function $f(x, y)$ over the subset of the domain defined as $g(x, y) = 0$ can be found by analysis of the so-called Lagrange function $\mathcal{L}(x, y, \lambda) = f(x, y) - \lambda g(x, y)$, where λ is the Lagrange multiplier. The critical points are found by solving the set of equations

$$\frac{\partial \mathcal{L}}{\partial x} = 0, \quad \frac{\partial \mathcal{L}}{\partial y} = 0, \quad \frac{\partial \mathcal{L}}{\partial \lambda} = 0. \quad (\text{D.1})$$

Similar principles can be generalized in functional calculus. Let's have a functional of free energy $F[\phi] = \int f(\phi, \nabla\phi) dV$ with equality constraint $G[\phi] =$

$\int g(\phi)dV = 0$. The Lagrangian now takes the form

$$\Lambda[\phi, \lambda] = F[\phi] - \lambda G[\phi] \quad (\text{D.2})$$

$$= \int f(\phi, \nabla\phi) - \lambda g(\phi)dV \quad (\text{D.3})$$

$$= \int l(\phi)dV, \quad (\text{D.4})$$

where $l(\phi)$ is the lagrangian energy density and $\lambda(t)$ is the Lagrange multiplier. It is a function of time, because its value is related to the state of the evolving system. When the phase field $\phi(\mathbf{r})$ evolves due to governing equations

$$\frac{\partial\phi}{\partial t} = \frac{\delta\Lambda}{\delta\phi}, \quad (\text{D.5})$$

the equality constraint $G[\phi] = \int g(\phi)dV = 0$ will hold throughout the simulation. The constraint can e.g. impose some conservation law¹, or enforce local sum of values of phase fields in a multi-phase field model like in all multi-phase field models in the legacy of [78].

The governing equations then read

$$\frac{\delta\Lambda}{\delta\phi} = \frac{\delta F}{\delta\phi} - \lambda(t)\frac{\partial g}{\partial\phi}, \quad (\text{D.6})$$

where it was assumed that the constraint is only functional of the phase field, not of its gradient. It can be seen that an additional term appeared, originating from the constraint.

Multiple constraints $G_1[\phi] = 0, G_2[\phi] = 0, \dots, G_p[\phi] = 0$ can be imposed on the system, each of which has its Lagrange multiplier $\lambda_1, \lambda_2, \dots, \lambda_p$. The Lagrangian is then

$$\Lambda[\phi, \lambda_1, \lambda_2, \dots, \lambda_p] = F[\phi] - \sum_i \lambda_i G_i[\phi], \quad (\text{D.7})$$

which leads to constrained governing equation

$$\frac{\delta\Lambda}{\delta\phi} = \frac{\delta F}{\delta\phi} - \sum_i \lambda_i(t)\frac{\partial g_i}{\partial\phi}, \quad (\text{D.8})$$

where $g_i(\phi)$ is the kernel of i -th constraint $G_i[\phi] = \int g_i(\phi)dV$.

¹typically volume, but e.g. in [119, 120] electric charge and behavior of other physical quantities were controlled by Lagrange multipliers

Lagrange multipliers for volume conservation in multi-phase field models

This approach allows to mathematically enforce certain behavior of the evolving fields. Volume conservation in Allen-Cahn equation is a typical application.

Moelans' model is a multi phase field model with non-conserved fields and with curvature-driven interfaces motion. Inspired by [121], an extension of this model is hereby proposed, which allows to conserve volume of selected phase fields.

The model by Nestler et al. [121] is an extension of a phase field model which differs from the Moelans' one in several aspects. The main difference is that the sum of all the phase fields locally is equal to 1, which allows to interpret them as order parameters in the strict mathematical sense. However, this comes with a cost - this model property is imposed using a suitable Lagrange multiplier, which introduces new terms in the governing equation(s). Moreover, every model extension must be such that this property is preserved. Nestler's model also differs in the double obstacle potential and in the choice of the non-local gradient term.

Concept - single conserved phase field

The simulated system over the domain Ω consists of n phase fields $\vec{\eta} = (\eta_1, \dots, \eta_n)$ and is described by the free energy functional F with free energy density $f(\vec{\eta}, \nabla \vec{\eta})$ being also function of the phase fields gradients $\nabla \vec{\eta} = (\nabla \eta_1, \dots, \nabla \eta_n)$ as is usual in phase field method

$$F = \int_{\Omega} f(\vec{\eta}, \nabla \vec{\eta}) dV \quad (\text{D.9})$$

The volume V_i occupied by i -th grain η_i in the domain Ω can be expressed in Moelans' model as

$$V_i = \int_{\Omega} \Phi_i(\vec{\eta}) dV, \quad (\text{D.10})$$

where $\Phi_i(\vec{\eta})$ is the i -th grain expressed using the special interpolation function [122]

$$\Phi_i(\vec{\eta}) = \frac{\eta_i^2}{\sum_k \eta_k^2}. \quad (\text{D.11})$$

The equality constraint $G = 0$ which conserves volume of η_i can be formulated as

$$G = \int \Phi_i(\vec{\eta}) dV - V_i^0, \quad (\text{D.12})$$

where V_i^0 is the initial volume of the phase field. Because the constant V_i^0 plays no role in the governing equation, it will be disregarded. The volume conservation is ensured by deriving the governing equations from Lagrangian

$$\Lambda[\vec{\eta}] = \int_{\Omega} f(\vec{\eta}, \nabla \vec{\eta}) - \lambda(t) \Phi_i(\vec{\eta}) dV, \quad (\text{D.13})$$

leading to equation for any p -th phase field

$$\frac{\partial \eta_p}{\partial t} = \frac{\delta \Lambda}{\delta \eta_p} \quad (\text{D.14})$$

$$= \frac{\delta F}{\delta \eta_p} - \lambda(t) \frac{\partial \Phi_i}{\partial \eta_p}. \quad (\text{D.15})$$

Expression for the Lagrange multiplier $\lambda(t)$ is obtained from the constraint itself, as the volume conservation of η_i implies

$$\frac{dV_i}{dt} = 0 = \frac{\partial}{\partial t} \int \Phi_i(\vec{\eta}) dV \quad (\text{D.16})$$

$$= \int \frac{\partial \Phi_i}{\partial t} dV \quad (\text{D.17})$$

$$= \int \sum_{k=1}^n \frac{\partial \Phi_i}{\partial \eta_k} \frac{\partial \eta_k}{\partial t} dV \quad (\text{D.18})$$

$$= -L \int \sum_{k=1}^n \frac{\partial \Phi_i}{\partial \eta_k} \left[\frac{\delta F}{\delta \eta_k} - \lambda(t) \frac{\partial \Phi_i}{\partial \eta_k} \right] dV. \quad (\text{D.19})$$

In the last equation, $\lambda(t)$ can already be taken out of the integral as it is not function of space, allowing to write

$$\lambda(t) = \frac{\int \sum_{k=1}^n \frac{\partial \Phi_i}{\partial \eta_k} \frac{\delta F}{\delta \eta_p} dV}{\int \sum_{k=1}^n \left(\frac{\partial \Phi_i}{\partial \eta_k} \right)^2 dV}. \quad (\text{D.20})$$

As can be seen, the expression is notably more complicated than in the original model by Nestler. One reason is that the interpolation function $\Phi(\vec{\eta})$ is a function of all the phase fields, whereas in Nestler the interpolation function $p_k = p_k(\eta_k)$ only. The second reason is that in Nestler's model the volume evolution can be expressed as $dV_i/dt = \partial \eta_i / \partial t$. In comparison to Nestler's model, the first complication adds the sum over all phase fields to the integrals and the second adds the term $\partial \Phi_i / \partial \eta_k$.

Multiple conserved phase fields

Hereby the case when all the phase fields are conserved is discussed. With n phase fields that implies $n - 1$ constraints $G_i = \int \Phi_i(\vec{\eta}) dV = 0$ as the n -th phase field must be conserved as well when all the others are. Without the loss of generality it is assumed that the n -th phase field does not have its constraint. The Lagrangian is

$$\Lambda[\vec{\eta}] = \int_{\Omega} f(\vec{\eta}, \nabla \vec{\eta}) - \sum_{l=1}^{n-1} \lambda_l(t) \Phi_l(\vec{\eta}) dV, \quad (\text{D.21})$$

with $\lambda_l(t)$ being the Lagrange multiplier corresponding to l -th phase field.

Each governing equation can then be written in the form

$$\frac{\partial \eta_p}{\partial t} = \frac{\delta \Lambda}{\delta \eta_p} \quad (\text{D.22})$$

$$= \frac{\delta F}{\delta \eta_p} - \sum_{l=1}^{n-1} \lambda_l(t) \frac{\partial \Phi_l}{\partial \eta_p}. \quad (\text{D.23})$$

The individual Lagrange multipliers are determined from equation analogical to (D.16), i.e. for arbitrary i

$$\frac{dV_i}{dt} = 0 = \int \sum_{k=1}^n \frac{\partial \Phi_i}{\partial \eta_k} \frac{\partial \eta_k}{\partial t} dV \quad (\text{D.24})$$

$$= -L \int \sum_{k=1}^n \frac{\partial \Phi_i}{\partial \eta_k} \left[\frac{\delta F}{\delta \eta_k} - \sum_{l=1}^{n-1} \lambda_l(t) \frac{\partial \Phi_l}{\partial \eta_k} \right] dV. \quad (\text{D.25})$$

This equation can be rearranged to give

$$\int \sum_{k=1}^n \frac{\partial \Phi_i}{\partial \eta_k} \frac{\delta F}{\delta \eta_k} dV = \sum_{l=1}^{n-1} \lambda_l(t) \int \sum_{k=1}^n \frac{\partial \Phi_i}{\partial \eta_k} \frac{\partial \Phi_l}{\partial \eta_k} dV, \quad (\text{D.26})$$

which is a linear equation for $n - 1$ variables $\lambda_l(t)$. Because such equation can be written for every i of the $n - 1$ constrained phase fields, it is a system of linear algebraic equations which can be compactly described using the following notation

$$b_i = \int \sum_{k=1}^n \frac{\partial \Phi_i}{\partial \eta_k} \frac{\delta F}{\delta \eta_k} dV \quad (\text{D.27})$$

$$A_{il} = \int \sum_{k=1}^n \frac{\partial \Phi_i}{\partial \eta_k} \frac{\partial \Phi_l}{\partial \eta_k} dV, \quad (\text{D.28})$$

where b_i is a component of a vector \mathbf{b} and A_{il} is a component of the matrix \mathbf{A} . Denoting the vector with variables $\boldsymbol{\lambda}$, the system of $n - 1$ equations for $n - 1$ variables can be written

$$\mathbf{A}\boldsymbol{\lambda} = \mathbf{b}. \quad (\text{D.29})$$

Evaluation of this system is computationally very expensive, because in every component of both \mathbf{b} and \mathbf{A} there is the sum over all n phase fields. Moreover, it must be evaluated at every time step and it is expected, that all the components of \mathbf{A} are non-zero. Even though the matrix is symmetric, the model does not seem to be practical for use in simulations with many conserved grains.

Appendix E

Selected Wulff shape properties

E.1 Selected geometric properties of Wulff shape

With $h(\theta) = 1 + \delta \cos(n\theta)$, the minimal distance R_{min} between the Wulff shape center and the contour can be related to R_W as

$$R_{min} = R_W(1 - \delta), \quad (\text{E.1})$$

which holds for arbitrarily strong anisotropy because the minimal-radius point normal is always inclined under a non-missing angle. This formula was used to find the radius R_W of the phase field contour. Then, the phase field contour was scaled to unit radius and compared to the analytic Wulff shape (by means of Hausdorff distance, see the next subsection).

The radius of curvature $\varrho(\theta)$ of Wulff shape is locally

$$\varrho(\theta) = R_W[h''(\theta) + h(\theta)], \quad (\text{E.2})$$

which may technically get negative for some θ . Because that does not have any geometric interpretation, the Wulff shape does not contain such oriented segments and the angles θ_m fulfilling $\varrho(\theta_m) \leq 0$ are called missing or forbidden.

For a given radius R_W , the area of a Wulff shape A_W differs from the area of a circle $A = \pi R_W^2$ by the anisotropy-dependent factor $C_W(\Omega, n) = A_W/A$. For

weak anisotropy $\Omega < 1$ there is an analytic expression

$$C_W = 1 - \frac{\Omega^2}{n^2 - 1}, \quad (\text{E.3})$$

but there is none for strong anisotropy $\Omega > 1$. The factor $C_W(\Omega, n)$ was obtained numerically for $n = 4$ in the range $0 \leq \Omega \leq 7.5$ (the Wulff shape was plotted, its area numerically computed and divided by πR^2). There, the Ω -dependence was fitted very well by a polynomial of 4-th order $C_W(\Omega, 4) = \sum_{i=0}^4 a_i \Omega^{N-i}$ with $a_0 = -0.00032, a_1 = 0.00639, a_2 = -0.04219, a_3 = 0.00034, a_4 = 1.00000$.

E.2 Shrinkage rate of a Wulff shape

The normal velocity of anisotropic curvature-driven interface in 2D is [23]

$$v_n(\theta, t) = -\frac{\mu}{\varrho(\theta, t)} \sigma_0[h''(\theta) + h(\theta)] \quad (\text{E.4})$$

where μ is the interface mobility and $\sigma_0[h''(\theta) + h(\theta)]$ is interface stiffness. When it is the Wulff shape shrinking, the radius of curvature $\varrho(\theta, t)$ can be expressed as in equation (E.2) and the inclination-dependent part of the interface stiffness is cancelled out. The normal velocity is then constant along the perimeter

$$v_n(t) = -\frac{\mu \sigma_0}{R_W(t)}. \quad (\text{E.5})$$

The sign is such that the interface moves towards the center of curvature.

Because the area of a Wulff shape is $A_W = \pi R_W^2 C_W(\Omega, n)$, the shrinkage rate of a Wulff shape is

$$\begin{aligned} \frac{dA_W}{dt} &= \frac{d}{dt} [\pi R_W^2(t) C_W(\Omega, n)] \\ &= 2\pi C_W(\Omega, n) R_W(t) \frac{dR_W}{dt}. \end{aligned} \quad (\text{E.6})$$

Because the normal velocity is constant along the perimeter, the point R_{min} from equation (E.1) moves also by $v_n(t)$. Importantly, the normal of interface in R_{min} is aligned with the radial direction of the polar coordinates, hence we can write $v_n = dR_{min}/dt$. From equation (E.1) then must be

$$\frac{dR_W}{dt} = \frac{1}{1-\delta} \frac{dR_{min}}{dt} = \frac{1}{1-\delta} v_n(t), \quad (\text{E.7})$$

which together with E.5 implies in E.6

$$\frac{dA_W}{dt} = 2\pi\mu\sigma_0 \frac{C_W(\Omega, n)}{1 - \delta} \quad (\text{E.8})$$

Taylor and Cahn [68] proved that the shrinkage rate for the equilibrium shape must be a constant, which is met by the final expression.

Bibliography

- [1] M. Schlesinger and M. Paunovic. *Modern electroplating*. fifth. 2010. ISBN: 0471549681.
- [2] R. E. Dinnebier and S. J. L. Billinge. *Powder Diffraction: Theory and Practice*. The Royal Society of Chemistry, Mar. 2008. ISBN: 978-0-85404-231-9. DOI: 10.1039/9781847558237. URL: <https://doi.org/10.1039/9781847558237>.
- [3] J. A. Szpunar. “Texture in films and Coatings”. In: *MRS Online Proceedings Library (OPL)* 472 (1997), p. 45.
- [4] S. Suwas and R. K. Ray. *Crystallographic Texture of Materials*. Springer London, 2014. ISBN: 978-1-4471-6313-8. DOI: 10.1007/978-1-4471-6314-5. URL: <https://link.springer.com/10.1007/978-1-4471-6314-5>.
- [5] P. Barna and M. Adamik. “Fundamental structure forming phenomena of polycrystalline films and the structure zone models”. In: *Thin Solid Films* 317 (1-2 Apr. 1998), pp. 27–33. ISSN: 0040-6090. DOI: 10.1016/S0040-6090(97)00503-8. URL: <https://www.sciencedirect.com/science/article/abs/pii/S0040609097005038>.
- [6] M. Schlesinger and M. Paunovic. *Fundamentals of Electrochemical Deposition*. 2nd. 2006, p. 374. ISBN: 9780471712213.
- [7] N. Moelans, B. Blanpain, and P. Wollants. “Quantitative analysis of grain boundary properties in a generalized phase field model for grain growth in anisotropic systems”. In: *Physical Review B - Condensed Matter and Materials Physics* 78.2 (2008). ISSN: 10980121. DOI: 10.1103/PhysRevB.78.024113.
- [8] M. Minar and N. Moelans. “Benchmarking of different strategies to include anisotropy in a curvature-driven multi-phase-field model”. In: *Physical Review Materials* 6 (10 Oct. 2022), p. 103404. ISSN: 2475-9953.

- DOI: 10.1103/PhysRevMaterials.6.103404. URL: <https://link.aps.org/doi/10.1103/PhysRevMaterials.6.103404>.
- [9] H. Alimadadi, A. B. Fanta, T. Kasama, M. A. Somers, and K. Pantleon. “Texture and microstructure evolution in nickel electrodeposited from an additive-free Watts electrolyte”. In: *Surface and Coatings Technology* 299 (Aug. 2016), pp. 1–6. ISSN: 02578972. DOI: 10.1016/j.surfcoat.2016.04.068.
 - [10] M. Minar and N. Moelans. “Influence of surface energy anisotropy on nucleation and crystallographic texture of polycrystalline deposits”. In: *Computational Materials Science* 231 (Jan. 2024), p. 112575. ISSN: 0927-0256. DOI: 10.1016/j.commatsci.2023.112575. URL: <https://www.sciencedirect.com/science/article/abs/pii/S0927025623005694>.
 - [11] M. Minar. “Benchmarking of different strategies to include anisotropy in a curvature-driven multi-phase-field model”. In: *Mendeley Data*, v2 (2022). DOI: 10.17632/5wrv3ky9pp.2. URL: <http://dx.doi.org/10.17632/5wrv3ky9pp.2>.
 - [12] M. Minar. “Influence of surface energy anisotropy on nucleation and crystallographic texture of polycrystalline deposits”. In: *Mendeley Data*, v1 (2023). DOI: 10.17632/bsdff8shbz.1.
 - [13] A. Milchev. *Electrococrystallization: fundamentals of nucleation and growth*. Kluwer Academic Publishers, 2002. ISBN: 1-4020-7090-X. DOI: 10.1007/b113784.
 - [14] J. S. Vermaak, C. W. Mays, and D. Kuhlmann-Wilsdorf. “On surface stress and surface tension: I. Theoretical considerations”. In: *Surface Science* 12 (2 Oct. 1968), pp. 128–133. ISSN: 0039-6028. DOI: 10.1016/0039-6028(68)90118-0.
 - [15] C. A. Johnson. “Generalization of the Gibbs-Thomson equation”. In: *Surface Science* 3 (5 Dec. 1965), pp. 429–444. ISSN: 0039-6028. DOI: 10.1016/0039-6028(65)90024-5.
 - [16] I. Steinbach and H. Salama. “Capillarity”. In: *Lectures on Phase Field* (2023), pp. 31–39. DOI: 10.1007/978-3-031-21171-3_3. URL: https://doi.org/10.1007/978-3-031-21171-3_3.
 - [17] R. Kobayashi and Y. Giga. “On Anisotropy and Curvature Effects for Growing Crystals”. In: *Japan Journal of Industrial and Applied Mathematics* 18.2 (2001), pp. 207–230. ISSN: 09167005. DOI: 10.1007/BF03168571.

- [18] D. W. Hoffman and J. W. Cahn. “A vector thermodynamics for anisotropic surfaces. I. Fundamentals and application to plane surface junctions”. In: *Surface Science* 31.C (1972), pp. 368–388. ISSN: 00396028. DOI: 10.1016/0039-6028(72)90268-3.
- [19] J. Cahn and D. Hoffman. “A vector thermodynamics for anisotropic surfaces—II. Curved and faceted surfaces”. In: *Acta Metallurgica* 22.10 (Oct. 1974), pp. 1205–1214. ISSN: 00016160. DOI: 10.1016/0001-6160(74)90134-5. URL: <https://linkinghub.elsevier.com/retrieve/pii/0001616074901345>.
- [20] D. Du, H. Zhang, and D. Srolovitz. “Properties and determination of the interface stiffness”. In: *Acta Materialia* 55 (2 Jan. 2007), pp. 467–471. ISSN: 13596454. DOI: 10.1016/j.actamat.2006.08.038. URL: <https://linkinghub.elsevier.com/retrieve/pii/S1359645406006161>.
- [21] C. Herring. “Surface Tension as a Motivation for Sintering”. In: *Fundamental Contributions to the Continuum Theory of Evolving Phase Interfaces in Solids* (1999), pp. 33–69. DOI: 10.1007/978-3-642-59938-5_2. URL: https://link.springer.com/chapter/10.1007/978-3-642-59938-5_2.
- [22] Z. Trautt and M. Upmanyu. “Direct two-dimensional calculations of grain boundary stiffness”. In: *Scripta Materialia* 52 (11 June 2005), pp. 1175–1179. ISSN: 13596462. DOI: 10.1016/j.scriptamat.2004.12.033. URL: <https://linkinghub.elsevier.com/retrieve/pii/S135964620500014X>.
- [23] F. Abdeljawad, S. M. Foiles, A. P. Moore, A. R. Hinkle, C. M. Barr, N. M. Heckman, K. Hattar, and B. L. Boyce. “The role of the interface stiffness tensor on grain boundary dynamics”. In: *Acta Materialia* 158 (Oct. 2018), pp. 440–453. ISSN: 1359-6454. DOI: 10.1016/J.ACTAMAT.2018.06.025. URL: <https://www-sciencedirect-com.kuleuven.ezproxy.kuleuven.be/science/article/pii/S1359645418304932>.
- [24] R. D. Moore, T. Beecroft, G. S. Rohrer, C. M. Barr, E. R. Homer, K. Hattar, B. L. Boyce, and F. Abdeljawad. “The grain boundary stiffness and its impact on equilibrium shapes and boundary migration: Analysis of the Sigma5, 7, 9, and 11 boundaries in Ni”. In: *Acta Materialia* 218 (Oct. 2021), p. 117220. ISSN: 1359-6454. DOI: 10.1016/J.ACTAMAT.2021.117220.
- [25] K. H. Blixt and H. Hallberg. “Evaluation of grain boundary energy, structure and stiffness from phase field crystal simulations”. In: *Modelling and Simulation in Materials Science and Engineering* 30 (1 Jan. 2022), p. 014002. ISSN: 0965-0393. DOI: 10.1088/1361-651X/ac3ca1. URL: <https://iopscience.iop.org/article/10.1088/1361-651X/ac3ca1>.

- [26] D. J. Rowenhorst and P. W. Voorhees. “Measurements of the grain boundary energy and anisotropy in tin”. In: *Metallurgical and Materials Transactions A: Physical Metallurgy and Materials Science* 36 (8 2005), pp. 2127–2135. ISSN: 10735623. DOI: 10.1007/s11661-005-0333-7.
- [27] D. L. Olmsted, S. M. Foiles, and E. A. Holm. “Survey of computed grain boundary properties in face-centered cubic metals: I. Grain boundary energy”. In: *Acta Materialia* 57.13 (2009), pp. 3694–3703. ISSN: 13596454. DOI: 10.1016/j.actamat.2009.04.007. URL: <http://dx.doi.org/10.1016/j.actamat.2009.04.007>.
- [28] V. V. Bulatov, B. W. Reed, and M. Kumar. “Grain boundary energy function for fcc metals”. In: *Acta Materialia* 65 (2014), pp. 161–175. ISSN: 13596454. DOI: 10.1016/j.actamat.2013.10.057. URL: <http://dx.doi.org/10.1016/j.actamat.2013.10.057>.
- [29] J. Eggleston, G. McFadden, and P. Voorhees. “A phase-field model for highly anisotropic interfacial energy”. In: *Physica D: Nonlinear Phenomena* 150.1-2 (Mar. 2001), pp. 91–103. ISSN: 01672789. DOI: 10.1016/S0167-2789(00)00222-0. URL: <https://linkinghub.elsevier.com/retrieve/pii/S0167278900002220>.
- [30] M. Salvalaglio, R. Backofen, R. Bergamaschini, F. Montalenti, and A. Voigt. “Faceting of Equilibrium and Metastable Nanostructures: A Phase-Field Model of Surface Diffusion Tackling Realistic Shapes”. In: *Crystal Growth & Design* 15 (6 June 2015), pp. 2787–2794. ISSN: 1528-7483. DOI: 10.1021/acs.cgd.5b00165. URL: <https://pubs.acs.org/doi/10.1021/acs.cgd.5b00165>.
- [31] M. Fleck, L. Mushongera, D. Pilipenko, K. Ankit, and H. Emmerich. “On phase-field modeling with a highly anisotropic interfacial energy”. In: *The European Physical Journal Plus* 126.10 (Oct. 2011), p. 95. ISSN: 2190-5444. DOI: 10.1140/epjp/i2011-11095-7. URL: <http://link.springer.com/10.1140/epjp/i2011-11095-7>.
- [32] J. M. Debierre, A. Karma, F. Celestini, and R. Guérin. “Phase-field approach for faceted solidification”. In: *Physical Review E* 68.4 (2003), pp. 1–13. ISSN: 1063651X. DOI: 10.1103/PhysRevE.68.041604. arXiv: 0302368 [cond-mat].
- [33] I. Loginova, J. Ågren, and G. Amberg. “On the formation of Widmanstätten ferrite in binary Fe–C – phase-field approach”. In: *Acta Materialia* 52.13 (Aug. 2004), pp. 4055–4063. ISSN: 13596454. DOI: 10.1016/j.actamat.2004.05.033. URL: <https://linkinghub.elsevier.com/retrieve/pii/S1359645404002952>.

- [34] R. A. Marks and A. M. Glaeser. "Equilibrium and stability of triple junctions in anisotropic systems". In: *Acta Materialia* 60.1 (2012), pp. 349–358. ISSN: 1359-6454. DOI: 10.1016/j.actamat.2011.09.043. URL: <http://dx.doi.org/10.1016/j.actamat.2011.09.043>.
- [35] E. Bormashenko and V. Valtsifer. *Interfacial crystallization at the intersection of thermodynamic and geometry*. Oct. 2021. DOI: 10.1016/j.cis.2021.102510.
- [36] N. Tian, Z.-Y. Zhou, S.-G. Sun, Y. Ding, and Z. L. Wang. "Synthesis of Tetrahedrahedral Platinum Nanocrystals with High-Index Facets and High Electro-Oxidation Activity". In: *Science* 316 (5825 May 2007), pp. 732–735. ISSN: 0036-8075. DOI: 10.1126/science.1140484. URL: <http://www.sciencemag.org/cgi/doi/10.1126/science.1140484>.
- [37] C. V. Thompson. "Solid-State Dewetting of Thin Films". In: *Annual Review of Materials Research* 42 (1 Aug. 2012), pp. 399–434. ISSN: 1531-7331. DOI: 10.1146/annurev-matsci-070511-155048. URL: <https://www.annualreviews.org/doi/10.1146/annurev-matsci-070511-155048>.
- [38] O. Pierre-Louis. "Solid-state wetting at the nanoscale". In: *Progress in Crystal Growth and Characterization of Materials* 62 (2 June 2016), pp. 177–202. ISSN: 09608974. DOI: 10.1016/j.pcrysgrow.2016.04.009. URL: <https://linkinghub.elsevier.com/retrieve/pii/S0960897416300122>.
- [39] W. Bao, W. Jiang, D. J. Srolovitz, and Y. Wang. "Stable Equilibria of Anisotropic Particles on Substrates: A Generalized Winterbottom Construction". In: *SIAM Journal on Applied Mathematics* 77 (6 Jan. 2017), pp. 2093–2118. ISSN: 0036-1399. DOI: 10.1137/16M1091599.
- [40] R. Kaischew. ""unknown title"". In: *Commun. Bulg. Acad. Sci.* 2 (1951). reference 1.50 by milchev 2002 about the first publication of the equilibrium stable shape of faceted particle on a plane, p. 191.
- [41] W. L. Winterbottom. "Equilibrium shape of a small particle in contact with a foreign substrate". In: *Acta Metallurgica* 15 (2 1967), pp. 303–310. ISSN: 00016160. DOI: 10.1016/0001-6160(67)90206-4.
- [42] C. Boukouvala, J. Daniel, and E. Ringe. "Approaches to modelling the shape of nanocrystals". In: *Nano Convergence* 8 (1 Sept. 2021), p. 26. ISSN: 2196-5404. DOI: 10.1186/s40580-021-00275-6. URL: <https://nanoconvergencejournal.springeropen.com/articles/10.1186/s40580-021-00275-6>.

- [43] R. V. Zucker, D. Chatain, U. Dahmen, S. Hagège, and W. C. Carter. “New software tools for the calculation and display of isolated and attached interfacial-energy minimizing particle shapes”. In: *Journal of Materials Science* 47 (24 Dec. 2012), pp. 8290–8302. ISSN: 0022-2461. DOI: 10.1007/s10853-012-6739-x. URL: <http://link.springer.com/10.1007/s10853-012-6739-x>.
- [44] R. K. P. Zia, J. E. Avron, and J. E. Taylor. “The summertop construction: Crystals in a corner”. In: *Journal of Statistical Physics* 50 (3-4 Feb. 1988), pp. 727–736. ISSN: 0022-4715. DOI: 10.1007/BF01026498.
- [45] D. A. Porter, K. E. Easterling, and K. E. Easterling. *Phase Transformations in Metals and Alloys (Revised Reprint)*. third. CRC Press, Feb. 2009. ISBN: 9780429112256. DOI: 10.1201/9781439883570. URL: <https://www.taylorfrancis.com/books/9781439883570>.
- [46] A. Milchev. “Electrocrystallization: Nucleation and growth of nanoclusters on solid surfaces”. In: *Russian Journal of Electrochemistry* 44 (6 June 2008), pp. 619–645. ISSN: 1023-1935. DOI: 10.1134/S1023193508060025. URL: <http://link.springer.com/10.1134/S1023193508060025>.
- [47] V. Kozlov and L. P. Bicelli. “Texture formation of electrodeposited fcc metals”. In: *Materials Chemistry and Physics* 77 (1 Jan. 2003), pp. 289–293. ISSN: 02540584. DOI: 10.1016/S0254-0584(02)00004-4.
- [48] A. Mariaux and M. Rappaz. “Influence of anisotropy on heterogeneous nucleation”. In: *Acta Materialia* 59 (3 2011), pp. 927–933. ISSN: 1359-6454. DOI: 10.1016/j.actamat.2010.10.015.
- [49] A. Damjanovic, T. H. V. Setty, and J. O. Bockris. “Effect of Crystal Plane on the Mechanism and the Kinetics of Copper Electrocrystallization”. In: *J. Electrochem. Soc.* 113.5 (May 1966), p. 429. URL: <http://jes.ecsdl.org/cgi/doi/10.1149/1.2423989>.
- [50] S. Wang, E. Tian, and C. Lung. “Surface energy of arbitrary crystal plane of bcc and fcc metals”. In: *J. Phys. Chem. Solids* 61.8 (Aug. 2000), pp. 1295–1300. URL: <https://www.sciencedirect.com/science/article/pii/S0022369799004151>.
- [51] R. Tran, Z. Xu, B. Radhakrishnan, D. Winston, W. Sun, K. A. Persson, and S. P. Ong. “Surface energies of elemental crystals”. In: *Sci. Data* 3.1 (Dec. 2016), p. 160080. ISSN: 2052-4463. URL: <http://www.nature.com/articles/sdata201680>.

- [52] F. Wendler, C. Mennerich, and B. Nestler. “A phase-field model for polycrystalline thin film growth”. In: *Journal of Crystal Growth* 327.1 (2011), pp. 189–201. ISSN: 00220248. DOI: 10.1016/j.jcrysGro.2011.04.044. URL: <http://dx.doi.org/10.1016/j.jcrysGro.2011.04.044>.
- [53] A. Anders. “A structure zone diagram including plasma-based deposition and ion etching”. In: *Thin Solid Films* 518 (15 May 2010), pp. 4087–4090. ISSN: 0040-6090. DOI: 10.1016/J.TSF.2009.10.145.
- [54] R. Winand. “Electrocrystallization - theory and applications”. In: *Hydrometallurgy* 29 (1-3 June 1992), pp. 567–598. ISSN: 0304386X. DOI: 10.1016/0304-386X(92)90033-V. URL: <https://linkinghub.elsevier.com/retrieve/pii/0304386X9290033V>.
- [55] J. A. Thornton and D. Hoffman. “Stress-related effects in thin films”. In: *Thin Solid Films* 171 (1 Apr. 1989), pp. 5–31. ISSN: 0040-6090. DOI: 10.1016/0040-6090(89)90030-8. URL: <https://www.sciencedirect.com/science/article/pii/0040609089900308>.
- [56] C. Thompson. “Texture evolution during grain growth in polycrystalline films”. In: *Scripta Metallurgica et Materialia* 28 (2 Jan. 1993), pp. 167–172. ISSN: 0956-716X. DOI: 10.1016/0956-716X(93)90557-9.
- [57] E. Chason and A. M. Engwall. “Relating residual stress to thin film growth processes via a kinetic model and real-time experiments”. In: *Thin Solid Films* 596 (2015), pp. 2–7. ISSN: 00406090. DOI: 10.1016/j.tsf.2015.06.061. URL: <http://dx.doi.org/10.1016/j.tsf.2015.06.061>.
- [58] G. Abadias, E. Chason, J. Keckes, M. Sebastiani, G. B. Thompson, E. Barthel, G. L. Doll, C. E. Murray, C. H. Stoessel, and L. Martinu. “Review Article: Stress in thin films and coatings: Current status, challenges, and prospects”. In: *Journal of Vacuum Science & Technology A: Vacuum, Surfaces, and Films* 36 (2 Mar. 2018), p. 020801. ISSN: 0734-2101. DOI: 10.1116/1.5011790. URL: <http://avs.scitation.org/doi/10.1116/1.5011790>.
- [59] E. Chason, B. W. Sheldon, L. B. Freund, J. A. Floro, and S. J. Hearne. “Origin of Compressive Residual Stress in Polycrystalline Thin Films”. In: *Physical Review Letters* 88 (15 2002), p. 4. ISSN: 10797114. DOI: 10.1103/PhysRevLett.88.156103.
- [60] J. Amblard, I. Epelboin, M. Froment, and G. Maurin. “Inhibition and nickel electrocrystallization”. In: *Journal of Applied Electrochemistry* 9 (2 Mar. 1979), pp. 233–242. ISSN: 0021-891X. DOI: 10.1007/BF00616093.

- [61] C. B. Nielsen, A. Horsewell, and M. J. Østergård. “On texture formation of nickel electrodeposits”. In: *Journal of Applied Electrochemistry* 27 (7 1997), pp. 839–845. ISSN: 0021891X. DOI: 10.1023/A:1018429013660.
- [62] A. A. Rasmussen, J. A. Jensen, A. Horsewell, and M. A. Somers. “Microstructure in electrodeposited copper layers; the role of the substrate”. In: *Electrochimica Acta* 47 (1-2 Sept. 2001), pp. 67–74. ISSN: 00134686. DOI: 10.1016/S0013-4686(01)00583-7.
- [63] R. Kobayashi. “Modeling and numerical simulations of dendritic crystal growth”. In: *Physica D* 63 (1993), pp. 410–423. ISSN: 01672789. DOI: 10.1016/0167-2789(93)90120-P.
- [64] I. Bellemans, N. Moelans, and K. Verbeken. “Phase-Field Modelling in Extractive Metallurgy”. In: *Critical Reviews in Solid State and Materials Sciences* 0 (0 2017), pp. 1–38. ISSN: 1040-8436. DOI: 10.1080/10408436.2017.1397500.
- [65] C. M. Elliott and R. Schätzle. “The limit of the anisotropic double-obstacle Allen-Cahn equation”. In: *Royal Society of Edinburgh - Proceedings A* 126.6 (1996), pp. 1217–1234. ISSN: 03082105. DOI: 10.1017/S0308210500023374.
- [66] O. Tschukin, A. Silberzahn, M. Selzer, P. G. K. Amos, D. Schneider, and B. Nestler. “Concepts of modeling surface energy anisotropy in phase - field approaches”. In: *Geothermal Energy* (2017). ISSN: 2195-9706. DOI: 10.1186/s40517-017-0077-9.
- [67] G. B. McFadden, A. A. Wheeler, R. J. Braun, S. R. Coriell, and R. F. Sekerka. “Phase-field models for anisotropic interfaces”. In: *Physical Review E* 48.3 (Sept. 1993), pp. 2016–2024. ISSN: 1063-651X. DOI: 10.1103/PhysRevE.48.2016. URL: <https://link.aps.org/doi/10.1103/PhysRevE.48.2016>.
- [68] J. E. Taylor and J. W. Cahn. “Diffuse interfaces with sharp corners and facets: Phase field models with strongly anisotropic surfaces”. In: *Physica D: Nonlinear Phenomena* 112.3-4 (Feb. 1998), pp. 381–411. ISSN: 01672789. DOI: 10.1016/S0167-2789(97)00177-2. URL: <https://linkinghub.elsevier.com/retrieve/pii/S0167278997001772>.
- [69] A. A. Wheeler. “Phase-field theory of edges in an anisotropic crystal”. In: *Proceedings of the Royal Society A: Mathematical, Physical and Engineering Sciences* 462.2075 (2006), pp. 3363–3384. ISSN: 14712946. DOI: 10.1098/rspa.2006.1721.

- [70] N. Ma, Q. Chen, and Y. Wang. “Implementation of high interfacial energy anisotropy in phase field simulations”. In: *Scripta Materialia* 54.11 (June 2006), pp. 1919–1924. ISSN: 1359-6462. DOI: 10.1016/J.SCRIPTAMAT.2006.02.005. URL: <https://www.sciencedirect.com/science/article/pii/S1359646206001266>.
- [71] S. Torabi, J. Lowengrub, A. Voigt, and S. Wise. “A new phase-field model for strongly anisotropic systems”. In: *Proceedings of the Royal Society A: Mathematical, Physical and Engineering Sciences* 465.2105 (2009), pp. 1337–1359. ISSN: 14712946. DOI: 10.1098/rspa.2008.0385.
- [72] G. Bellettini and M. Paolini. “Anisotropic motion by mean curvature in the context of finsler geometry”. In: *Hokkaido Mathematical Journal* 25.3 (1996), pp. 537–566. ISSN: 03854035. DOI: 10.14492/hokmj/1351516749.
- [73] M. Beneš. “Diffuse-interface treatment of the anisotropic mean-curvature flow”. In: *Applications of Mathematics* 48.6 (2003), pp. 437–453. ISSN: 08627940. DOI: 10.1023/B:APOM.0000024485.24886.b9.
- [74] H. Miura. “Anisotropy function of kinetic coefficient for phase-field simulations: Reproduction of kinetic Wulff shape with arbitrary face angles”. In: *Journal of Crystal Growth* 367 (2013), pp. 8–17. ISSN: 00220248. DOI: 10.1016/j.jcrysGro.2013.01.014. URL: <http://dx.doi.org/10.1016/j.jcrysGro.2013.01.014>.
- [75] G. I. Tóth, T. Pusztai, and L. Gránásy. “Consistent multiphase-field theory for interface driven multidomain dynamics”. In: *Physical Review B - Condensed Matter and Materials Physics* 92.18 (2015), pp. 1–19. ISSN: 1550235X. DOI: 10.1103/PhysRevB.92.184105. arXiv: 1508.04311.
- [76] V. Yadav and N. Moelans. “Investigation on the existence of a ‘Hillert regime’ in normal grain growth”. In: *Scripta Materialia* 142 (Jan. 2018), pp. 148–152. ISSN: 1359-6462. DOI: 10.1016/J.SCRIPTAMAT.2017.08.036. URL: <https://www.sciencedirect.com.kuleuven.ezproxy.kuleuven.be/science/article/pii/S1359646217305006>.
- [77] L.-Q. Chen and W. Yang. “Computer simulation of the domain dynamics of a quenched system with a large number of nonconserved order parameters: The grain-growth kinetics”. In: *Physical Review B* 50 (21 Dec. 1994), pp. 15752–15756. ISSN: 0163-1829. DOI: 10.1103/PhysRevB.50.15752. URL: <https://link.aps.org/doi/10.1103/PhysRevB.50.15752>.
- [78] I. Steinbach, F. Pezzolla, B. Nestler, M. Sedlberg, R. G. J. Ptiele, and J. L. L. Rezende. “A phase field concept for multiphase systems”. In: *Physica D* 94 (1996), pp. 135–147. URL: [https://doi.org/10.1016/0167-2789\(95\)00298-7](https://doi.org/10.1016/0167-2789(95)00298-7).

- [79] R. Kobayashi, J. Warren, and W. Carter. “Vector-valued phase field model for crystallization and grain boundary formation”. In: *Physica D: Nonlinear Phenomena* 119 (3-4 Aug. 1998), pp. 415–423. ISSN: 0167-2789. DOI: 10.1016/S0167-2789(98)00026-8. URL: <https://www.sciencedirect.com.kuleuven.ezproxy.kuleuven.be/science/article/pii/S0167278998000268>.
- [80] N. Moelans, F. Wendler, and B. Nestler. “Comparative study of two phase-field models for grain growth”. In: *Computational Materials Science* 46.2 (2009), pp. 479–490. ISSN: 0927-0256. DOI: 10.1016/j.commatsci.2009.03.037. URL: <http://dx.doi.org/10.1016/j.commatsci.2009.03.037>.
- [81] S. Daubner, P. W. Hoffrogge, M. Minar, and B. Nestler. “Triple junction benchmark for multiphase-field and multi-order parameter models”. In: *Computational Materials Science* 219 (Feb. 2023), p. 111995. ISSN: 0927-0256. DOI: 10.1016/j.commatsci.2022.111995. URL: <https://www.sciencedirect.com/science/article/abs/pii/S0927025622007066>.
- [82] J. Eiken, B. Böttger, and I. Steinbach. “Multiphase-field approach for multicomponent alloys with extrapolation scheme for numerical application”. In: *Physical Review E* 73 (6 June 2006), p. 066122. ISSN: 15393755. DOI: 10.1103/PhysRevE.73.066122. URL: <https://journals.aps.org.kuleuven.e-bronnen.be/pre/abstract/10.1103/PhysRevE.73.066122>.
- [83] C. J. Permann, D. R. Gaston, D. Andrš, R. W. Carlsen, F. Kong, A. D. Lindsay, J. M. Miller, J. W. Peterson, A. E. Slaughter, R. H. Stogner, and R. C. Martineau. “MOOSE: Enabling massively parallel multiphysics simulation”. In: *SoftwareX* 11 (Jan. 2020), p. 100430. ISSN: 2352-7110. DOI: 10.1016/J.SOFTX.2020.100430.
- [84] V. Yadav, L. Vanherpe, and N. Moelans. “Effect of volume fractions on microstructure evolution in isotropic volume-conserved two-phase alloys: A phase-field study”. In: *Computational Materials Science* 125 (2016), pp. 297–308. ISSN: 09270256. DOI: 10.1016/j.commatsci.2016.08.037. URL: <http://dx.doi.org/10.1016/j.commatsci.2016.08.037>.
- [85] K. Sadamoto, Y. Tadano, and S. Morita. “A Three-Dimensional Formulation of Phase Field Model Representing Polycrystalline Solidification”. In: *Key Engineering Materials* 794 (2019), pp. 208–213. ISSN: 1662-9795. DOI: 10.4028/WWW.SCIENTIFIC.NET/KEM.794.208. URL: <https://www.scientific-net.kuleuven.e-bronnen.be/KEM.794.208>.

- [86] H. Garcke, B. Stoth, and B. Nestler. “Anisotropy in multi-phase systems: a phase field approach”. In: *Interfaces and Free Boundaries* 1.2 (1999), pp. 175–198. ISSN: 1463-9963. DOI: 10.4171/IFB/8. URL: <http://www.ems-ph.org/doi/10.4171/IFB/8>.
- [87] H. Salama, J. Kundin, O. Shchyglo, V. Mohles, K. Marquardt, and I. Steinbach. “Role of inclination dependence of grain boundary energy on the microstructure evolution during grain growth”. In: *Acta Materialia* 188 (2020), pp. 641–651. ISSN: 13596454. DOI: 10.1016/j.actamat.2020.02.043. URL: <https://doi.org/10.1016/j.actamat.2020.02.043>.
- [88] A. Kazaryan, Y. Wang, and S. Dregia. “Generalized phase-field model for computer simulation of grain growth in anisotropic systems”. In: *Physical Review B - Condensed Matter and Materials Physics* 61.21 (2000), pp. 14275–14278. ISSN: 1550235X. DOI: 10.1103/PhysRevB.61.14275. arXiv: 9912044 [cond-mat].
- [89] H. Henry, J. Mellenthin, and M. Plapp. “Orientation-field model for polycrystalline solidification with a singular coupling between order and orientation”. In: *Physical Review B - Condensed Matter and Materials Physics* 86 (5 2012), pp. 1–15. ISSN: 1550235X. DOI: 10.1103/PhysRevB.86.054117.
- [90] B. Korbuly, M. Plapp, H. Henry, J. A. Warren, L. Gránásy, and T. Pusztai. “Topological defects in two-dimensional orientation-field models for grain growth”. In: *Physical Review E* 96 (5 2017), pp. 1–15. ISSN: 24700053. DOI: 10.1103/PhysRevE.96.052802.
- [91] L. Chen, H. W. Zhang, L. Y. Liang, Z. Liu, Y. Qi, P. Lu, J. Chen, and L. Q. Chen. “Modulation of dendritic patterns during electrodeposition: A nonlinear phase-field model”. In: *Journal of Power Sources* 300 (2015), pp. 376–385. ISSN: 03787753. DOI: 10.1016/j.jpowsour.2015.09.055. URL: <http://dx.doi.org/10.1016/j.jpowsour.2015.09.055>.
- [92] A. Jokisaari, P. Voorhees, J. Guyer, J. Warren, and O. Heinonen. “Benchmark problems for numerical implementations of phase field models”. In: *Computational Materials Science* 126 (Jan. 2017), pp. 139–151. ISSN: 0927-0256. DOI: 10.1016/J.COMMATSCI.2016.09.022. URL: <https://www.sciencedirect.com/science/article/pii/S0927025616304712>.
- [93] E. Miyoshi, T. Takaki, M. Ohno, and Y. Shibuta. “Accuracy evaluation of phase-field models for grain growth simulation with anisotropic grain boundary properties”. In: *ISIJ International* 60.1 (2020), pp. 160–167. ISSN: 09151559. DOI: 10.2355/isijinternational.ISIJINT-2019-305.

- [94] N. Moelans, F. Spaepen, and P. Wollants. “Grain growth in thin films with a fibre texture studied by phase-field simulations and mean field modelling”. In: *Philosophical Magazine* 90.1-4 (2010), pp. 501–523. ISSN: 14786435. DOI: 10.1080/14786430902998129.
- [95] H. Ravash, J. Vleugels, and N. Moelans. “Three-dimensional phase-field simulation of microstructural evolution in three-phase materials with different interfacial energies and different diffusivities”. In: *Journal of Materials Science* 52.24 (Dec. 2017), pp. 13852–13867. ISSN: 0022-2461. DOI: 10.1007/s10853-017-1465-z. URL: <http://link.springer.com/10.1007/s10853-017-1465-z>.
- [96] M. Minar and N. Moelans. “See Supplemental material at xxx for the best practices in parameters determination in Moelans’ model and for further details on the implementation.” In: *Phys. Rev. Mat.* (2022).
- [97] H. Alt, C. Knauer, and C. Wenk. “Comparison of Distance Measures for Planar Curves”. In: *Algorithmica* 38.1 (Jan. 2004), pp. 45–58. ISSN: 0178-4617. DOI: 10.1007/s00453-003-1042-5. URL: <http://link.springer.com/10.1007/s00453-003-1042-5>.
- [98] Li Zhu and Chun-qiang Zhu. “Application of Hausdorff distance in image matching”. In: *2014 IEEE Workshop on Electronics, Computer and Applications*. 3. IEEE, May 2014, pp. 97–100. ISBN: 978-1-4799-4565-8. DOI: 10.1109/IWECA.2014.6845566. URL: <http://ieeexplore.ieee.org/document/6845566/>.
- [99] M. V. Landau, R. Vidruk, D. Vingurt, D. Fuks, and M. Herskowitz. “Grain boundaries in nanocrystalline catalytic materials as a source of surface chemical functionality”. In: *Reviews in Chemical Engineering* 30 (4 Aug. 2014), pp. 379–401. ISSN: 01678299. DOI: 10.1515/REVCE-2014-0011/MACHINEREADABLECITATION/RIS. URL: <https://www.degruyter.com/document/doi/10.1515/revce-2014-0011/html>.
- [100] X. Xu, Y. Zhong, M. Wajrak, T. Bhatelia, S. P. Jiang, and Z. Shao. “Grain boundary engineering: An emerging pathway toward efficient electrocatalysis”. In: *InfoMat* 6 (8 Aug. 2024), e12608. ISSN: 2567-3165. DOI: 10.1002/INF2.12608. URL: <https://onlinelibrary.wiley.com/doi/abs/10.1002/inf2.12608>.
- [101] L. Wang, X. Yao, H. Fruehwald, D. Akhmetzyanov, M. Hanson, N. Chen, R. Smith, C. V. Singh, Z. Tan, and Y. A. Wu. “Revealing Real Active Sites in Intricate Grain Boundaries Assemblies on Electroreduction of CO₂ to C₂+ Products”. In: *Advanced Energy Materials* (2024), p. 2402636. ISSN: 1614-6840. DOI: 10.1002/AENM.202402636. URL: <https://onlinelibrary.wiley.com/doi/abs/10.1002/aenm.202402636>.

- [102] L. Gránásy, T. Pusztai, D. Saylor, and J. A. Warren. “Phase Field Theory of Heterogeneous Crystal Nucleation”. In: *Physical Review Letters* 98 (3 Jan. 2007), p. 035703. ISSN: 0031-9007. DOI: 10.1103/PhysRevLett.98.035703. URL: <https://link.aps.org/doi/10.1103/PhysRevLett.98.035703>.
- [103] V. Yadav and N. Moelans. “Comparison of coarsening behaviour in non-conserved and volume-conserved isotropic two-phase grain structures”. In: *Scripta Materialia* 146 (2018), pp. 142–145. ISSN: 13596462. DOI: 10.1016/j.scriptamat.2017.11.023. URL: <https://doi.org/10.1016/j.scriptamat.2017.11.023>.
- [104] J. Ustarroz, J. A. Hammons, T. Altantzis, A. Hubin, S. Bals, and H. Terryn. “A generalized electrochemical aggregative growth mechanism”. In: *Journal of the American Chemical Society* 135 (31 2013), pp. 11550–11561. ISSN: 00027863. DOI: 10.1021/ja402598k.
- [105] W. Monnens, B. Zhang, Z. Zhou, L. Snels, K. Binnemans, F. Molina-Lopez, and J. Fransaer. “Scalable Electrodeposition of Liquid Metal from an Acetonitrile-Based Electrolyte for Highly Integrated Stretchable Electronics”. In: *Advanced Materials* 35 (51 Dec. 2023), p. 2305967. ISSN: 1521-4095. DOI: 10.1002/adma.202305967. URL: <https://onlinelibrary.wiley.com/doi/abs/10.1002/adma.202305967>.
- [106] V. Consonni, G. Feuillet, and P. Gergaud. “The flow stress in polycrystalline films: Dimensional constraints and strengthening effects”. In: *Acta Materialia* 56 (20 Dec. 2008), pp. 6087–6096. ISSN: 1359-6454. DOI: 10.1016/J.ACTAMAT.2008.08.019.
- [107] P. Sonnweber-Ribic, P. Gruber, G. Dehm, and E. Arzt. “Texture transition in Cu thin films: Electron backscatter diffraction vs. X-ray diffraction”. In: *Acta Materialia* 54 (15 Sept. 2006), pp. 3863–3870. ISSN: 13596454. DOI: 10.1016/j.actamat.2006.03.057.
- [108] J. Sanchez and E. Arzt. “Effects of grain orientation on hillock formation and grain growth in aluminum films on silicon substrates”. In: *Scripta Metallurgica et Materialia* 27 (3 Aug. 1992), pp. 285–290. ISSN: 0956-716X. DOI: 10.1016/0956-716X(92)90513-E.
- [109] N. Pangarov. “The crystal orientation of electrodeposited metals”. In: *Electrochimica Acta* 7 (1 Jan. 1962), pp. 139–146. ISSN: 00134686. DOI: 10.1016/0013-4686(62)80023-1.
- [110] N. A. Pangarov. “On the crystal orientation of electrodeposited metals”. In: *Electrochimica Acta* 9 (6 1964), pp. 721–726. ISSN: 00134686. DOI: 10.1016/0013-4686(64)80060-8.

- [111] G. Wulff. "XXV. Zur Frage der Geschwindigkeit des Wachstums und der Auflösung der Krystallflächen". In: *Zeitschrift für Kristallographie - Crystalline Materials* 34 (1-6 Dec. 1901), pp. 449–530. ISSN: 2196-7105. DOI: 10.1524/zkri.1901.34.1.449.
- [112] W. E. Kingston. *The Physics of Powder Metallurgy: A Symposium Held at Bayside, LI, New York, August 24-26, 1949*. McGraw-Hill, 1951, p. 143.
- [113] W. K. Burton, N. Cabrera, and F. C. Frank. "The Growth of Crystals and the Equilibrium Structure of their Surfaces". In: *Philosophical Transactions of the Royal Society A: Mathematical, Physical and Engineering Sciences* 243.866 (1951), pp. 299–358. ISSN: 1364-503X. DOI: 10.1098/rsta.1951.0006.
- [114] Wikipedia. *Modulo*. 2023. (Visited on 05/11/2023).
- [115] D. Li and J. Szpunar. "A Monte Carlo simulation approach to the texture formation during electrodeposition—I. The simulation model". In: *Electrochimica Acta* 42 (1 Jan. 1997), pp. 37–45. ISSN: 00134686. DOI: 10.1016/0013-4686(96)00164-8.
- [116] D. Li and J. Szpunar. "A Monte Carlo simulation approach to the texture formation during electrodeposition—II. Simulation and experiment". In: *Electrochimica Acta* 42 (1 Jan. 1997), pp. 47–60. ISSN: 00134686. DOI: 10.1016/0013-4686(96)00158-2.
- [117] I. Steinbach and F. Pezzolla. "A generalized field method for multiphase transformations using interface fields". In: *Physica D: Nonlinear Phenomena* 134.4 (1999), pp. 385–393. ISSN: 01672789. DOI: 10.1016/S0167-2789(99)00129-3.
- [118] B. Nestler, H. Garcke, and B. Stinner. "Multicomponent alloy solidification: Phase-field modeling and simulations". In: *Physical Review E* 71.4 (2005), p. 041609. DOI: 10.1103/PhysRevE.71.041609. URL: <https://link.aps.org/doi/10.1103/PhysRevE.71.041609>.
- [119] J. E. Guyer, W. J. Boettinger, J. A. Warren, and G. B. McFadden. "Phase field modeling of electrochemistry. I. Equilibrium". In: *Physical Review E* 69 (2 Feb. 2004), p. 021603. ISSN: 1539-3755. DOI: 10.1103/PhysRevE.69.021603. URL: <https://link.aps.org/doi/10.1103/PhysRevE.69.021603>.
- [120] J. E. Guyer, W. J. Boettinger, J. A. Warren, and G. B. McFadden. "Phase field modeling of electrochemistry. II. Kinetics". In: *Physical Review E* 69 (2 Feb. 2004), p. 021604. ISSN: 1539-3755. DOI: 10.1103/PhysRevE.69.021604. URL: <http://arxiv.org/abs/cond-mat/0308179%0Ahttp://dx.doi.org/10.1103/PhysRevE.69.021604%20https://link.aps.org/doi/10.1103/PhysRevE.69.021604>.

- [121] B. Nestler, F. Wendler, M. Selzer, B. Stinner, and H. Garcke. “Phase-field model for multiphase systems with preserved volume fractions”. In: *Physical Review E - Statistical, Nonlinear, and Soft Matter Physics* 78 (1 2008), pp. 1–7. ISSN: 15393755. DOI: 10.1103/PhysRevE.78.011604.
- [122] N. Moelans. “A quantitative and thermodynamically consistent phase-field interpolation function for multi-phase systems”. In: *Acta Materialia* 59.3 (2011), pp. 1077–1086. ISSN: 13596454. URL: <http://dx.doi.org/10.1016/j.actamat.2010.10.038>.

List of publications

First-author publications

[8] Minar, M., Moelans, N. (2022). Benchmarking of different strategies to include anisotropy in a curvature-driven multi-phase-field model. *Physical Review Materials*, 6(10), 103404.

<https://doi.org/10.1103/PhysRevMaterials.6.103404>

[10] Minar, M., Moelans, N. (2024). Influence of surface energy anisotropy on nucleation and crystallographic texture of polycrystalline deposits. *Computational Materials Science*, 231, 112575.

<https://doi.org/10.1016/J.COMMATSCI.2023.112575>

Collaborations

[81] Daubner, S., Hoffrogge, P. W., Minar, M., Nestler, B. (2023). Triple junction benchmark for multiphase-field and multi-order parameter models. *Computational Materials Science*, 219, 111995.

<https://doi.org/10.1016/J.COMMATSCI.2022.111995>